UNIVERSIDADE ESTADUAL DE CAMPINAS
SCHOOL OF ELECTRICAL AND COMPUTER ENGINEERING (FEEC)

DANILO IGLESIAS BRANDÃO

COORDINATED POWER-BASED CONTROL AND UTILITY INTERFACE CONVERTER IN LOW VOLTAGE MICROGRIDS

CONTROLE COORDENADO EM MICRORREDES DE BAIXA TENSÃO BASEADO NO ALGORITMO POWER-BASED CONTROL E CONVERSOR UTILITY INTERFACE

CAMPINAS
2015

DANILO IGLESIAS BRANDÃO

COORDINATED POWER-BASED CONTROL AND UTILITY INTERFACE CONVERTER IN LOW VOLTAGE MICROGRIDS

CONTROLE COORDENADO EM MICRORREDES DE BAIXA TENSÃO BASEADO NO ALGORITMO POWER-BASED CONTROL E CONVERSOR UTILITY INTERFACE

Thesis presented to the School of Electrical and Computer Engineering of the University of Campinas in partial fulfillment of the requirements for the degree of Doctor, in the area of electrical energy

Tese apresentada à Faculdade de Engenharia Elétrica e de Computação da Universidade Estadual de Campinas como parte dos requisitos exigidos para a obtenção do título de Doutor em Engenharia Elétrica na área de concentração Energia Elétrica

Adviser: Prof. José Antenor Pomilio, PhD
Co-adviser: Prof. Fernando Pinhabel Marafão, PhD

ESTE EXEMPLAR CORRESPONDE À VERSÃO FINAL DA TESE DEFENDIDA PELO ALUNO DANILO IGLESIAS BRANDÃO, E ORIENTADA PELO PROF. JOSÉ ANTENOR POMILIO

CAMPINAS
2015

Ficha catalográfica
Universidade Estadual de Campinas
Biblioteca da Área de Engenharia e Arquitetura
Elizangela Aparecida dos Santos Souza - CRB 8/8098

Informações para Biblioteca Digital

COMISSÃO JULGADORA – TESE DE DOUTORADO

Candidato: Danilo Iglesias Brandão RA: 124248

Data da Defesa: 25 de setembro de 2015

Título da Tese: "Coordinated Power-Based Control and Utility Interface Converter in Low Voltage Microgrids (Controle Coordenado em Microrredes de Baixa Tensão Baseado no Algoritmo Power-Based Control e Conversor Utility Interface)".

Prof. Dr. Fernando Pinhabel Marafão (Presidente, FEEC/UNICAMP)

Prof. Dr. Ricardo Quadros Machado (EESC/USP-São Carlos)

Prof. Dr.Wilson Komatsu (POLI/USP)

Prof. Dr. Daniel Dotta (FEEC/UNICAMP)

Profa. Dra. Fernanda Caseño Trindade Arioli (FEEC/UNICAMP)

A ata de defesa, com as respectivas assinaturas dos membros da Comissão Julgadora, encontra-se no processo de vida acadêmica do aluno.

Acknowledgments

Abstract

This thesis presents a flexible and robust architecture and corresponding control strategy for modern low voltage microgrids with distributed energy resources. The strategy fully exploits the potential of distributed energy resources, under grid-connected and islanded operating modes. In grid-connected operation, under *global optimization mode*, the control strategy pursues quasi-optimum operation of the microgrid, so as to reduce distribution loss and voltage deviations. In islanded mode, it effectively manages any available energy source to ensure a safe and smooth autonomous operation of the microgrid. Such strategy is applied to a fully-dispatchable microgrid structure, based on a master-slave control architecture, in which the distributed units are coordinated by means of the recently developed power-based control. The main advantages of the proposed architecture are the scalability (plug-and-play) and capability to run the distributed units without synchronization or knowledge of line impedances. Moreover, the proposed microgrid topology manages promptly the interaction with the mains by means of a utility interface, which is a grid-interactive inverter equipped with energy storage. This allows a number of advantages, including compensation of load unbalance, reduction of harmonic injection, fast reaction to load and line transients, and smooth transition between different operating modes. On the other hand, in order to provide demand response, proportional power sharing, reactive power control, and full utilization of distributed energy resources, the microgrid employs a reliable communication link with limited bit rate that does not involve time-critical communications among distributed units. It has been shown that a communication failure does not jeopardize the system, and just impairs the global optimization mode. However, the system keeps properly operating under the *local optimization mode*, which is managed by a linear algorithm in order to optimize the compensation of reactive power, harmonic distortion and load unbalance by means of distributed electronic power processors, for example, active power filters and other grid-connected inverters, especially when their capability is limited. It consists in attain several power quality performance indexes, defined at the grid side and within a feasible power region in terms of the power converter capability. Based on measured load quantities and a certain objective function, the algorithm tracks the expected optimal source currents, which are thereupon used to calculate some scaling coefficients and, therefore, the optimal compensation current references. Finally, the thesis also proposes an efficient technique to control single-phase converters, arbitrarily connected to a three-phase distribution system (line-to-neutral or line-to-line), aiming to reduce unbalance load and control the power flow among different phases. It enhances the power quality at the point-of-common-coupling of the microgrid, improve voltage profile through the lines, and reduce the overall distribution loss. The master-slave microgrid architecture has been analyzed and validated by means of computer simulations and experimental results under sinusoidal/symmetrical and nonsinusoidal/asymmetrical voltage conditions, considering both the steady-state and dynamic performances. The local optimization mode, i.e., linear algorithm for optimized compensation, has been analyzed by simulation results.

Resumo

Esta tese apresenta uma possível arquitetura e sua respectiva estratégia de controle para microrredes de baixa tensão, considerando-se a existência de geradores distribuídos pela rede. A técnica explora totalmente a capacidade dos geradores distribuídos em ambos os modos de operação: conectado à rede e ilhado. Quando conectado à rede, sob o *modo de otimização global*, o controle busca a operação quase ótima da microrrede, reduzindo as perdas de distribuição e os desvios de tensão. Quando em modo ilhado, a técnica regula de forma eficaz os geradores distribuídos disponíveis, garantindo a operação autônoma, segura e suave da microrrede. A estratégia de controle é aplicada a uma estrutura de microrrede completamente despachável, baseada em uma arquitetura de controle mestre-escravo, em que as unidades distribuídas são coordenadas por meio do recém-desenvolvido algoritmo *Power-Based Control*. As principais vantagens da arquitetura proposta são a expansividade e a capacidade de operar sem sincronização ou sem conhecimento das impedâncias de linha. Além disso, a microrrede regula as interações com a rede por meio do conversor chamado de *Utility Interface*, o qual é um inversor trifásico com armazenador de energia. Esta estrutura de microrrede permite algumas vantagens como: compensação de desbalanço e reativo, rápida resposta aos transitórios de carga e de rede, e suave transição entre os modos de operação. Em contrapartida, para compartilhar a potência ativa e reativa proporcionalmente entre as unidades distribuídas, controlar a circulação de reativos, e maximizar a operação, a comunicação da microrrede requer em um canal de comunicação confiável, ainda que sem grandes exigências em termos de resolução ou velocidade de transmissão. Neste sentido, foi demonstrado que uma falha na comunicação não colapsa o sistema, apenas prejudica o modo de otimização global. Entretanto, o sistema continua a operar corretamente sob o *modo de otimização local*, que é baseado em um algoritmo de programação linear que visa otimizar a compensação de reativos, harmônicos e desbalanço de cargas por meio dos gerador distribuído, particularmente, quando sua capacidade de potência é limitada. Esta formulação consiste em atingir melhores índices de qualidade de energia, definidos pelo lado da rede e dentro de uma região factível em termos de capacidade do conversor. Baseado nas medições de tensão e corrente de carga e uma determinada função objetiva, o algoritmo rastreia as correntes da rede ótima, as quais são utilizadas para calcular os coeficientes escalares e finalmente estes são aplicados para encontrar as referências da corrente de compensação. Finalmente, ainda é proposta uma técnica eficiente para controlar os conversores monofásicos conectados arbitrariamente ao sistema de distribuição trifásico, sejam conectados entre fase e neutro ou entre fase e fase, com o objetivo de compensar o desbalanço de carga e controlar o fluxo de potência entre as diferentes fases da microrrede. Isto melhora a qualidade da energia elétrica no ponto de acoplamento comum, melhora o perfil de tensão nas linhas, e reduz as perdas de distribuição. A arquitetura da microrrede e a estratégia de controle foi analisada e validada através de simulações computacionais e resultados experimentais, sob condições de tensão senoidal/simétrica e não-senoidal/assimétrica, avaliando-se o comportamento em regime permanente e dinâmico do sistema. O algoritmo de programação linear que visa otimizar a compensação foi analisado por meio de resultados de simulação.

Preface

This Ph.D. thesis corresponds to a period of thirty months and it involves a large international collaboration among University of Campinas – UNICAMP, Brazil; Univ. Estadual Paulista – UNESP, Brazil; Colorado School of Minas – CSM, USA; and University of Padova – UniPD, Italy and their corresponding research groups in the areas of power electronics and smart grids.

In order to avoid the readers misunderstanding the contributions from different institutions and research groups, this preface aims to highlight the author's contributions, as well as to clarify the contributions from other co-workers for this project.

All the figures and tables previously published are properly referenced and authorized.

Chapter 1 was written with many collaborators.

I was the main investigator for the contributions in Chapter 2, being responsible for most of the concept formulations, data collection and analysis, as well as for the majority of manuscript writing. Hildo Guillardi Júnior was engaged in the simulation results of Appendix B, while Tommaso Caldognetto contributed to the concept formulation and to manuscript edition in Section 2.5. A version of Section 2.5 has been published in [43], in which I am an author.

Chapter 3 was based on two published papers, whose I am an author. A version of Section 3.2 has been published in [100], while a version of Section 3.3 has been published in [36]. The construction and tests in Section 3.4, Section 3.5 and Section 3.6 were performed by Tommaso Caldognetto and I, with assistance mainly from Prof. Simone Buso.

A version of Chapter 4 has been published in [35] where I am an author. Tommaso Caldognetto was involved in the simulation results, while Prof. Paolo Tenti was the supervisory author on this issue.

The construction and tests in Chapter 5 was performed by Tommaso Caldognetto and I.

I was the lead investigator for the contributions in Chapter 6, being responsible for all major of concept formulation, data collection and analysis, as well as the majority of manuscript writing. Prof. Fernando P. Marafão and Prof. Marcelo G. Simões were involved in the early stages of concept formulation regarding to the arbitrary connection of single-phase inverters (i.e., line-to-neutral or line-to-line) to a three-phase microgrid.

Finally, I underline that Prof. José A. Pomilio and Prof. Fernando P. Marafão were, respectively, the main adviser and co-adviser of this Ph.D at UNICAMP, and Prof. Paolo Mattavelli was the supervisor during the abroad period at UniPD.

List of Figures

List of Tables

List of Acronyms and Abbreviations

AC	alternating current
ADC	analog to digital converter
APC	active power curtailment
APF	active power filter
CB_1	circuit breaker at the grid side
CB_2	circuit breaker at the microgrid side
CB_{UI}	UI circuit breaker for protection
CF	crest factor
CPT	Conservative Power Theory
DC	direct current
DER	distributed energy resource
DFT	discrete Fourier transform
DPWM	digital pulse width modulation
DSO	distribution system operator
DSP	digital signal processor
EG	energy gateways
EPP	electronic power processor
ES	energy storage
ESR	equivalent series resistance
FPGA	field programmable gate array
ICT	information and communication technology
IGBT	insulated gate bipolar transistor
IP	internet protocol
L	load
LC	local controller
LC	inductive and capacitive filter
LCO	limit cycle oscillation
LSB	least significant bit
LV	low voltage
LVN	low voltage network
M'	number of active nodes of the microgrid
MAF	moving average filter

MC	master controller
MPP	maximum power point
MPPT	maximum power point tracking
MV	middle voltage
N'	number of passive nodes of the microgrid
OLTC	on-load tap changer
OV	overvoltage
p.u.	per unit
PB	power-based
PCC	point of common coupling
PES	primary energy source
PI	proportional-integral
PI + R	proportional-integral plus resonant
PLL	phase locked loop
PV	photovoltaic
PWM	pulse width modulation
RMS	root mean square
SOC	state of charge
SW	switch
TCP	transmission control protocol
THD	total harmonic distortion
UI	utility interface
UPS	uninterruptible power source
VSI	voltage source inverter
ZOH	zero order hold
Σ	distributed hub

List of Variables

$*$	indicates reference value
$\hat{A}$	rated apparent power of EG
$\hat{A}^{over}$	temporary overloading capability of EG
$\underline{A}$	matrix of the constraint coefficients
A	apparent power
$\underline{b}$	matrix of the limits
B^b	equivalent balanced reactivity
B_m	equivalent reactivity of phase m
$\underline{c}$	matrix of the objective function coefficients
C	filter capacitor of UI
C_{DC}	capacitor of DC link
C_{ES}	capacitor of ES
C_i	controller of the output current control loop of EG
C_{iDC}	controller of the DC current control loop of EG
C_{PV}	capacitor of PV
C_{vDC}	controller of the DC link voltage control loop of EG
C_{vs}	controller of the overvoltage control of EG
D	distortion power
e_G	AC main grid voltage
f	frequency
f_1	fundamental frequency
f_{sw}	switching frequency
G^b	equivalent balanced conductance
G_m	equivalent conductance of phase m
I_C^{min}	minimum collective RMS current
I_G^{thres}	threshold for RMS value of the grid current
i_{Lna}	instantaneous non-active load current
i_{Lr}^b	instantaneous balanced reactive load current

i_L^u	instantaneous unbalanced load current
i_{Lv}	instantaneous void load current
i_{am}^b	instantaneous balanced active current of phase m
i_{am}^u	instantaneous unbalanced active current of phase m
i_m^u	instantaneous unbalanced current of phase m
i_{nam}	instantaneous non-active current of phase m
i_{rm}^b	instantaneous balanced reactive current of phase m
i_{rm}^u	instantaneous unbalanced reactive current of phase m
i_{vm}	instantaneous void current of phase m
i	AC current through UI filter inductance
$\boldsymbol{I}$	collective value of currents
$I(s)$	integrative controller
i^*_a	active current reference
i^*_C	compensation current reference
i^*_{EG}	reference current for the EG's current control loop
I^*_{PES}	PES available active current reference
i^*_r	reactive current reference
i_c	shunt filter capacitor current
i_{DC}	DC link current
i_{EG}	output current of the EG
I_{EG}	RMS value of EG current
i_{ES}	energy storage output current
i_G	grid current
I_G	RMS value of grid current
i_L	load current
I_L	RMS value of load current
i_m	instantaneous current of phase m
I_{nom}	nominal current value
i_{PV}	PV output current
i_{ref}	current reference
i_{UI}	UI output current after filter capacitor
j	j-th EG connected to the microgrid
k_D	distortion scaling coefficient

k_N	unbalance scaling coefficient
k_{na}	non-active scaling coefficient
k_Q	reactive scaling coefficient
$K_{sense,i}$	current sensor gain
$K_{sense,v}$	voltage sensor gain
L	filter inductance of UI
l	l-th control cycle
L_G	line inductance
m	m-th phase of the electrical system
n	n-th phase of the electrical system
N	unbalance power
N_a	unbalance active power
N_r	unbalance reactive power
$\hat{P}_S^{in}$	maximum power that can be absorbed by EG
$\hat{P}_S^{out}$	maximum power that can be delivered by EG
$\hat{P}^{max}$	estimated maximum active power
$\hat{P}^{min}$	estimated minimum active power
$\hat{P}$	estimated active power
P_j^{err}	off-set error made by EGs
P	average active power
P_G	grid power
P_L	load power
P_{Load}	load power
P_{tot}	total active power
$\hat{Q}^{max}$	estimated maximum reactive power
$\hat{Q}^{over}$	temporary overloading capability of EG
Q	average reactive power
Q'	oversampling factor
Q_{tot}	total reactive power
$P(s)$	proportional controller
$R(s)$	resonant controller
R_G	line resistance

T	line voltage fundamental period
$\hat{v}_m$	instantaneous unbiased voltage integral of phase m
$\widehat{V}$	collective value of unbiased integral voltages
V	collective value of voltages
v	instantaneous PCC voltage / UI voltage / microgrid voltage
V	RMS value of voltage
v^f	fundamental voltage
v_{DC}	DC link voltage
v_{ES}	energy storage output voltage
v_G	grid voltage
v_m	instantaneous voltage of phase m
V^{max}	maximum allowed voltage limit
v_{PCC}	instantaneous PCC voltage / UI voltage / microgrid voltage
v_{PV}	PV output voltage
W	average reactive energy
W_i	controller of the output current control loop of UI
W^i_{i*}	transfer function of the fast current control loop of UI
$\underline{x}$	non-negative state variables
X_D	collective squared value of the grid void currents
X_N	collective squared value of the grid unbalanced currents
X_P	collective squared value of the grid balanced active currents
X_Q	collective squared value of the grid balanced reactive currents
y	can assume Q, D or N
Y_v	controller of the voltage control loop of UI
Z_G	line impedance
Z_{iG}	controller of the grid current control loop of UI
Z_O	UI converter output impedance
α_P	balanced coefficient of power-based control for active power set-point
α_{Pm}	phase coefficient of power-based control for active power set-point
α_Q	balanced coefficient of power-based control for reactive power set-point
α_{Qm}	phase coefficient of power-based control for reactive power set-point
$\Delta v_\%^{max}$	maximum voltage deviation
ΔI_{EG}	EG available current capacity

Δv^*	voltage correction from grid current controller output of UI
ΔV_{MG}	voltage discrepancy factor of microgrid
ΔV_{NI}	voltage discrepancy factor of PCC
ε_i	current error
ε_v	voltage error
η	efficiency
γ_{PCC}^m	gain error of measurement instruments at PCC
γ_j^g	gain error made by EGs
γ_j^m	gain error of measurement instruments of EGs
λ	power factor
λ_D	distortion factor
λ_N	unbalance factor
λ_Q	reactivity factor
ϕ_1	phase angle between fundamental phase voltage and current
ω	line voltage fundamental angular frequency

List of Contents

Chapter 1

1.   Introduction

The U.S. Energy Information Administration through the International Energy Outlook 2013 [**1**] anticipates that world energy consumption will increase 56 % between 2010 and 2040. To support the economic growth during such period, the energy providers are now challenged to supply the expected rising energy demand avoiding using fossil fuel due to environment concerns, such as: air pollution, climate change, carbon footprint regulations and greenhouse effects. On the other hand, providers have the opportunity to take advantage of modern power electronics, especially in the scenario of renewable energies, and to promote great energy technology developments.

The Brazilian energy trends are about the same, with increasing energy consumption and an appealing call for distributed renewable power sources. Moreover, Brazil undergoes a period of high price of electrical energy, which is basically related to its energy matrix configuration. In Brazil, most of the energy matrix (65%) is based on hydroelectric power plants [**2**] and since 2013 the country has experienced a severe water crisis, requiring the operation of (standby) thermal power plants, which deliver more expensive energy to the grid. Furthermore, Brazil's power system infrastructure is characterized by a unidirectional power flow, such that the large generation power plants are connected to the transmission network, whereas most of the loads are connected to the distribution networks. Conversely, several other countries, for example Germany, have a power system infrastructure characterized by bidirectional power flow, where generation and consumption are combined through transmission and distribution networks. This latter scenario enhances the system reliability, thanks to the

variety of energy resources, and pushes the electrical energy market into a more dynamic scenario. Now, Brazil is taking the first steps toward this promising scenario [3], where microgrids play an important role and, academic researches and discussions on this field are ripe for the first stage of development.

According to the U.S. Department of Energy Microgrid Exchange Group, a microgrid is a group of loads and distributed energy resources (DERs) connected to each other acting as a single-controllable entity that can efficiently operates in either grid-connected or islanded modes. This structure carries a number of advantages in terms of flexibility, sustainability and reliability. Indeed, smart microgrids can bring valuable benefits, including the possibility to install several kinds of DERs without needing to reform the current distribution power systems. Moreover, microgrids may integrate a wider share of low-carbon technologies, while providing a more effective management of power flow [4], [5], [6]. However, an increasing penetration of DERs in low voltage (LV) distribution networks points to new operation problems, as for example: the distributed active power generation tends to increase the voltage profile due to usually high R/X ratio in LV networks; bidirectional power flow challenges conventional protection schemes; maximization of DER's electronic power processors (EPPs) capability, and mitigation of unwanted current terms[1] circulation are expected. Many of these challenges need new devices or methods, such as: smart meters; bidirectional protection schemes; communication protocols; renewable power sources; energy storage systems; grid-tied inverters and also a new method for revenue metering. Summarizing, a novel economic and technological market is emerging where power electronic devices aiming efficient and reliable operation for low voltage microgrids are very welcome [7], [8], [9], [10], [11].

To handle the power loss in distribution conductors, the presence of DERs close to the consumers tends to reduce the current through transmission and distribution lines, which may reduce the system's loss. However, controlling the active power flow is not the only way to improve the system efficiency. The multi-task inverters can inject active power, and additionally compensate unwanted current terms, further enhancing the system's power quality and efficiency [12], [13], [14], [15]. Usually, the utilities use capacitor banks, transformers, passive tuned power filters and active power filters (APFs) in order to mitigate possible electrical disturbances, and to avoid excessive distribution loss, undervoltage, harmonics propagation, etc. However, the aforementioned solutions require significant additional costs. Therefore, a good solution is to use the surplus capability of EPP associated to each DER to supply local active power and, simultaneously, to compensate, totally or partially, the electrical disturbances [14].

Moreover, it is important to notice that handling the DERs locally (by means of local controllers - LC) may not prevent the overvoltage caused by high feed-in power [16]; or to ensure stability under grid parameters variation [17], and under non-intentional islanding; or to control active and reactive power sharing among the distributed units [18]; and to prevent the undesired harmonic interaction over the system [19]. To overcome the aforementioned situations and fully exploit DERs capability, the distributed

---

[1] Unwanted current terms are portions of reactive, distortion and unbalanced currents that correspond to different load characteristics.

units require a distributed control strategy [5]. Basically, the microgrid architectures can be classified into two distinctive groups: *centralized* [20], [21] (multimaster operation [22] or master-slave [23], [24]) and *decentralized* [25], [26] (token ring [27]; plug-and-play [28]; surround [29], multiagent control [30], and droop control [31], [32], [33]). These distributed control strategies can be further split into *wired* and *nonwired* interconnected units [4], as it is addressed in Section 1.2.

Besides, it is usually more appealing to control the system in a cooperative concept [34], which means that several individual distributed units are coordinated to attaining a mutual goal. Hence, this work proposes a master-slave microgrid architecture, whose the master controller (MC) is located at the point of common coupling (PCC) of the microgrid and coordinates a set of slave units (i.e., energy gateways - EGs) that are distributed around the low voltage grid and interconnected with the MC through a reliable communication link. The interaction among the MC and the slave units is led by the power-based (PB) control [35] and, the operation in grid-connected and islanded modes are guaranteed by a utility interface (UI) [36], [37].

1.1.   General microgrid architecture

Fig. 1.1 shows the structure of a master-slave microgrid, which includes *N'* active nodes, *M'* passive nodes, and the UI endowed with the MC. Each active node hosts an energy resource (e.g., a renewable power source or an energy storage device) and an energy gateway (EG), which controls the active and reactive power flow to the grid. In the general microgrid architecture, all the slave units are controlled as *current sources*, ensuring good robustness, thanks to the high output impedance emulated by converters, and in compliance with current standards [38]. They can be single- or three-phase grid-interactive inverters

Fig. 1.1: General microgrid structure, © IEEE 2015 [35].

equipped with a communication module. The passive nodes comprise loads only and are not necessarily endowed with any particular kind of intelligent measurement or control device. The UI is a grid-interactive inverter usually connected at the LV terminals of a three-phase step-down transformer, feeding the four-wire distribution network, and it consists of a three-phase inverter with line-side *LC* filter, energy storage (ES) unit with a bidirectional DC/DC converter, and a communication module. It is always controlled as *voltage source*, and it operates either as a grid forming unit (i.e., it defines the voltage and frequency of the islanded system), when the mains is absent, or as a voltage supporting unit, in grid-connected mode; mitigating grid voltage disturbances, compensating load unbalance and harmonic distortion generated within the microgrid, and smoothing power transients generated by variable loads. Additionally, it manages the transition from grid-connected to islanded mode, and *vice-versa*. The UI can also host physically the MC that controls the microgrid's EGs to achieve proportional power sharing.

The components constituting such architecture cover three kinds of services: the first is the *power service*, demanded to UI, consisting in providing high power output for relatively short periods of time (a few seconds to a few minutes), in case of transients and temporary power imbalances. The second is the *capacity service*, demanded to EGs, consisting in providing limited amounts of energy for relatively long periods of time [39], in order to fulfil temporary local energy requirements. The third is the *energy service*, carried out by the aggregation of EGs and UI, consisting in supplying relatively large amounts of energy for extended period of time (minutes to hours), required, for example, during islanded conditions. From this perspective, guidelines for microgrid implementation are provided by IEEE standard 2030.2 [40].

The interconnection of master and slave units is performed through an information and communication technology (ICT) infrastructure enabling a coordinated operation of the active nodes by means of the power-based control algorithm, as shown in Fig. 1.2 and explained in Chapter 4. This algorithm uses only average power and energy terms, avoiding any time-critical communication among grid nodes (like transferring instantaneous voltage or current references [41], [42]), thus involving only limited bit rates. The centralized control can take advantage of a hierarchical tree-shaped communication topology, where the MC is the central hub and some slave units act as distributed hubs (Σ). In this way, the

Fig. 1.2: Proposed microgrid architecture with power-based control, © IEEE 2015 [43].

ICT infrastructure presents the advantage of reduced communication distances, a high throughput, and an easy scalability and flexibility. Of course, other communication topologies can be used for this purpose.

In order to meet communication requirements, the IEC 61850 standard can be applied to the microgrid control. This standard can be implemented over TCP/IP networks using the existing infrastructure, only requiring minimum adaptations in particular circumstances. It will be shown that with the proposed control strategy, the communication is not crucial and its failure will not lead the system to collapse. However, in the event of failure, though the local controllers can autonomously keep DERs safety operating (thanks to: current/voltage control, maximum power point tracking (MPPT), voltage stabilization, etc.), the power sharing may be impaired.

A *global optimization* is achieved by means of the coordinated operation of EGs by employing the power-based control algorithm. The operating principles of the power-based control tightly regulate the power flow through the microgrid PCC by making the EGs contribute to the microgrid power needs in proportion of their energy availability. To this end, the interaction among the MC and the EGs takes place in two phases. In the first phase, the MC *gathers* from each EG and UI a data packet that conveys the information of its local energy availability. In the second stage, the MC *broadcasts* to all the active agents a common control packet – consisting of two coefficients (α_P and α_Q) – that is finally translated by each EG into a local active and reactive power references. This procedure leads to a proportional and accurate active and reactive power sharing, assuring a uniform utilization of EGs and equalizing the thermal stress in each EG's EPPs.

The control packet sent to each EG is computed by the MC on the basis of the information collected during the *gathering phase* and represents the fraction of the local available power that each EG should provide so that a predefined power flow is attained at the PCC. However, the *local optimization* operation, injecting into the grid all the power that is locally produced, can be performed any time by the distributed unit, whether it conforms to the standard requirements of the distribution system operator (DSO). This is detailed in Section 1.2.1.

New DERs or EGs[2] can be any time connected to the grid. The EGs must send a connection request to the MC, and this periodically calls for active agents, updating the list of the microgrid's active nodes, thus giving plug-and-play capability to the microgrid architecture.

1.2. Microgrid hierarchical control

As mentioned before, microgrid control methods can be classified into two distinctive groups [**44**]: *centralized* and *decentralized*. In the former, a centralized controller optimizes the microgrid operation on the basis of multiple information, which may include the status of DERs, main grid, market and weather conditions [**21**], [**45**]. In the latter, each DER is controlled on the basis of locally measured

---

[2] Herein, DERs are active nodes with no agent, which means no communication unit; while EGs are active node with communication unit participating of PB control.

quantities and power sharing is attained without explicit communication among units [46]. The droop control is the most well-known strategy applied to this latter class [46], [47], [48], [49].

In systems based on the conventional droop control, DERs operate as voltage sources, with the same control algorithm, thus bringing the remarkable advantage in terms of reliability that a failure of a subset of the generators does not compromise the integrity of the whole system. The main prevailing concerns in this approach are a tradeoff between power sharing accuracy and frequency and voltage steadiness, relatively slow transient responses, the inability to autonomously perform black-starts, and performance that is sensitive to grid parameters. Some modified droop control methods have been proposed aiming at overcoming the aforementioned drawbacks. In [50], a *virtual output impedance* is proposed to attenuate the effect of unknown line impedances. Similarly, in [31] and [51], a *virtual output resistance* is employed to achieve automatically harmonic power sharing among DERs. In [52], a *virtual oscillator control* was proposed to share the load in proportion to DERs ratings without needing communication, by means of emulating the dynamics of dead-zone oscillator circuits; though, this approach still shows slow dynamics and sensitive performance to grid parameters. Recently, in [53] a *droop-free control*, that does not rely on droop mechanism, shares the power among DERs through a sparse communication around neighbors; however, it was not evaluated under nonlinear load conditions.

The *centralized control* considered in this work is based on the local measurements, whose output data are collected through a reliable communication channel [54] linking the slave units to a MC. It does not rely on detailed models of the controlled system, neither on tight synchronization among distributed units. This implies high robustness against parameter variations [35], and avoids the use of sophisticated synchronization techniques and phase measurement devices [55]. Owing to the peculiarities stated above, this control may be classified as a non-model-based approach, which appears to be an interesting solution for microgrid applications [5]. The decentralized and centralized hierarchical control architectures are simplified in Table 1.1. They slightly differ about the control level that contains the *power sharing* [23], [31]; it is discussed in the following.

Table 1.1: Hierarchical control architecture in a microgrid.

Control level	Decentralized hierarchical architecture	Centralized hierarchical architecture
Primary	Inverter output control, voltage and frequency stability, **power sharing**, islanded detection, MPPT, SOC[3] control and plug-and-play capability	Inverter output control, voltage and frequency stability, islanded detection, MPPT, SOC control and plug-and-play capability
Secondary	Compensation of voltage and frequency deviations caused by the primary level	**Power sharing**
Tertiary	PCC power flow control and power quality	PCC power flow control and power quality

---

[3] SOC means state of charge.

1.2.1. Primary control level of microgrid

Considering the operation of EGs and UI, a primary control level based on quantities measured locally and independent of communication is fundamental in terms of reliability. So doing, under communication failures, the system may be able to keep an efficient local operation, losing those features that are only relevant to a global point of view. In the following, the main functions performed by the EGs and the UI are discussed.

1) Energy gateway: it measures the output voltage and current and may implement any of the current controllers employed for DERs in a microgrid. These controllers have been extensively discussed in the literature [12], [56], [57], [58]. Fig. 1.3 shows three different ways for generating the power reference, classifying three modes of operation: 1) *global optimization mode*, when the communication link is properly working and the voltage amplitude at the point of connection is within acceptable limits; 2) *local optimization mode*, when EGs inject into the grid all the power that is locally produced, usually activated under communication failure between MC and EG; and 3) *overvoltage control mode*, when the local voltage exceeds the required voltage levels due to, e.g., too high power feed-in. The EG local control scheme is detailed in Chapter 2.

2) Utility interface: it measures its output voltages and currents, and grid voltages and currents. In order to perform as grid-forming during islanded operation and grid-support during grid-connected, its control scheme, defined in *abc* reference frame, consists of three control loops: *fast inner inductor current loop*, *output voltage loop*, and *slow outer grid current loop* (Z_{iG}), as shown in Fig. 1.4. The UI has three modes of operation: 1) *global optimization mode*, which applies if the communication link is properly working, either in grid-connected or islanded operation. 2) *Islanded mode*, which applies when the mains is absent. In such case the grid power/current reference is set to zero, regardless of the communication status. 3) *Emergency operation mode*, in which the UI is disconnected (by means of circuit breaker − CB_{UI}, see Fig. 3.1) from the microgrid. This latter mode may occur due to communication failure between MC and UI, or hardware failure triggered by protection devices, such as thermal or overcurrent sensors. It is
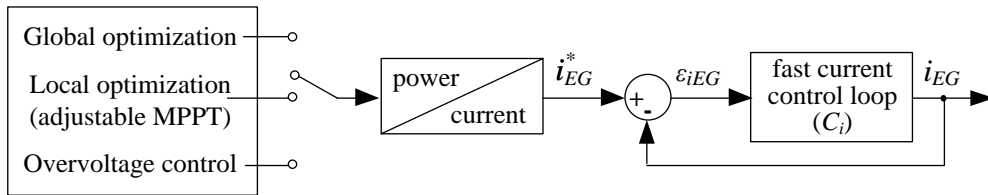
Fig. 1.3: Simplified block diagram of power reference generation for EGs.
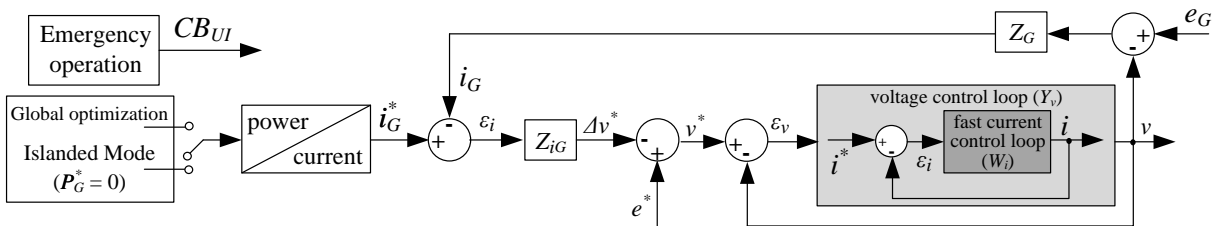
Fig. 1.4: Simplified block diagram of power reference generation for UI.

important to highlight that the former case barely occurs, because MC and UI may consist in the same hardware or, at least, may be installed in the same site, that is, close to each other.

If an emergency operation mode occurs while operating in grid-connected, the UI is automatically disconnected and the MC maintains an effective microgrid operation coordinating EGs for global optimization purposes. However, if it occurs during islanded operation, the microgrid must be shut down promptly. The implemented islanding detection algorithm is based on measured local quantities and guarantees the proper and safe operation of the microgrid, as it is discussed in Section 3.5. The UI structure and local control scheme is described in Chapter 3.

The problem of controlling DERs as voltage or current sources has been extensively addressed in the literature [56], [57], [59], showing advantages and drawbacks from both sides. However, the problem is still under discussion due to the evolution of national and international standards and grid codes (e.g., EN 61000-3, IEEE 519, IEEE 1547, CEI EN 021, CEI EN 016, IEEE 929) [38], [60], [61], [62], [63].

In conventional droop-controlled microgrids, the distributed units perform as *voltage sources*, and the primary control is aimed at adjusting the amplitude and frequency of local voltage references, thus avoiding circulation of unwanted current terms among DERs. It also allows plug-and-play connection of DERs.

In this proposal, the EGs perform as *current sources* and automatically adapt to existing grid voltage and frequency references. The principle to control the active and reactive currents to avoid useless circulation of power around the system is still valid, as well as contributing to voltage and frequency stabilization by properly managing the power exchanges within the microgrid. The primary control level definition includes every control function that can be done locally, without inputs from the rest of the microgrid (i.e., without communication). Examples are local compensation of reactive power and harmonic currents generated by loads, management of local ES if it exists, support of local voltage if limits are exceeded, and emergency supply to local loads in case of microgrid failure (i.e., basic, specific and ancillary services).

1.2.2. Secondary control level of microgrid

The meaning of the secondary control in conventional droop-controlled microgrids is to compensate for the amplitude and frequency deviations caused by primary control [23], [64]. This enables voltage stabilization, regulates power flow, and generally, enhances accurately the active and reactive power sharing, in steady state.

In this approach, frequency stabilization is not an issue; however, microgrid steady state operation can still be improved by adjusting the set-points of local controllers. To this end, the MC can process the data collected over the entire microgrid and feed globally references into EGs. It is performed by the power-based control algorithm. The secondary control definition includes every coordinated control function that can be implemented to improve the global operation of the microgrid (i.e., services based on the communication between MC and EGs). Examples are stabilization of voltage profiles, reduction of

distribution and conversion losses, effective load power sharing among active nodes, and unbalance compensation.

1.2.3. Tertiary control level of microgrid

Commonly, tertiary control is the highest level of hierarchical microgrid control and it is committed to manage the interaction between microgrid and utility during grid-connected mode and to ensure effective control of the power flow at the PCC [**5**]. Tertiary control can be considered part of the host grid and it can be defined as the services that make use of communication between DSO, MC and EGs. Hence, this control level is not discussed further in this work.

Finally, Table **1.2** simplifies the centralized microgrid hierarchical control.

Table 1.2: Hierarchical control architecture in centralized microgrid.

Control level	Agents involved	Function	Objective
Primary (*local*)	EGs and UI	Current/voltage control, synchronization, MPPT, energy storage, local voltage stabilization, reactive and harmonic compensation, etc.	Ensure autonomous and proper operation without communication, optimize local operation
Secondary (*distributed*)	EGs, UI and MC	Power sharing, maximize DERs operation	Manage DERs cooperatively, manage microgrid efficiently
Tertiary (*global*)	EGs, UI, MC and DSO	PCC power flow control, power quality	From the UI terminals show the microgrid as a single-controllable entity

1.3. Thesis structure

Although the discussed proposal be applied to a general microgrid, a particular scenario was set to this work, in which the EGs do not have ES devices. Consequently, the energy service during islanded operation is impaired, and this condition cannot be maintained for extended period of time, since only the UI has ES capability. Nevertheless, we have decided for this approach because, in Brazil, the generation power system is predominantly based on hydroelectric power plants. Thus, we believe that DERs without ESs are more profitable for this scenario, since battery devices are still expensive and the storage water in the dams can replace the distributed ESs acting like a huge centralized energy storage device. Of course, if islanding operation during long period of time is major requirement, EGs endowed with ESs must be considered.

The thesis main goal is to study, analyze, evaluate and validate a fully-dispatchable microgrid structure based on a master-slave control architecture, as in Fig. 1.5, where the distributed generation units are coordinated by means of the recently developed power-based control. The main advantages of the proposed distributed control strategy and architecture are the scalability (plug-and-play) and capability to distributively manage the DERs without synchronization. Moreover, the microgrid manages

promptly the interaction with the mains by means of an UI, which is a grid-interactive inverter equipped with ES. This allows a number of advantages, including compensation of load unbalance, reduction of harmonic injection, fast reaction to load and line transients, and smooth transition between operating modes. It is important to point out that in order to provide demand response, reactive power control, and full utilization of DERs, the microgrid requires a good communication link among distributed units; however, this subject was out of the scope of this work.

Considering the awareness of the author and his co-workers, this thesis also contributes to the investigation of a subject that has not been approached in the literature: the control of single-phase DERs arbitrarily connected (i.e., connected line-to-line or line-to-neutral) to a three-phase LV distribution system, for the sake of compensating power unbalance and regulating the power flow among the phases. Though line-to-line connection scheme is not usual around the world, it is a common practice in some regions of South America, especially in Brazil.

Regarding to the organization of this document, Chapter 2 describes the microgrid primary control level applied to EG and its control scheme shown in Fig. 1.3. It also presents a formulated linear problem using standard algorithm to optimize the compensation of reactive power, harmonic distortion and load unbalance by means of DERs. Finally, it describes the dynamic overvoltage limiting technique applied for local voltage stabilization. Chapter 3 addresses the UI converter, firstly comparing three different current controllers aiming at achieving the fastest response to enhance the UI performance and, secondly, the UI modeling and control are described. Finally, a passive technique of islanding detection is proposed in order to assist the smooth transition from islanded to grid-connected mode, and vice-versa. Chapter 4 explains the power-based (PB) control algorithm used in the MC to coordinate the slave units (i.e., EGs) and to achieve a global optimization proportionality to share the active and reactive power among the EGs. It describes the data packet and power commands exchanged between MC and EGs. Chapter 5 describes the experimental laboratory-scale prototype of a single-phase microgrid and shows the experimental results in order to analyze and validate the UI and PB control operation, in both steady state and dynamic conditions. Chapter 6 details the three-phase microgrid of Fig. 1.5 and proposes a power unbalance and power flow control among different phases by means of arbitrarily connected single-phase inverters. This study is supported by simulation results considering the model of a real urban power distribution grid under nonsinusoidal and asymmetrical voltage conditions. Lastly, Chapter 7 brings the main conclusions and contributions of the thesis.
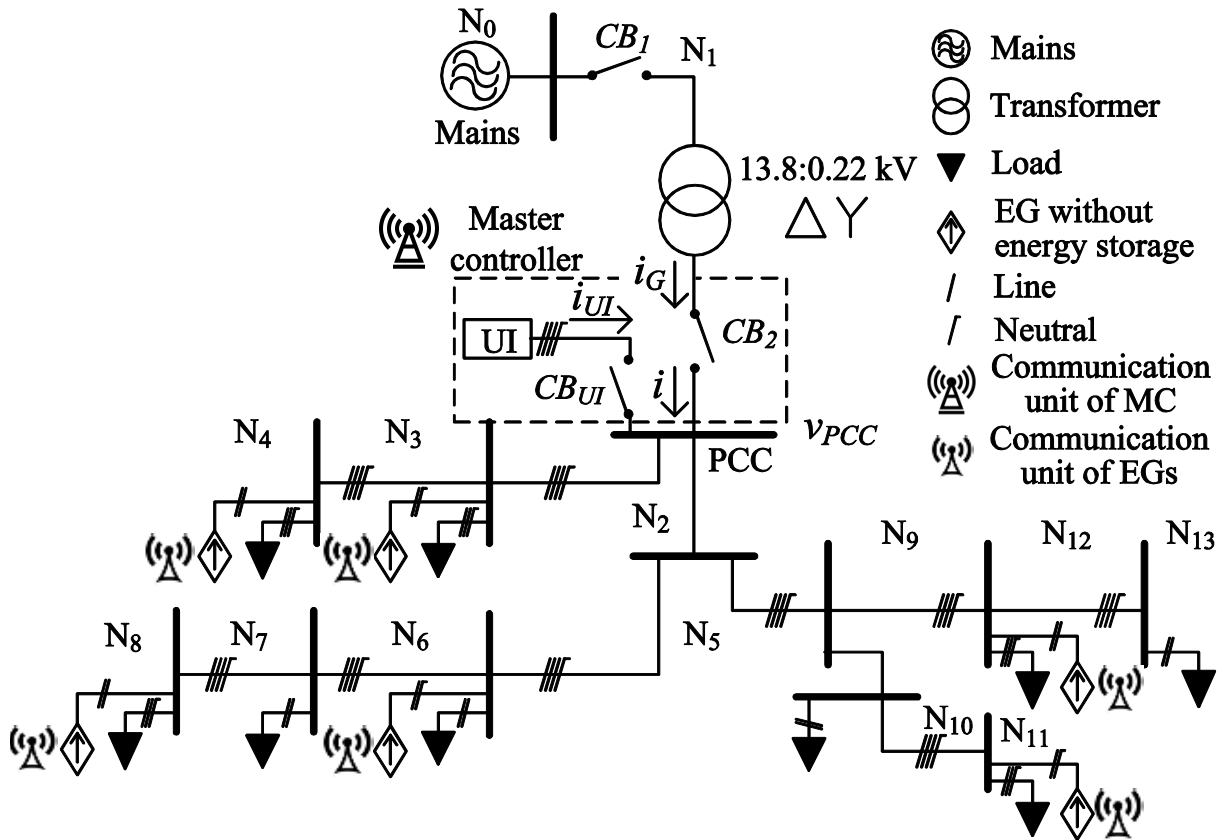
Fig. 1.5: Considered microgrid structure based on master-slave control architecture with MC and UI connected at PCC and PB control coordinating the distributed operation of EGs without ESs.

Chapter 2

2.   Local Control of Energy Gateways

As previously mentioned, the EG can be a conventional single- or three-phase grid-interactive inverter controlled as *current source* and equipped with a communication unit. The single-phase EGs can be connected line-to-neutral or line-to-line, and this section addresses both sorts of connection. Thus, let us introduce, when referring to a particular EG connected at the *j*-th node (N_j), the notation EG_{mnNj}, where *m* and *n* indicate the two particular phases (phase *a*, phase *b*, phase *c*, or neutral conductor) at which the EG is connected. Therefore, for example, EG_{abN4} indicates an EG connected at node 4 between phase *a* and phase *b*, while EG_{cN6} indicates an EG connected at node 6 between phase *c* and neutral conductor. We underline that the measured quantities in an EG is always the current injected by the EPP and the voltage across its connection point. Further, each EG has *basic control functions*, *specific functions* and *ancillary services* as shown in Fig. 2.1. Hence, this chapter describes the main EG's functions and services addressed in this work.

Nowadays, the use of EPPs interfacing DERs only to inject active power from the primary energy source (PES) into the grid may be understood as a waste of power electronic capability [**9**], [**44**]. The recent multi-task inverters can inject active power, ensure local voltage stability and compensate unwanted current terms (reactive, distortion and unbalance), improving the system power quality and efficiency [**12**], [**65**].

Fig. 2.2 depicts the block diagram of the proposed single-phase EG system including the power circuit and its local control scheme. The left side block (PES) represents any sort of renewable energy

source or ES, including a DC-DC first stage converter, if required. We underline that a possible closed-loop power control, to regulate the injectable power, has not been implemented herein; however, it can be included in this control scheme as in [66].
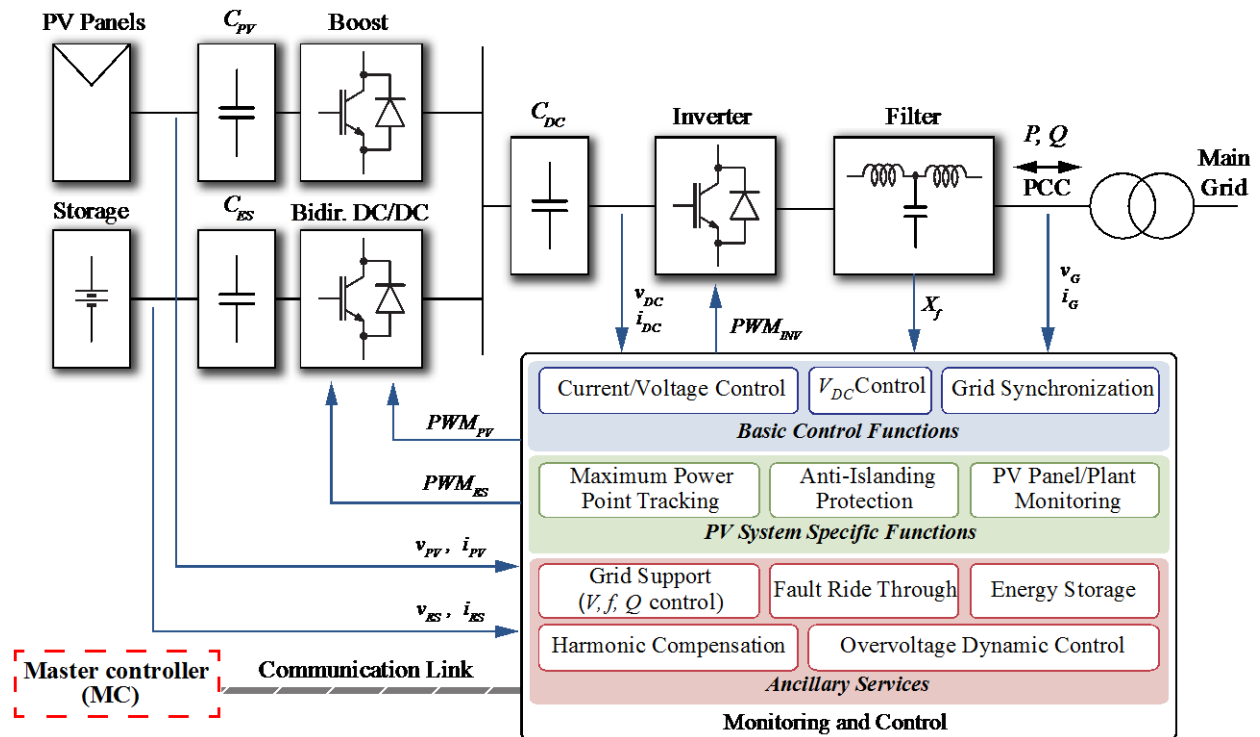
Fig. 2.1: General structure of energy gateway.
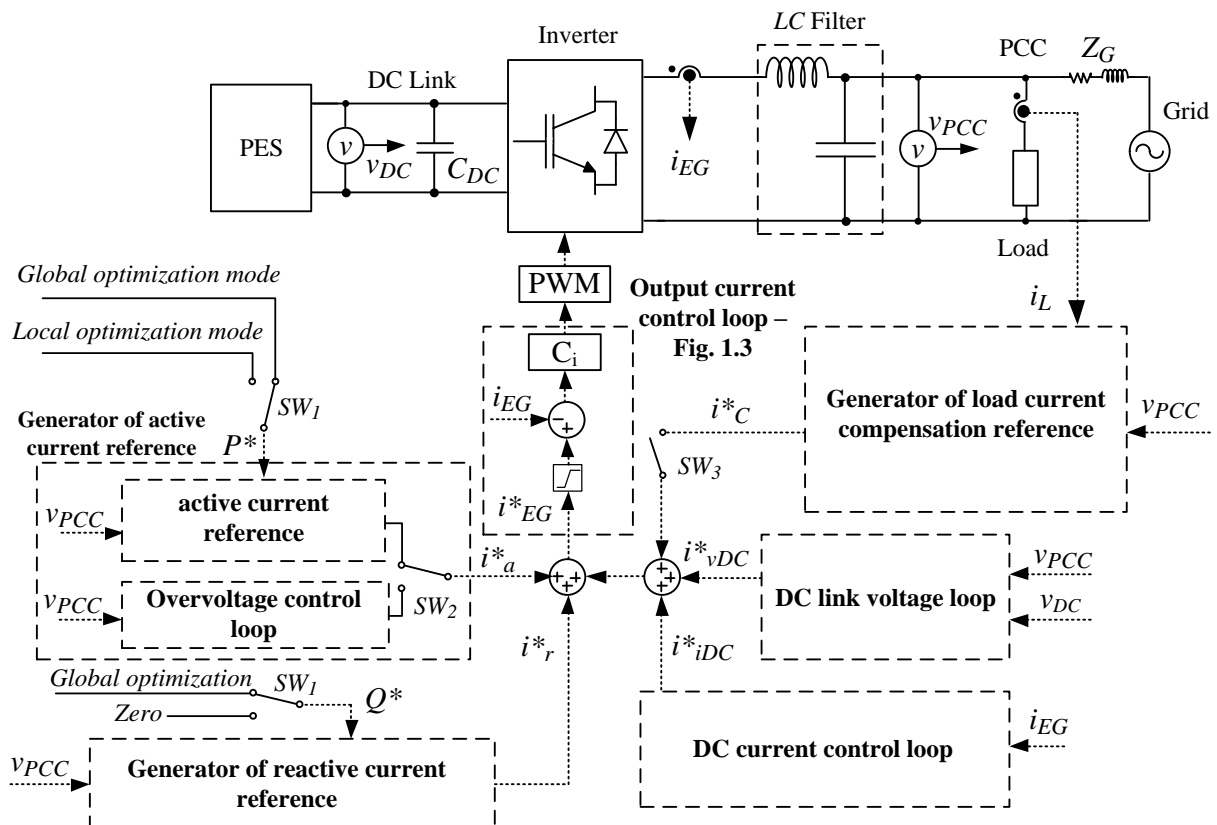
Fig. 2.2: Block diagram of the proposed distributed energy gateway, © IET 2015 [65].

The *output current control loop* is responsible for injecting the desired reference current (i^*_{EG}) into the grid, as represented in Fig. 1.3. The *DC link voltage loop* regulates the DC link voltage, while the *DC current control loop* guarantees that the inverter output current does not present DC component. Both control loops are decoupled from the first one assuming a design that ensures adequate difference between the respective crossover frequencies and their corresponding control loops are detailed in Fig. 2.3. The stiff-frequency based moving average filter (MAF) is implemented with time response of one fundamental cycle. However, if needed, an adaptive window MAF could be implemented, as compared in [67].

(**a**)   (**b**)
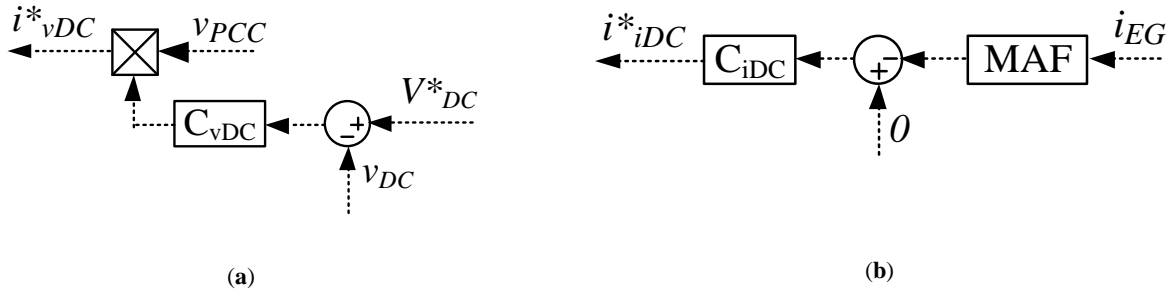
Fig. 2.3: Block diagram of the basic control functions. (a) DC link voltage control loop and (b) DC current control loop.

The *generator of active current reference* and the *generator of reactive current reference* provide, respectively, the active current (i^*_a) and reactive current (i^*_r) references, based on the actual mode of operation, as explained in Section 1.2.1. The *overvoltage control loop* limits the amount of active power injection, during overvoltage conditions, ensuring voltage stability. Finally, the *generator of load current compensation reference* provides the CPT's current terms to perform the selective local compensation. In sequence, the basics of Conservative Power Theory (CPT) [68] is presented, since it has been adopted as power theory for designing and analyzing the local and distributed controllers, as well as the above mentioned functions and services.

2.1.   Basics of the Conservative Power Theory

The CPT [68], [69] is a time-domain based power theory, valid for any voltage operating condition and applicable to single- or poly-phase systems. Using the natural (*abc*) frame, CPT proposes a decomposition of power and current quantities in their several subcomponents, which are associated to distinct electrical characteristics, such as: average active power transfer, reactive energy, load unbalance, and nonlinearities.

In order to introduce the fundamental notation of CPT, let us consider a generic poly-phase circuit under periodic operation. In the following, instantaneous quantities are denoted with lowercase symbols, average or RMS values are denoted with uppercase symbols, vector quantities (i.e., collective values[4]) with boldface symbols, and subscript *m* indicates the specific *m*-th phase.

---

[4] The collective value of voltages or currents from a three-phase circuit has been defined as: $Y = \sqrt{Y_a^2 + Y_b^2 + Y_c^2}$, where Y_a, Y_b, Y_c are RMS values of the corresponding phase quantities.

According to the CPT, the *active power* is defined by the internal product:

$$P = \frac{1}{T} \cdot \sum_{m=1}^{M} \int_0^T v_m \cdot i_m \, dt \; , \tag{2.1}$$

where T is the line voltage fundamental period; the *reactive energy* is defined by:

$$W = \frac{1}{T} \cdot \sum_{m=1}^{M} \int_0^T \hat{v}_m \cdot i_m \, dt \; , \tag{2.2}$$

where $\hat{v}_m$ is the unbiased voltage integral (i.e., integral of phase voltage v_m without its average value), defined as:

$$\hat{v}_m = \int_0^t v_m \, d\tau - \frac{1}{T} \cdot \int_0^T v_m \, dt \; . \tag{2.3}$$

Multiplying W by the system fundamental frequency (ω) we obtain the *reactive power* $Q = \omega \cdot W$.

2.1.1. Current decomposition

The CPT is based on the orthogonal decomposition of instantaneous phase currents into decoupled terms:

$$i_m = i_{am}^b + i_{nam} = i_{am}^b + i_{rm}^b + i_{am}^u + i_{rm}^u + i_{vm} \; , \tag{2.4}$$

such that $i^b{}_a$ is the balanced active current, $i^b{}_r$ is the balanced reactive current, $i^u{}_a$ is the unbalanced active current, $i^u{}_r$ is the unbalanced reactive current, i_{na} is the void current, and i_{na} is the non-active current.

The *balanced active currents* are defined as the minimum RMS currents needed to convey the total active power. These are given by:

$$i_{am}^b = \frac{P}{V^2} \cdot v_m = G^b \cdot v_m \; , \tag{2.5}$$

where V is the collective RMS voltage value, and G^b is the *equivalent balanced conductance* as defined by Fryze [70].

Similarly, the *balanced reactive currents* are defined as the minimum RMS currents needed to convey the total reactive energy. These are given by:

$$i_{rm}^b = \frac{W}{\widehat{V}^2} \cdot \hat{v}_m = B^b \cdot \hat{v}_m \; , \tag{2.6}$$

where $\widehat{V}$ is the collective RMS value of the unbiased voltage integral, and B^b is the *equivalent balanced reactivity*. Note that B^b is in some sense dual to the concept of G^b.

If the load is balanced, the PCC only absorbs balanced active and reactive currents; otherwise, it also drains *unbalance currents*, which are defined by:

$$i_m^u = (G_m - G^b) \cdot v_m + (B_m - B^b) \cdot \hat{v}_m = i_{am}^u + i_{rm}^u \; , \tag{2.7.a}$$

$$G_m = \frac{P_m}{V_m^2} \; ; \; G^b = \frac{P}{V^2} \quad and \quad B_m = \frac{W_m}{\widehat{V}_m^2} \; ; \; B^b = \frac{W}{\widehat{V}^2} \; , \tag{2.7.b}$$

such that G_m and B_m are the *equivalent phase conductance* and *reactivity* and $i^u{}_{am}$ and $i^u{}_{rm}$ are the unbalanced active and reactive currents, respectively. Note that if the load is balanced the *equivalent*

phase conductance is equal to the *equivalent balanced conductance* ($G_m = G^b$). Similarly, the reactivity parameters are equal ($B_m = B^b$).

Finally, the *void currents* are defined as the remaining phase currents. These represent all the load nonlinearity currents (i.e., harmonics):

$$i_{vm} = i_m - i_{am}^b - i_{rm}^b - i_m^u \ . \tag{2.8}$$

Since all the previous current components are orthogonal to each other, the collective RMS current can be calculated as:

$$\boldsymbol{I}^2 = \boldsymbol{I}_a^{b\,2} + \boldsymbol{I}_{na}^2 = \boldsymbol{I}_a^{b\,2} + \boldsymbol{I}_r^{b\,2} + \boldsymbol{I}^{u\,2} + \boldsymbol{I}_v^2 \ . \tag{2.9}$$

Accordingly, multiplying the collective RMS current ($\boldsymbol{I}$) and voltage ($\boldsymbol{V}$), the apparent power (A) can also be split into:

$$A^2 = \boldsymbol{V}^2 \cdot \boldsymbol{I}^2 = P^2 + Q^2 + N^2 + D^2 \ , \tag{2.10}$$

such that:

- *P* is the active power and corresponds to the real power converted into work;

- *Q* is the reactive power and reveals the presence of reactive energy in linear inductors and capacitors, or even fundamental phase shift caused by nonlinear loads (e.g., thyristor rectifiers);

- *N* is the unbalance power, equal to $\sqrt{N_a^2 + N_r^2}$, where N_a is caused by unbalanced loads with resistive characteristic (elements that do not cause fundamental phase shift) and N_r is caused by unbalanced loads with non-resistive characteristic (elements that cause fundamental phase shift);

- *D* is the distortion power and it is related to the load nonlinearities.

Note that only the active power and the reactive energy are conservative quantities regardless the voltage and current waveforms.

2.1.2. Load conformity factors

In order to characterize different aspects of *load behavior*, the load conformity factors have been proposed in [**71**], and the following paragraphs summarize them.

- *power factor* (λ) is a general poly-phase efficiency ratio, which is affected by reactive power, unbalanced loads and nonlinearities. Unity power factor represents current waveforms proportional to voltage waveforms (as in case of *balanced resistive loads*);

- *reactivity factor* (λ_Q) reveals the presence of reactive energy in linear inductors or capacitors, or even phases shift in electronic devices;

- *distortion factor* (λ_D) indicates the presence of distortion currents, related to voltage and current's nonlinearities;

- *unbalance factor* (λ_N) indicates the effect of load unbalance.

Except for the power factor, all the other conformity factors are zero for ideal conditions, regardless of the voltage distortion or symmetry. They are related as follows:

$$\lambda = \sqrt{(1 - \lambda_Q^2) \cdot (1 - \lambda_D^2) \cdot (1 - \lambda_N^2)} \ , \tag{2.11}$$

$$\lambda = \frac{I_a^b}{\sqrt{I_a^{b\,2} + I_{na}^2}} = \frac{I_a^b}{I} = \frac{P}{A} \ , \tag{2.12.a}$$

$$\lambda_Q = \frac{I_r^b}{\sqrt{I_a^{b\,2} + I_r^{b\,2}}} = \frac{Q}{\sqrt{P^2 + Q^2}} \ , \tag{2.12.b}$$

$$\lambda_D = \frac{I_v}{\sqrt{I_a^{b\,2} + I_r^{b\,2} + I^{u\,2} + I_v^2}} = \frac{I_v}{I} = \frac{D}{A} \ , \tag{2.12.c}$$

$$\lambda_N = \frac{I^u}{\sqrt{I_a^{b\,2} + I_r^{b\,2} + I^{u\,2}}} = \frac{N}{\sqrt{P^2 + Q^2 + N^2}} \ . \tag{2.12.d}$$

2.1.3. Relation of CPT conformity factors to conventional power quality indexes

CPT is a theoretical formulation for the analysis of electrical circuits focused on the *load behavior*. Indeed, other power theory formulations mix the effects of supply voltages and load features [72]. Under ideal voltage conditions and for single or balanced circuits, the CPT's factors lead to the same conclusions and values of conventional power quality indexes, such as: total harmonic distortion (THD), unbalance factors, displacement factor, etc. Thus, considering sinusoidal and symmetrical voltage and current conditions, λ results equal to the traditional fundamental displacement factor (*cos ϕ_1*), where ϕ_1 is the phase angle between fundamental phase voltage and current. For single- or balanced three-phase circuits, λ_Q could be calculated as $\lambda_Q = sin(\phi_1)$. λ_D can be associated to the conventional current THD_I by $\lambda_D = THD_I / \sqrt{1 + THD_I^2}$. And finally, λ_N can be related to the traditional positive, negative and zero sequence unbalance factors.

However, if the voltages are not sinusoidal or symmetrical, the CPT's factors inform on how a generic load circuits affect the current and power terms at the PCC. Besides, their information is related to the entire poly-phase circuit, and not only to single phase variables.

2.2. Generator of active and reactive current references

From the scheme of Fig. 2.2, the controllable active current reference to be injected (i^*_a) comes from the *equivalent conductance* (G), which is based on the locally measured PCC voltage and on the power reference (P^*) to be transferred from PES to the grid. The waveform of the injected current is always sinusoidal, since G is multiplied by the fundamental PCC voltage (v_{PCC}^f), as discussed in [65]. It is the safest method to inject active power, regardless of the voltage distortion and symmetry. Thus, the active current reference is always generated by:

$$i_{amn}^* = G \cdot v_{PCCmn}^f = \frac{P^*}{V_{mn}^2} \cdot v_{PCCmn}^f \; , \tag{2.13}$$

where P^* is provided depending on the EG operating mode (i.e., global optimization mode, local optimization mode and overvoltage mode, accordingly to Fig. 2.2). In *global optimization mode*, P^* comes from MC based on the power-based control algorithm [**35**] as explained in Chapter 4, and it performs the global optimization power sharing. When operating in *local optimization mode*, P^* is provided, e.g., by MPPT techniques [**73**]. Lastly, the *overvoltage control mode* takes place when the local voltage exceeds the permissible voltage levels due to high active power injection, as it is detailed in Section 2.5. The generation of current references is locally controlled by switches SW_1 and SW_2, as shown in Fig. 2.2.

Note that i_a^* refers to the controllable component of the active current, added to the active current component coming from the *DC link control loop* (i_{vDC}^*), that guarantees the DC link voltage regulation through power balance between PES and grid. Notice that the DC link voltage loop is normally enough to guarantee the power balance, but when the information of P^* is available, the generation of the additive term (i_a^*) acts as a feedforward control term improving the dynamics of the DC link voltage regulation.

Similarly, the reactive current reference (i_r^*) is generated as:

$$i_{rmn}^* = B \cdot \omega \cdot \hat{v}_{PCCmn} = \frac{Q^*}{V_{mn}^2} \cdot \omega \cdot \hat{v}_{PCCmn} \; , \tag{2.14}$$

such that Q^* is provided by means of power-based control algorithm or it is set to zero (controlling SW_1), since the local reactive compensation is always performed by the *generator of current compensation reference*.

2.3. Selective generator of current compensation reference

As previously mentioned, CPT can provide the compensation current reference (i_C^*) to selectively reduce the load current disturbances [**74**]. So, each decomposed current term (i_{na}, i_r^b, i_v, i^u) can define a different compensation strategy, which can be included on the EG in order to maximize its utilization and improve the power quality at its connection point. Of course, the local compensation functionality should be activated only when the EG is not using the full inverter capability to inject active power into the grid, or in case of other financial or technical constraints [**45**]. Such task is activated by the local controller itself, using switch SW_3, thus, it does not need to communicate with MC corresponding to an ancillary service.

According to [**65**], the *resistive load synthesis* compensation strategy appears more interesting than *sinusoidal source current synthesis* for compensation purposes [**75**]. Thus, the PCC measured voltage is directly used in the CPT decompositions. After compensating the non-active load current, the equivalent system (loads plus DERs) is viewed by the grid as an *equivalent resistive load*, draining current proportional to the instantaneous grid voltage waveform.

Fig. 2.4 shows the simplified schematic of a three-phase four-wire circuit with the block diagram of the selective compensation strategy to generate the current compensation references (i^*_C). The load quantities are measured and used to the CPT's decomposition. The EG currents are also measured and used into the output current control loop, as usually employed in DERs [56] and not shown in Fig. 2.4. For the sake of total or partial compensation of the unwanted current terms, a flexible and selective generator of load current compensation reference adjusts some coefficients to scale the magnitude of the decomposed CPT's current terms, within any percentage. Thanks to their orthogonal characteristic, it is possible to minimize individually and accurately any of the current disturbances.

Based on Kirchhoff's current law, each scaling coefficient is a ratio of its collective load current term. By definition, they must range from zero to one:

$$k_y = \frac{I_{Ly} - I^*_{Gy}}{I_{Ly}} \ , \ \ 0 \le k_y \le 1 \ ; \tag{2.15}$$

such that the superscript "*" means desired (reference) value and the subscript "y" can assume Q, D or N to represent the balanced reactive, distortion or unbalance scaling coefficients.

Therefore, in order to generate the EG compensation current reference (i^*_{Cmn}), for each phase, according to the notation criteria defined in Fig. 2.4, it has been defined:

$$i^*_{Cmn} = k_Q \cdot i^b_{Lrmn} + k_D \cdot i_{Lvmn} + k_N \cdot i^u_{Lmn} = k_{na} \cdot i_{Lnamn} \ . \tag{2.16}$$

Note that unity scaling coefficients correspond to full compensation, because the references turn equal to the non-active load currents (i_{Lnamn}), allowing EG to cancel them. The zero scaling coefficients mean no compensation ($i^*_{Cmn} = 0$).

In order to analyze and validate the selective and partial compensation, experimental results of an active power filter (APF) application are shown in Appendix A.

Fig. 2.4: Three-phase four-wire circuit with the block diagram of the selective compensation strategy, © IEEE 2015 [76].

2.4. Optimized compensation based on linear programming

At this point, after describing the selective and partial compensation, someone could ask which are the best scaling coefficients (k_y) to attain a particular requirement in steady state. Accordingly, this section addresses the additional optimization block in Fig. 2.5, formulating a linear problem using standard algorithm to optimize the compensation of reactive power, harmonic distortion and load unbalance by means of DERs, especially when their power capacity is limited. The compensation consists in achieving, in terms of power quality, the best performance indexes, defined at the source side and within a feasible power region in terms of the power converter capability. Based on measured load quantities and a certain objective function, the algorithm tracks the expected grid currents, which are thereupon used to calculate some scaling coefficients and, therefore, the compensation current references. It is defined as an *online open loop strategy* that improves the power quality at the PCC and enables full exploitation of DERs, increasing their cost-effectiveness[5]. The compensation is based on an orthogonal current decomposition and on an optimization-based algorithm.

From (2.15) and (2.16) one can note that to generate the compensation current references, it is sufficient to find the grid current terms ($\boldsymbol{I}^*_{Gy}$), which is the aim of the optimization block of Fig. 2.5, as described in the following.

The optimized compensation strategy is formulated as a linear iterative algorithm using standard Simplex method [77]. Simplex has been chosen because of its simplicity, it takes advantage of geometry, and it is still good and fast for problems with limited number of variables. Its standard model is:

Fig. 2.5: Three-phase four-wire circuit with the block diagram of the optimized compensation strategy, © IEEE 2015 [76].

---

[5] Cost-effectiveness is meant herein to express the capability to process more amount of power/current in an efficient way without modifying the nominal capacity and design cost of an electronic power converter.

$$(min) \; z = \underline{c} \cdot \underline{x}$$
$$s.t. \; \underline{A} \cdot \underline{x} \leq \underline{b} \; ; \tag{2.17}$$
$$\underline{x} \geq \underline{0}$$

where z is the objective function and the underlined variables are matrices; $\underline{c}$ is the matrix of the objective function coefficients; $\underline{A}$ is the matrix of the constraint coefficients and $\underline{b}$ is the matrix of the limits. The last constraint requires that all variables ($\underline{x}$) be non-negative.

In order to apply Simplex, in the sequence we linearize the equations, formulate the objective function, define the constraints and limits and geometrically interpret the problem.

2.4.1. Linearization

To preserve the orthogonality among decomposed CPT's current terms, the variables of the linear problem are defined as the collective squared values of each unwanted grid current term, which are all non-negative variables, as follows:

- X_P: collective squared value of the grid balanced active currents ($I_{Ga}^{b}{}^{2}$);

- X_Q: collective squared value of the grid balanced reactive currents ($I_{Gr}^{b}{}^{2}$);

- X_D: collective squared value of the grid void currents ($I_{Gv}{}^{2}$);

- X_N: collective squared value of the grid unbalanced currents ($I_{G}^{u}{}^{2}$).

Accordingly, rewriting (1.11) based on the previous linear variables, the squared values of each load conformity factor are, respectively:

$$\lambda^2 = \frac{X_P}{X_P + X_Q + X_D + X_N} \; ; \tag{2.18.a}$$

$$\lambda_Q^2 = \frac{X_Q}{X_P + X_Q} \; ; \tag{2.18.b}$$

$$\lambda_D^2 = \frac{X_D}{X_P + X_Q + X_D + X_N} \; ; \tag{2.18.c}$$

$$\lambda_N^2 = \frac{X_N}{X_P + X_Q + X_N} \; . \tag{2.18.d}$$

2.4.2. Objective function

The objective function is set to minimize the unwanted grid current terms, prioritizing some of them over the others by weighting coefficients. These coefficients are represented in (2.19) by the squared values of each unwanted load current term. Thus, the highest collective RMS value is prioritized, unlike other proposals [78], [79].

$$(min)z = \; X_Q \cdot I_{Lr}^{b}{}^{2} + X_D \cdot I_{Lv}{}^{2} + X_N \cdot I_{L}^{u}{}^{2} \; . \tag{2.19}$$

2.4.3. Constraints and limits

The problem formulation based on grid quantities allows us to define a set of conformity factor constraints. It goes beyond of other approaches [78] that have defined only current limitation constraints, which are also taken into account here.

The conformity factor constraints are defined handling (2.6) and setting the factors as preset references (*), respectively:

$$X_Q + X_D + X_N \leq X_P \cdot \left(\frac{1 - \lambda^{*2}}{\lambda^{*2}} \right) \; ; \tag{2.20.a}$$

$$X_Q \leq X_P \cdot \left(\frac{\lambda_Q^{*2}}{1 - \lambda_Q^{*2}} \right) \; ; \tag{2.20.b}$$

$$-X_Q + X_D \cdot \frac{(1 - \lambda_D^{*2})}{\lambda_D^{*2}} - X_N \leq X_P \; ; \tag{2.20.c}$$

$$-X_Q + X_N \cdot \frac{(1 - \lambda_N^{*2})}{\lambda_N^{*2}} \leq X_P \; . \tag{2.20.d}$$

The reference values of the conformity factors must be set according to current standards relating the conventional power quality indexes to CPT's conformity factors, as in Section 2.1.3.

X_P can always be calculated as (according to Fig. 2.5):

$$X_P = \boldsymbol{I}_{La}^{b\,2} - I_{PES}^{*\,2} \; , \tag{2.21}$$

where I^*_{PES} is the actual active current reference of PES. Naturally, for APF applications it is always zero, whereas for DERs, I^*_{PES} can be provided, for example, by MPPT techniques.

In addition, the value of the collective RMS current through the EPP must not be higher than its nominal collective rate ($\boldsymbol{I}_{EG} \leq I_{nom}$). Considering the polarities of Fig. 2.5, we have:

$$(\boldsymbol{I}_L - \boldsymbol{I}_G) \leq I_{nom} \; . \tag{2.22}$$

The active power injection takes priority over compensation. Consequently, the EG available capacity ($\Delta \boldsymbol{I}_{EG}$) for current compensation is:

$$\Delta \boldsymbol{I}_{EG} = \sqrt{I_{nom}^2 - I_{PES}^{*\,2}} \; . \tag{2.23}$$

Of course, for APF applications, $\Delta \boldsymbol{I}_{EG}$ is always equal to its own nominal power.

Hence, considering only unwanted current terms and assuming top priority to the active current injection, (2.22) can be rewritten using (2.23), as:

$$(\boldsymbol{I}_{Lna} - \boldsymbol{I}_{Gna}) \leq \Delta \boldsymbol{I}_{EG} \quad \leftrightarrow \quad \boldsymbol{I}_{Gna} \geq (\boldsymbol{I}_{Lna} - \Delta \boldsymbol{I}_{EG}) \; . \tag{2.24}$$

Thus, after further rewriting (2.24), in basis of their squared values, the current constraint is found:

$$X_Q + X_D + X_N \geq (\boldsymbol{I}_{Lna} - \Delta \boldsymbol{I}_{EG})^2 \; , \tag{2.25}$$

such that $\Delta \boldsymbol{I}_{EG} > \boldsymbol{I}_{Lna}$ means full compensation.

It is worth mentioning that (2.25) takes care of current limitation in steady state condition. To ensure proper and safe operation under transitory conditions, it is still needed current limiters into the output current control loop, as shown in Fig. 2.5.

2.4.4. Standard linear programming model

Finally, the linear programming problem in its standard model as in (2.17) is described. Thus, the matrices are:

$$\underline{c_1} = \begin{bmatrix} I_{Lr}^{b\ 2} & I_{Lv}^{2} & I_{L}^{u\,2} \end{bmatrix} \; ; \qquad \underline{A} = \begin{bmatrix} 1 & 1 & 1 \\ 1 & 0 & 0 \\ -1 & \dfrac{(1 - \lambda_D^{*\,2})}{\lambda_D^{*\,2}} & -1 \\ -1 & 0 & \dfrac{(1 - \lambda_N^{*\,2})}{\lambda_N^{*\,2}} \\ -1 & -1 & -1 \end{bmatrix} \; ;$$

$$\underline{x} = \begin{bmatrix} X_Q \\ X_D \\ X_N \end{bmatrix} \; ; \qquad \underline{b} = X_P \cdot \begin{bmatrix} \left(\dfrac{1 - \lambda^{*2}}{\lambda^{*2}}\right) \\ \left(\dfrac{\lambda_Q^{*\,2}}{1 - \lambda_Q^{*\,2}}\right) \\ 1 \\ 1 \\ \dfrac{-(I_{Lna} - \Delta I_{EG})^2}{X_P} \end{bmatrix} . \tag{2.26}$$

where all variables are non-negative. Note that (2.25) has been multiplied by "-1" to conform to the Simplex standard model. For single-phase applications, the quantities related to unbalance component must be disregarded.

The solution found through Simplex represents the expected optimal grid current terms ($\boldsymbol{I}^{*}_{Gy}$). Therefore, the scaling coefficients are calculated by (2.15) and applied to (2.16) to generate the compensation current references for each phase (i^{*}_{Cmn}).

2.4.5. Geometrical interpretation

Simplex method allows a geometrical interpretation of the linear problem, where the axes of Fig. 2.6 are the linear variables defined in Section 2.4.1 and the constraint inequalities (2.20) and (2.25) shape the planes. The feasible solutions made up the bound volume (darker areas) and the optimal feasible solution is always located in one of its corners, driven by the objective function. In summary, the Simplex algorithm moves along the boundary of the feasible area until reaching the optimal point. Note that the plane formed by (2.25) is variable with the PES actual power and dependable of the available capability of EG (ΔI_{EG}).
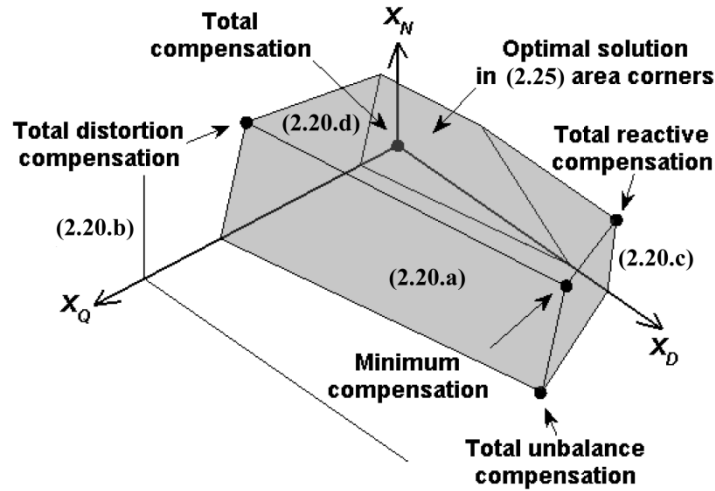
Fig. 2.6: Geometrical interpretation of the optimized compensation by means of Simplex method, © IEEE 2015 [76].

By construction, the full unwanted currents compensation is located at the origin $(X_Q, X_D, X_N) = (0, 0, 0)$, meaning that those have vanished at the grid side. One can see that every corner in Fig. 2.6 has a particular meaning that represents different compensation strategies (e.g., total unbalance compensation). The optimal solution is always located in one of the area corners formed by (2.25), because it has the minimum value of the objective function and complies with all the constraints.

We have also defined the minimum compensation point, which corresponds to the minimum collective RMS current (I_C^{min}) through the EPP requested to comply with the preset conformity factor requirements (constraints). It can be found by changing the weighting coefficients of matrix $\underline{c}$ to (2.27), and this point is the minimum value of this objective function.

$$\underline{c}_2 = \begin{bmatrix} \dfrac{-1}{{I_{Lr}^{b}}^2} & \dfrac{-1}{{I_{Lv}}^2} & \dfrac{-1}{{I_L^{u}}^2} \end{bmatrix} . \tag{2.27}$$

If ΔI_{EG} becomes too limited up to not allow the current compensation to comply with requirements, which means $\Delta I_{EG} < I_C^{min}$, then, the Simplex algorithm must be, temporally, disregarded and the EG should compensate as much as possible, calculating the non-active scaling coefficient as:

$$k_{na} = \frac{\Delta I_{EG}}{I_{Lna}} , \tag{2.28}$$

and applying it in (2.16). This strategy (*non-active current compensation*) corresponds to setting all the weighting coefficients equally, not assigning priority to compensation.

2.4.6. Computational results

To analyze and evaluate the proposed method for compensation and its impact on the EPP cost-effectiveness, a nonlinear and unbalance three-phase four-wire circuit of Fig. 2.7 has been implemented into a MatLab code. Let us consider a stiff grid where the PCC voltages are constant along the compensation process and a three-phase four-leg inverter with wide bandwidth current control loop was connected to the system representing an APF. The grid voltages (v_{Gm}) and the three-phase load are shown in Table 2.1. The respective CPT's load current terms and conformity factors are shown in Table 2.2. Table 2.3 shows the theoretical results, using the preset conformity factor references shown in its top row.
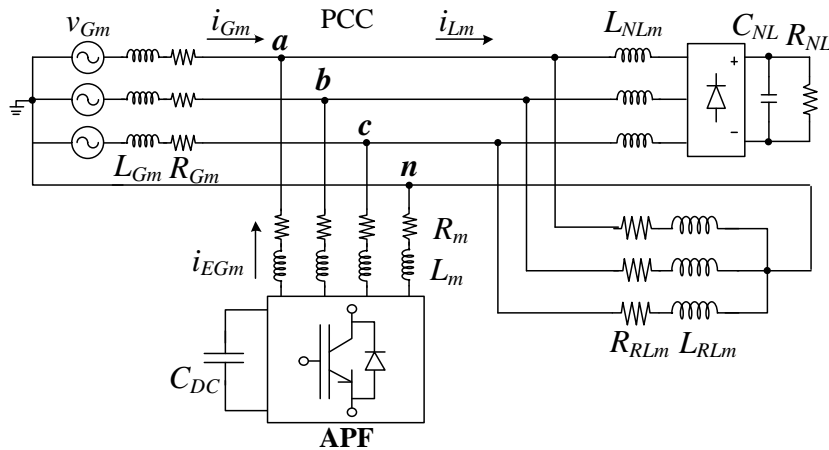
Fig. 2.7: Nonlinear and unbalance three-phase four-wire circuit, © IET 2015 [80].

Table 2.1: Parameters of the system, © IEEE 2015 [76].

Load parameters
R_{RLa}=4.4Ω; L_{RLa}=15mH;
R_{RLb}=4.1Ω; L_{RLb}=18mH;
R_{RLc}=3.7Ω; L_{RLc}=30mH.
L_{NLa}=1mH; L_{NLb}=1mH; L_{NLc}=1mH;
R_{NL}=42Ω; C_{NL}=2.35mF.
Sinusoidal three-phase source (60Hz)
V_{Ga}=127∠0°V; V_{Gb}=127∠-120°V; V_{Gc}=127∠120°V;
L_{Gm}=0.5mH; R_{Gm}=0.05Ω.
Distorted and asymmetrical three-phase source (60Hz)
V_{Ga}=122∠0° + 3.7∠3·0° + 3.7∠5·0° + 1.8∠7·0°V;
V_{Gb}=127∠-120° + 3.8∠3·(-120°) + 3.8∠5·(-120°) + 1.9∠7·(-120°)V;
V_{Gc}=115∠120° + 3.4∠3·(120°) + 3.4∠5·(120°) + 1.7∠7·(120°)V.

Table 2.2: Load current terms and load conformity factors, © IEEE 2015 [76].

Collective RMS load current values [A]				
I_L=32.6	I_{La}^{b}=21.7	I_{Lr}^{b}=23.3	I_{Lv}=4.3	I_{L}^{u}=5.8
Load conformity factors				
λ_L=0.666		λ_{LQ}=0.732	λ_{LD}=0.132	λ_{LN}=0.179

The minimum compensation objective function (2.27) applied to Simplex method (2.17) returns the minimum grid current terms (second row), which are thereupon used to calculate the scaling coefficients (2.15). Finally, through (2.16), the compensation current references (i^*_{EGm}) are generated. For this theoretical study, $i^*_{EGm} = i^{min}_{Cm}$, since for APF $I^*_{PES} = 0$. The EG's current controller tracks i^*_{EGm} minimizing the unwanted grid currents (fifth row). Lastly, for quantitative analysis, the PCC conformity factors are calculated, and they match to the requested factors.

The minimum compensation point $(X_Q, X_D, X_N) = (8.90^2, 1.89^2, 1.65^2)$, as shown in Fig. 2.6, requires 15.18 A of collective current through the EPP (square root of the quadratic sum of the values of the fourth row of Table 2.3). Considering any other point, for example, $(X_Q, X_D, X_N) = (9.24^2, 0.00^2, 0.00^2)$, whose PCC factors are ($\lambda^{pcc} = 0.916$, $\lambda_Q^{pcc} = 0.4$, $\lambda_D^{pcc} = 0$ and $\lambda_N^{pcc} = 0$) and also complies with the initial requirements (but with *worse* power factor), needs 15.82 A. The difference of 0.64 A is negligible considering linear scale (≈4 %). However, it is significant in orthogonal scale

Table 2.3: Minimum compensation (MatLab), © IEEE 2015 [76].

λ^*=0.920	λ^*_Q=0.400	λ^*_D=0.080	λ^*_N=0.070
I_a^b=21.70A	$I_r^{b\_min}$=8.90A	I_v^{min}=1.89A	I^{u_min}=1.65A
---	k_Q=0.618	k_D=0.561	k_N=0.716
---	I_{EGr}^b=14.40A	I_{EGv}=2.41A	I_{EG}^u=4.15A
I_{Ga}^b=21.70A	I_{Gr}^b=8.90A	I_{Gv}=1.89A	I_{G}^u=1.64A
λ^{PCC}=0.920	λ_Q^{PCC}=0.379	λ_D^{PCC}=0.080	λ_N^{PCC}=0.070

($\sqrt{15.82^2 - 15.18^2} = 4.45 \, A$), representing about 30 %. Therefore, applying the optimization to EGs allows them to save extra 30 % amperes for any ancillary services, such as compensation of unwanted current terms.

1)   Discussion of prioritized selective compensation

Prioritization in selective compensation schemes has been discussed in some recent papers, such as in [78] that recommended equal ranking the disturbing current references. On the other hand, [79] proposed to give preference first to harmonics, then to unbalance and last to reactive compensation. Here, we have proposed to prioritize the highest collective RMS value of load current, as in (2.19). Thus, assuming the feasible area of Table 2.3 (top row), the three proposals have been theoretically analyzed through the circuit of Fig. 2.7. In order to get similar behavior in terms of the relative importance given to the unwanted current terms, proposal [78] was performed by (2.28), which corresponds to set all the weighting coefficients equally; while proposal [79] was performed by (2.19) replacing the weighting coefficients ($I_{Lr}^{b}{}^2$, $I_{Lv}{}^2$, $I_L^{u}{}^2$) to (10, 500, 100) as did in [78]. The comparison results are shown in Table 2.4.

From Table 2.4, one can notice that the solution proposed in [78] needs 17.68 A to attend the requested conformity factors, or 15.10 A to comply with the power factor. However, $\lambda_N = 0.093$ remains out of feasible solution. The proposal in [79], needs 15.67 A to attend the feasible solution. Conversely, the method proposed here requests 15.08 A to match all the preset conformity factors.

Additional simulation results, approaching individually grid-tied inverter operating based on the proposed compensation strategy are shown in Appendix B.

Table 2.4: Comparison of prioritization of selective compensation.

Proposal	Scaling coefficients	Conformity factors	Currents [A]
[78]	$k_Q=k_D=k_N=0.728$.	$\lambda=0.956$; $\lambda_Q=0.280$; $\lambda_D=0.051$; $\lambda_N=0.070$;	$I_G = 22.55$; $I_{EG} = \mathbf{17.68}$.
[78]	$k_Q=k_D=k_N=0.622$.	$\lambda=0.920$; $\lambda_Q=0.376$; $\lambda_D=0.069$; $\lambda_N=\mathbf{0.093}$;	$I_G = 23.22$; $I_{EG} = \mathbf{15.10}$.
[79]	$k_Q=0.603$; $k_D=1$; $k_N=1$.	$\lambda=0.920$; $\lambda_Q=0.393$; $\lambda_D=0.000$; $\lambda_N=0.000$;	$I_G = 23.51$; $I_{EG} = \mathbf{15.67}$.
Here	$k_Q=0.618$; $k_D=0.561$; $k_N=0.716$.	$\lambda=0.920$; $\lambda_Q=0.379$; $\lambda_D=0.080$; $\lambda_N=0.070$;	$I_G = 23.31$; $I_{EG} = \mathbf{15.08}$.

2.5. Dynamic overvoltage control technique

Many of the grid connection standards, originally expecting rooftop PV systems to operate tracking their MPPT and not allowing DERs to participate to grid voltage regulation [38], are now being reviewed to enable a more proactive behavior of DERs into the operation of the distribution system [81], [82], [62]. These provisions also envisage particular voltage support functionalities [83], aiming at

improving the hosting capacity of LV grids and assuring a sustainable growth of the power share from renewables in the overall power production.

Various technical provisions are possible to enhance the hosting capacity of distribution networks [84], [85]. Beyond the obvious solution of upgrading the distribution infrastructure (grid reinforcement), control techniques based on on-load tap changers (OLTC), reactive power control, and active power curtailment (APC) have been investigated in the literature [86], [87], [88], [89], [90]. Techniques based on OLTCs can effectively adjust the voltage at the point of connection of the feeder, according to specific requirements on voltage profiles, but are penalized by wearing of components and limited flexibility in regulating the voltages along the grid, especially for those nodes which are far from the OLTC. Appealing solutions may be found by exploiting the available surplus apparent power capacity of the EPPs interfacing DERs to the grid. According to [85], four different classes of techniques based on EPPs of DERs may be distinguished: limitation of active power feed-in, static reactive power provision, automatic active power control, and combined active/reactive power control. The approaches can operate locally [88], [16], by employing local measurements, or distributedly [87], by involving a coordination among neighboring agents. Some information from a central controller may also be exploited to optimize particular control aspects, as shown in [87], [88].

This section focuses on overvoltage issues in low voltage distribution grids due to excessive active power injection from renewable sources. It describes a dynamic overvoltage control technique that, integrated in a master-slave architecture, allows to coordinately fulfill both local voltage constraints and the global power needs of the microgrid. It provides a precise control of active power injection if the measured voltage at the point of connection transcends the nominal operating range.

The advantages of the control approach are its simplicity, flexibility to accommodate local operational constraints, and limited needs in terms of computation and communication resources. In addition, it results to be more economical than installing new ES devices or retrofitting the distribution system infrastructure, and it is more efficient than reducing DER installations, controlling OLTC, or commanding simple cut-offs of the PV systems during peak production [91].

2.5.1. Overvoltage control

Each EG participating in the global optimization control, coordinated by MC, can accommodate local constraints by acting on the declared minimum and maximum injectable power $\hat{P}_j^{min}$ and $\hat{P}_j^{max}$ of power-based control or switching the EG operating mode (see Fig. 2.2). Specifically, to the particular purpose of limiting the maximum voltage amplitude at active nodes, the EGs can switch to local optimization mode (SW_1) and to overvoltage control (SW_2), so as to limit their active power injection and, as a result, maintaining the local voltage amplitude within the standard limits. At this operating mode, the equivalent conductance G of (2.13) is provided by the overvoltage control loop $C_{vs}(s)$, as shown in Fig. 2.8. The overvoltage modeling and controller design are detailed in [92].
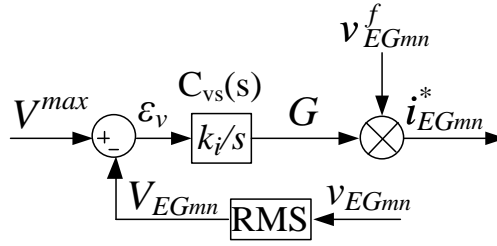
Fig. 2.8: Block diagram of the overvoltage control loop.

The automatic overvoltage limitation technique is represented in Fig. 2.9. It ensures that the voltage amplitude at active grid nodes does not exceed the allowed upper limit V^{max}. According to the scheme, if the j-th EG detects an overvoltage condition at its point of connection, that is, if $V_{EGj} > V^{max}$, then its active power reference P_j^* becomes regulated locally on the basis of the measured output voltage magnitude V_{EGj}, so that $V_{EGj} = V^{max}$. Accordingly, the resulting $P_j^*(V_{EGj})$ is, in steady state, the maximum power that the node of EG$_j$ can generate without causing overvoltages. The overvoltage condition is cleared when the power reference $P_j^*(\alpha_P)$, which is determined through power-based control, on the basis of the received α_P coefficient and the actual local power availability, is lower than the locally calculated reference $P_j^*(V_{EGj})$. During the overvoltage condition, the overproduction can be stored locally, or curtailed, as described, for example, in [93].

2.5.2. Application example

To exemplify the behavior of the proposed control scheme, the microgrid circuit shown in Fig. 2.10 is developed in PSIM environment. The parameters of the EGs and UI are reported in Table 2.5, while the distribution grid parameters are reported in Table 2.6. The microgrid is composed of a MC, UI, two EGs (EG$_1$ and EG$_2$), a PV source, a nonlinear load (L), and the mains. The MC is deployed in the UI, which is endowed with ES. A narrow bandwidth communication link allows the information exchange among the MC and the EGs. The line impedances are of low voltage type, thus presenting a high R/X ratio, and the overvoltage limit V^{max} for EGs is set equal to 240 V$_{RMS}$.
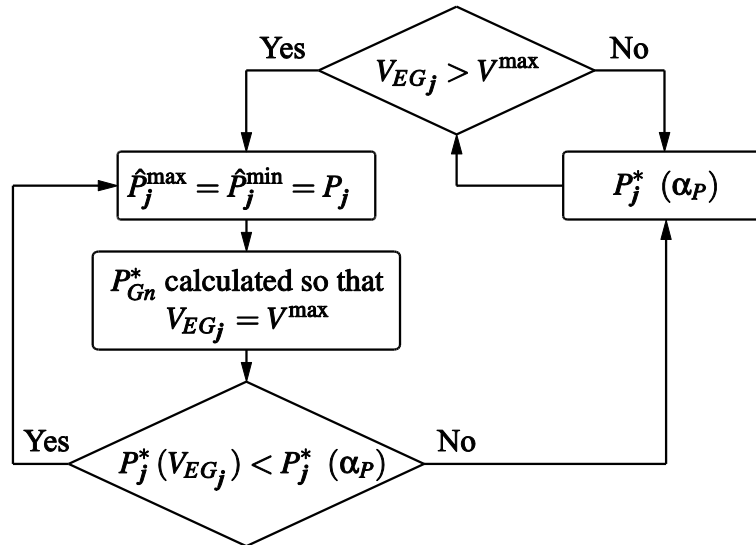
Fig. 2.9: Flow chart of the overvoltage control scheme, © IEEE 2015 [43].
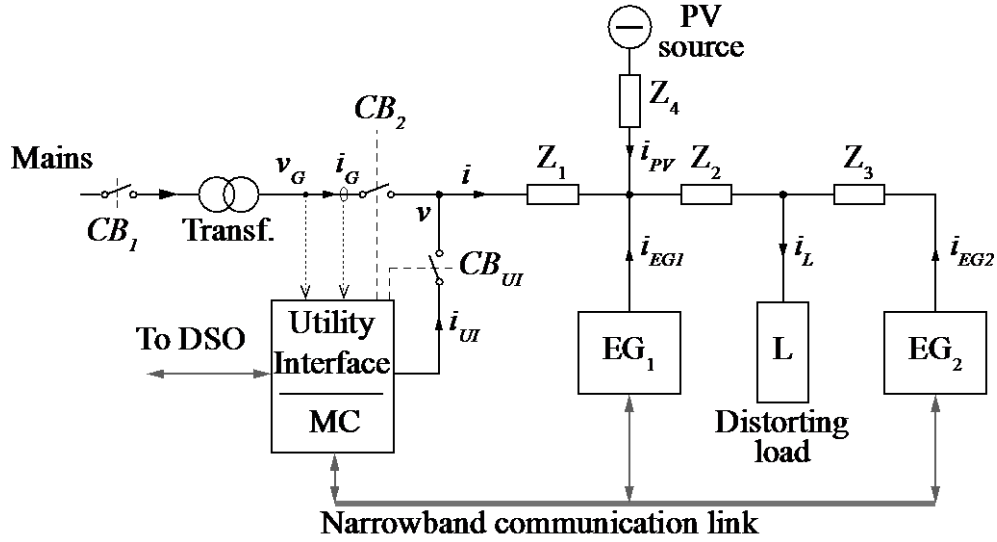
Fig. 2.10: Electrical circuit of the considered microgrid, © IEEE 2015 [43].

Table 2.5: Parameters of the energy gateways and utility interface, © IEEE 2015 [43].

Parameter	Description	Value
$P_{UI}^{min}, P_1^{min}, P_2^{min}$	Min. generable power	0, 0, 0 kW
P_{UI}, P_1, P_2	Generated PV power	3.0, 0.8, 3.0 kW
$P_{UI}^{max}, P_1^{max}, P_2^{max}$	Max. generable power	3.0, 0.8, 3.0 kW
A_{UI}, A_1, A_2	Power rating	3.0, 3.0, 3.0 kVA
$A_{UI}^{over}, A_1^{over}, A_2^{over}$	Overload power rating	3.3, 3.3, 3.3 kVA

Table 2.6: Distribution system parameters, © IEEE 2015 [43].

Parameter	Description	Value
e_G	Nominal grid voltage	230 V_{RMS}
f_0	Nominal grid frequency	50 Hz
Z_1	Z_1 impedance	350+j75 mΩ
Z_2	Z_2 impedance	267+j75 mΩ
Z_3	Z_3 impedance	222+j0 mΩ
Z_4	Z_4 impedance	267+j75 mΩ
L_G	Transformer inductance	0.6 mH

The current reference generation blocks for the PV source and EGs are shown in Fig. 2.11, such as that the implemented phase locked loop (PLL) can be found in [**94**]. Fig. 2.11(a) shows the current reference generation for a PV inverter operating at its maximum power point (MPP) or for an EG_j operating under local optimization mode. Fig. 2.11(b) shows the current reference generation for an EG_j during global optimization mode, and Fig. 2.8 shows the current reference generation for an EG_j during overvoltage condition.

(a) PV source operating at MPP.

(b) Slave unit under global optimization mode.
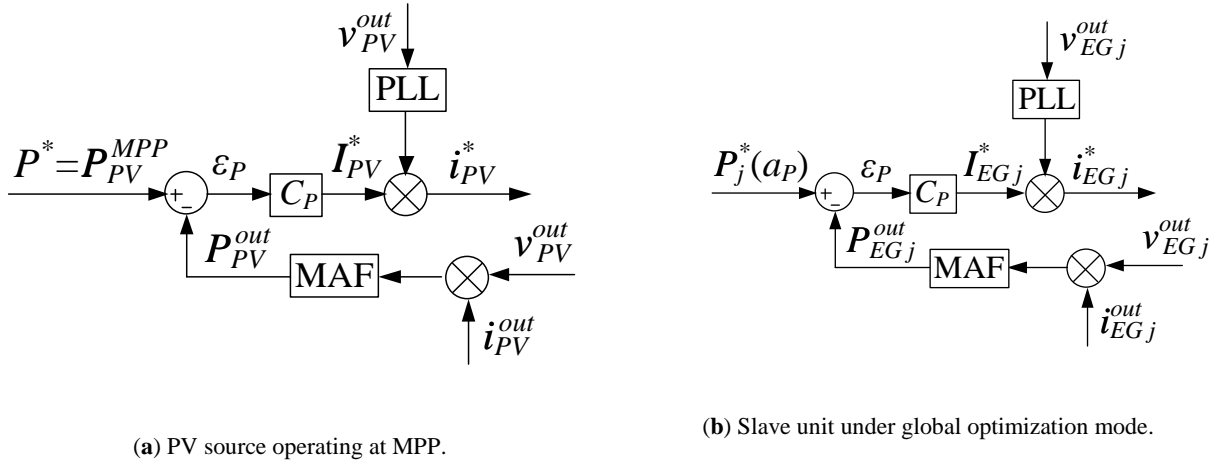
Fig. 2.11: Current reference generation, © IEEE 2015 [43].

In order to evaluate the proposed overvoltage control technique, a situation is considered where the EGs are exporting their maximum power to the grid (i.e., $P_{EG1} = 0.8$ kW and $P_{EG2} = 3.0$ kW, see Table 2.5). Initially, in Fig. 2.12, the load power absorption is 0.5 kW, the PV source is disconnected, the UI charges its local energy storage by absorbing 0.5 kW, and there are no overvoltage conditions.

At 0.7 s, the PV source [controlled as in Fig. 2.11(a)] is connected and its power production starts to progressively increase up to its nominal value (3 kW). This causes the magnitude of the grid voltage at the point of connection of EG_2 to transcend the allowable range and to locally fire an overvoltage condition for EG_2. Then, the EG_2 changes its operating mode from global optimization mode [Fig. 2.11(b)] to overvoltage control (Fig. 2.8) and begins to modulate its power reference P^*_{EG2} to maintain its output voltage below the maximum limit $V^{max} = 240$V$_{RMS}$. Concurrently, see Fig. 2.9, $\hat{P}_2^{max}$ becomes equal to $P_2(V_{EG2})$, so that the MC is informed about the reduced availability of EG_2. The zoomed-in view of this transition is shown in Fig. 2.13. In particular, we note how the overvoltage control basically reduces the EG_2 active power feed-in in response to the overvoltage condition; the exceeding of locally produced energy can be stored into a local ES device or curtailed by modifying the PV operating point [83]. Note that the resulting curtailment of the 13 % of EG_2 production, needed to fulfill the overvoltage constraint, is more advantageous than limiting the PV source generation, since, in this latter case, the 50 % curtailment of PV production would be necessary (see Fig. 2.12).

At 1 s, the nonlinear load power absorption increases to 1.6 kW, causing a higher voltage drop in the distribution lines. This drop makes the voltage at EG_2, to fall below the maximum value V^{max}, thus, the power reference $P_2(V_{EG2})$ exceeds the $P_2(\alpha_P)$, and, finally, the EG_2 returns to be guided by the power-based control. Fig. 2.14 shows the behavior of the main devices of the microgrid across this transient. Experimental results are provided in the Chapter 5.
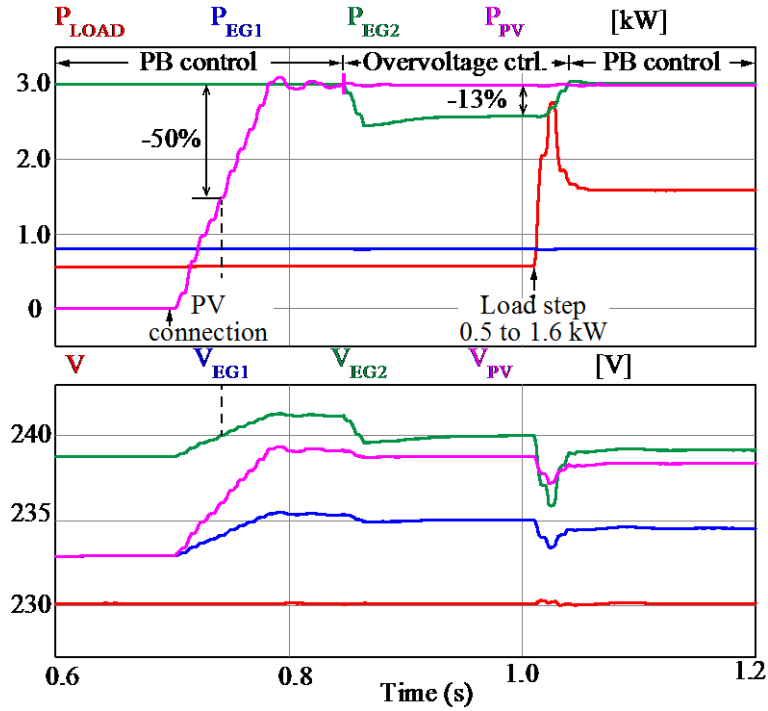
Fig. 2.12: Simulation results: power and RMS voltage values during the considered sequence of events.
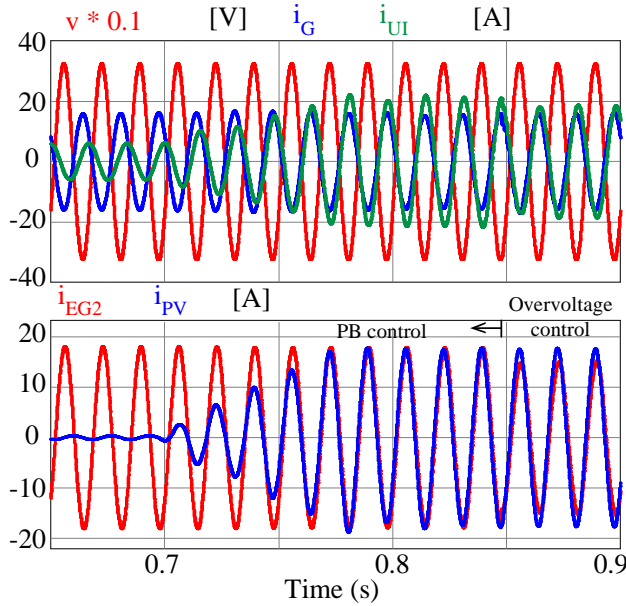
Fig. 2.13: Simulation result: current behavior during PV source connection. Top: PCC voltage (red), grid (blue) and UI (green) currents. Bottom: EG$_2$ (red) and PV (blue) currents.
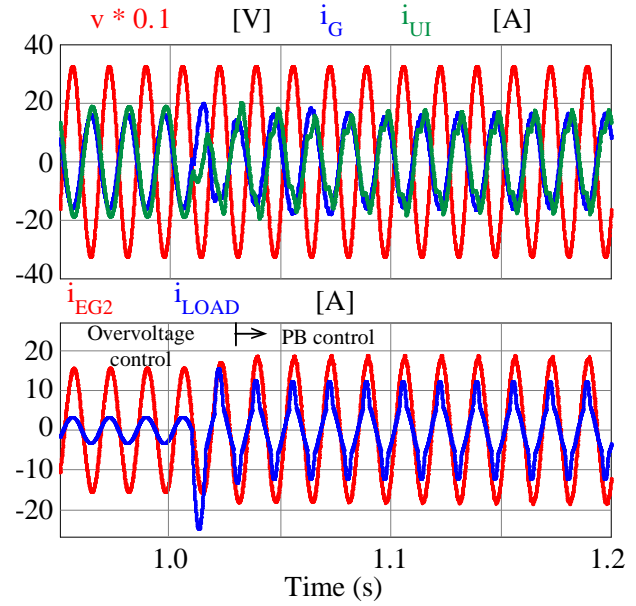
Fig. 2.14: Simulation result: current behavior during the load step change. Top: PCC voltage (red), grid (blue) and UI (green) currents. Bottom: EG$_2$ (red) and load (blue) currents.

2.6. Conclusions

At this point, Fig. 2.2 can be redrawn in Fig. 2.15 showing up the detailed block diagram of the proposed single-phase EG system including the power circuit and its local control scheme, all discussed in this chapter. This chapter has described the main basic, specific and ancillary functions of EGs applied to both connection sorts: line-to-neutral or line-to-line. In general, for local optimization strategy, the approach is identical for both connections; only the voltage measurement must change, following the own

device connection. It will be shown in Chapter 6 that for global optimization strategy different consideration is applied depending on the DER connection scheme.

It has been presented a linear problem formulation for compensation purposes, in particular, the reactive power, harmonic distortion and load unbalance by means of DERs under limited power capacity, due to renewables intermittent power generation. The proposed approach takes advantage of the formulated linear problem, based on power quality requirements, to define a set of grid performance indexes constraints. It goes beyond of other approaches that usually consider only current constraints. In addition, it enables full exploitation of DERs capability.

It has also presented a dynamic overvoltage control technique for low voltage microgrids. Under overvoltage condition, DERs are locally controlled so as to limit their power injection and maintain node voltages within nominal ranges. In [**43**] was shown that the proposed overvoltage control reduces the occurrence of overvoltage conditions by decreasing the power feed-in from DERs. This unavoidably causes a certain reduction in the total power generation. However, this drawback can be eliminated by integrating storage devices at specific critical nodes.

It will be shown in Chapter 5 that the control of the power flow (taking place centrally, at the microgrid PCC) and the local overvoltage control (performed distributedly, at each DER) cooperate so that both the power flow at microgrid PCC and the voltage magnitudes at the point of connection of DERs can be simultaneously regulated.
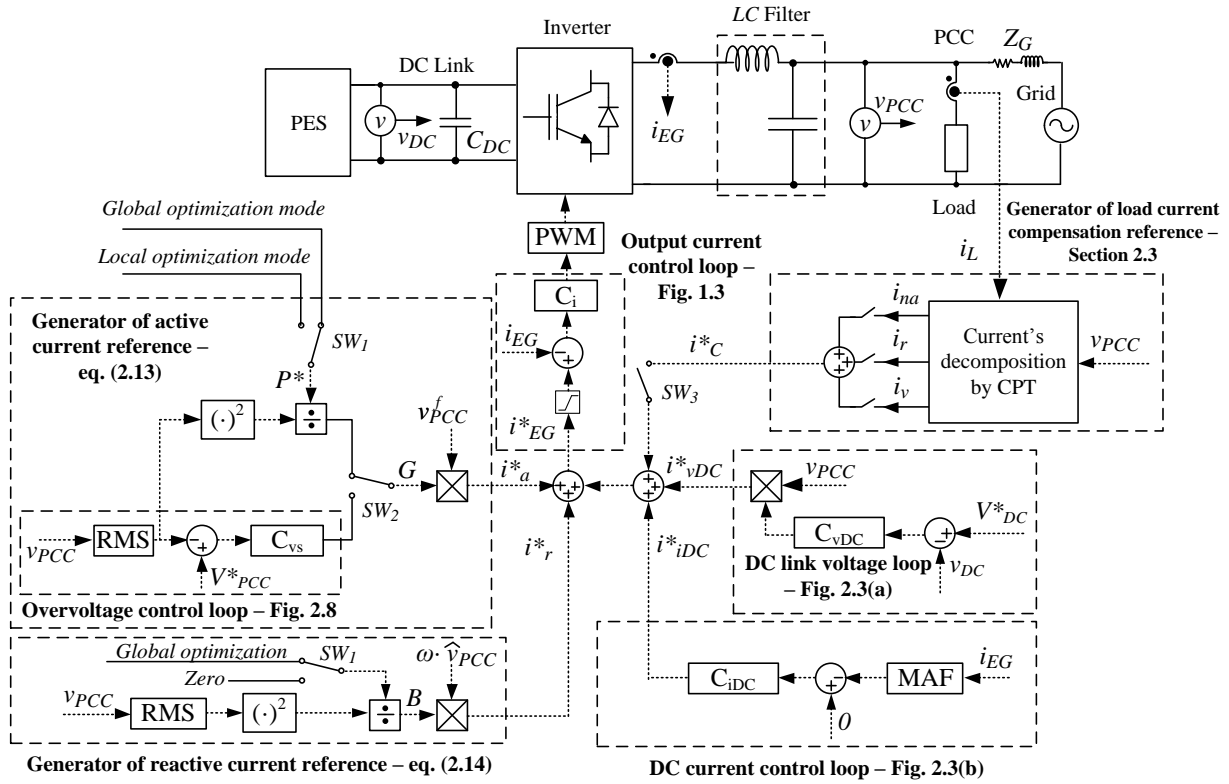
Fig. 2.15: Block diagram of the proposed distributed energy gateway with complete control scheme, © IET 2015 [**65**].

Chapter 3

3. Utility Interface

This chapter presents the main principles and a general control technique for UIs in low voltage microgrids. The typical connection and set-up of UI is shown in Fig. 3.1(a). Usually, an UI should be connected at the low voltage terminals of a three-phase step-down transformer feeding the four-wire distribution grid, and it consists of a three-phase inverter with line-side *LC* filter, ES unit (e.g., battery, ultracapacitor) with a bidirectional DC/DC converter, and a communication module. The UI can also host the microgrid's master controller. The UI is therefore a crucial component, which need to be analyzed carefully to ensure safe and reliable operation for the microgrid. In this chapter, a possible control approach that provides all required functionalities and ensures proper microgrid operation, even in case of non-intentional islanding or severe load transients, is discussed.

Considering the proposed microgrid architecture of Fig. 1.2, the UI allows effective and prompt interaction between host utility and microgrid, and provide grid voltage and frequency references during microgrid islanded operating mode. If compared to other devices known from the literature, it is possible to point out some advantageous features with respect to: 1) *hybrid voltage and current control mode* [**95**], which must switch between control modes; 2) usual *line-interactive uninterruptible power source (UPS) systems* [**96**], which present only some specific functionalities, and 3) *indirect current controls* where no provisions are taken to control the grid current harmonics under heavily distorted mains voltage [**37**], [**97**]. Precisely, the UI provides the following functionalities:
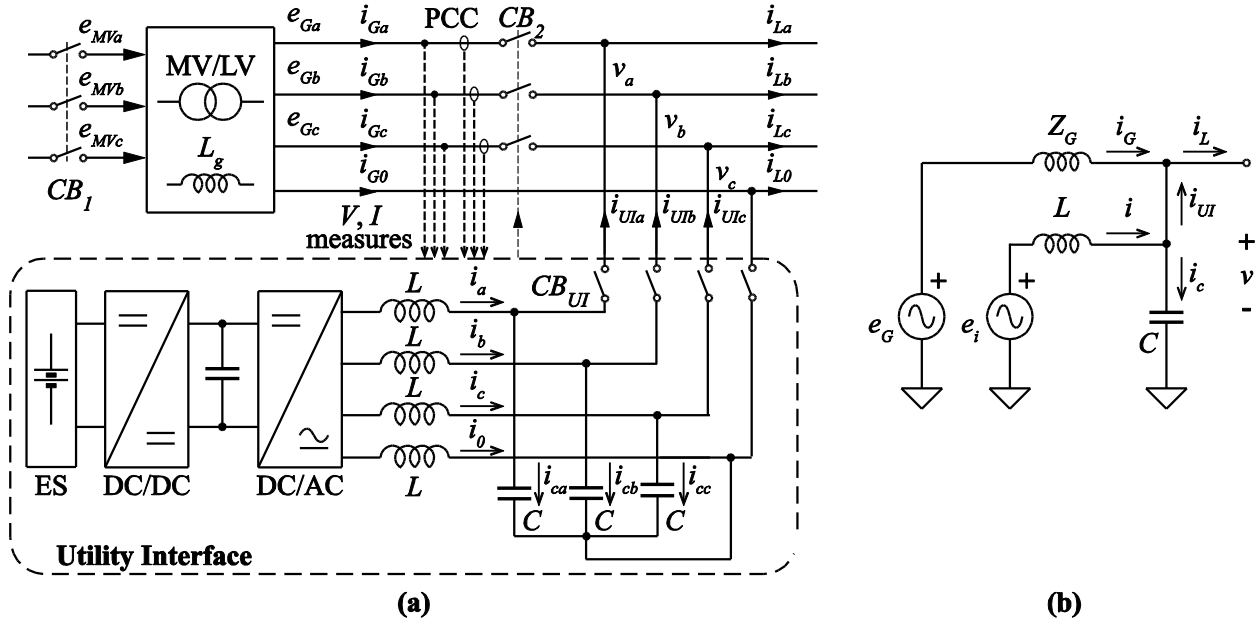
Fig. 3.1: Utility interface connected at PCC: (a) typical UI set-up; (b) equivalent single-phase representation, © IEEE 2014 [36].

- In grid-connected operation, it performs as a grid-supporting voltage source. In addition, a slow grid current control loop adapts the inverter AC voltages to ensure that the total currents absorbed by the microgrid meet the active and reactive power requirements of the mains. Moreover, negative-sequence and harmonic currents generated by the loads are (totally or partially) compensated, thus limiting their propagation through the distribution system. It is similar to shunt APF that aims to compensate current disturbances;

- In islanded operation, it performs as a grid-forming voltage source, providing voltage and frequency references for the entire microgrid and keeping the PCC voltages synchronized with the utility voltages, when available. It is similar to conventional UPS that ensures voltage supplying during grid faults;

- During transitions from grid-connected to islanded operation, and vice-versa, it ensures a proper grid voltage for the microgrid.

- During changes of load and/or supply, it performs as an active decoupling device, avoiding perturbations to propagate from microgrid to utility and vice-versa.

3.1. Utility interface control principles

For simplicity, let us consider the equivalent single-phase (line-to-neutral) representation of the UI shown in Fig. 3.1(b). The utility supplies AC voltage e_G through MV/LV transformer impedance Z_G, and the UI inverter feeds AC current i through filter inductance L. This current is partially absorbed by shunt filter capacitor C (i_c), and partially flows to the PCC (i_{UI}), where load current i_L is drawn.

As mentioned before, the UI must always perform as a *voltage source* with low internal impedance, capable to sustain fast power changes. A voltage control loop is therefore needed, complemented by a fast internal inductor current loop to improve dynamic response and prevent over-

currents. A slow external grid current loop is also needed, so that it adjusts the inverter currents in order to compensate the load disturbing effects (reactive power, harmonic and unbalance).

An equivalent single-phase scheme of UI control is shown in Fig. 3.2. It includes the three control loops previously mentioned. The outer grid current loop has a limited bandwidth (a few Hz) and enforces line current i_G to track reference i^*_G at low frequency, for PCC power flow control and for compensation purposes. The intermediate voltage loop has a wider bandwidth (a few hundred Hz), and enforces phase voltage v to track reference v^* in the mid-frequency range, thus providing the voltage source functionality required by the UI. The inner inductor current loop has a large bandwidth (a few thousand Hz), and enforces inverter current i to track reference i^* in the high-frequency range.

Note that the voltage reference v^* is obtained from ideal voltage reference e^*, by subtracting the voltage correction Δv^*, which is derived by amplifying the line current error $\varepsilon_i = i^*_G - i_G$.

Since the UI is always controlled as voltage source, the proposed control structure allows soft transition from grid-connected to islanded operation. With such a goal, it is sufficient to set line current reference i^*_G to zero; within the time response of the external loop, the line current vanishes and the voltage loop brings the PCC voltage at reference value e^*. In case of non-intentional islanding, the behavior is the same, with the additional time delay necessary to detect line current zeroing.

In general, the proposed control performs as follows:

- In grid-connected operation, the UI performs as a grid-supporting voltage source and, inverter voltage v is adjusted to enforce line current i_G to track reference i^*_G. If i^*_G is properly chosen (e.g., purely sinusoidal positive-sequence or normalized instantaneous PCC voltage), a slow control action occurs, which removes the reactive and unbalance current terms at the fundamental frequency, thus, improving the power factor at PCC. Besides, if the grid current control loop is fast enough, the voltage correction Δv^* drives the inverter to compensate for harmonic currents, thus reducing the THD_{iG} as well.

- In islanded operation, error signals ε_i vanishes, so that voltage correction Δv^* is brought to zero and inverter voltage reference v^* matches with e^*. Therefore, the UI performs as a grid-forming unit and keeps the PCC voltage at the specified amplitude and frequency. Controller Y_v must damp the oscillations caused by the resonance of filter capacitor C with inductance L_G. Moreover, it must provide enough control bandwidth to preserve the voltage purity at PCC in spite of load current harmonics.
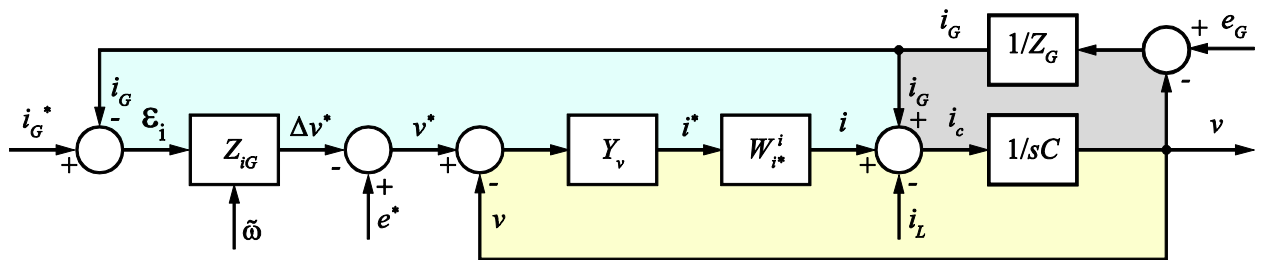
Fig. 3.2: Block scheme of UI. Upper-left area: outer grid current control loop; lower-right area: voltage control loop; upper-right area: *LC* resonant loop, © IEEE 2014 [36].

- The transitions from grid-connected to islanded operation run smoothly since the control discontinuities are prevented. In fact, voltage correction Δv^* is driven to zero as fast as islanding is detected.

3.2. Comparison of oversampled current controllers for UI converters

This section presents a comparison of three different fully-digital, large bandwidth inverter current controllers (i.e., ≈ 3 kHz) for UI converter, in order to perform as a *voltage source* with low internal impedance. In order to be capable of sustaining fast power changes, a voltage control loop is needed, and it has to be complemented by a fast internal inductor current loop to improve dynamic response and protect the converter from dangerous overload conditions. The purpose is to determine which one allows to achieve the most appropriate final performance, when adopted for the implementation of the inner inductor current control loop (W_{i*}^i) of the UI converter. Different large bandwidth digital current controllers can be employed for this purpose, which the capability to allow a satisfactory voltage control needs to be comparatively assessed.

In order to achieve good voltage regulation, the current loop small-signal bandwidth needs to be maximized. To prevent saturation of the voltage loop, a fast large-signal response is also beneficial. Thus, this chapter analyzes three possible current controllers and determines their small-signal bandwidths. All controllers are implemented on the same field programmable gate array (FPGA) chip and acquire their input signals through the same analog to digital conversion board. The goal of such discussion is to identify the feasible performance limits for each technique rather than discussing the implementation details, therefore a single-phase converter is taken into account as the test bench.

Extension to a three-phase converter is almost straightforward, both if the three-phase electrical system is turned into a two phase equivalent model via Park's transformation, and if the current controller is implemented directly in the natural (*abc*) reference frame, as performed here.

This section comprises, in the first place, an overview of the considered controller organizations. Following, the expected performance limitations are explored, with particular reference to both small-signal stability limits and large-signal tracking performance. A generalized equivalent model of the internal current loop is then presented that can be used to analyze the voltage loop performance. Finally, the voltage loop design is illustrated and the feasible performance estimated.

3.2.1. Oversampled current controllers

This section summarizes the basic features of the considered digital current control circuits:

A.   the oversampled PI current controller;

B.   the oversampled predictive current controller [98];

C.   the fixed frequency digital hysteresis current controller [99].

To fairly compare the performance, a common application test bench, schematically represented in Fig. 3.3, is considered for all controllers. Its parameters are listed in Table 3.1 and correspond to a simplified, single-phase, example of a UI converter. Besides, controllers are designed using the same sensing and signal condition circuitry, which employs a high performance 12-bit analog to digital converter (ADC) and the same FPGA chip. In all cases, signal processing is performed on 16-bits fixed point arithmetic. The basic features of the considered FPGA and ADC hardware are summarized in Table 3.2. For simplicity, the applied modulation strategy is a basic two level pulse width modulation (PWM), where switches S_1 and S_4 share the same command, as well as S_2 and S_3, so as to impose either $+ V_{DC}$ or $- V_{DC}$ at the converter terminals. Accordingly, a commercial PV inverter, designed to operate grid-connected with two level modulation, has been used for these experimental tests.
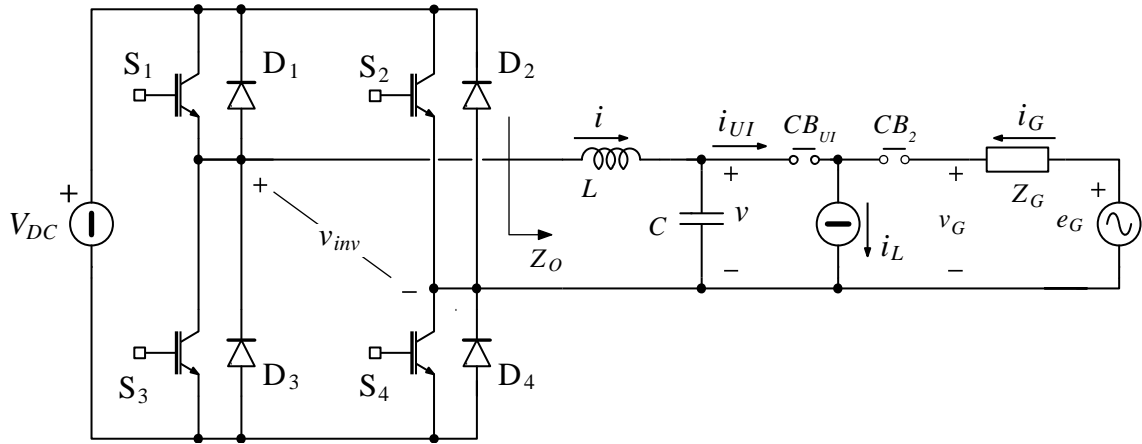
Fig. 3.3: Considered full bridge inverter topology, © IEEE 2015 [**100**].

Table 3.1: Converter parameters, © IEEE 2015 [100].

Parameter	Symbol	Value	p.u.
Output power	S_O	3 kVA	1
Input voltage	V_{DC}	400 V	1.74
RMS output voltage	V	230 V	1
Fundamental frequency	f_n	50 Hz	1
Switching frequency	f_{sw}	20 kHz	400
Filter inductance	L	1.45 mH	0.021
Inductor ESR	ESR_L	150 mΩ	0.0085
Filter capacitance	C	100 µF	0.554
Line inductance	L_G	0.6 mH	0.0089
Line resistance	R_G	500 mΩ	0.028
Current sensor gain	$K_{sense,1}$	25 mV/A	---
Voltage sensor gain	$K_{sense,v}$	2.5 mV/A	---

Table 3.2: FPGA and ADC chip characteristics, © IEEE 2015 [100].

Component	Model	Parameter	Value
FPGA	Spartan-6 LX 45	Slices	6822
		DSP48s	58
		Max. clock frequency	200 MHz
		Arithmetic resolution	16 bit
ADC	AD9226	Max. sampling rate	65 MSample
		Full scale range	2 V
		Resolution	12 bit
		Latency @ 28MHz	0.286 μs

The output filter is made up of a series inductor and a shunt capacitor to provide voltage source characteristics. Because of the grid voltage source and the UI output voltage are decoupled by the connection impedance $Z_G = R_G + sL_G$, the output voltage (v) is a system's state variable, not just an exogenous[6] input, even in the grid-connected mode of operation. In principle, this could imply a dynamic coupling between the system's state variables (i.e., inductor current and output voltage) and complicate the current control design. However, this is seldom the case. To prove it, let us analyze the Bode plot of the converter output admittance, $1/Z_O$, shown in Fig. 3.4.

Because of the relatively large size of the capacitive filter, that typically lies in the p.u. range [0.2-0.8], from the current loop standpoint, the admittance presents ideal inductive characteristics, at least at the frequencies of interest for the current loop design. This happens both in the islanded and in the grid-connected mode of operation, where also the inductance L_G comes into play. In other words, the presence of the capacitive filter is not really relevant for the current loop design, meaning that the two state variables are actually dynamically decoupled.
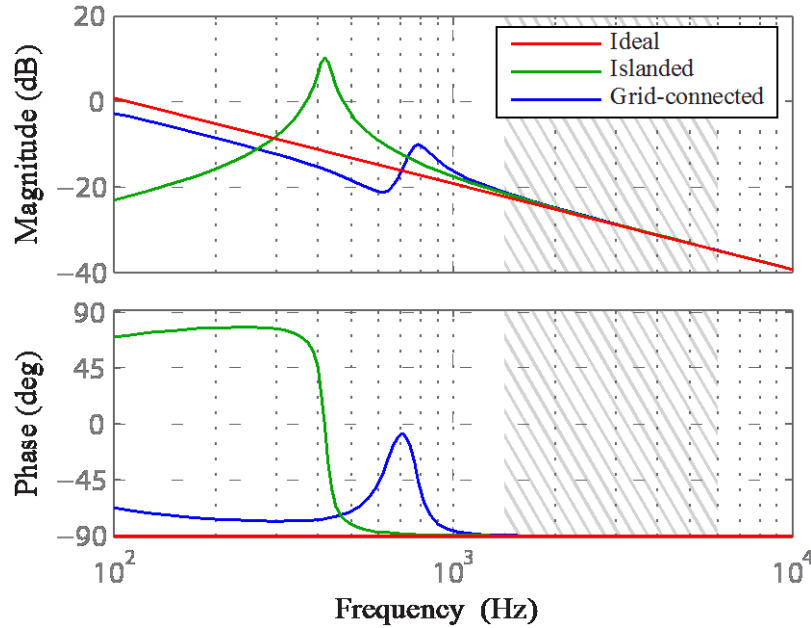
Fig. 3.4: Bode plot of the typical UI converter output admittance, $1/Z_O$ according to the schematic of Fig. 3.3. The shaded area corresponds to the expected range of the current controller's bandwidth, © IEEE 2015 [100].

---

[6] Exogenous variables are independent quantities that affect the model without being affected by it, and whose qualitative characteristics and method of generation are not specified.

It is worth noting that relatively large capacitance values are required not just for current ripple filtering, but rather to provide the inverter with sufficiently low output impedance, even outside the voltage loop bandwidth. Indeed, during UI operation, the trajectory of the output voltage reference is a line-frequency sinusoidal waveform of specified amplitude and phase, automatically adjusted to regulate the active and reactive power exchanged with the utility grid. A low capacitive impedance outside the voltage loop bandwidth obviously enhance the converter capability to track the sinusoidal reference, even in the presence of significant harmonic content in the microgrid current i_L, and thus helps to reduce the harmonic distortion of both the grid current, i_G, and the microgrid voltage, v.

In order to make the UI perform like expected, the inner inductor current control loop, that is used to protect the UI and to improve the voltage loop dynamic response, needs to present large small-signal bandwidth. If the microgrid current is measured and feed-forwarded to the current loop, a fast large-signal bandwidth can prevent the voltage loop saturation and greatly help in keeping the microgrid voltage unperturbed. Thus, a fast response in the presence of large current reference transients is another highly desirable feature for the inner inductor current loop.

A.   Oversampled PI current controller

The hardware configuration of the PI controller is schematically shown in Fig. 3.5. As it can be seen, the current error (ε_i) is sampled and subsequently processed at the occurrence of a clock pulse, that is also the digital PWM (DPWM) clock, determining the time resolution of the modulation period. The typical signals for this type of controller are shown in Fig. 3.6, where the considered symmetrical DPWM implementation is shown. As can be seen, the DPWM clock frequency is an integer multiple of the switching frequency, so that each modulation period is divided into 2*N* DPWM clock periods, with:

$$N = \frac{f_{DPWM}}{2 \cdot f_{sw}} \ . \tag{3.1}$$

The current error is acquired every *M* DPWM clock cycles with *M* chosen among the integer submultiples of *N*, i.e., $N/M = P$; $P \in \mathbb{N}$. As a result, the oversampling factor of the controller, *Q'*, can be defined as:

$$Q' = 2 \cdot \frac{N}{M} \ . \tag{3.2}$$

As well known, closing a control loop around a DPWM may cause the occurrence of limit cycle oscillations (LCOs), even when oversampling is not considered [101]. A detailed analysis of this phenomenon for oversampled voltage regulation loops in buck converters is presented in [102].

The PI controller gains can be selected imposing the desired crossover frequency and phase margin. Exploiting oversampling, the small-signal delay of the DPWM with symmetrical, triangular carrier, reduces by a factor *Q'* with respect to its natural implementation (i.e., $T_{sw} = 2$), which exactly corresponds to a zero order hold (ZOH) model delay for the applied switching frequency [103]. Therefore, the current loop bandwidth can be pushed closer to its theoretical limit, determined by the converter output impedance.
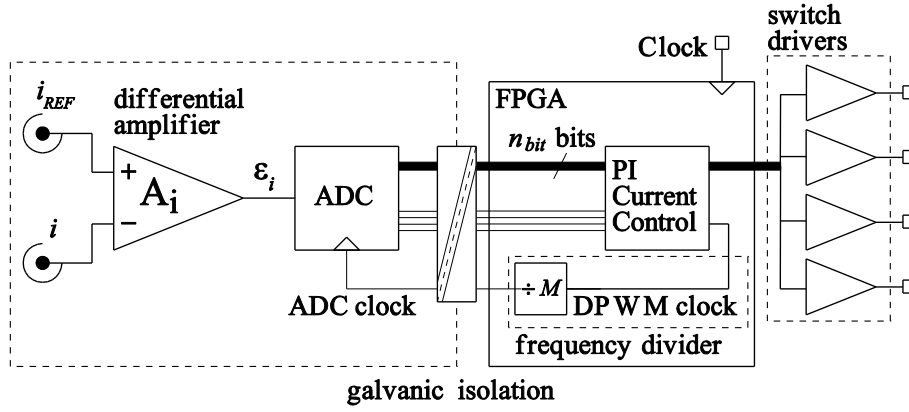
Fig. 3.5: Oversampled PI current controller hardware organization, © IEEE 2015 [**100**].
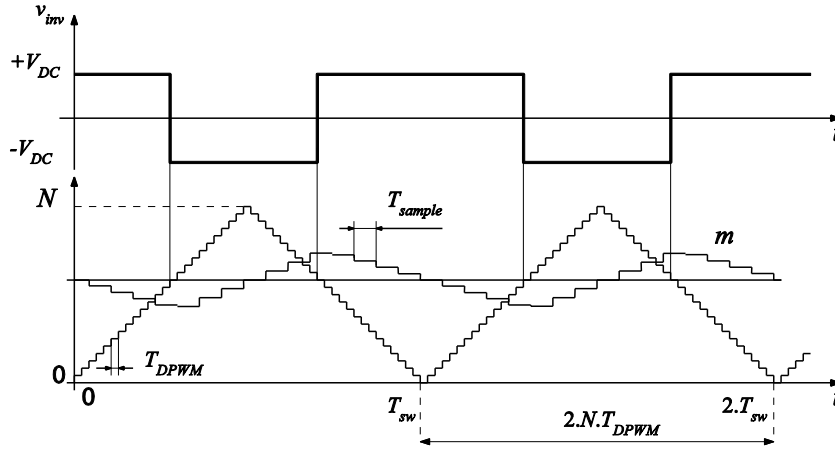
Fig. 3.6: DPWM operation with a multi-sampled PI current controller. The modulating signal *m* is the PI controller output, © IEEE 2015 [**100**].

It is easy to prove that the closed loop transfer function between the current reference and the inverter output current is given by the following expression:

$$W_{IPI}(s) = \frac{I_{ref}(s)}{I(s)} = \frac{\frac{G_{PWM}(s)}{Z_O(s)} \cdot H(s)}{1 + \frac{G_{PWM}(s)}{Z_O(s)} \cdot H(s)} \ , \tag{3.3}$$

where:

$$G_{PWM}(s) = K_{i,sense} \cdot \frac{2 \cdot V_{DC}}{N} \cdot e^{-\frac{T_{sw}}{2 \cdot Q}} \ ,$$

$$Z_O(s) = \frac{1}{sC} + sL + ESR_L \ , \tag{3.4}$$

$$H(s) = K_P + \frac{K_I}{s} \ .$$

Equation (3.3) is important to estimate the equivalent small-signal delay of the closed loop current controller.

B.   *Oversampled predictive current controller*

The hardware arrangement of the predictive current controller is shown in Fig. 3.7. As can be seen, the circuit is very similar to the PI controller's one, because of the current error is sampled and subsequently processed at the occurrence of a synchronization clock pulse, which is derived by frequency

division from the DPWM clock. The average current dynamic equation is [98]:

$$I_L(k+1) = I_L(k) + d(k) \cdot \frac{V_{DC}}{2 \cdot L \cdot f_{sw}} - [1 - d(k)] \cdot \frac{V_{DC}}{2 \cdot L \cdot f_{sw}} - \frac{v(k)}{2 \cdot L \cdot f_{sw}} \ . \tag{3.5}$$

Differently from the PI controller, though, in this case the current error is down sampled, so that the control circuits only uses the average current error samples available twice per modulation period. It then generates a new duty-cycle every half a switching period, implementing the following algorithm:

$$d(k) = \frac{L \cdot f_{sw}}{V_{DC}} \cdot \varepsilon_i(k) + \frac{v(k)}{2 \cdot V_{DC}} + \frac{1}{2} \ . \tag{3.6}$$

Again, LCO limitation requires attention. A detailed presentation of this controller's characteristics is given in [98]. Its most important feature is that, supposing, if there are *no* parameter mismatches and *unmodelled* dynamics, concerning, for example, the inductor equivalent series resistance (ESR) of the internal model, the closed loop small-signal response is exactly equivalent to *half a switching period* delay (i.e., to a single dead-beat response). Indeed, the closed loop transfer function between the current reference and the converter current sample sequence is given by:

$$W_{IDB}(z) = \frac{I_{ref}(z)}{I(z)} = \frac{G(z) \cdot H(z)}{1 + G(z) \cdot H(z)} = z^{-1} \ , \tag{3.7}$$

where:

$$H(z) = \frac{L \cdot f_{sw}}{V_{DC}} \ .$$
$$G(z) = \frac{V_{DC}}{L \cdot f_{sw}} \cdot \frac{z^{-1}}{1 - z^{-1}} \ , \tag{3.8}$$

such that *H(z)* is found applying Z-transforming in (3.6), and *G(z)* applying Z-transforming in (3.5).

Note that, when deriving (3.8), an ideal converter impedance has been considered, with no ESR and negligible capacitive component. Therefore, under these assumptions, the equivalent continuous time, transfer function of the closed loop predictive current controller is given by:

$$W_{IDB}(s) = e^{-\frac{sT_{sw}}{2}} \ , \tag{3.9}$$

which can be directly compared to (3.3). Interestingly, the dead-beat controller presents a linear phase response, differently from the PI current controller.
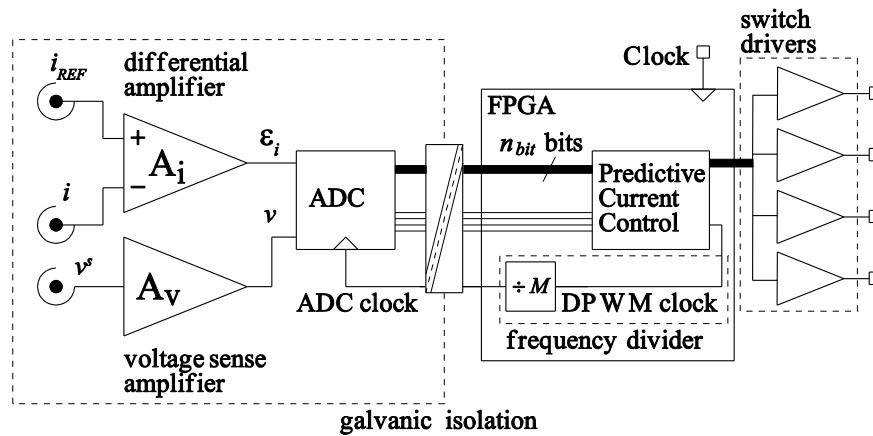
Fig. 3.7: Oversampled predictive current controller hardware organization, © IEEE 2015 [100].

C.   Digital, fixed frequency hysteresis current controller

Fig. 3.8 shows the hysteresis current control that is, in principle, capable of excellent steady state and dynamic performance. However, it normally implies variable switching frequency operation, because, in the applications of higher interest, like the one here considered, neither the converter's output voltage nor the current reference signal are perfectly constant. Frequency stabilization is possible and has been proven to be quite effective in making the controller, from the spectral performance standpoint, practically equivalent to a PWM based one, especially when digital hardware is used to the purpose. The resulting controller implementation is detailed in [**99**].

Because of the nonlinear behavior of the controller, it is not possible to analytically derive any equivalent transfer function and verify these considerations. It is possible, however, to implement a simulation model that allows us to test the controller response to small sinusoidal perturbations of the steady state reference current. Indeed, considering the controlled current and isolating, by discrete Fourier transform (DFT), the perturbation effect, the phase shift can be numerically estimated. In small-signal, continuous time terms, it should lead to a dynamic behavior compatible with the equivalent ZOH of a pure delay, whose entity can be estimated in half the control period. It can be confirmed or proved false by means of the results presented in the following section.
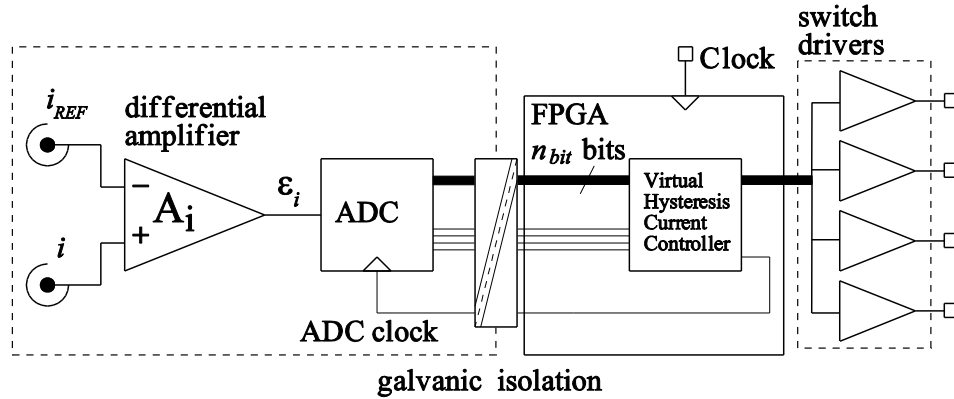
Fig. 3.8: Digital, fixed frequency hysteresis current controller hardware organization, © IEEE 2015 [**100**].

3.2.2. Current controllers performance assessment

The performance of the considered controllers has been verified both in the small-signal response to small (i.e., lower than 5 % in relative terms) current reference perturbations and in the large-signal response to step variations of the current reference of 50 % the nominal current.

The PI controller is designed for a 3 kHz bandwidth and 60° minimum phase margin. The oversampling factor is set to $Q' = 20$. The same factor has been used for the predictive controller as well. Instead, for the hysteresis controller, the oversampling factor was increased to $Q'_{Hyst} = 100$; this is necessary to guarantee a sufficiently tight control of the converter switching frequency, which kept to its set-point $f_{sw} = 20$ kHz with a 2 % of accuracy.

A.   Small-signal response test

As stated previously, one of the expected outcomes of the comparison presented in this section is an estimation of the small-signal delay characteristic of the evaluated current controllers. For the linear controllers, an analytical solution to the problem, although under some simplifying assumptions, has been determined in Sections 3.2.1–A and –B. For the nonlinear controller of Section 3.2.1–C, only numerical simulation or experimental measurements can give an estimation of the achievable phase shift. Also, experimental measurements have been performed for the three controllers and compared to analytical or, for the hysteresis controller, simulation results.

The tests have been performed by injecting a sinusoidal perturbation signal into the current control loop and measuring the output current. DFT has been calculated on a sufficiently large time span, so as to determine, with adequate resolution and precision, the phase and amplitude of the injected perturbation effect. In all tests, the converter output voltage has been externally controlled to a constant DC level so as to achieve constant modulation index operation. The modulation index, defined as:

$$m(t) = \frac{v(t)}{V_{DC}} \, , \tag{3.10}$$

was set to the value corresponding to the peak of the expected sinusoidal voltage, i.e., to about 0.82 p.u.

The results are presented in Fig. 3.9. It is interesting to observe how experiments confirm the analytical results for the linear controllers and the hypothesis on the hysteresis controller dynamic performance. In absolute terms, all the controllers guarantee a high performance level. In the considered bandwidth, extending from 10 Hz to 3.0 kHz, the amplitude response is practically flat (maximum deviation is lower than 3 dB) while the phase shift is minimum for the hysteresis controller, -3° at 3.0 kHz, maximum for the PI controller -49° at 3.0 kHz. Table 3.3 reports the results of all the tests.

B.   Large-signal response test

In this case, the controllers are compared by considering the response delay to a step change of the constant reference current. The obtained experimental results are shown in Fig. 3.10. In particular, Fig. 3.10(a) and Fig. 3.10(b) show the measured responses to a change in the reference current from 0 A to 10 A, and from 10 A to 0 A, respectively, when the converter output is connected to a voltage source imposing $v = 280$ V.

With respect to the situation where $v = 0$ V, the non-zero output voltage causes the rising slopes to be slower and the falling slopes to be faster, thus allowing to notice different dynamics. Indeed, in the fastest transients, shown in Fig. 3.10(b), we can discern that the best responsiveness is given by the hysteresis and the predictive controllers, while the worse one is given by the PI controller.

In all cases, the reference step change is detected with minimum delay. Consistent results are obtained in grid-connected operation as well; Fig. 3.10(c) shows the response to a phase jump in a 50 Hz sinusoidal reference current. A different test consisted in tracking a 50 Hz, 10 A_{peak} amplitude, sinusoidal reference signal and measuring the resulting distortion, considering harmonic components up to order 40.

In general terms, the hysteresis controller presents the best performance, with maximum phase margin up to the crossover frequency. The predictive controller also shows a very good performance attainable with less stringent hardware and computation requirements if compared with the hysteresis controller's one. The PI controller shows a satisfactory performance. Thus, the hysteresis controller has been chosen to the inner inductor current control loop.
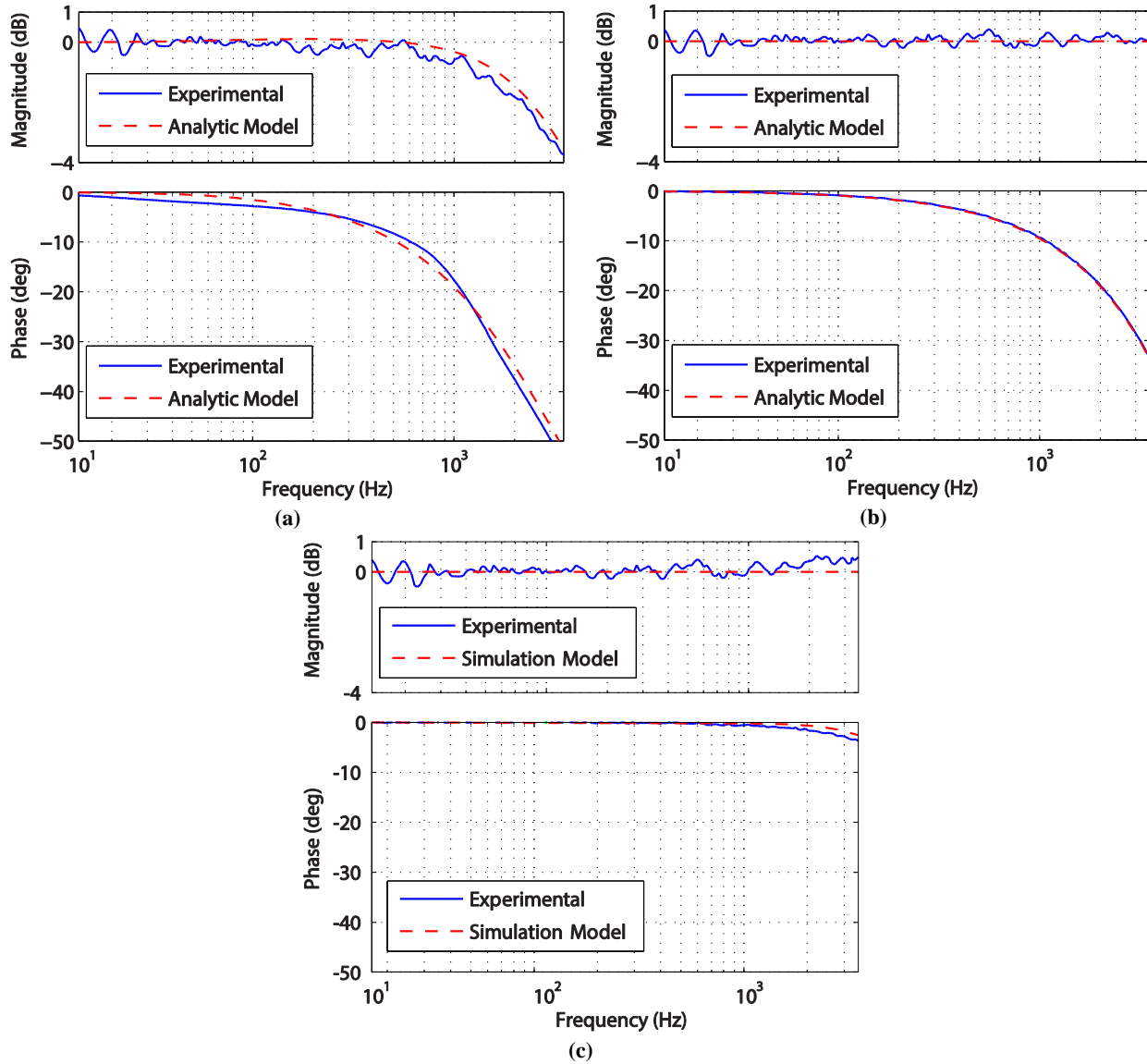
Fig. 3.9: Controller small-signal response in gain (upper plot) and phase (lower plot) according to: analysis (dashed), experiments (solid): (a) oversampled PI current controller; (b) oversampled predictive current controller; (c) digital, fixed frequency hysteresis current controller (analysis replaced by simulation), © IEEE 2015 [**100**].

Table 3.3: Experimental results: phase margin and voltage THD © IEEE 2015 [100].

	PI	**Predictive**	**Hysteresis**
Phase shift @ 0.5 kHz	-8°	-5°	0°
Phase shift @ 1.0 kHz	-18°	-10°	-1°
Phase shift @ 2.0 kHz	-37°	-19°	-2°
Phase shift @ 3.0 kHz	-49°	-28°	-3°
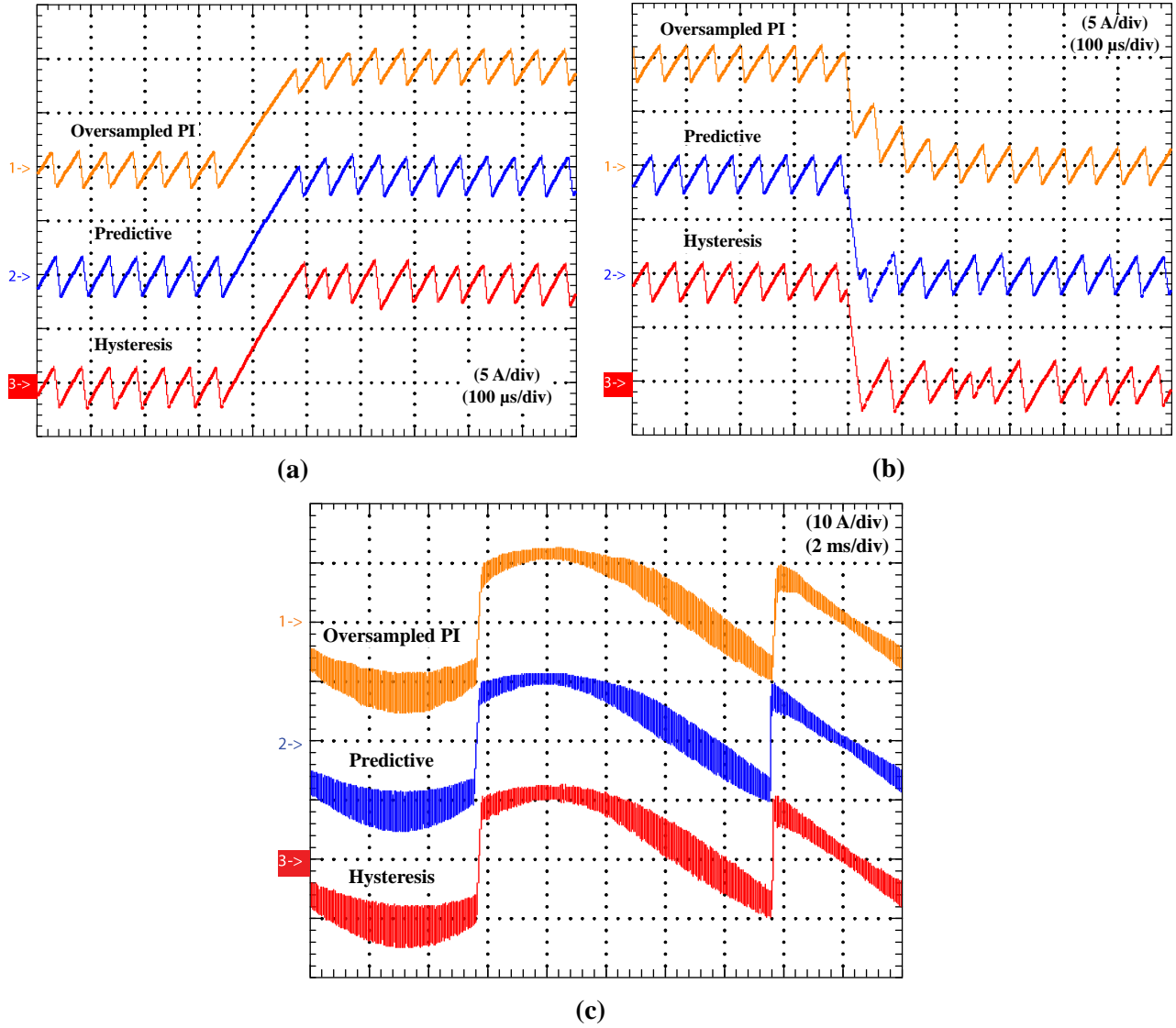
Fig. 3.10: Experimental measurement of the considered controllers' large-signal step responses: (a) response to a positive step of the reference current (v = 280 V); (b) response to a negative step of reference current (v = 280 V); (c) response to 180º phase step of a sinusoidal reference current during grid-connected operation (v_G = 230 V_{RMS}, f_1 = 50 Hz), © IEEE 2015 [**100**].

3.3. Transfer functions and control design of the UI

3.3.1. Transfer functions

In order to design the controllers, the main transfer functions of the control scheme in Fig. 3.2 are determined. Let us consider first the resonant loop shown in upper-right part of Fig. 3.2 (grey area). We derive the transfer functions from input i to outputs v and i_G in the form G_{in}^{out}:

$$G_i^v = \frac{Z_G}{1 + sZ_G C} \ , \tag{3.11}$$

$$G_i^{iG} = \frac{1}{1 + sZ_G C} \ . \tag{3.12}$$

Then, we close the voltage control loop (yellow area) and determine the closed-loop transfer functions between input v^* to output v in the form H_{in}^{out}:

$$H_{v*}^v = \frac{Y_v \, W_{i*}^i \, G_i^v}{1 + Y_v \, W_{i*}^i \, G_i^v} \; , \tag{3.13}$$

where W_{i*}^i is the UI's closed internal inductor current control loop. As discussed in [**100**], W_{i*}^i can be adequately modeled nearly to a unitary gain, as shown in Fig. 3.9.

Finally, the external close-loop transfer function between input i_G^* and output i_G in the form W_{in}^{out}:

$$W_{iG*}^{iG} = \frac{\dfrac{Z_{iG} \, H_{v*}^v}{Z_G}}{1 + \dfrac{Z_{iG} \, H_{v*}^v}{Z_G}} \; . \tag{3.14}$$

In (3.13) and (3.14), the terms Y_v and Z_{iG} are, respectively, the regulator of the intermediate voltage control loop and the outer grid current control loop. The regulators can be designed on the basis of the open voltage control loop and the open grid current control loop transfer functions.

Note that all transfer functions depend on line impedance Z_G, which can be measured *off-line* or estimated from the short circuit impedance of MV/LV transformer and distribution line impedance.

3.3.2. Control design

The above considerations show that, by proper design of control parameters and selection of current and voltage references, the UI can provide all desirable features: grid-supporting and grid-forming function, smooth dynamics from grid-connected to islanded transition and vice-versa, compensation of reactive, harmonic and unbalance currents. Moreover, due to the low impedance of shunt capacitors C at high frequency, the UI can filter out a large part of the current harmonics generated by nonlinear loads.

In general, the control of multifunctional grid-connected converters for microgrid applications is a delicate subject. The main aspects to be tackled in the design are steady state accuracy, large-signal dynamic response, stability robustness, and grid synchronization [**58**], [**104**]. Various approaches have been analyzed in the literature to address the various aspects [**58**], [**104**]. In [**105**] is shown that, for a voltage controlled voltage source inverters (VSI), a PI plus resonant controller (PI + R) provides satisfactory behavior over a wide range of operating modes, whereas grid current feed-forward and load current feed-forward can degrade stability in particular load conditions. Instead, [**106**] proposes the analysis and design of synchronous reference frame controllers (SRFC) applied to single-phase VSIs. Though the advantages of this approach are, in general, still not well defined, the paper shows that SRFC, combined with capacitor current active damping, grid voltage feed-forward, and multi-resonant harmonic compensation, can lead to effective solutions. In [**82**], [**107**] the H^∞ design approach combined with repetitive controllers is applied for robust control of grid-connected voltage-controlled VSIs. As concerns grid synchronization, new PLL-free synchronization strategies have been recently proposed and implemented [**59**], [**108**]; nevertheless, solutions based on conventional PLL still attract interest for their flexibility.

In our implementation, we took advantage of a *fixed frequency digital hysteresis controller*, detailed in [**109**], for the inner inductor current loop and a *PI regulator* for the intermediate voltage loop.

The reference for the voltage loop is obtained from grid voltage reference e^* corrected by term Δv^*, which is generated by grid current controller Z_{iG} so as to regulate the current flow at PCC. Controller Z_{iG} is implemented as in Fig. 3.11 [14], [110], and integrates a $PI + R$. The resonant controller is tuned to grid frequency to minimize the steady state tracking error up to seventh harmonic component. Finally, a natural (*abc*) reference frame PLL [94] is used to estimate the fundamental angular frequency ω_1 for automatic tuning of the resonant controller (R).
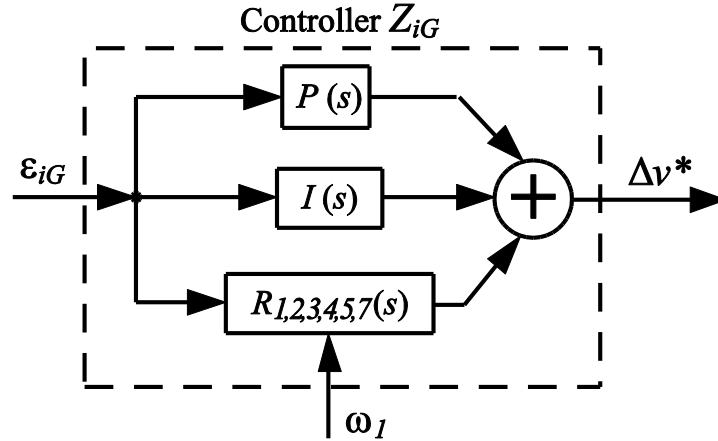
Fig. 3.11: Continuous time equivalent dynamic model of the adopted PI plus resonant controller.

For the design of regulator Y_v, shown in Fig. 3.2, let us consider the worst condition (i.e., no-load operation in islanded mode). In this situation, assuming that $W_{i*}^i \approx 1$ in the frequency range of interest for the design of voltage regulator Y_v, a suitable PI regulator can be devised. Notice that the transfer function G_i^v in islanded operation comprises only the capacitor C, because of $|Z_G| \to \infty$. Once Y_v is designed, its performance must be verified for both grid-connected and islanded cases. Fig. 3.12 shows the Bode plots of the open loop gain obtained by a PI regulator with target phase margin of 70° and crossover frequency of 1.3 kHz, during both operating modes with no load.

At this point, it is possible to design the regulator Z_{iG} of the outer grid current control loop. To this end, we refer to the external open loop transfer function without Z_{iG}:

$$\frac{H_{v*}^v}{Z_G} = \frac{Y_v\, W_{i*}^i\, G_i^v}{1 + Y_v\, W_{i*}^i\, G_i^v} \cdot \frac{1}{Z_G} = \frac{Y_v\, W_{i*}^i\, G_i^{iG}}{1 + Y_v\, W_{i*}^i\, G_i^v} \; . \tag{3.15}$$

For the selection of the regulator, we note firstly that the considered control loop has to fulfill two targets. The main one is to control the power flow at PCC, which is accomplished by $PI(s) + R_1(s)$; the second, ancillary, is to compensate the harmonic currents at PCC in the steady state, which is accomplished by $R_{2,3,4,5,7}(s)$. These two targets can be accomplished by the use of a PI + R controller.
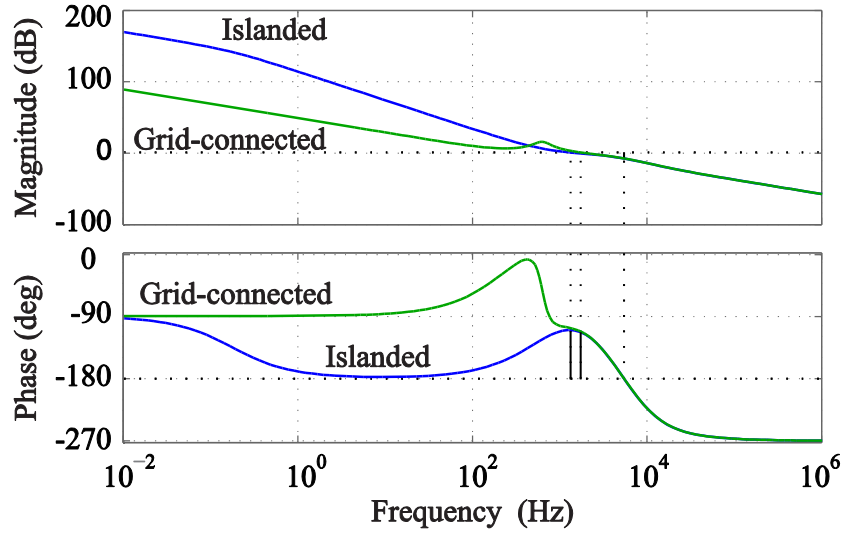
Fig. 3.12: Open loop gain of voltage control loop, © IEEE 2014 [36].

controller tuned to grid frequency up to seventh harmonic component. The implementation of this controller is shown in Fig. 3.11 and has the form described in [14], [110]:

$$P(s) + I(s) + R(s) = K_P + \frac{K_{I0}}{s} + \sum_{h=1,2,3,4}^{5,7} \frac{K_{Ih} \cdot \omega_b \cdot s}{s^2 + 2\omega_b s + (h \cdot \omega_1^2)} \ , \tag{3.16}$$

where ω_b is the resonance bandwidth. Note that ω_1 can be adjusted to effectively tune the filter resonances to grid frequency. Fig. 3.13 shows the open loop gain of the outer grid current control loop, where ω_b is set to 4.1 rad/s. The stability of the system is verified by inspection of the Nyquist plot, as in [104], [111]. Besides, it is important to take into account the effects of discretization method and computational delay on the implementation and performance of resonant controllers, since they are very sensitive to accuracy of the resonant frequency [112].
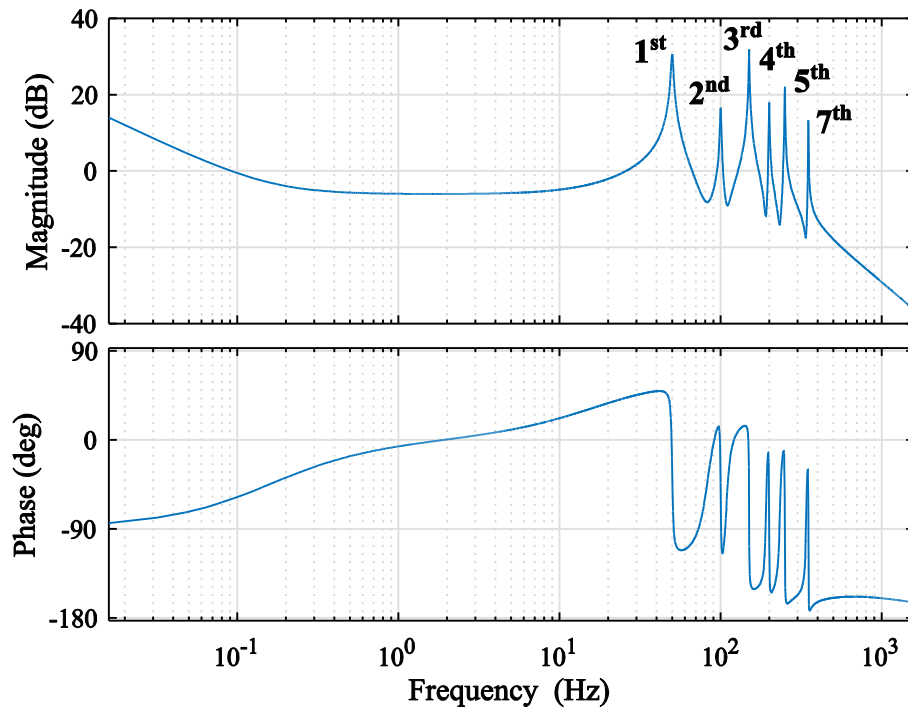
Fig. 3.13: Open loop gain of outer grid current control loop.

3.4. Discussion of DC side design of UI

The DC side of an UI may be endowed with an ES unit (battery and/or super-capacitor) and, if needed, a backup generator (micro-turbine, fuel cell, diesel gen-set). The former is used for promptly and short-term response, whereas the latter is for long-term maintenance. The design of the DC side is strictly related to the specific microgrid application, grid standard requirements and user needs, for example, factors that influence this aspect are the degree of adoption of ES devices, and the expected frequency and duration of islanded operation, among others.

Anyway, the UI design must be evaluated for short- and long-term responses. The first must be considered under transients of load and line, then, it has to be fast enough and endures maximum peak values of voltage and current. Moreover, it must, at least, guarantee temporarily energy needs during the transition up to the steady state operation. The latter is handled for ensure islanding operation for relative long periods of time, and it must take into account the distributed ES capability, over the EGs; the requested time of islanding operation and; of course, generation and demand profiles. In basis of these two specifications, the ES unit and backup generator of the UI can be properly designed. This analysis is not further addressed herein.

3.5. Islanding detection and grid synchronization

Islanded operation means that the microgrid is energized solely by one or more local sources, while it is electrically decoupled from the mains. It occurs when the external circuit breaker (CB_1), usually driven by the DSO, or the internal electromechanical circuit breaker (CB_2) are open (see Fig. 3.1). The UI drives CB_2 to open, and set P_G^* to zero when an *islanded* condition is detected [i.e., when CB_1 is opened or the quality of voltage at PCC transcends allowable limits (*grid absent* condition)]. In any case, the transition to islanded operating mode makes the UI automatically become the grid-forming device for the entire islanded microgrid, having to autonomously and timely adapt its voltage reference to guarantee a seamless transition. For such purpose, effective islanding detection and synchronization techniques are required. However, the islanding detection is not the focus of this work, and several islanding detection techniques have been proposed in the literature [113], so as we have decided to implemented a simple passive islanding detection, taking advantage of the grid current measurement used in the UI control scheme.

The adopted islanding detection technique is shown in Fig. 3.14. It is a passive technique that does not need to perturb neither voltages nor currents and, differently from active methods, as the one discussed in [37], cannot become unstable under distorted load and/or voltages. To describe its operation principle, let us assume the operation in steady state before transition. Thanks to the proper UI control it is reasonable

to consider $I_G \approx I^*_G$. By denoting I_G^{thres}[7] as the threshold for RMS value of the grid current, that is much smaller than the nominal grid current, we can distinguish two cases of operation:

- $I_G > I_G^{thres}$: in this case, the transition to islanded operation is characterized by the reduction of measured value of I_G with respect to its reference I^*_G. Then, the *islanded* operation is triggered when the current error becomes significant, i.e., when $I_G^* - I_G > I_G^{thres}$ while $\partial I_G/\partial t < 0 \leq \partial I_G^*/\partial t$;

- $I_G < I_G^{thres}$: in this case, the transition to islanded operation, though having little effect on the measured I_G, opens the grid current control loop leading its regulator to deviate from the ideal equilibrium point $(i^*_G, i_G, \Delta v^*) = (0, 0, 0)$ due to the noise and non-idealities presented in the real application (sensors, signal conditioner, etc). Then, based on these conditions, the *islanded* operation is triggered when the voltage correction term ΔV^* becomes significant, i.e., $\Delta V^* > \Delta V^{*thres}$.

The distinction made above allows a prompt islanding detection if islanding occurs while the microgrid is exchanging power with the mains, and a method that is resilient to external noise if the islanding event occurs when there is even negligible current exchange at the PCC.

Finally, the *grid absent* condition can be detected by verifying whether the measured grid voltage complies with the acceptable limits in terms of both amplitude and frequency. *Programmed intentional islanding*, possibly due to grid maintenance, can be performed as well, just by setting a variable (*flag*), starting a microgrid disconnection sequence. The operating modes and transitions, along with the corresponding state of circuit breakers are shown in Fig. 3.15.
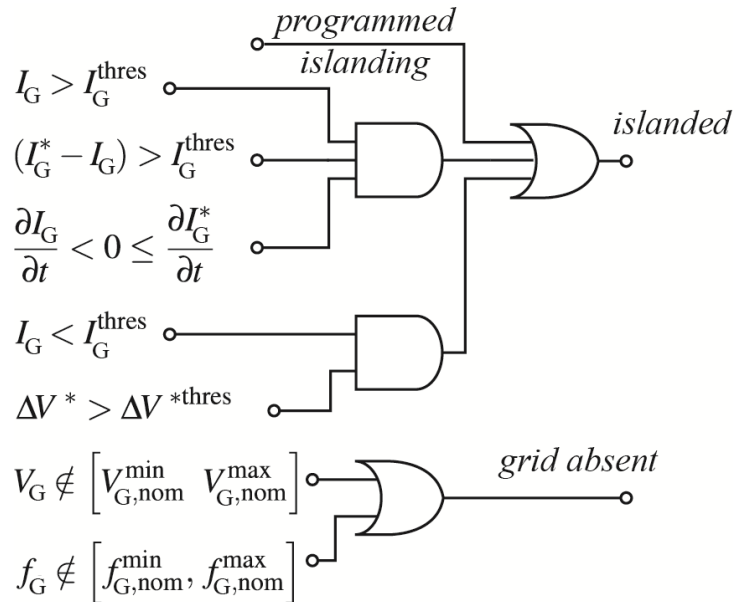
Fig. 3.14: Passive islanding detection scheme.

---

[7] I_G^{thres} value is chosen to be between the average value of the noise and non-idealities presented in the grid current sensor and the average value of the perturbed noise presented in the grid current controller, when $P^*_G = 0$.

X = 0 ⇒ Intentional
X = 1 ⇒ Non-Intential

islanded = X
grid absent = 1

islanded = 1
grid absent = 0

Islanded with grid absent

$\overline{CB_1 \text{ open/close}}$
CB_2 open

Islanded with grid present

$\overline{CB_1 \text{ close}}$
CB_2 open

Grid-connected

$\overline{CB_1 \text{ close}}$
CB_2 closed

islanded = 1
grid absent = 0

islanded = 0
grid absent = 0
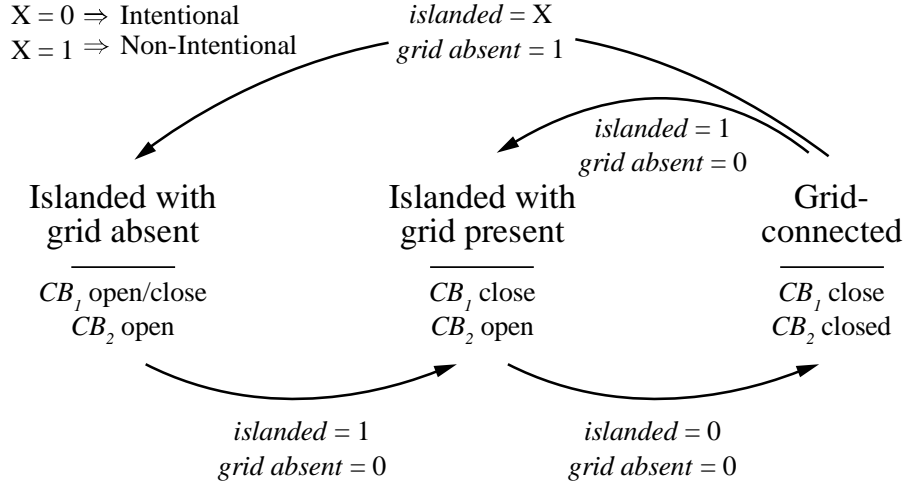
Fig. 3.15: Possible operating modes and transitions.

Fig. 3.16 shows how the phase voltage reference e^* and phase grid current reference i^*_G are generated. If grid voltage is present and within permissible limits (i.e., *grid absent* signal of Fig. 3.14 is not asserted), e^* is set as a positive-sequence sinusoidal with frequency $\widetilde{\omega}$ and amplitude $\widetilde{E}$. Instead, if grid voltage is not present (i.e., *grid absent* signal is asserted), e^* is set as positive-sequence sinusoidal at nominal frequency ω^*_{nom} and nominal amplitude E^*_{nom}, as in Fig. 3.16(b). With regards to i^*_G, in grid-connected operation it is determined according to the desired active and reactive power absorption from the grid (P^*_G, Q^*_G), whereas in islanded operation it is set to zero, as in (3.17) and shown in Fig. 3.16(c). Note that (3.17) uses the instantaneous PCC voltage to perform *resistive load synthesis* compensation.

$$i^*_{Gm} = \frac{P^*_{Gm}}{V^2_{Gm}} \cdot v_{PCCm} \ . \tag{3.17}$$

For what concerns the transitions of amplitude and frequency parameters, these are performed gradually by employing slew rate limiting blocks. Finally, we highlight that PLL frequency is bounded around the nominal grid frequency within values $\omega_{nom} \pm \Delta\omega^{max}_{nom}$ [see Fig. 3.16(a)]. The width of the band is dynamically changed during operating mode transitions, in particular, the band is gradually reduced to zero (decreasing) in the transition to the *islanded* operation with *grid absent*, thus making the islanded microgrid to operate at nominal voltage and frequency ($\omega^{max}_{nom} = \omega^{min}_{nom} = \omega_{nom}$), and immediately reinitiated to the maximum allowed frequency variation when the voltage is restored.

3.6.   Experimental application example

The final set-up of Fig. 3.17, which is detailed in Chapter 5, employs the inner inductor current controller, voltage regulator, grid current regulator, and islanding detector block, all of them discussed in the previous section, and an additional grid connection block. The function of this latter block aims to prevent high inrush currents at the connection of the islanded system to the main grid and to guarantee a non-saturated operation of Z_{iG}. Indeed, while Z_{iG} should be active at the connection with the mains to keep control on grid current i_G, the actual status of the grid depends on the response delay of electromechanical
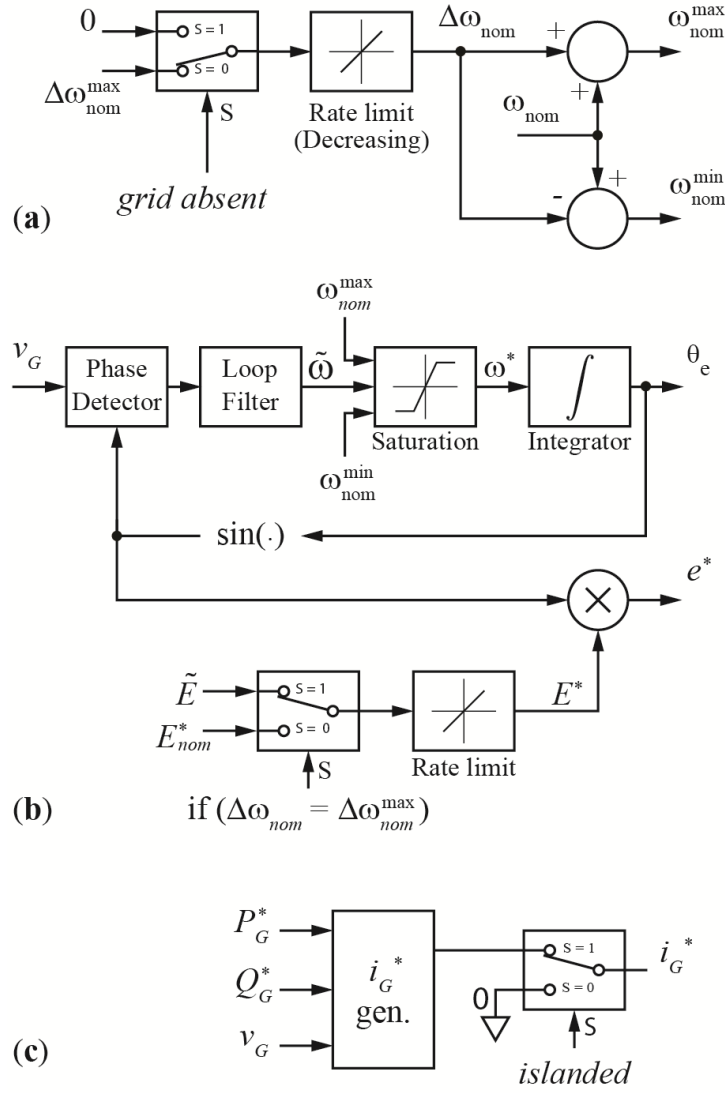
Fig. 3.16: Frequency (a), voltage (b) and grid current (c) reference generator (per phase).

circuit breaker CB_2 (typically ranging from tens to thousands of milliseconds), that is, generally unknown. During the clearing time, the regulator Z_{iG} operates in open loop: it reacts to spurious error signals introduced by the hardware, which can cause saturation. To alleviate these problems, the connection block ignores the current error ε_i below a suitable threshold, which is removed once the time response of CB_2 is elapsed. This allows both to limit inrush currents exceeding the deadband and to prevent spurious signals to perturb the regulator while CB_2 has not yet finalized the committed reclosure.

The supply reference i^*_G is set to be proportional to v_G, as in (3.17) performing a *resistive load synthesis* compensation, and to draw the full load power from the utility. The set-up parameters are detailed in Table 3.1.

An experimental realization of the circuit shown in Fig. 3.17 was developed to verify the actual behavior of the final system. These paragraphs report the acquired results. In particular, the system operation was investigated in the following operating conditions.
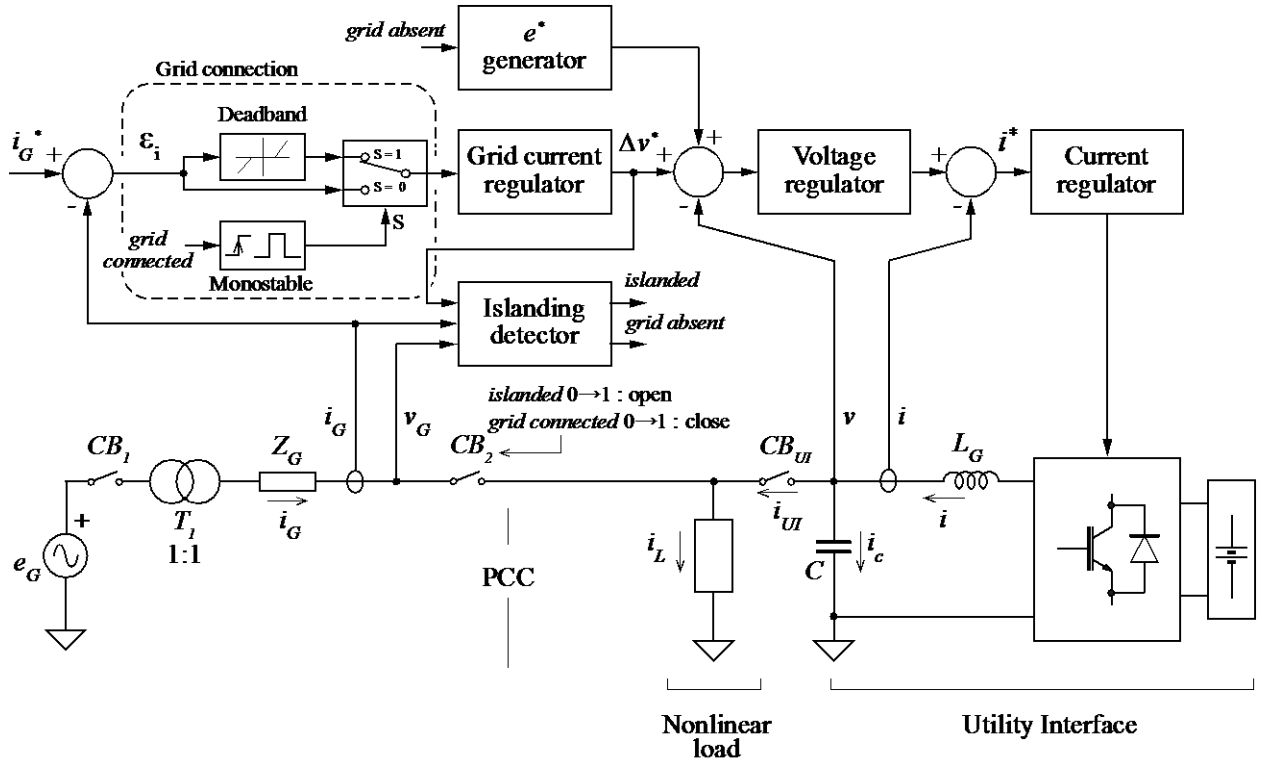
Fig. 3.17: Block diagram of the case study test bench, with power circuit, control scheme and transition management.

1) *Islanded operating mode*: A programmable electronic load absorbing 2.0 kW with crest factor CF = 2 is connected to the set-up. Fig. 3.18 shows grid voltage v_G, UI voltage v, and the current absorbed by the local load i_L in steady state conditions. We notice that the UI manages to feed the local load with an adequate voltage quality v ($\text{THD}_v = 2.6\ \%$) and synchronized with the grid voltage for a possible smooth and prompt transition to grid-connected operation. Table 3.4 reports the measured THD for other different loads.

Table 3.4: Experimental results of voltage quality.

	No load	47 Ω[1]	0.5 kVA[2]	1.0 kVA[2]	1.5 kVA[2]
THD at PCC	0.09 %	0.16 %	0.35 %	0.72 %	1.04 %

(1)   Purely resistive load;
(2)   Programmable electronic load, crest factor CF = 2.

2) *Grid-connected operating mode*: Fig. 3.19 shows system response at the connection of a nonlinear load during grid-connected operation with zero grid reference current ($P^*_G = 0$). In these conditions, an ideal operation would require a constant zero current flow at PCC. Due to the finite time response of grid current regulator Z_{iG}, the behavior shows a small transient on i_G during the connection.

The steady state behavior reached during grid-connected operation is shown in Fig. 3.20(a). The acquired waveforms of the voltage mains v_G, UI voltage v, current exchanged with the main grid i_G, and current absorbed by the local load i_L are reported while the current reference I^*_G is equal to 7.5 A_{RMS}. The THD of the grid voltage and current are, respectively, 0.6 % and 2.8 %.

The same measurement is performed with 5 % of third harmonic present on grid voltage e_G. As expected, in this situation, the grid current is correspondingly distorted due to the proportional relation between grid voltage and grid current waveforms (*resistive load synthesis* strategy). The acquired results are reported in Fig. 3.20(b), while the steady state amplitudes and THD levels are reported in Table 3.5.

3) *Transition from islanded to grid-connected mode*: Fig. 3.21 shows the behavior during a transition to grid-connected operating mode. First, we remark the absence of any inrush current at the connection instant, due to the adopted deadband-based connection technique (see Fig. 3.17). Second, that the voltage provided by the UI is well synchronized with grid voltage, thus v maintains smooth and with desired amplitude around the transition. The grid connection process completes when the deadband period is elapsed. Finally, the amplitude of i^*_G is changed progressively with a suitable slew-rate. A zoomed-in view around the connection instant is reported in Fig. 3.22. In the considered case, deadband duration is set equal to 1s, though shortest values can be selected.

Table 3.5 allows us to compare the results obtained from the experimental tests in terms of THD. The experimental tests have shown acceptable distortion values, even under nonlinear load and distorted utility grid. Other experimental results, specially, validating the islanding detection are reported in Chapter 5.
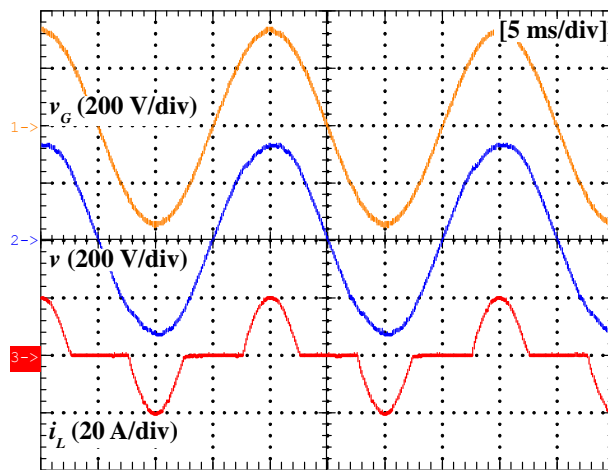
Fig. 3.18: Islanded operation with nonlinear load.
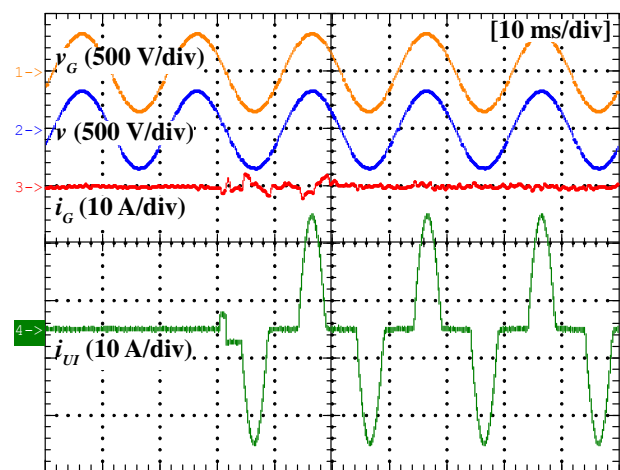
Fig. 3.19: Connection of nonlinear load in grid-connected mode.

Table 3.5: Steady state results from experimental set-up.

	Islanded, no load	Islanded, with load[1]	Grid conn., no load	Grid conn. + load[1]	Grid conn. + load[1] + 5 % 3th harm.
V_G [V] / THD_{vG} [%]	237 / 0.5	237 / 0.5	244 / 0.5	232 / 0.6	233 / 4.6
I_G [A] / THD_{iG} [%]	0 / ---	0 / ---	10.3 / 1.8	7.5 / 2.8	6.7 / 7
V [V] / THD_v [%]	237 / 0.2	236 / 2.6	258 / 0.4	223 / 0.7	224 / 4.5
I_{UI} [A] / THD_{iUI} [%]	0 / ---	10.2 / 61.9	10.3 / 1.8	4.45 / 360	3.85 / 230
i_L [A] / THD_{iL} [%]	0 / ---	10.2 / 61.9	0 / ---	10.2 / 61.9	10.2 / 61.9

(1)   Programmable electronic load absorbing 2 kW of active power with crest factor CF = 2.

(a) grid voltage with THD$_\text{vG}$ of 0.5 %.

(b) grid voltage with 5 % of 3$^\text{th}$ harmonic.
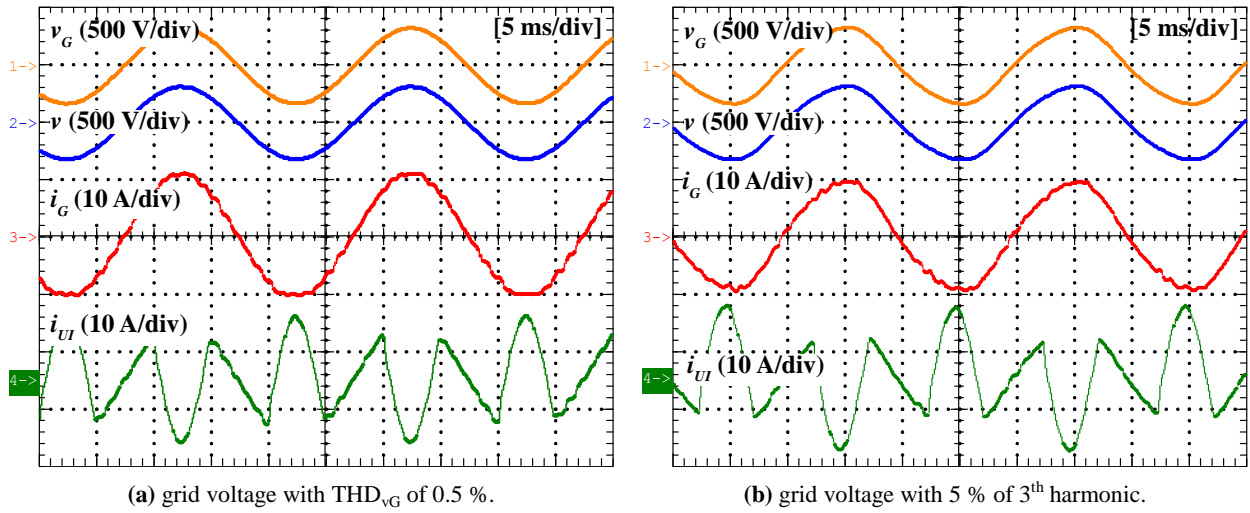
Fig. 3.20: Grid-connected operation with nonlinear load.
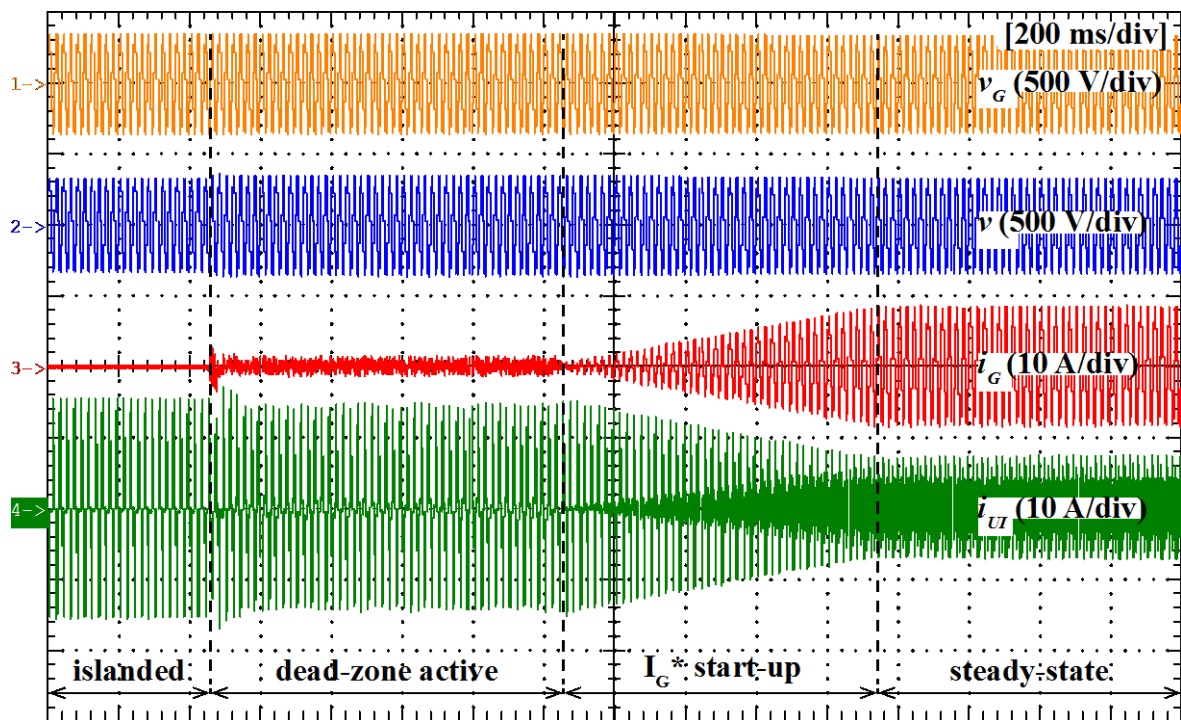
Fig. 3.21: Transition from islanded to grid-connected operating mode.
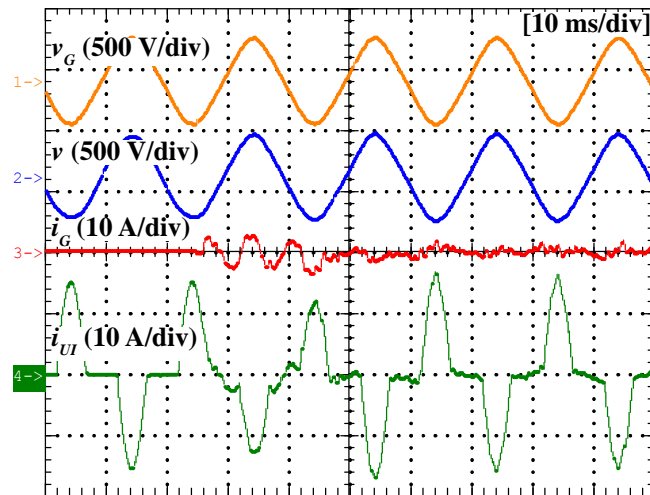
Fig. 3.22: Zoomed-in view around the connection appearing in Fig. 3.21.

3.7. Conclusions

Three different current controllers for a voltage source inverter performing as an UI are considered in this chapter. The three controllers, namely an oversampled PI, a predictive and a fully digital hysteresis controller exploit oversampling and a FPGA implementation to maximize their reference tracking performance.

The different small-signal characteristics are analyzed and experimentally evaluated. Based on this assessment, the fully digital hysteresis controller is chosen to sustain the UI's voltage control loop. This latter is implemented as a PI regulator. Altogether, the controller guarantees excellent rejection of load perturbations and smooth transitions between grid-connected and islanded operation modes. The grid current control loop is implemented as a PI plus resonant controller.

A control approach for UI power converter interfacing the utility grid and the microgrid has been presented, which provides all desired operational features both in grid-connected and islanded operation. The control is devised to provide maximum power quality during grid-connected operation, effective voltage stabilization during islanded operation, and smooth transitions between the two operating modes. For these capabilities, the proposed solution meets the requirements of most demanding grid codes. As an additional benefit, the UI can also act as MC for distributed resources acting in the microgrid. The proposed solution was tested through a laboratory-scale experimental realization to show the control features in a significant case study. All tests have shown satisfactory results.

So far, we have presented the power electronic units involved in the proposed microgrid structure, and from now on, we will describe how to coordinately control them in order to achieve a fair power sharing and to compensate all the load current disturbances, using for this purpose the surplus power capacity of EGs and the UI.

Chapter 4

4.   Power-Based Control

The increasing penetration of DERs interfacing with the distribution grid through EPPs poses new control requirements and, at the same time, enables new efficient operating regimes for LV microgrids [**8**], [**114**]. The challenge lies in the necessity of allowing prompt and effective integration of distributed and heterogeneous energy resources, which calls for flexible and scalable supporting infrastructure and plug-and-play connection standards [**4**], [**5**]. These requirements along with the need of preventing detrimental interaction of distributed control agents, make the control problem a crucial issue for the actual development of low voltage microgrids [**115**]. Important contributions to the study of the structure and management of microgrids are brought by research on droop-based networks [**4**], [**31**], [**57**], and on the optimal control techniques for these complex systems, whose typical goals are, for example, the minimization of distribution loss [**116**], [**117**], [**118**], the definition of communication architectures [**119**], and the effective management of transient conditions [**120**].

This chapter describes the algorithm responsible to coordinately control the slave units under the global optimization mode, as previously mentioned in Section 2.2. This algorithm, named power-based control corresponds to the MC program, and here it is implemented in the UI. We underline that the use of a common control packet for all the EGs limits the communication traffic in the network of agents. Moreover, the data exchange is limited only to CPT power and energy terms, which thanks to their conservativeness [**68**], can be univocally interpreted by the distributed agents, removing the need for common time bases for DERs. Due to its simple implementation and good performance, the proposed

power-based control approach represents a viable alternative to other solutions described in literature. It features excellent stability, good robustness to grid parameter variations, avoidance of saturation of the power capability of DERs, and fast dynamic response. From this standpoint, it shows competitive performance as compared to the most advanced droop-based control approaches [57], [17], [121], and it is less demanding in terms of network knowledge as compared to optimum control approaches [122], [123], [124]. Though this work does not approach and analyze the EGs endowed with ESs, the power-based control presented at this chapter takes into account the storage capability of DERs, and it is easily adapted for EG without ES.

4.1.   Data collection and processing

At the beginning of each control cycle, which equals a few periods of line voltage, the MC polls each active node of the microgrid. The EGs return the amount of their power capability that can be shared with the microgrid, taking into account the locally generated power and the stored energy. Then the MC computes the power contribution required to each active node in the next cycle based on the data collected by responding EGs and the power flow measured at PCC.

Periodically, the MC also broadcasts a call for active agents, and all the EGs which are currently active in the microgrid identify themselves and are added to the list of active agents. This allows, on the one hand, a periodic update of the microgrid agents and, on the other hand, easy and fast plug-and-play connection (or disconnection) of DERs.

4.1.1. Data collection

Precisely, the centralized control strategy performs as follows. At the end of the l-th control cycle, the MC determines the total active power $P_{PCC}(l)$ and reactive power $Q_{PCC}(l)$ absorbed by the microgrid at PCC during that cycle. This power is equal to the sum of the power drawn from the mains (i.e., P_G, Q_G) and the power delivered by the UI (i.e., P_{UI}, Q_{UI}). Moreover, the local controller of the #j-th EG ($j = 1,2,…, J$) sends the following data to the MC:

- the active power $P_j(l)$ and the reactive power $Q_j(l)$ generated during the l-th control cycle;

- the estimated active power $\hat{P}_j(l+1)$ that will be generated locally in the next control cycle;

- the estimated minimum active power $\hat{P}_j^{min}(l+1)$ and maximum active power $\hat{P}_j^{max}(l+1)$ that the node can generate in the following cycle by taking advantage of the maximum power that can be delivered ($\hat{P}_{Sj}^{out}$) or absorbed ($\hat{P}_{Sj}^{in}$) by the local ES unit, if any. We have:

$$\begin{cases} \hat{P}_j^{min}(l+1) = \hat{P}_j(l+1) - \hat{P}_{Sj}^{in}(l+1) \\ \hat{P}_j^{max}(l+1) = \hat{P}_j(l+1) + \hat{P}_{Sj}^{out}(l+1) \end{cases},$$ (4.1)

during grid-connected operation and:

$$\begin{cases} \hat{P}_j^{min}(l+1) = -\hat{P}_{Sj}^{in}(l+1) \\ \hat{P}_j^{max}(l+1) = \hat{P}_j(l+1) + \hat{P}_{Sj}^{out}(l+1) \end{cases},$$ (4.2)

during islanded operation;

- the rated apparent power $\hat{A}_j(l+1)$ of the EG inverter and its temporary overloading capability $\hat{A}_j^{over}(l+1)$.

In a basic implementation, the estimated quantities for cycle $l+1$ are simply considered equal to the values at control cycle l. In more advanced implementations, during grid-connected operation it is possible to take advantage of additional information (e.g., node voltage statistics, weather forecasts) to learn how to conveniently define, on a long-term basis, the parameters $\hat{P}_{Sj}^{out}$ and $\hat{P}_{Sj}^{in}$, for example, in order to maximize the local energy production [21].

We observe how definitions (4.1) and (4.2) given for the estimated minimum active power $\hat{P}_j^{min}$ reflect the different control priorities in grid-connected and islanded operation. Indeed, during grid-connected operation it is more advantageous to extract all the power available from renewables (e.g., by operating PV sources at their MPP), whereas during islanded operation it is of paramount importance to guarantee the active power balance for the islanded system. In this light, $\hat{P}_j^{min}$ is set equal to $\hat{P}_j$ - $\hat{P}_{Sj}^{in}$ during grid-connected mode, so that each EG would at least inject the power produced from the local PES, independently from the state of charge (SOC) of the local ES, and equal to $-\hat{P}_{Sj}^{in}$, during islanded mode, to allow the EGs to provide non-positive active power injection when generation exceeds absorption.

4.1.2. Processing

Based on the collected data, the MC determines:

- the total active and reactive power delivered by DERs along cycle l:

$$P_{tot}(l) = \sum_{j=1}^{J} P_j(l) \,, \tag{4.3}$$

$$Q_{tot}(l) = \sum_{j=1}^{J} Q_j(l) \,. \tag{4.4}$$

- the total active and reactive power absorbed within the microgrid along cycle l:

$$P_{Ltot}(l) = P_{PCC}(l) + P_{tot}(l) \,, \tag{4.5}$$

$$Q_{Ltot}(l) = Q_{PCC}(l) + Q_{tot}(l) \,. \tag{4.6}$$

- the estimated active power $\hat{P}_{Ltot}(l+1)$ and reactive power $\hat{Q}_{Ltot}(l+1)$ that will be absorbed by microgrid loads in the next control cycle $l+1$ and the reference for the total power $P_{tot}^*(l+1)$, $Q_{tot}^*(l+1)$ to be delivered by EGs:

$$
\begin{aligned}
\hat{P}_{Ltot}(l+1) &= P_{Ltot}(l) \,, \\
P_{tot}^*(l+1) &= \hat{P}_{Ltot}(l+1) - P_{PCC}^*(l+1) \,,
\end{aligned}
\tag{4.7}
$$

$$
\begin{aligned}
\hat{Q}_{Ltot}(l+1) &= Q_{Ltot}(l) \,, \\
Q_{tot}^*(l+1) &= \hat{Q}_{Ltot}(l+1) - Q_{PCC}^*(l+1) \,,
\end{aligned}
\tag{4.8}
$$

where $P_{PCC}^*(l+1)$ and $Q_{PCC}^*(l+1)$ represent the assigned reference power flow at the PCC for the next control cycle;

- the estimated total active power generated by DERs in cycle $l+1$ and the corresponding upper and lower limits:

$$\hat{P}_{tot}(l+1) = \sum_{j=1}^{J} \hat{P}_j(l+1) \ , \tag{4.9}$$

$$\hat{P}_{tot}^{min}(l+1) = \sum_{j=1}^{J} \hat{P}_j^{min}(l+1) \ , \tag{4.10}$$

$$\hat{P}_{tot}^{max}(l+1) = \sum_{j=1}^{J} \hat{P}_j^{max}(l+1) \ ; \tag{4.11}$$

- the estimated maximum reactive power that the active nodes can deliver in normal operation or in overloading condition in cycle $l+1$:

$$\hat{Q}_j^{max}(l+1) = \sqrt{\hat{A}_j^2(l+1) - \hat{P}_j^2(l+1)} \ ,$$
$$\hat{Q}_{tot}^{max}(l+1) = \sum_{j=1}^{J} \hat{Q}_j^{max}(l+1) \qquad , \tag{4.12}$$

$$\hat{Q}_j^{over}(l+1) = \sqrt{\hat{A}_j^{over\,2}(l+1) - \hat{P}_j^2(l+1)} \ ,$$
$$\hat{Q}_{tot}^{over}(l+1) = \sum_{j=1}^{J} \hat{Q}_j^{over}(l+1) \qquad ; \tag{4.13}$$

Based on the global status of controllable EGs obtained above, the MC regulates the power flow at the PCC to track the references P_{PCC}^*, Q_{PCC}^*, given a fixed power flow from the mains P_G^*, Q_G^*. Accordingly, the power exchange at the terminals of UI are:

$$\hat{P}_{UI}(l+1) = P_{PCC}^*(l+1) + P_G^*(l+1) \ , \tag{4.14}$$

$$\hat{Q}_{UI}(l+1) = Q_{PCC}^*(l+1) + Q_G^*(l+1) \ . \tag{4.15}$$

While references P_G^*, Q_G^*, that are actuated by the UI [97], [36], are either set according to the negotiation on energy exchange with the DSO (taking place in the tertiary control layer [31], Section 1.2.3) or set to zero during the islanded operating mode. References P_{PCC}^*, Q_{PCC}^* are set by the MC according to the energy state of the UI, as in [125].

4.2. Power-based algorithm

The estimated quantities (4.7)-(4.13) are the input data for the control algorithm that drives the distributed EGs. In order to actuate it, the MC generates two control variables α_P and α_Q (both ranging in the interval [0, 2]), which are then broadcasted to all the EGs, i.e., applied to the whole microgrid. We first describe the control algorithm for *islanded operation*, which is then easily adapted to *grid-connected mode*.

4.2.1. Active power control

The active power is controlled by variable α_P, which is set by the MC depending on the operation mode. We distinguish four operating modes:

1) $P^*_{tot}(l+1) < \hat{P}^{min}_{tot}(l+1)$: in this case, the loads are expected to absorb a total active power lower than the minimum power that the active nodes can deliver. As a result, the MC sets:

$$\alpha_P = 0 \ , \tag{4.16}$$

and each EG sets its active power reference $P^*_j(l+1)$ at the minimum allowed value:

$$P^*_j(l+1) = \hat{P}^{min}_j(l+1) \ . \tag{4.17}$$

The power balance can temporarily be ensured by diverting the power in excess to the UI, that stores it in its ES device, as described in [126]. Of course, this situation can be sustained for a limited time, then, loads and/or generators must be readjusted (e.g., MPPT must be detuned so as to extract less power [93]) to restore the equilibrium.

2) $\hat{P}^{min}_{tot}(l+1) \le P^*_{tot}(l+1) < \hat{P}_{tot}(l+1)$: the expected load power is lower than the generated power but the excess of generation can be temporarily diverted into distributed storage units. In this case, the UI does not contribute to power balance, and the MC sets the value of α_P as:

$$\alpha_P = \frac{P^*_{tot}(l+1) - \hat{P}^{min}_{tot}(l+1)}{\hat{P}_{tot}(l+1) - \hat{P}^{min}_{tot}(l+1)} \ , \qquad 0 \le \alpha_P \le 1 \ . \tag{4.18}$$

Correspondingly, each active node sets its active power reference as:

$$P^*_j(l+1) = \hat{P}^{min}_j(l+1) + \alpha_P \cdot \left[\hat{P}_j(l+1) - \hat{P}^{min}_j(l+1)\right] \ . \tag{4.19}$$

3) $\hat{P}_{tot}(l+1) \le P^*_{tot}(l+1) \le \hat{P}^{max}_{tot}(l+1)$: the expected load power is higher than generated power but the difference can be supported, temporarily, by distributed ES. In this case, the UI does not contribute to power balance, and the MC sets the value of α_P as:

$$\alpha_P = 1 + \frac{P^*_{tot}(l+1) - \hat{P}_{tot}(l+1)}{\hat{P}^{max}_{tot}(l+1) - \hat{P}_{tot}(l+1)} \ , \qquad 1 \le \alpha_P \le 2 \ . \tag{4.20}$$

Correspondingly, each active node sets its active power reference as:

$$P^*_j(l+1) = \hat{P}_j(l+1) + (\alpha_P - 1) \cdot \left[\hat{P}^{max}_j(l+1) - \hat{P}_j(l+1)\right] \ . \tag{4.21}$$

4) $P^*_{tot}(l+1) > \hat{P}^{max}_{tot}(l+1)$: the loads are expected to absorb a total power which is greater than the maximum power the active nodes can deliver. In this case the MC sets:

$$\alpha_P = 2 \ . \tag{4.22}$$

Correspondingly, each active node sets its active power reference as:

$$P^*_j(l+1) = \hat{P}^{max}_j(l+1) \ . \tag{4.23}$$

The power balance can temporarily be ensured at the expense of the energy stored in the UI. After some time, of course, some of the loads and/or generators will have to be readjusted to restore the equilibrium.

4.2.2. Reactive power control

The reactive power is controlled by variable α_Q, which is set by the MC depending on the operation mode. There are two operation modes:

1) $Q_{tot}^*(l+1) \leq \hat{Q}_{tot}^{max}(l+1)$: load requirements can be met by distributed EGs. In this case the MC sets:

$$\alpha_Q = \frac{Q_{tot}^*(l+1)}{\hat{Q}_{tot}^{max}(l+1)} \ , \qquad 0 \leq \alpha_Q \leq 1 \ . \tag{4.24}$$

Correspondingly, each active node sets its reactive power reference as:

$$Q_j^*(l+1) = \alpha_Q \cdot \hat{Q}_j^{max}(l+1) \ . \tag{4.25}$$

2) $Q_{tot}^*(l+1) > \hat{Q}_{tot}^{max}(l+1)$: loads requirement can only be met by overloading the EGs. In this case the MC sets:

$$\alpha_Q = 1 + \frac{Q_{tot}^*(l+1) - \hat{Q}_{tot}^{max}(l+1)}{\hat{Q}_{tot}^{over}(l+1) - \hat{Q}_{tot}^{max}(l+1)} \ , \qquad 1 \leq \alpha_Q \leq 2 \ . \tag{4.26}$$

Correspondingly, each active node sets its reactive power reference as:

$$Q_j^*(l+1) = \hat{Q}_j^{max}(l+1) + \left(\alpha_Q - 1\right) \cdot \left[\hat{Q}_j^{over}(l+1) - \hat{Q}_j^{max}(l+1)\right] \ . \tag{4.27}$$

A simplified block diagram representing the main operations of the power-based control for what concerns active power balance is shown in Fig. 4.1; a corresponding scheme can be derived for reactive power control, shown in Fig. 4.2. Gain errors and off-set errors are included to take into account the main non-idealities of a realistic application case. In general, gain errors affect the loop gain of the feedback system and have to be considered to assess system stability, whereas off-set errors have to be taken into account to analyze its steady state accuracy in regulating the controlled quantities. In Fig. 4.1(a), variables γ_j^g and P_j^{err} represent the gain and off-set errors made by EGs in producing the assigned power reference P_j^*; γ_j^m and γ_{PCC}^m represent the gain errors of measurement instruments, while off-set errors in measurements are, for now, neglected. On the base of Fig. 4.1(a), the simplified model of Fig. 4.1(b) can be drawn, that is used for the analysis of the power-based control stability.

By employing the block diagram of Fig. 4.1(b) we can derive the discrete time transfer function between the total absorbed power P_{Ltot} and the reference P_{tot}^*. By neglecting the reference input P_{PCC}^*, since it varies very slowly, as mentioned in Section 4.1.2, it is possible to find:

$$P_{tot}^*(z) = \frac{\gamma_{PCC}^m}{z + \gamma^g \cdot (\gamma^m - \gamma_{PCC}^m)} \cdot P_{Ltot}(z) \ . \tag{4.28}$$

(a) Generation of power commands.   (b) Calculation of power references.
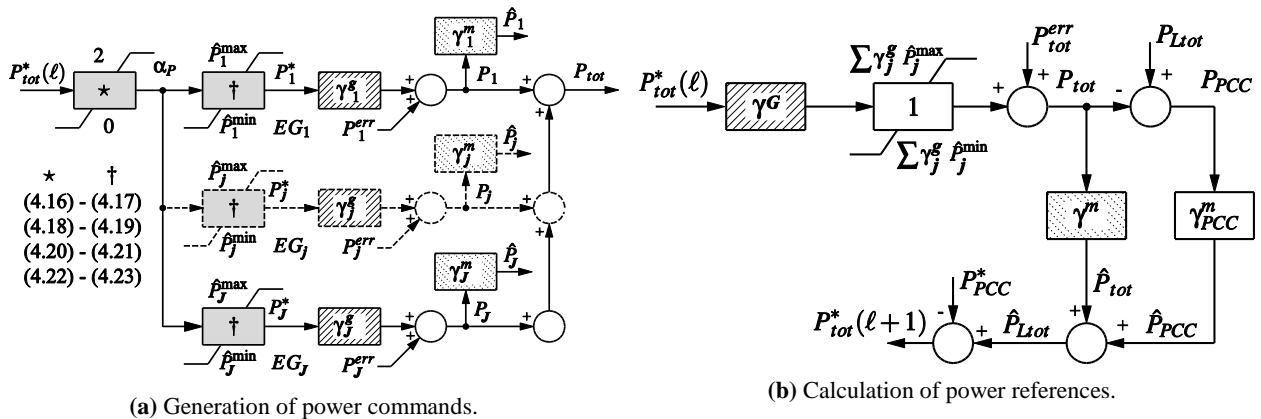
Fig. 4.1: Simplified model of the power-based control (active power balance), © IEEE 2015 [35].

Equation (4.28) shows that, if the system is ideal (i.e., γ_j^g, γ_j^m, γ_{PCC}^m are equal to one and P_j^{err} is equal to zero) then the power reference of EGs are committed to going to track the total absorbed power in the microgrid (with one control cycle delay); secondly, that the stability condition for active power reference generation, in general, can be expressed as: $|\gamma^g \cdot (\gamma^m - \gamma_{PCC}^m)| < 1$, that can easily be met by any commercial power meter. This proves a stable control operation for the operating modes 2) and 3) referred to in Section 4.2.1.

The diagrams in Fig. 4.1 also highlight that, if the power requested by the load exceeds the total power capability of EGs, the coefficient α_P seamlessly saturates to its upper limit, so that, each EG continuously delivers the maximum power that is locally available (P_j^{max}). When the opposite situation occurs, i.e., the minimum injectable power from EGs is higher than the load power, the coefficient α_P is automatically saturated at its lower limit and each EG continuously delivers the minimum power (P_j^{min}). Because the control system operates on a cycle by cycle basis, with no memory of the grid state during previous cycles, a stable control operation is guaranteed, as well, for the operating modes 1) and 4) referred to in Section 4.2.1.

For what concerns the regulation accuracy of the power flow at the PCC, we first observe that:

$$P_{PCC}(l) = P_{Ltot}(l) - \gamma^g \cdot \hat{P}_{tot}^*(l) - P_{tot}^{err}(l) \;, \tag{4.29}$$

where P_{PCC} is shared among the UI (P_{UI}) and the mains (P_G) [equations (4.14)-(4.15)] according to the negotiation on energy exchange with the DSO. From (4.29), the power flow at the PCC is equal to the power reference P_{PCC} minus the error introduced by EGs. This error can be canceled by the MC, e.g., employing a local integrative regulator to properly modulate the power term P_{PCC} [125]. Similarly, the fluctuations in local power production can be modeled as exogenous inputs, that only affect the limits $\hat{P}_j^{min}$ and $\hat{P}_j^{max}$ and do not impair the stability of the system. The limits are acquired and processed by the MC at each control cycle, allowing to accordingly update the control commands to EGs, so as to account for the actual generation profile. Finally, although temporary mismatches (i.e., lasting few line cycles) among the effectively generated power and its estimate can have an effect on the injected power, this can be limited by a proper design of EG hardware. In any case, DC-link voltage deviations caused by

(a) Generation of power commands.

(b) Calculation of power references.
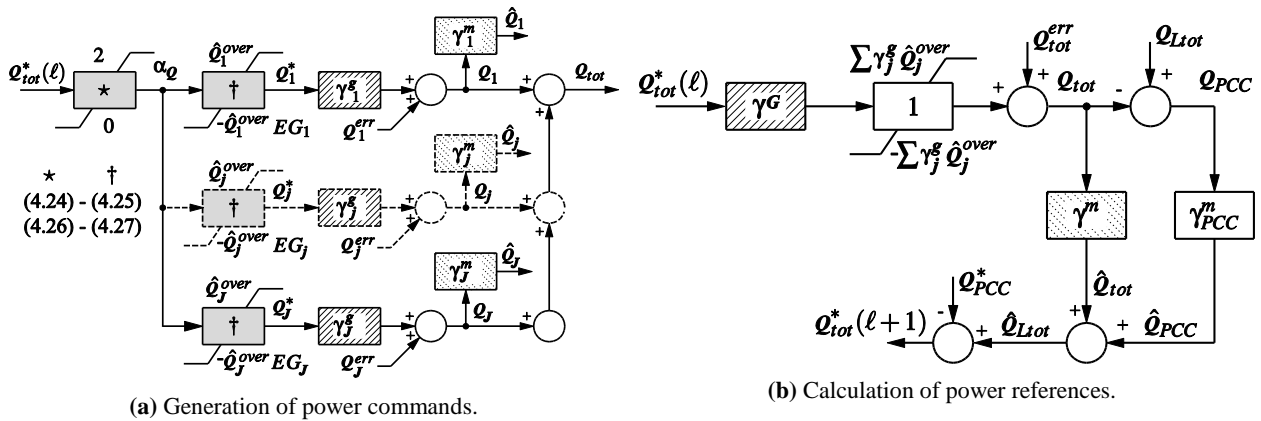
Fig. 4.2: Simplified model of the power-based control (reactive power balance).

abrupt changes in operating conditions, which may affect primarily voltage controlled inverters [57], are attenuated in the considered EG structure thanks to the adopted current controlled approach [127]. The same aforementioned considerations can be addressed for reactive power balance, differing only for the saturation limits, that is for reactive the positive and negative value of the temporary overloading capability, since the reactive power can be either inductive or capacitive.

4.2.3. Grid-connected mode: active and reactive power control

While operating connected to the mains, the above control strategy can be adapted to obtain a conventional grid-connected operation, where DERs simply inject the locally generated power in compliance with grid standards. In fact, in this case, the MC can simply set $\alpha_P = 1$, causing the total power generated by DERs to be injected into the grid. Local power needs (e.g., to restore the SOC of ES at the nominal value) can be considered by correcting the estimates of generated power $\hat{P}_j(l+1)$. In any case, the power balance is ensured by the utility grid.

As far as reactive power compensation is concerned, the UI first decides its contribution Q^*_{UI} for the next control cycle. Then, it adjusts the total reactive power requested to the EGs according to:

$$Q^*_{tot}(l + 1) = \hat{Q}_{Ltot}(l) - Q^*_{UI}(l + 1) \ , \tag{4.30}$$

Both for active and reactive power, the UI can also distribute the references differently in the three phases to compensate load unbalance. It is shown in Chapter 6.

Considering only EGs without ESs, but with adjustable operating point, (i.e., *reduced power mode* [93]), then, (4.1) and (4.2) can be rewritten, accordingly, $\hat{P}_j^{min} = 0$ and $\hat{P}_j^{max} = \hat{P}_j$, for both operating modes:

$$\begin{cases} \hat{P}_j^{min}(l + 1) = 0 \\ \hat{P}_j^{max}(l + 1) = \hat{P}_j(l + 1) \end{cases} , \tag{4.31}$$

thus, Table 4.1 shows α_P and α_Q considering EGs without ESs for different power conditions.

Table 4.1: Power-based control scaling coefficients for EGs without ESs.

Power condition	Scaling coefficients
$P^*_{tot}(l + 1) < \hat{P}_{tot}^{min}(l + 1)$	$\alpha_P = 0$
$P^*_{tot}(l + 1) < \hat{P}_{tot}(l + 1)$	$\alpha_P = \dfrac{P^*_{tot}(l + 1)}{\hat{P}_{tot}(l + 1)}$
$P^*_{tot}(l + 1) \geq \hat{P}_{tot}(l + 1)$	$\alpha_P = 1$
$Q^*_{tot}(l + 1) \leq \hat{Q}_{tot}^{max}(l + 1)$	$\alpha_Q = \dfrac{Q^*_{tot}(l + 1)}{\hat{Q}_{tot}^{max}(l + 1)}$
$Q^*_{tot}(l + 1) > \hat{Q}_{tot}^{max}(l + 1)$	$\alpha_Q = 1 + \dfrac{Q^*_{tot}(l + 1) - \hat{Q}_{tot}^{max}(l + 1)}{\hat{Q}_{tot}^{over}(l + 1) - \hat{Q}_{tot}^{max}(l + 1)}$

4.3. Application example

The proposed power-based control algorithm has been tested for different network topologies and operating conditions, both static and dynamic, in grid-connected and islanded mode. To clearly illustrate the control features, it is considered here a simple microgrid circuit shown in Fig. 4.3. It includes two EGs, one load, and the UI with the MC.

The considered power system has low voltage and the parameters of the adopted power electronic interfaces, PV sources are those of commercial devices suited for residential applications. Distribution grid parameters are reported in Table 4.2, while the parameters of EG_1 and EG_2 are shown in Table 4.3, respectively. A narrowband communication link provides the required information exchange among the UI and the couple of EGs.
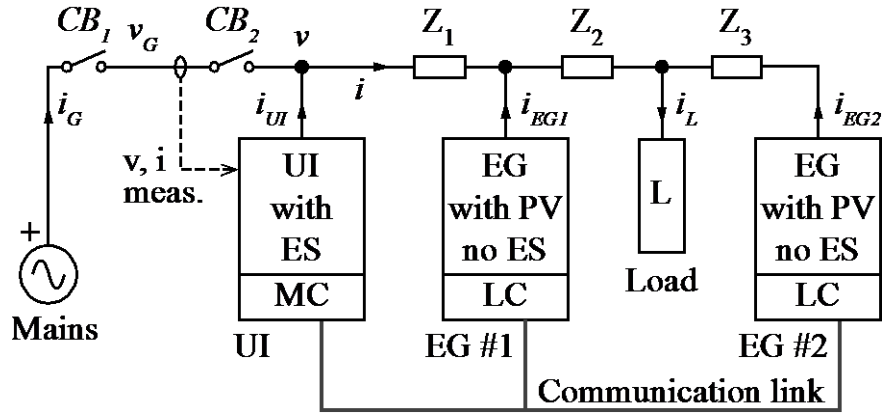
Fig. 4.3: Considered low voltage power system, © IEEE 2015 [35].

Table 4.2: Distribution grid parameters, © IEEE 2015 [35].

Parameter	Symbol	Value
Grid voltage	V_G	230 V
Grid frequency	f_G	50 Hz
Max. voltage deviation	$\Delta v_\%^{max}$	4.0 %
Z_1 impedance	Z_1	$0.17 + j0.04\ \Omega$
Z_2 impedance	Z_2	$0.26 + j0.06\ \Omega$
Z_3 impedance	Z_3	$0.70 + j0.16\ \Omega$
Load power factor	PF	0.95

Table 4.3: Energy gateway parameters, © IEEE 2015 [35].

Parameter	(EG#1)		(EG#2)	
	Symbol	Value	Symbol	Value
EG power rating	A_{EG1}	4.2 kVA	A_{EG2}	5.0 kVA
EG overload power rating	A_{EG1}^{over}	4.6 kVA	A_{EG2}^{over}	5.4 kVA
EG nominal efficiency	η_{EG1}	0.95	η_{EG2}	0.95
PV nominal power rating	P_{PV1}	4.0 kW	P_{PV2}	4.0 kW

4.3.1. Simulation results

The results obtained from the simulation of the low voltage power system of Fig. 4.3 in response to typical absorption and generation profiles are discussed in the following. In order to highlight the effect of the proposed control approach on the microgrid performance, two specific cases of operation are considered:

- *Case A – no power-based control*: in this case the EGs operate independently, injecting into the grid the total active power extracted from the local PV source. No communication and reactive power compensation is implemented.

- *Case B – power-based control*: in this case EGs operate under the supervision of the MC. The EGs inject into the grid the active power extracted from the local PV source and the reactive power that corresponds to the received coefficient α_Q. The local active power generation is automatically curtailed in case of overvoltage detection, by the overvoltage dynamic control presented in Section 2.5.

1)   *Active power profiles*: Fig. 4.4 show the behavior of the measured active power flows for the considered cases in response to given generation and absorption profiles.

In *case A*, Fig. 4.4(a), EG_1 and EG_2 exchange with the grid only the active power produced by the PV sources, without taking into account any reactive compensation and overvoltage constraint at grid nodes. Then, the power drawn from the PCC is equal to the total power absorbed by the load minus the total power generated by the PV sources. Consequently, the power flow at the PCC shows the same variability of generation and absorption profiles.

In *case B*, Fig. 4.4(b), the power-based control and the overvoltage control are active. For what concerns the active power injection, when voltage magnitudes of active nodes are within nominal values, the active power flow behaviors in *case A* and *case B* are identical. A different situation is established for reactive power. Indeed, the power-based control instructs the EGs to completely compensate the net reactive power produced within the microgrid, thus causing a constant zero reactive power exchange at the PCC. Further details are given with the discussion of Table 4.4.

(a) without power-based control.   (b) with power-based control.
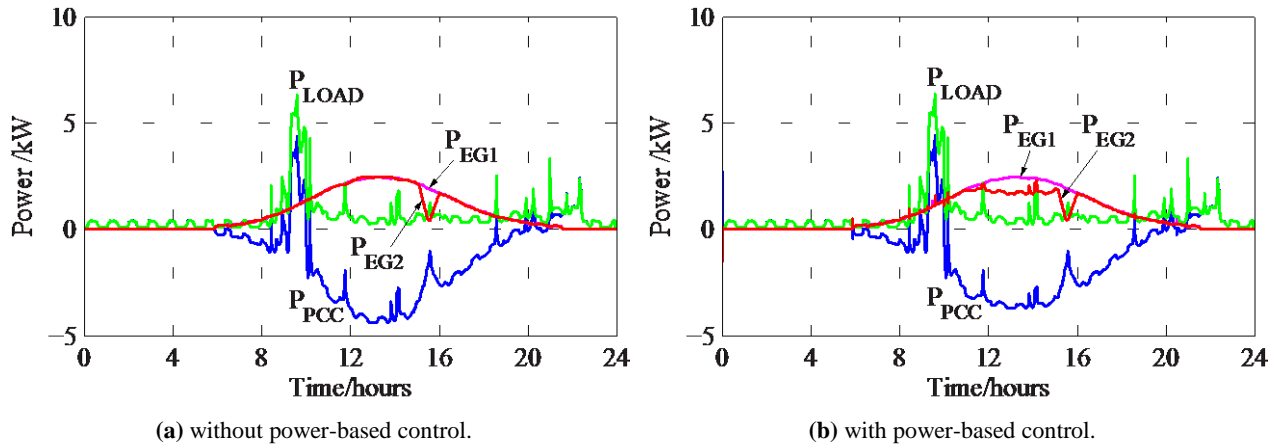
Fig. 4.4: Active power profiles, © IEEE 2015 [35].

Finally, considering *case B* we observe the effect of the overvoltage limitation by dynamic active power control, that causes the reduction in EG_2 power generation, needed to fulfill the imposed grid voltage magnitude constraint (see Table 4.2, parameter $\Delta v_\%^{max}$).

2)   *Power flow at PCC*: Fig. 4.5 shows the behavior of the active power flow through the PCC for the considered cases. The slightly mismatch between the two cases is causes by the overvoltage dynamic control that limits the active power injection detuning the MPP.
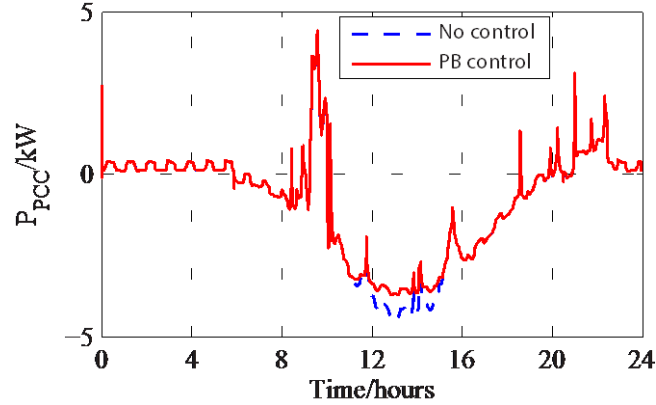
Fig. 4.5: Active power at PCC, © IEEE 2015 [35].

3)   *Distribution loss*: Fig. 4.6 shows the obtained distribution power loss for the considered cases. The proposed power-based control formulation inherently compensates unwanted reactive power flows within the grid in a distributed fashion. This is beneficial in terms of distribution loss [85], [128].

4)   *Voltage deviations at grid nodes*: Low voltage distribution lines are mainly resistive [4], therefore, the active power flow significantly affects voltage amplitudes at grid nodes. Indeed, during periods of peak production from renewables, undesirable voltage deviations from nominal values can be registered due to abnormal active power injection. In the considered simulation set-up, overvoltage conditions are automatically detected and managed locally by the active nodes by regulating dynamically the active power injected into the grid, as described in Section 2.5.

Fig. 4.7 shows the voltage deviation at the point of connection of EG_2. This node is more affected by these phenomena since it is the farthest from the PCC. In particular, the figure shows how the overvoltage control feature integrated into the control scheme allows an accurate and precise limitation of voltage magnitude at critical nodes. In the considered case, the generation is curtailed by acting on the power point tracker, as, for example, in [93]. The power output from EGs are steadily equal to the maximum power that can be generated locally while complying with the overvoltage constraint $\Delta v_\%^{max}$, and it is regulated by the overvoltage control loop shown in Fig. 2.8. Indeed, to meet the $\Delta v_\%^{max}$ constraint can necessarily lead to a reduced power production from renewables in grids where the distribution lines have high R/X ratios. Fig. 4.8 reports the profile of the total maximum power that can be ideally extracted from PV sources and the actual total power production obtained in *case B*. Since the power injection is limited during an overvoltage condition, the power in excess is totally curtailed.

The behavior of coefficients α_P and α_Q along the considered simulation scenario is reported in Fig. 4.9, just for *case B*. The coefficient α_P assumes only the values corresponding to Table 4.1, due to the absence of storage devices.

5)   *Performance indexes*: In order to emphasize the main results illustrated so far, Table 4.4 reports some performance indexes applied to the considered application example. In particular, the total produced energy, the energy dissipated in distribution lines, the overvoltage measured at grid nodes, and the power factor measured at the PCC are reported. We notice the following aspects:

- The measured distribution loss in *case B* is reduced by 20 % with respect to *case A*. The maximum registered overvoltage stays within the programmed 4 % limit when the corresponding control functionality is active, i.e., in *case B*. On the other hand, if no provisions are taken, *case A* reveals a maximum reached overvoltage of 5.5 %.

- In the considered application example, the power-based control accomplishes the full compensation of the reactive power produced by the loads, achieving a unity power factor measured at the PCC. Fig. 4.10 shows the obtained share of reactive power between EG_1, EG_2, and the PCC, together with the reactive power absorbed by the load.

- Thanks to the effective management of the generated energy performed by the proposed control scheme, a reduction of only 6 % in the total produced energy can be noticed in spite of the stringent overvoltage limitation of 4 % with respect to the nominal value V_G.
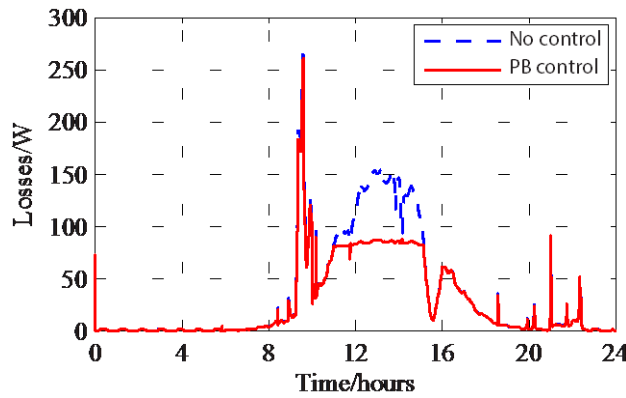
Fig. 4.6: Distribution loss over the grid, © IEEE 2015 [35].
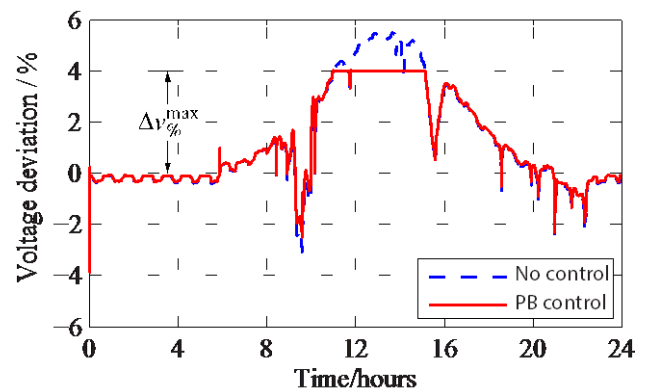
Fig. 4.7: Voltage deviation at EG_2 node, © IEEE 2015 [35].
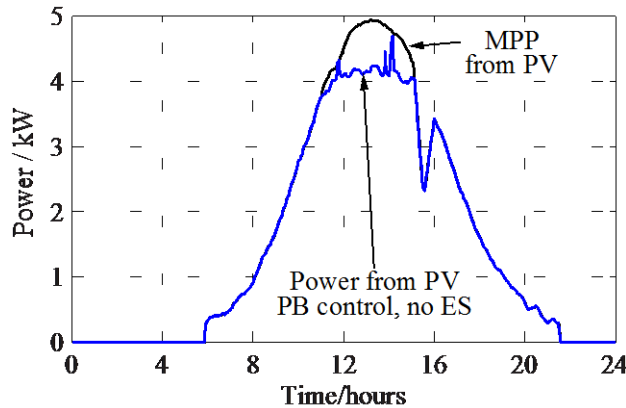
Fig. 4.8: Total power production from PV sources, © IEEE 2015 [35].
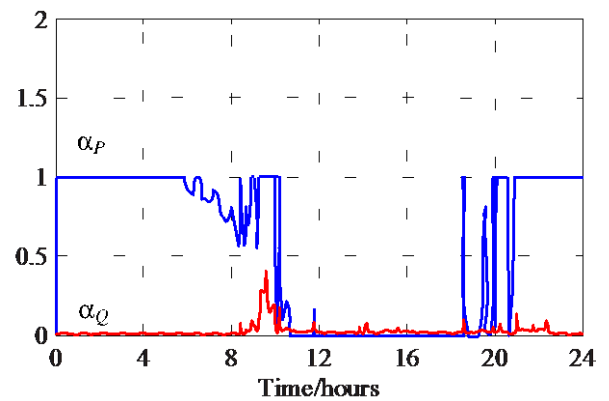
Fig. 4.9: Behavior of coefficients α_P and α_Q (*case B*).
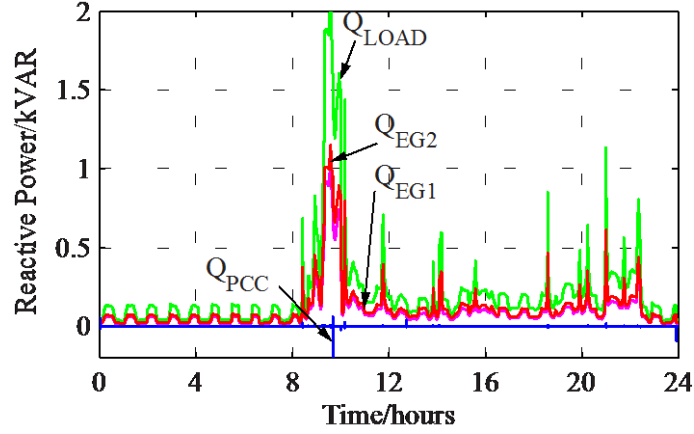
Fig. 4.10: Reactive power contribution from EG_1, EG_2, and the PCC, together with the absorbed load power, © IEEE 2015 [35].

Table 4.4: Performance indexes computed at microgrid PCC, © IEEE 2015 [35].

	Produced energy (kWh)	Distribution loss (kWh)	v_{EG1} max. overvoltage (%)	V_L max. overvoltage (%)	v_{EG2} max. overvoltage (%)	PCC power factor
Case A – No control	36.5	0.83	1.4	2.4	5.5	0.93
Case B – power-based control	34.1	0.65	1.2	1.8	4.0	1.00

We highlight that EGs endowed with ES capability can turn the distribution system even more efficient, so as the active power exchanged at the PCC becomes smoother than in *case A* and *case B*, thanks to the inherent peak shaving capability of the microgrid. The power that cannot be injected into the grid due to overvoltage limitations could be stored in the local accumulators and, in Fig. 4.8, the power could be partially curtailed, since a portion of power could be storage. Further analyses, including EGs equipped with ESs can be found in [**35**].

4.3.2. Experimental results

A laboratory-scale microgrid prototype has been developed to replicate the case study shown in Fig. 4.3. In the considered implementation, the MC resides in the UI and broadcasts once every 0.02 s the power commands to EGs, as described in Section 4.2. The two EGs with no ES have the same power rating of 3 kVA, and a local power availability such that $(\hat{P}_1^{min}, \hat{P}_1, \hat{P}_1^{max}) = (0, 0.8, 0.8)$ kW and $(\hat{P}_2^{min}, \hat{P}_2, \hat{P}_2^{max}) = (0, 3.0, 3.0)$ kW. This microgrid set-up is described and used in Chapter 5.

Fig. 4.11 shows the system response to a load step from 2 kW to 4 kW during the grid-connected operation. Initially, the grid power reference P^*_G is equal to zero (due to, for example, host utility restriction related to DSO) and the power absorbed by the load is 2 kW. In this situation the two EGs can completely supply the load needs and the coefficient α_P is equal to 0.526. Immediately after the step transition the UI promptly supply the load needs, while the power-based control gradually adjusts the power contribution from the EGs. Since the load absorption after the transient, equal to 4 kW, exceeds the total power availability of EGs, equal to 3.8 kW, the coefficient α_P in steady state is equal to 1. This

corresponds to the operating mode 4) of Section 4.2.1, where the EGs deliver the maximum locally available power, while the UI delivers the power needed to ensure the power balance.

For a comparison with other approaches, we remark that the dynamic response of the power-based control in the experimental set-up is determined by the control cycle duration, the response speed of the local current controller, and the communication bandwidth. The dynamics shown in Fig. 4.11 are dominated by the implemented current controller of EG_2, that presents a constraint on the maximum rate of change of the injected current, to limit the stress to its hardware. We observe that, by removing this constraint, the response speed would be limited by only the power measurement calculations and the communication bandwidth. Neglecting the effect of the communication bandwidth, in the considered scenario the power measurement calculation bandwidth represents the upper bound for both the response speed of the power sharing among EGs and the achievable bandwidth of the power flow regulation at the PCC. The same upper bound is present in conventional droop-control schemes, for what concerns the primary control (defining the power sharing among DERs), while the tertiary control layer (concerning the regulation of the power flow at the PCC), intrinsically, has even slower time response [17], [129].
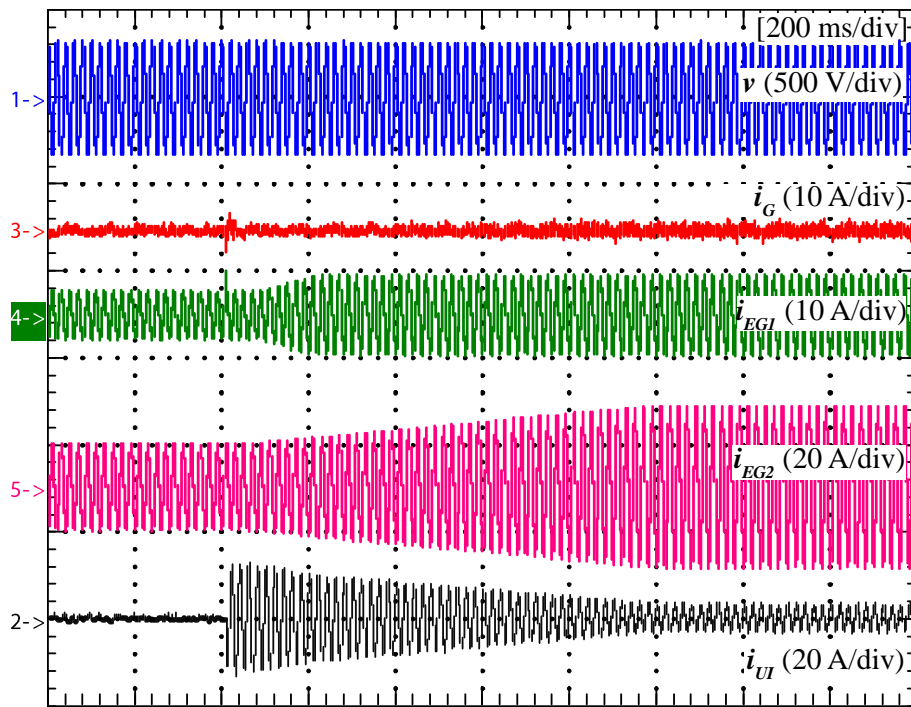
Fig. 4.11: Load step (2 kW to 4 kW) during grid-connected operation, © IEEE 2015 [35].

4.4. Conclusions

A simple approach to the synergistic control of distributed energy resources in low voltage microgrids was presented and analyzed. It only requires non-time-critical power data to be transferred from the active nodes to a MC through a narrowband communication link, so that the centralized controller is able to broadcast active and reactive power set-points for all the active nodes. No further studies about communication were performed in this work, and for the simulations, an ideal

communication link was used. For the experimental results, a fast TCP/IP Ethernet network was used, while the data packet and power command coefficients were exchanged once per fundamental cycle of voltage grid, as shown in Fig. 4.12.

Thanks to an UI converter located at the PCC, the proposed control is capable of driving the microgrid in both grid-connected and islanded operation, even during fast transients, while guaranteeing a proper power sharing between distributed resources, a regulated power flow at the PCC, and preventing the overload of DER converters.

The strategy was tested by simulations and a basic application example has been presented and discussed. The results have shown that the centralized power-based control strategy smooths the active power exchanged at PCC, significantly reduces the power loss, and avoids overvoltage conditions.

Finally, the experimental verification of the short-term energy flow control capability has been presented, which demonstrates the good control performance of the microgrid, as expected from the theoretical formulation. In grid-connected mode, the control pursues quasi-optimum operation of the microgrid, so as to reduce distribution loss and voltage deviation, while fully exploiting renewable energy sources. Further experimental results are shown in Chapter 5, focusing on more complex operating conditions, such as operation during communication failure, islanding detection with zero current exchange at the PCC, among others.
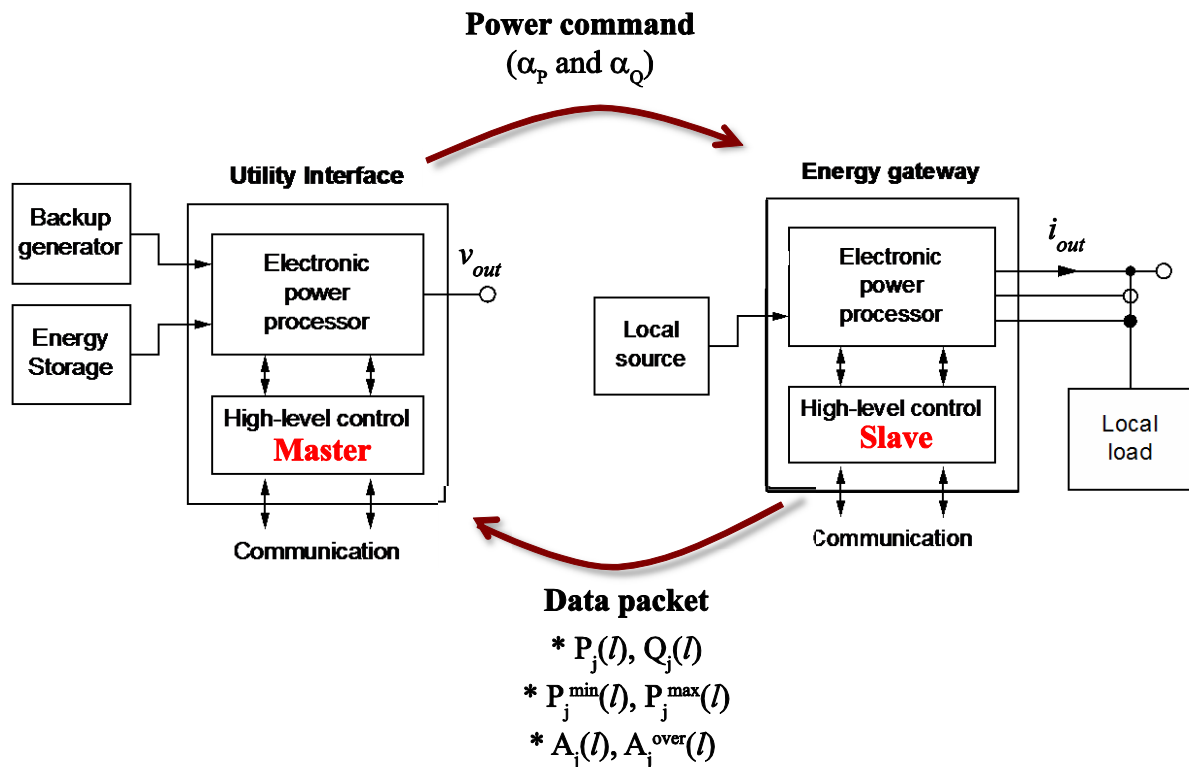
Fig. 4.12: Data packet and power command exchanged among master and slave units once per fundamental cycle of grid voltage.

Chapter 5

5. Fully-Dispatchable Single-Phase Low Voltage Microgrid: An Experimental Validation

This chapter describes a fully-dispatchable single-phase microgrid structure, based on the previous master-slave control architecture (Chapter 1), where the distributed generation units (i.e., EGs – Chapter 2) are coordinated by means of the explained power-based control algorithm (Chapter 4). Through the modeled and designed UI (Chapter 3), the microgrid manages promptly the interaction with the mains. Hence, the focus of this chapter is to validate the functionalities of the proposed microgrid structure and control strategy, by means of a laboratory-scale microgrid implemented at University of Padova, in Italy. A variety of results are presented in order to validate: the microgrid structure; the basic, specific and ancillary functions of EGs, such as active power control, overvoltage control, distributed reactive compensation, among others; the islanding detection of UI; the microgrid performance under grid voltage variation and communication failure.

5.1. Single-phase microgrid set-up

The electrical circuit of the laboratory-scale microgrid implemented at University of Padova, Italy, and considered in this analysis is shown in Fig. 5.1, while the energy gateways and system

parameters are shown in Table 2.5 and Table 2.6. Fig. 5.2 shows the picture of the implemented microgrid. The mains is emulated by an 80 kVA bidirectional three-phase AC/AC power supply. CB_1 is a circuit breaker driven by the mains, while CB_2 and CB_{UI} are electromechanical circuit breakers driven by UI, the former being needed to manage the islanded operation, the latter to isolate the UI systems in case of failures, as explained in Section 1.2.1. The microgrid is connected to the mains through an isolation transformer. A programmable load and a commercial PV source represent, respectively, passive and active nodes without communication capability. The distribution grid topology and interconnection of electrical sources and loads are provided by a custom switchboard, which, giving access to various sections of low voltage distribution conductors, allows flexible configuration of the microgrid topology. The UI and the two EGs are developed by employing commercial 3 kVA inverters properly modified. National Instruments RIO platforms are employed for control, monitoring, and emulation purposes. The UI is controlled by a cRIO system, while each EG is controlled by a GPIC system [130]. A TCP/IP Ethernet network provides the information exchange among the MC and the EGs. The MC resides in the UI and periodically (once every 0.02 s) dispatches the power commands computed on the basis of the microgrid state.
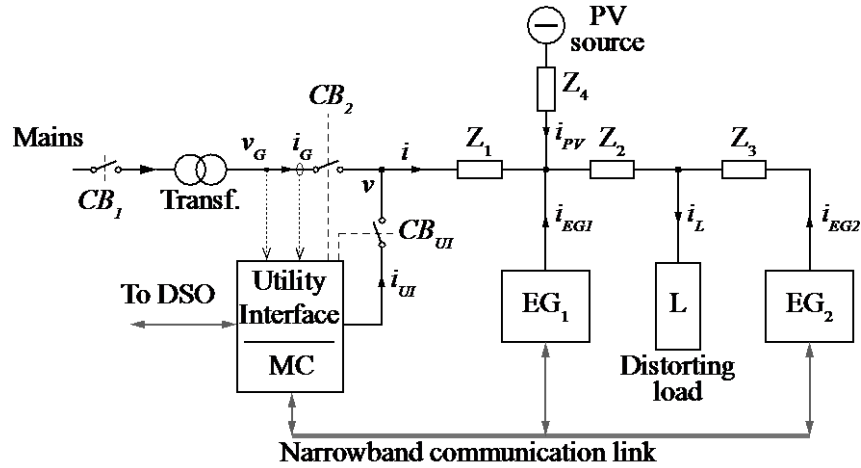
Fig. 5.1: Electrical circuit of the single-phase microgrid, © IEEE 2015 [43].

5.2. Experimental results

In order to validate the functionalities of the proposed system, the steady state and dynamic behaviors of the laboratory prototype have been exhaustively tested in both grid-connected and islanded operating modes. In this section, the following aspects of microgrid operation are considered:

- overvoltage condition;
- compensation of harmonic and reactive current terms drawn at PCC under distorted load conditions;
- power sharing among EG units in dynamic conditions;
- management of intentional and non-intentional islanding transitions;
- communication link failure between MC and one slave unit;
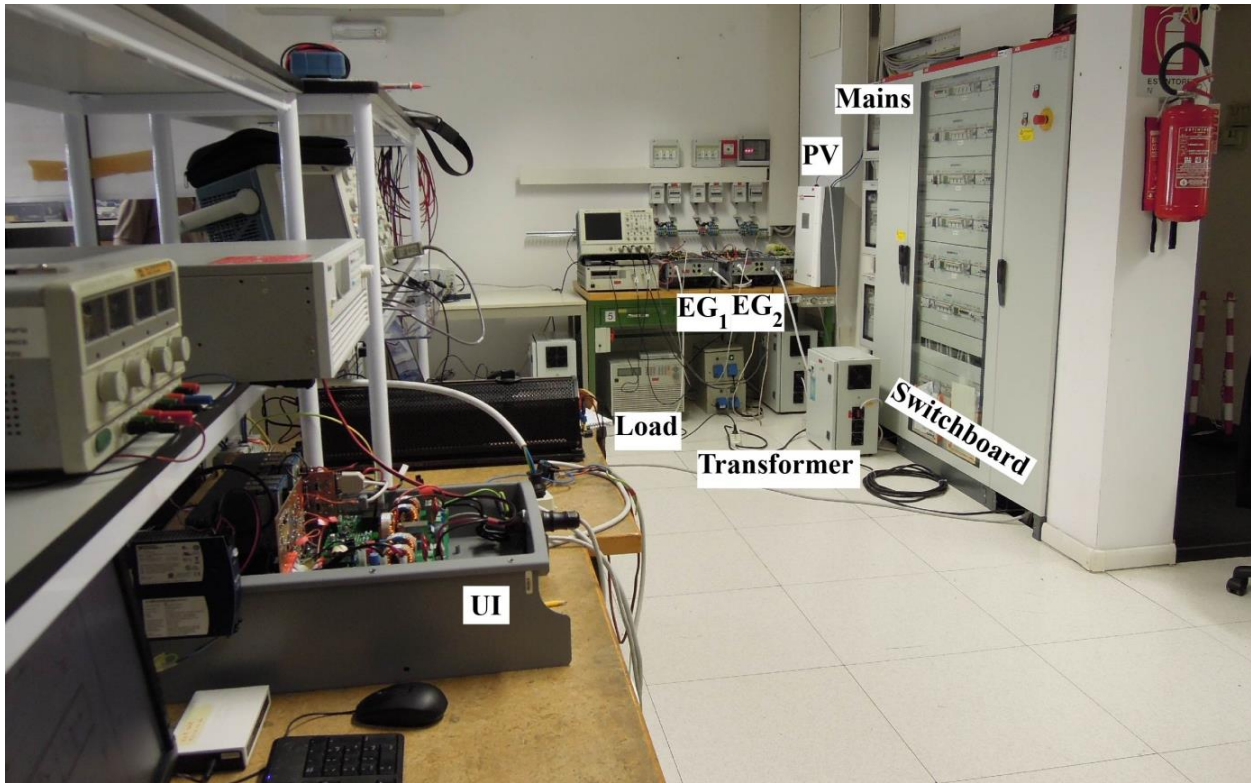
(**a**) Panoramic view of the experimental microgrid.
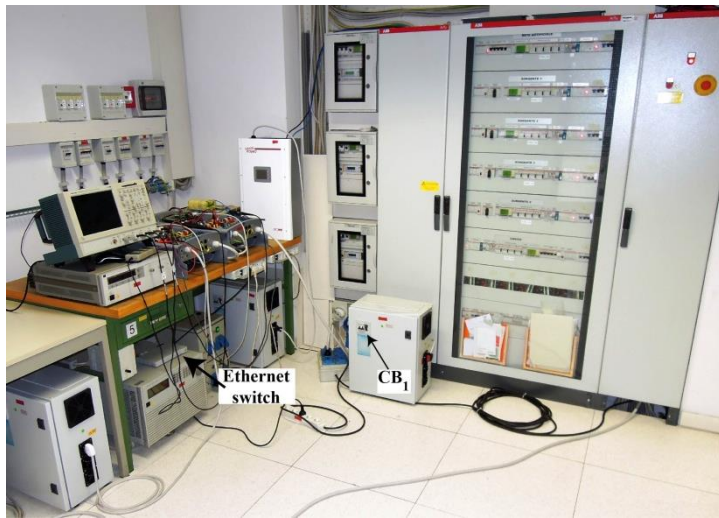
(**b**) View of the EGs, load, PV source, transformer and Ethernet switch.   (**c**) UI inverter and control board.
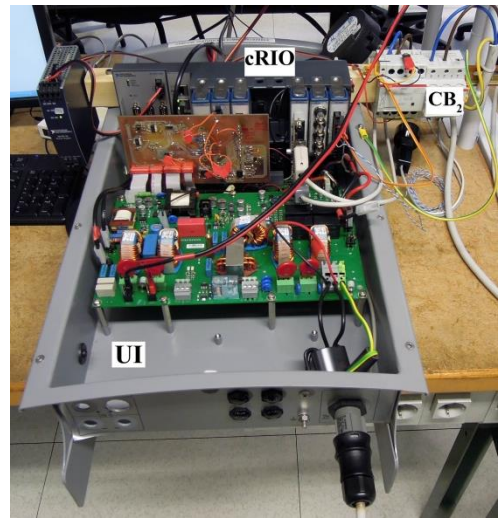
Fig. 5.2: Pictures of the experimental laboratory-scale microgrid implemented at University of Padova, Italy.

1.   Operation under overvoltage condition

Initially, to validate the stability and to analyze the dynamic response of the overvoltage (OV) control loop, we have activated it on EG_2 during 8 s and, thereupon EG_2 was released from it. The current waveform of EG_2 is shown in Fig. 5.3(a), while its RMS voltage profile along the test is shown in Fig. 5.3(b). One can see that the transition to OV operation is slow, avoiding any inrush current; its steady state is quite stable, without possible occurrence of LCOs, and finally, when the EG_2 is released from OV control, it returns faster to the previous operating mode (e.g., *either global optimization mode* or *local optimization mode*).

Secondly, in Fig. 5.4, a situation where the DSO requires to the microgrid's MC step charge in the power delivered at the PCC (P_G) is experimentally verified. Initially, the microgrid fulfills its power needs autonomously, so that $P_G = 0$ kW. Power injections from EGs are approximately $P_{EG1} = 0.42$ kW and $P_{EG2} = 1.58$ kW. We note that the power requested by the load, $P_L = 2$ kW, is shared among EG$_1$ and EG$_2$ in proportion to the EGs availability (see Table 2.5), according to the power-based.

At $t = 4$ s it is assumed that the power requested at the PCC from the MC changes to -1.5 kW (e.g., due to a specific request from the DSO). At this time, power references would be equal to: $P_{EG1} = 0.74$ kW and $P_{EG2} = 2.76$ kW. These are the power references calculated locally by the EGs on the basis of the power-based control and actuated. The increased generation from the EGs rises the voltage along the distribution network, causing the occurrence of an overvoltage condition at the point of connection of EG$_2$. In particular, V_{EG2} transcends the maximum voltage limit $V^{max} = 240$ V and triggers the overvoltage control for EG$_2$ (switch SW_2 of Fig. 2.2 driven by the flow chart of Fig. 2.9). The local
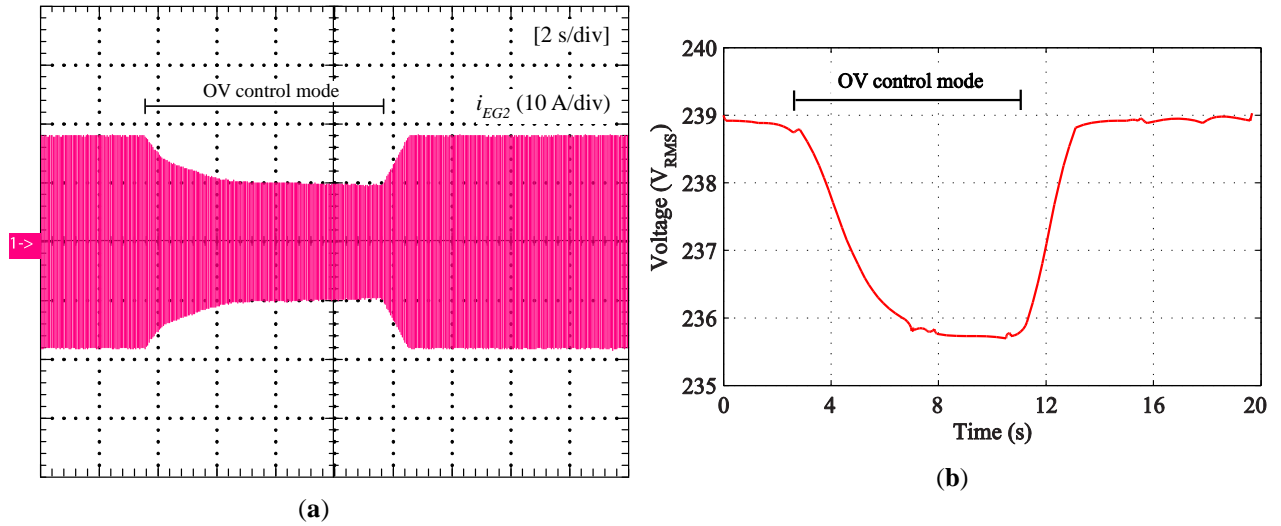
Fig. 5.3: Analyses of overvoltage control stability and dynamics. (a) EG$_2$ current waveform and (b) RMS voltage profile of EG$_2$.
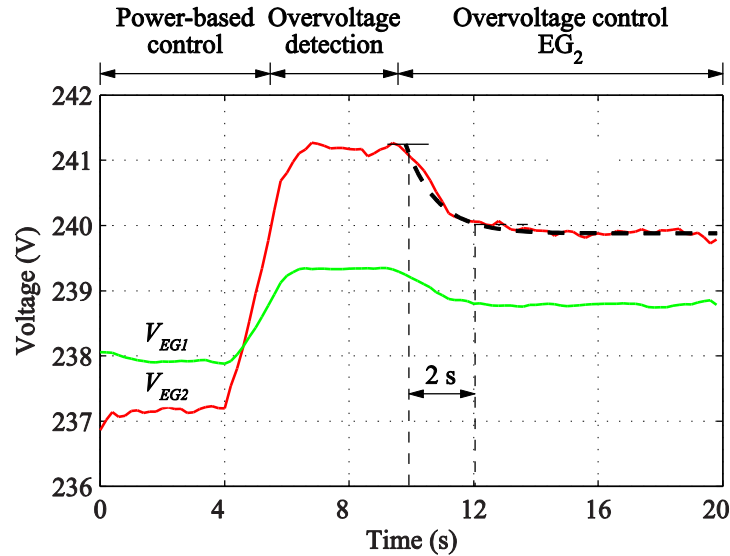
Fig. 5.4: Experimental result of an overvoltage condition. The dashed line represents the ideal first order behavior of the expected response of V_{EG2}, © IEEE 2015 [43].

overvoltage control makes the power injection from EG_2 decrease, so as to limit the measured output voltage V_{EG2} below V^{max}. Concurrently, the power injection from EG_1 increases to supply the power that cannot be delivered by EG_2, because of the voltage limitation. Finally, in the transient, EG_1 reaches its maximum value $\hat{P}_{EG1}^{max}$, whereas EG_2 generates the active power that, in the considered situation, corresponds to a measured output voltage equal to the maximum value V^{max}. In steady state, the following power injections were obtained: $P_G = -1.2$ kW, $P_{EG1} = 0.8$ kW, $P_{EG2} = 2.4$ kW, and $P_L = 2$ kW. The dashed line represents the ideal first order behavior of the expected response of V_{EG2}.

2.   *Grid-connected operation*

Fig. 5.5 and Fig. 5.6 show the dynamic behavior of the system while feeding distorting loads and the ability of the power-based control to effectively manage the power sharing among EGs. To the purpose, a nonlinear distorting load (L, in Fig. 2.10) absorbing 1.0 kW with CF = 1.8 (THD$_{iL}$ = 39.1 %) is *disconnected* from the microgrid. The EGs are inactive and the grid absorbs -1.3 kW, provided from the DC side of the UI. Fig. 5.5 shows the prompt reaction of the UI control that, in a few line cycles, drives the microgrid to a steady state condition with THD$_{iG}$ decreased to 4.2 %.

The opposite situation is shown in Fig. 5.6, where the transient following the *connection* of a distorting load absorbing 2.0 kW with CF = 1.8 is considered. Here, the EGs are active and the grid current reference ($P^{*}_G = 0$) is set to zero. Also in this case, the UI control reacts quickly, meeting temporarily energy needs. At the same time, the power-based control effectively manages the power sharing among DERs–in proportion to their local energy availability–in a way that fully exploits any available resource to achieve the power balance, and avoid the saturation of DERs, even during transient conditions. Note that EG_1 responds faster than EG_2, because, for the latter, a slower current control scheme was chosen with the purpose to show that different dynamic responses among slave units and delays in the actuation of power references do not impair system stability.
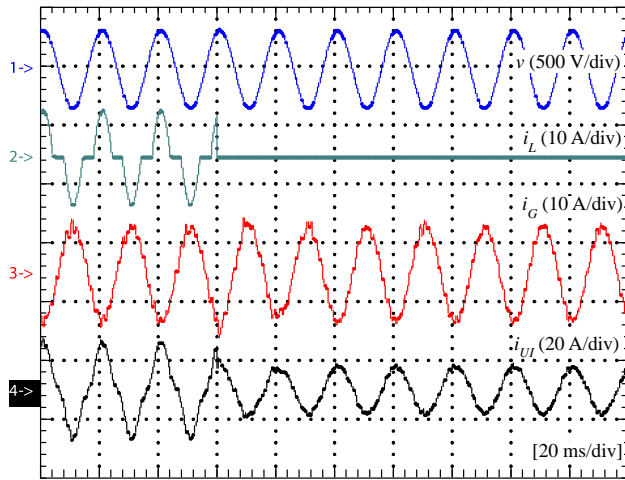
Fig. 5.5: Disconnection of a 1 kW nonlinear load, grid-connected mode.
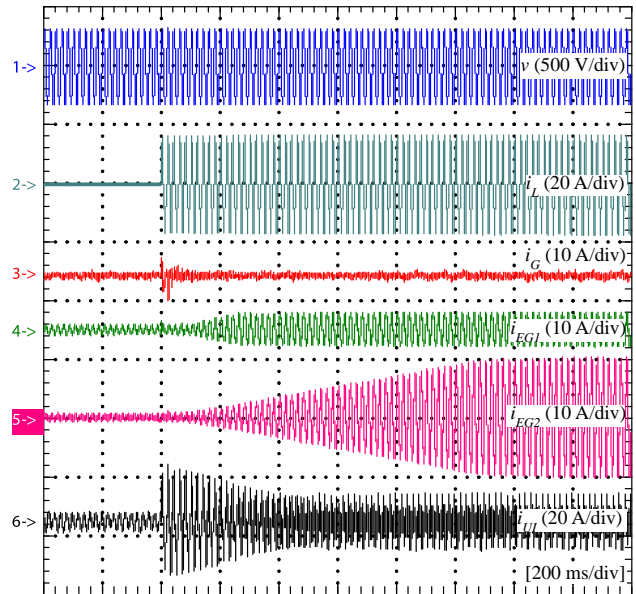
Fig. 5.6: Connection of a 2 kW nonlinear load, grid-connected mode.

In steady state, the power injection from EG_1 and EG_2 is 0.42 kW (with THD_{iEG1} equal to 2.8 %) and 1.58 kW (with THD_{iEG2} equal to 4.1 %), respectively. The mains and the UI provide no active or reactive power. Besides, UI performs harmonic compensation at PCC ensuring practically zero grid current. Despite the high impact on the circulating fundamental and harmonic currents due to the insertion of the distorting load, the measured PCC voltage waveform remains nearly unaffected, thanks to the UI effectiveness in controlling grid current i_G. With the connection of the load, shown in Fig. 5.6, THDv increases from 0.67 % to 0.80 %. The small change is due to the residual high frequency harmonic circulation not compensated by the narrow bandwidth grid current control of the UI, Z_{iG} in Fig. 3.2.

A further advantage in controlling i_G can be highlighted when the mains voltage is distorted. By applying a 2.3 % of third harmonic on the grid voltage (e_G), with the microgrid importing 2 kW from the mains, i_G presents a third harmonic of 40.1 % if the harmonic control in the grid current control loop, $R_{2,3,4,5,7,}$ (s) in Fig. 3.11, is *disabled*. Instead, by *enabling* the harmonic control, the total grid current distortion equals to 2.9 % (the ideal case, requiring i_G proportional to v_G, would give 2.3 %).

3.   Transition from grid-connected to islanded operation

1)   Intentional islanding

Fig. 5.7 shows the behavior of the microgrid in response to an intentional islanding transition (e.g., scheduled maintenance). In this case, the MC sets P^*_G to zero before opening CB_2 (*islanded mode* of Fig. 1.4 and *programmed islanding* of Fig. 3.14). From now on, in islanded operation, the UI runs as a grid-forming voltage source providing the voltage and frequency references for the entire microgrid. It is naturally responsible for instantaneous power balance. The power-based control drives the distributed EGs to meet the load power needs.
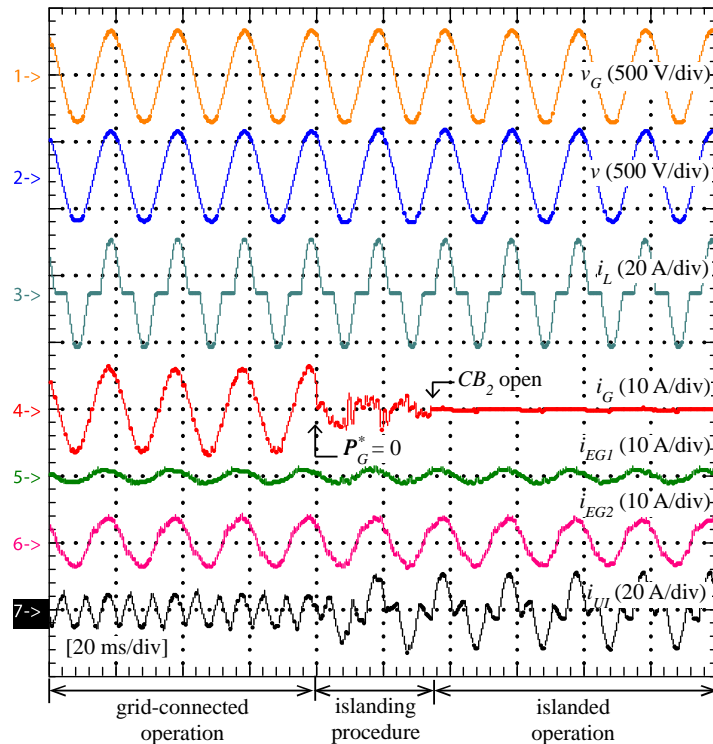
Fig. 5.7: Intentional islanding transition.

2) *Intentional islanding due to voltage out of range*

Fig. 5.8 shows the behavior of the microgrid in response to intentional islanding due to voltage out of range, as per Fig. 3.14 and Fig. 3.15. In this case, the grid voltage varies in a ramp exceeding the safety voltage limit (set equal to 245 V_{RMS}) and the MC must execute the intentional islanding with grid absent. The MC sets the grid power reference (P^*_G) to zero and bounds the PLL frequency around the nominal value, as in Fig. 3.16, before opening CB_2, see Fig. 5.9, thereupon the microgrid voltage returns to its nominal operation value, as shown in Fig. 5.10, since e^* is set to be the positive-sequence of the PCC voltage with nominal frequency $\tilde{\omega}$ and amplitude $\tilde{E}$.
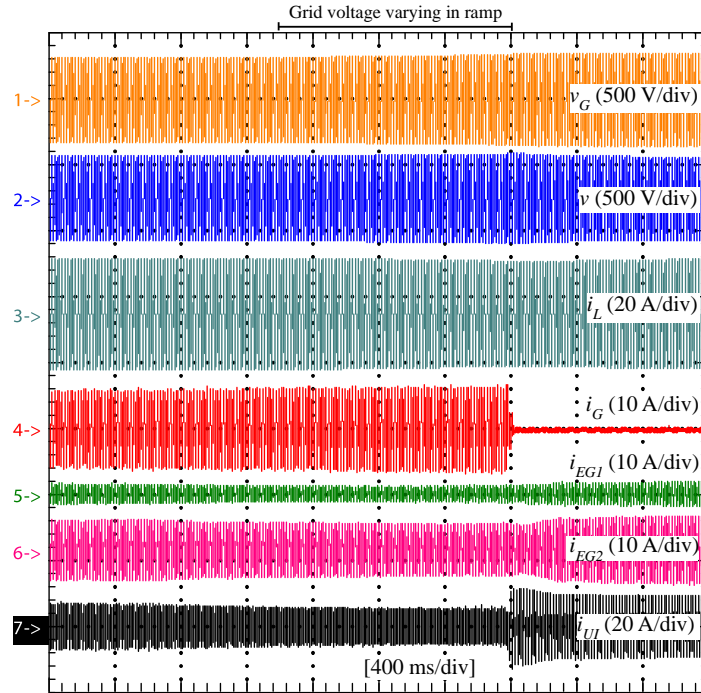
Fig. 5.8: Intentional islanding due to voltage out range.
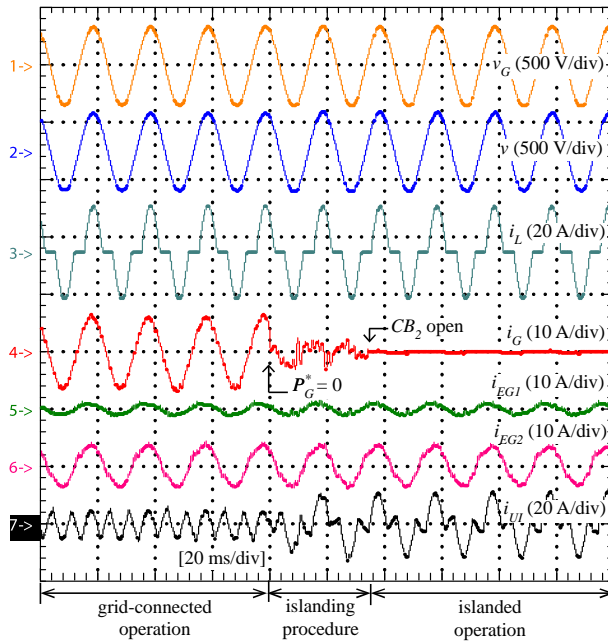
Fig. 5.9: Zoomed-in view around the disconnection shown in Fig. 5.8.
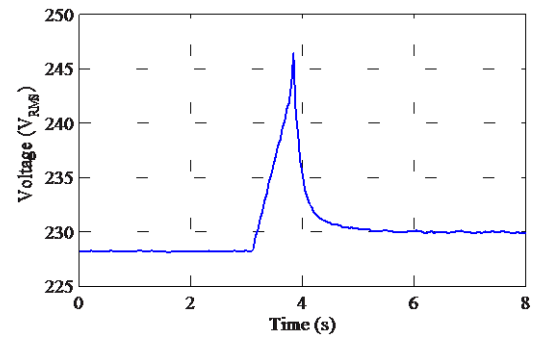
Fig. 5.10: RMS value of the PCC voltage under intentional islanding due to voltage out of range.

3)   Non-intentional islanding

Fig. 5.11 shows the microgrid under non-intentional islanding. In this case, the nonlinear load absorbs 2 kW with CF = 2.0, the utility grid provides 0.65 kW, and the PV source generates 0.8 kW. To validate the non-intentional islanding transition process, the circuit breaker (CB_1) located at the grid side of the transformer (see Fig. 2.10) is suddenly opened by the DSO (e.g., due to a grid fault). The islanding condition is detected by the UI on the basis of the quantities measured at PCC, Section 3.5. When this occurs, the CB_2 at the secondary side of the transformer is opened by the UI. Fig. 5.12 shows the microgrid voltage and frequency, regulated by the UI, across the transition. The transient following the non-intentional islanding happens smoothly and the system is driven to a new steady state condition, where the power balance is ensured by taking full advantage of the total energy available, within the microgrid. Besides, inspecting waveform i_{PV}, we notice that the transition occurs unobserved by the commercial PV source, which further proves the capability of the microgrid to guarantee adequate continuity and smoothness in grid voltage characteristics across transitions of operating modes.
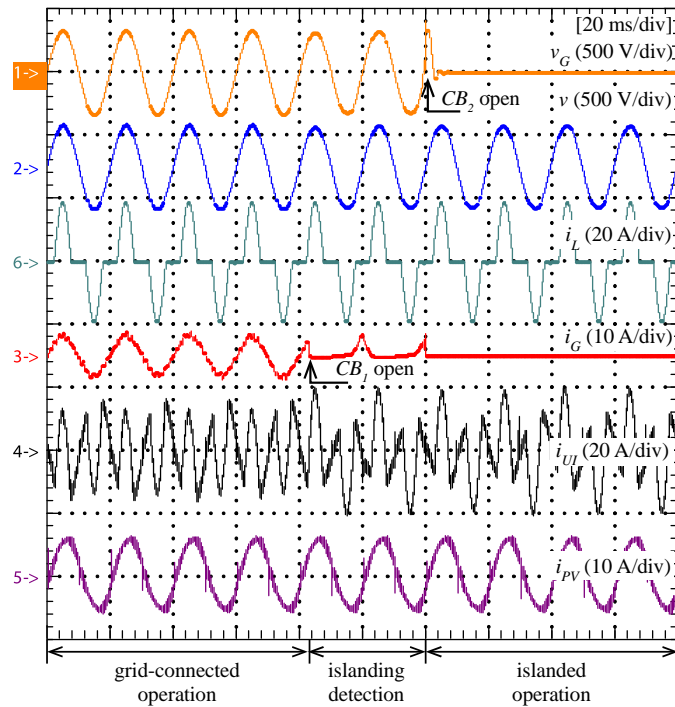
Fig. 5.11: Non-intentional islanding transition, with PV source connected.
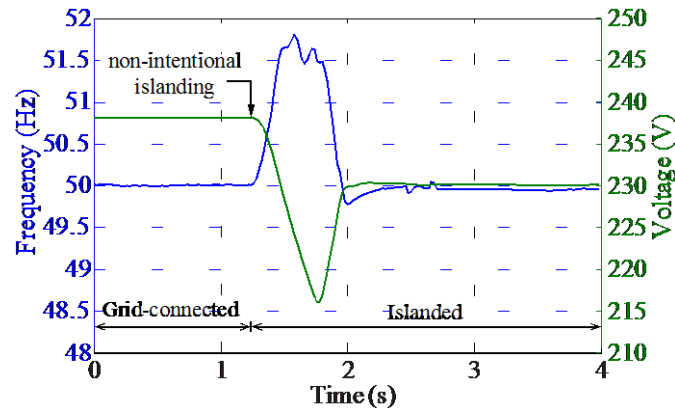
Fig. 5.12: Microgrid voltage and frequency across a non-intentional islanding transition.

4)   Critical non-intentional islanding

In order to validate the proposed islanding detection scheme of Fig. 3.14 at a critical case, namely, the non-intentional islanding with zero current exchange at the PCC, is tested and shown in Fig. 5.13. One can see that the transition occurs seamlessly, despite of the seven cycles needed for detection. In fact, in transitions with low PCC current, where the voltage drop over the line impedance is minimum, a fast detection is not required; the system must just comply with the standards [**38**], [**62**]. Instead, when there is considerable PCC current flow, the detection must be fast. Accordingly, in this case, the proposed detection scheme needs about two cycles as shown in Fig. 5.11.
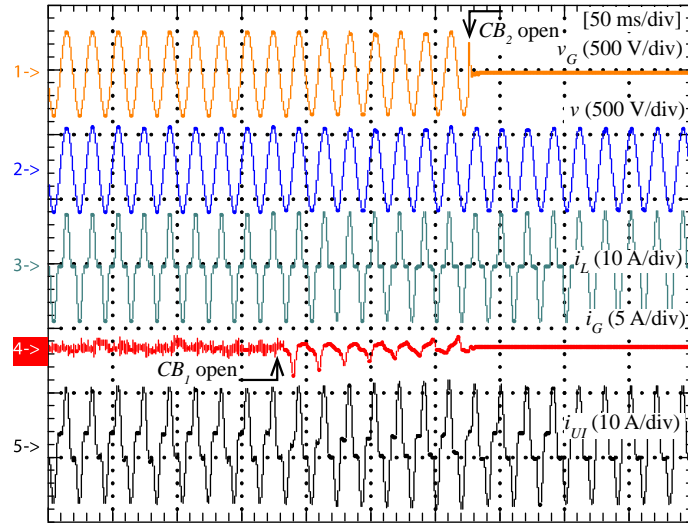
Fig. 5.13: Critical non-intentional islanding transition.

4.   Islanded operation

Fig. 5.14 shows the dynamic performance during islanded operation in feeding distorting loads. In particular, the response to a step in the distorting load power absorption, with the PV source disconnected, is considered. The UI supplies the local load with an adequate voltage quality: the grid voltage harmonic distortion, THD_v, modifies from 0.77 % to 2.73 %.

The long term dynamic response is identical to what is achieved during the grid-connected operating mode (Fig. 5.6): the UI responds promptly to transients, while the power-based control provides to distribute the load among generators in steady state.

5.   Communication failure

Fig. 5.15 shows a communication failure occurring between MC and EG_2 during islanded operation. Before the communication failure, the EGs are coordinated by the MC (*global optimization mode*). After the failure, EG_1 keeps running regularly (driven by MC) whereas EG_2 changes its power reference from *global optimization mode* to *local optimization mode*, as indicated in Fig. 1.3. In this case, the UI ensures the power balancing, up to the instant when the communication is restored or loads and generators readjusted. We remark how a communication failure does not jeopardize the system, which is instead able to ride through the abnormal event smoothly and without triggering any irregular behavior.
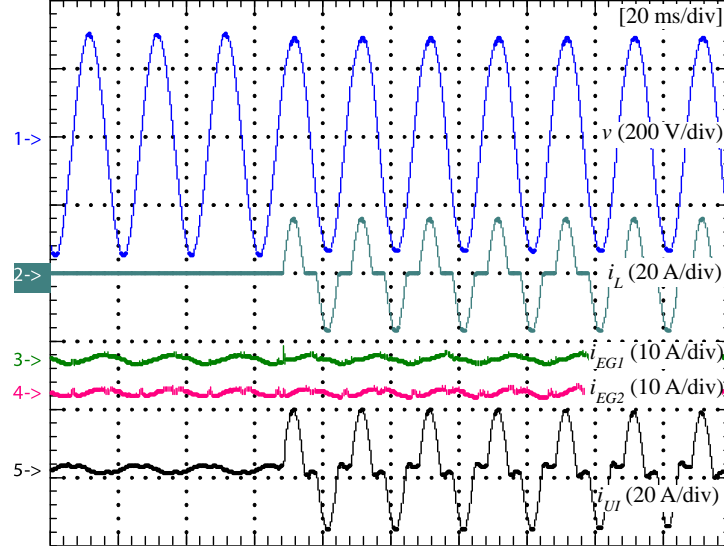
Fig. 5.14: Connection of a 2 kW nonlinear load during islanded mode.
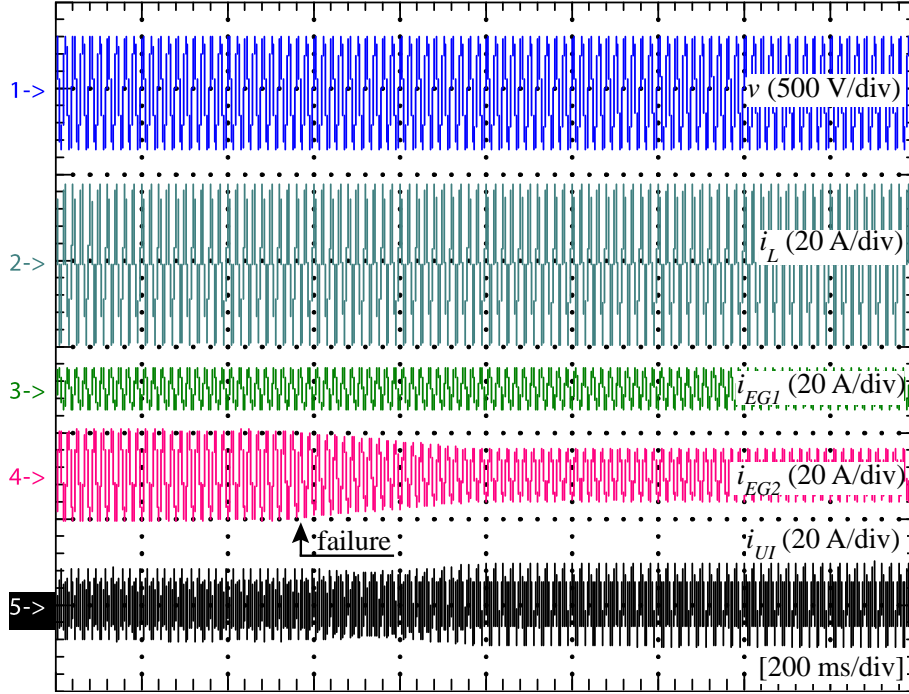
Fig. 5.15: Communication failure between MC and EG$_2$.

6. *Transition from islanded to grid-connected operation*

Fig. 5.16 shows the process of reconnection to the mains after the grid is restored and the microgrid voltage, v, resynchronized with the grid voltage (v_G). The procedure occurs smoothly while the power-based control adjusts the EGs to adapt to the new power demand of the microgrid.

The long-term behavior during a transition to grid-connected operating mode can be appreciated in Fig. 5.16. First, we remark the absence of any inrush current at the connection instant. Secondly, that the voltage provided by the UI is well synchronized with grid voltage, thus v maintains smooth and with the desired amplitude around the transition. Finally, the amplitude of i^*_G is changed progressively with a suitable slew-rate. A zoomed-in view around the connection instant is reported in Fig. 5.17. Here the deadband duration is set to 10 ms.
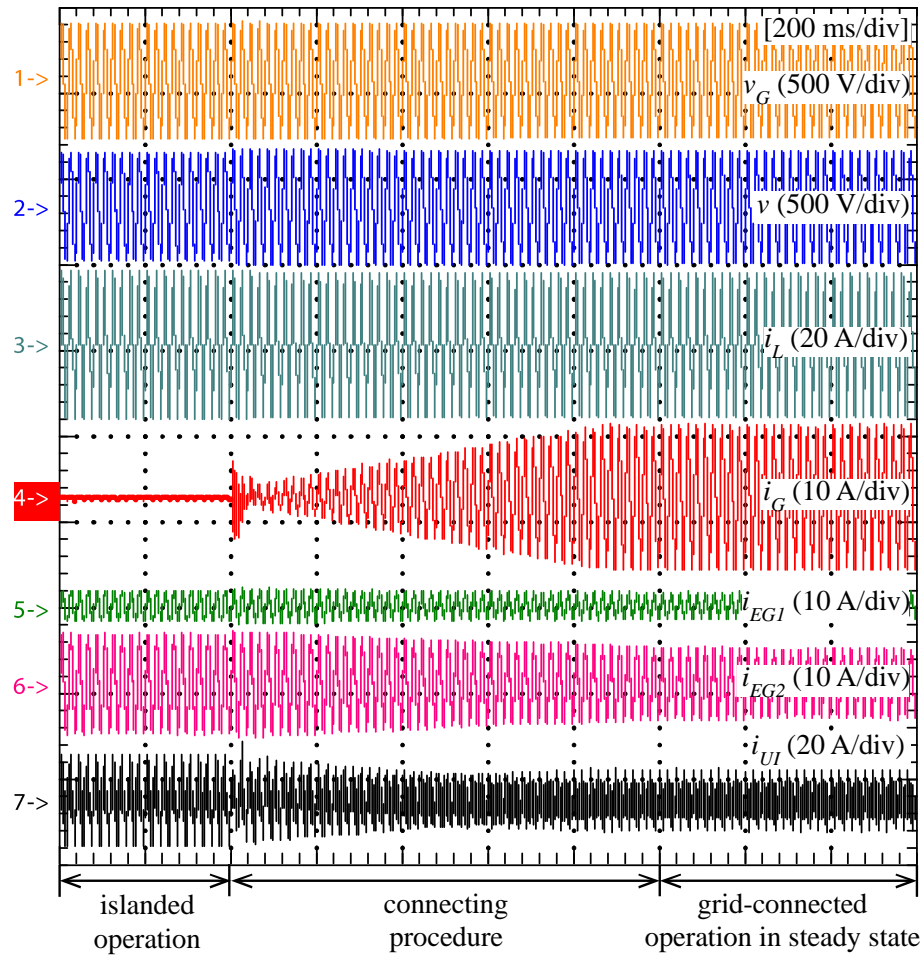
Fig. 5.16 Transition from islanded to grid-connected operation.
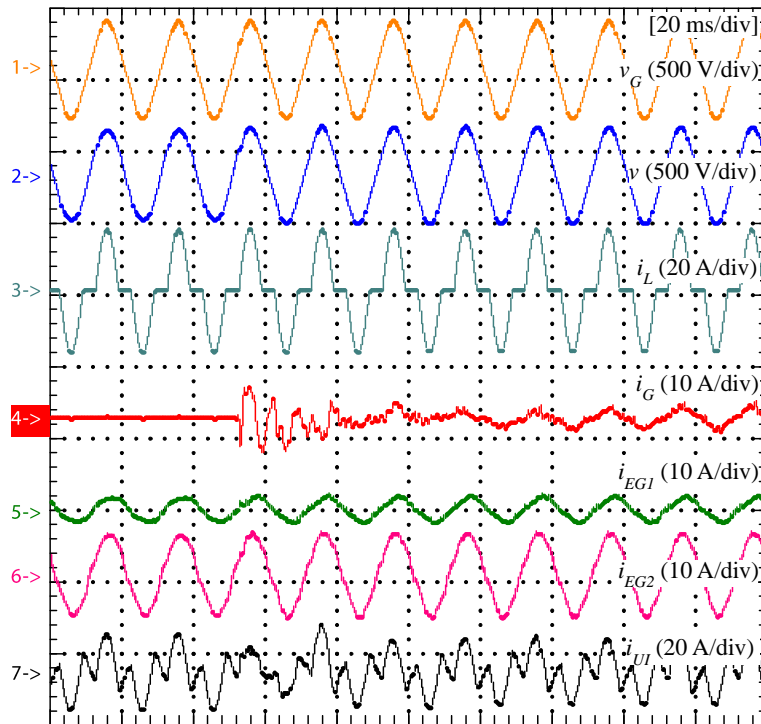
Fig. 5.17 Zoomed-in view around the connection shown in Fig. 5.16.

5.3. Conclusions

A general approach to control the DERs in a microgrid has been validated, which allows the considered microgrid to operate as a fully-dispatchable and integrated power source. The control uses only average power commands and ensures uniform power sharing among distributed generators, good distribution efficiency, full exploitation of renewable resources, and fast response to the power demands coming from the utility and loads.

The key element to assure high performance levels is the UI connected at the PCC with the mains of the microgrid. Such unit performs as a flexible power interface to the mains, and acts as a MC for the various distributed units over the microgrid. As a result, the microgrid ensures good power quality to the loads, reacts rapidly to load steps, and can manage fast transitions from grid-connected to islanded operation, even in case of non-intentional islanding. Moreover, communication failure does not jeopardize the microgrid operation. The microgrid functionalities were experimentally validated by means of a laboratory-scale set-up.

At this point, we have validated the local control of EGs, the design and performance of the UI, and the central algorithm, namely, power-based control used to coordinate the EGs operation under a single-phase microgrid. The next chapter analyzes a three-phase microgrid, in which the same power electronics units, and the power-based algorithm, are used to tightly control the power flow at the microgrid PCC, performing unbalance load current compensation by means of single-phase inverters arbitrarily connected to the network.

Chapter 6

6. Fully-Dispatchable Three-Phase Low Voltage Microgrid

The last chapter has validated a fully-dispatchable single-phase microgrid, in which the distributed control strategy based on the power-based control algorithm implemented in the UI and used to coordinate the power sharing among the EGs. Nevertheless, the three-phase AC power systems represent a solid basis to support DER integration and the development of the new concept [131], facilitating power exchange among microgrids while taking advantage of the existing distribution network infrastructure. Thus, this chapter evaluates the previous fully-dispatchable master-slave microgrid architecture, based on UI converter and power-based control over a three-phase system.

On the other hand, different electrical distribution system topologies are adopted around the world, such as: a) three-phase three-wire; b) three-phase three-wire with grounded neutral; c) three-phase four-wire with non-grounded neutral; d) three-phase four-wire with grounded neutral and contiguous ground, as shown in Fig. 6.1 [132]. If we also consider how loads are actually connected in each country, the scenario gets even more intricate, since dual port devices can be either connected line-to-neutral or line-to-line. From the standpoint of microgrid control, the connection code is extremely relevant, particularly for compensation purposes.

In three-phase systems, load balancing is a critical issue and, at the same time, an inherent need of the electrical system [133]. Indeed, load unbalances may cause detrimental effects, like voltage
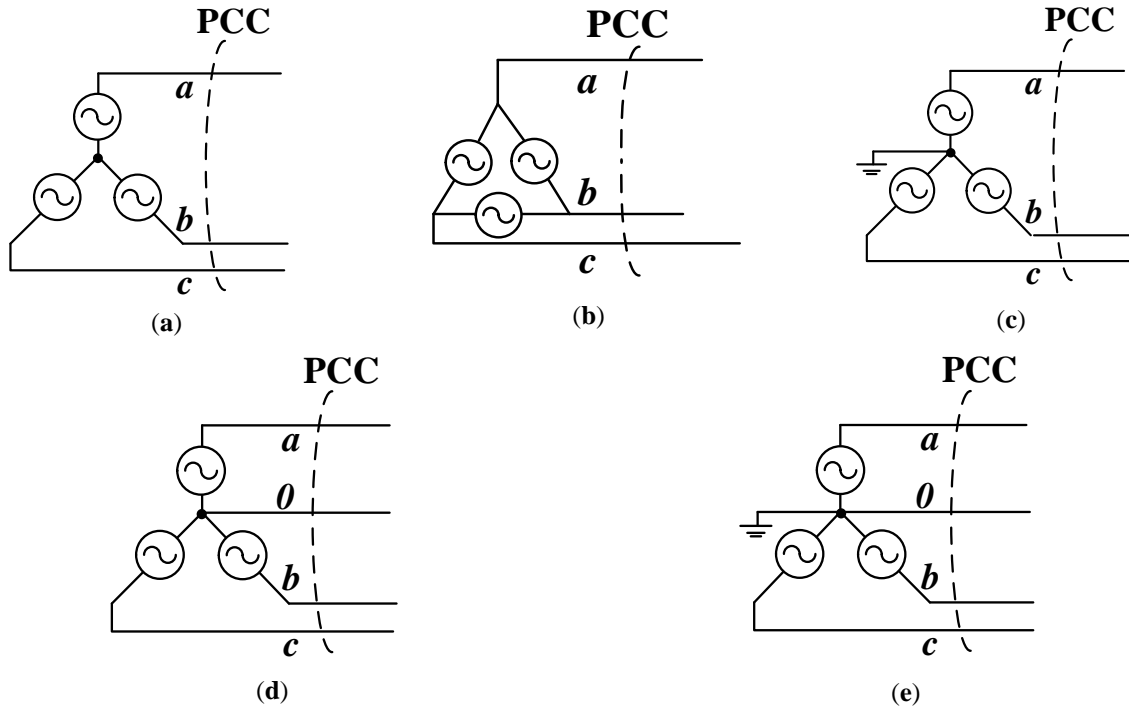
Fig. 6.1: Common electrical three-phase distribution system.

asymmetry and increased distribution loss. A direct solution, viable especially for newly designed microgrids, is to fix the connection code of the loads; however, this may be unfeasible in most existing distribution systems. Employing compensators for voltage asymmetry can also be another solution [**134**], though it involves additional costs. Whereas, exploiting the surplus power capability of DERs to compensate unbalance power has been proven to be a good solution not requiring additional investments [**133**], [**135**], as it has been previously done for reactive power.

Therefore, this chapter proposes an efficient strategy to control the power flow among different phases of three-phase microgrids and perform unbalance power compensation by means of single-phase converters, arbitrarily connected among the phases. The aim is to enhance the power quality measured at the PCC of the microgrid, to improve the voltage profile through the lines, and to reduce the overall distribution loss, while preserving an efficient operation of DERs.

6.1. Three-phase low voltage microgrid structure

As several topologies of electrical distribution system and connection codes exist, then, we have picked up a general scenario: a wye three-phase four-wire topology with non-grounded neutral, as shown in Fig. 6.1(d), where loads and rooftop PV inverters are arbitrarily connected, such as: line-to-neutral or line-to-line. Fig. 6.2 illustrates a microgrid of a real three-phase four-wire metropolitan distribution system based on aerial wiring, considering linear and nonlinear loads, and currently installed in Brazil. This LV microgrid consists in fourteen nodes, nine distinct nonlinear loads, and six multi-task EGs without ES.
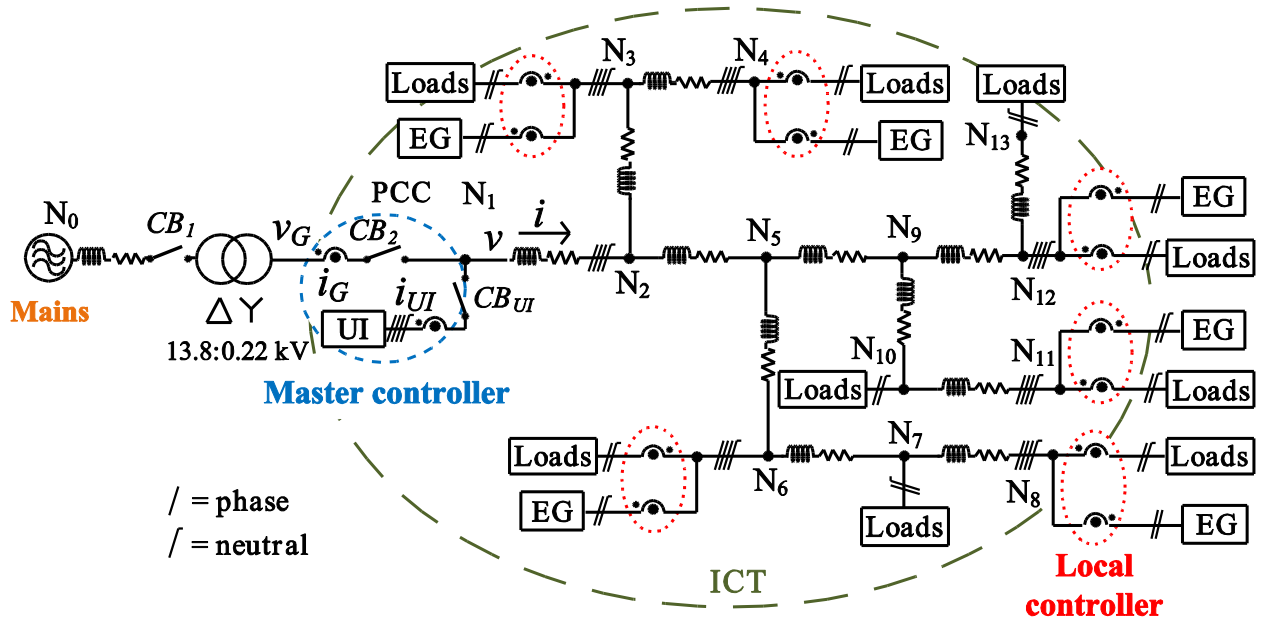
Fig. 6.2: Considered microgrid infrastructure based on master-slave architecture.

Table 6.1: Parameters of the three-phase low voltage microgrid.

Sinusoidal and symmetrical phase voltages [kV]
V_a=7.97∠0°; V_b=7.97∠-120°; V_c=7.97∠-240°.

Distorted and asymmetrical phase voltages [kV]
V_a=8.37∠0° + 0.24∠3·0° + 0.24∠5·0° + 0.24∠7·0°;
V_b=7.57∠-120° + 0.24∠3·(-120)° + 0.24∠5·(-120)° + 0.24∠7·(-120)°;
V_c=7.97∠-240° + 0.24∠3·(-240)° + 0.24∠5·(-240)° + 0.24∠7·(-240)°.

Line impedances		Z [mΩ]
From	**To**	
N_0	N_1	460+j1850
N_1, N_2, N_5, N_6	N_2, N_5, N_6, N_7	7.0+j9.7
N_2, N_3, N_7	N_3, N_4, N_8	48.3+j10.3
N_5, N_9	N_9, N_{12}	22.3+j11.4
N_9, N_{10}	N_{10}, N_{11}	20.3+j6.9
N_{12}	N_{13}	19.1+j9.8

Table 6.2: Parameters of the distributed EGs.

Parameters	EG_j (N_3, N_4, N_6, N_8, N_{11}, N_{12})
Power rating [kVA]	(5.0, 9.0, 7.0, 10.0, 6.0, 5.0)
Overload power rating [kVA]	(5.0, 9.0, 7.0, 10.0, 6.0, 5.0)
Power capacity [kW]	(4.5, 8.0, 1.5, 8.5, 5.0, 2.5)
Max. power capacity [kW]	(4.5, 8.0, 1.5, 8.5, 5.0, 2.5)
Min. power capacity [kW]	(0, 0, 0, 0, 0, 0)

Node N1 is the main PCC, while the utility grid behaves as a voltage source at node (N_0). The UI, endowed with the MC and ES device, is installed at the PCC. Regarding to the slave units (i.e., EGs), the circuit of Fig. 6.2 has three single-phase EGs connected line-to-neutral (EG_{aN3}, EG_{bN11}, EG_{cN6}) and three connected line-to-line (EG_{abN4}, EG_{bcN12}, EG_{caN8}). All the EGs are controlled as current sources synchronized with the fundamental grid voltage and they are equipped with communication unit and linked with the MC through an ICT infrastructure. The nominal microgrid power rate is 60 kVA, the utility grid voltage is 220V line-to-line, 60 Hz, (the frequency here is different from that in Chapter 5, to show that the proposed approaches are valid for both 50 or 60 Hz), and the values of the network's, non-homogeneous, impedances are shown in Table 6.1. The EG parameters are reported in Table 6.2. For the best knowledge of the authors, a subject that has not been investigated in the literature is the control of DERs arbitrarily connected to the three-phase distribution system. Though this latter connection scheme is not generally accepted, it is a common practice in some regions of South America, especially in Brazil, even for residential consumers. Fig. 6.3 shows the equivalent three-phase circuit corresponding to the scheme of Fig. 6.2. From Fig. 6.3, it is easy to realize that the current flowing through the single-phase DER units, from the MC point of view (wye connected at the PCC), is *line current* for the line-to-neutral connected inverters, or *phase current* for the line-to-line connected inverters. Therefore, the MC has to be aware of the specific connection of DERs.

An advantage of line-to-line connected DERs is the reduced current exchange through their corresponding EPPs, thanks to the higher voltage value across the point of connection. On the other hand, by standing on only two phases, the line-to-line connected DERs are decoupled from the neutral wire, which prevents the neutral (i.e., homopolar) current compensation. Finally, we remark that, although local harmonic is always possible, it must be prevented due to unpredictable harmonic interaction among phases, nodes, and complex line impedances [136].

Following, the modified power-based control algorithm is presented in order to perform independent per phase power sharing, regardless of the inverter connection scheme. It allows unbalance power compensation and power flow control among the different phases of the microgrid. All the formulation is analyzed and evaluated, in both steady state and dynamics, by means of simulation results.
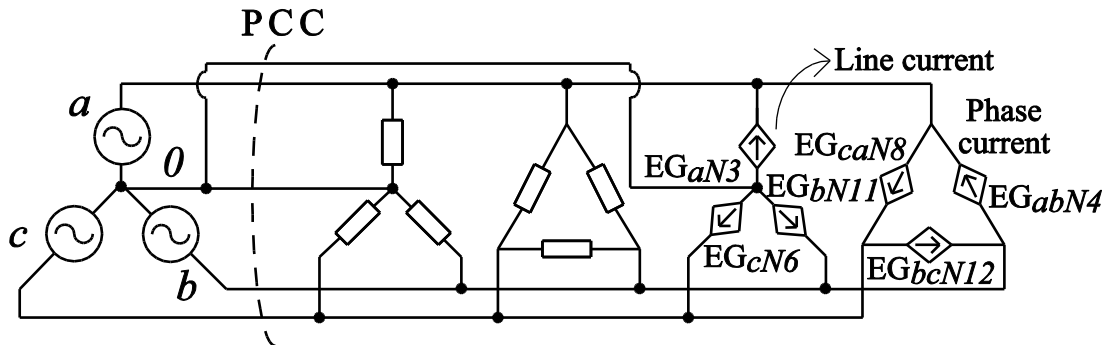
Fig. 6.3: Equivalent three-phase distribution system of the circuit shown in Fig. 6.2.

6.2. Power-based control algorithm per phase

The previously presented power-based control in Chapter 4 drives the EGs so that they contribute to microgrid power needs in proportion of their actual capability to deliver active and reactive power. This approach achieves the regulation of the power flow at the PCC by using the so called *scaling coefficients* (α_P, α_Q), broadcasted to all the EGs, that scale the power contributions to exploit DERs uniformly with respect to the entire three-phase microgrid, while requiring only minimal communication and measurement capability. This strategy is called *phase-independent.*

This section applies the power-based control algorithm to each phase *m* of the microgrid individually, and broadcasts the *phase scaling coefficients* (α_{Pm}, α_{Qm}) to all EGs arbitrarily connected to that phase. It causes unbalance currents compensation and allows power flow control among the three phases. It is named *phase-dependent strategy*, and it is worth recalling that each EG must inform the MC of the particular phase at which it is connected. For an EG connected between phases "*m*" and "*n*", it is sufficient to inform only the phase "*m*", following the adopted polarities of Fig. 6.3, and to measure the voltage v_{mn}, as explained in Chapter 2.

The coordinated control strategy applied per phase *m* performs as follows. At the end of the *l*-th control cycle, the MC determines the total *per phase* active power $P^*_{mtot}(l)$ and reactive power $Q^*_{mtot}(l)$ that must be shared among EGs along that cycle. Moreover, the *j*-th EG (j = 1, 2, …, *J*) sends the following information to MC:

- the active power $P_j(l)$ and reactive power $Q_j(l)$ generated during the *l*-th control cycle;
- the minimum active power $P_j^{min}(l)$ and the maximum active power $P_j^{max}(l)$ that the EG can generate, on the basis of the state of its energy storage, if any;
- the rated apparent power $A_j(l)$ of the local EPP and its temporary overloading capability $A_j^{over}(l)$. On the basis of the collected data, MC calculates:
- the total active and reactive phase power delivered by the EGs along cycle *l*:

$$P_{mtot}(l) = \sum_{j=1}^{J} P_{Gmj}(l) \, , \tag{6.1}$$

$$Q_{mtot}(l) = \sum_{j=1}^{J} Q_{Gmj}(l) \, ; \tag{6.2}$$

as the total minimum [$P_{mtot}^{min}(l)$] and maximum [$P_{mtot}^{max}(l)$] active phase power and total maximum [$Q_{mtot}^{max}(l)$] and overloading [$Q_{mtot}^{over}(l)$] reactive phase power, as in Chapter 4;
- the total active and reactive phase power absorbed within the microgrid during cycle *l*:

$$P_{Lmtot}(l) = P_{Gm}(l) + P_{UIm}(l) + P_{mtot}(l) \, , \tag{6.3}$$

$$Q_{Lmtot}(l) = Q_{Gm}(l) + Q_{UIm}(l) + Q_{mtot}(l) \, , \tag{6.4}$$

where P_{Gm} and Q_{Gm} are the active and reactive phase power measured at grid side of the PCC and P_{UIm} and Q_{UIm} are the active and reactive phase power delivered by the UI;

- the references for the total active $[P^*_{mtot}(l+1)]$ and reactive $[Q^*_{mtot}(l+1)]$ phase power to be provided by the EGs in the next control cycle $l+1$:

$$P^*_{mtot}(l+1) = P_{Lmtot}(l) - P^*_{PCCm}(l+1),$$ (6.5)

$$Q^*_{mtot}(l+1) = Q_{Lmtot}(l) - Q^*_{PCCm}(l+1),$$ (6.6)

where $P^*_{PCCm}(l+1)$ and $Q^*_{PCCm}(l+1)$ are, respectively, the active and reactive references of the phase power flow at the PCC. Considering the polarities of Fig. 6.2, the exchanged powers at the terminals of the UI are:

$$P_{UIm}(l+1) = P^*_{PCCm}(l+1) - P^*_{Gm}(l+1),$$ (6.7)

$$Q_{UIm}(l+1) = Q^*_{PCCm}(l+1) - Q^*_{Gm}(l+1),$$ (6.8)

while references P^*_{Gm} and Q^*_{Gm} are set on the basis of a long term energy management strategy (e.g., negotiations with the DSO) or set to zero during islanded mode, as explained in Section 1.2. References P^*_{PCCm} and Q^*_{PCCm} are set by MC to regulate the power flow at the PCC among different phases, according to the energy state of the UI and EGs (see, e.g., [**125**]).

- finally, the *phase scaling coefficients* α_{Pm} and α_{Qm} (both ranging in the interval [0, 2]) are computed and broadcasted to all the EGs connected to the corresponding phase m. α_{Pm} and α_{Qm} calculated for different conditions are reported in Table 6.3.

Thus, given α_{Pm} and α_{Qm}, the j-th EG (EG$_j$) controls its local active and reactive power injection according to:

$$P^*_j(l+1) = P^{min}_j + \left(P_j - P^{min}_j\right) \cdot min(\alpha_{Pm}, 1) + \left(P^{max}_j - P_j\right) \cdot max(\alpha_{Pm} - 1, 0),$$ (6.9)

$$Q^*_j(l+1) = Q^{max}_j \cdot min(\alpha_{Qm}, 1) + \left(Q^{over}_j - Q^{max}_j\right) \cdot max(\alpha_{Qm} - 1, 0),$$ (6.10)

where $P^*_j(l+1)$ and $Q^*_j(l+1)$ are respectively the active and reactive power references for EG$_j$ in the next control cycle. Equations (6.9) and (6.10) hold for the control of the power flow at PCC, in both grid-connected and islanded operation.

Table 6.3: Phase scaling coefficients.

Power condition	Scaling coefficients
$P^*_{mtot}(l+1) < P^{min}_{mtot}(l)$	$\alpha_{Pm} = 0$
$P^{min}_{mtot}(l) \le P^*_{mtot}(l+1) < P_{mtot}(l)$	$\alpha_{Pm} = \dfrac{P^*_{mtot}(l+1) - P^{min}_{mtot}(l)}{P_{mtot}(l) - P^{min}_{mtot}(l)}$
$P_{mtot}(l) \le P^*_{mtot}(l+1) \le P^{max}_{mtot}(l)$	$\alpha_{Pm} = 1 + \dfrac{P^*_{mtot}(l+1) - P_{mtot}(l)}{P^{max}_{mtot}(l) - P_{mtot}(l)}$
$P^*_{mtot}(l+1) > P^{max}_{mtot}(l)$	$\alpha_{Pm} = 2$
$Q^*_{mtot}(l+1) \le Q^{max}_{mtot}(l)$	$\alpha_{Qm} = \dfrac{Q^*_{mtot}(l+1)}{Q^{max}_{mtot}(l)}$
$Q^*_{mtot}(l+1) > Q^{max}_{mtot}(l)$	$\alpha_{Qm} = 1 + \dfrac{Q^*_{mtot}(l+1) - Q^{max}_{mtot}(l)}{Q^{over}_{mtot}(l) - Q^{max}_{mtot}(l)}$

Summarizing the statements of Section 4.2 applied per phase, *i*) if $\alpha_{Pm,Qm} = 0$, all EGs connected to phase *m* supply minimal power; *ii*) if $0 \leq \alpha_{Pm,Qm} < 1$, these EGs ensure the power balance by operating in reduced power mode [**93**], or sharing the excess of generated power to distributed storage units, if any; *iii*) if $1 \leq \alpha_{Pm,Qm} < 2$, the EGs meet the microgrid power demand by drawing energy from energy storage devices; and *iv*) if $\alpha_{Pm,Qm} = 2$, all EGs connected to phase *m* supply the maximum power. The power balance is ensured by exploiting the energy storage in the UI and/or by readjusting loads and generators or, in grid-connected operation, by taking power from the mains. In every operating condition, both grid-connected and islanded, the power balance must be ensured by the mains and/or by the centralized (UI) or distributed (EGs) energy storage, if any.

For system without ES, the same consideration of (4.31) and Table 4.1 can be done. The adapted power-based control results in EGs contributing in proportion of their actual power capacity for each phase *m*.

6.2.1. The concept of unbalanced currents compensation

Let us consider Fig. 6.4 to explain the concept of the distributed compensation of the unbalance currents with imbalance EGs contributions among the phases. We first explain the unbalanced active currents compensation, which is subsequently extended to unbalanced reactive compensation.

Assuming the area of each solid line circle to represent the *equivalent phase conductance* (G_m), refer to Section 2.1, which can also correspond to the amount of active power per phase *m* absorbed within the microgrid (P_{Lm}). In Fig. 6.4(a), solid line circles have different areas to indicate an unbalanced system ($G_a \neq G_b \neq G_c$) [**68**]. Then, solid areas split into two parts: the circles surrounded by dotted line, with equal areas for all the phases, representing the *equivalent balanced conductance* (G^b), and the dark grey areas, that represent the difference between the *equivalent phase conductance* and the *equivalent balanced conductance*, per phase [G_m - G^b, as per (2.7)]. The sum of the areas enclosed by dotted lines represents the total active power in the microgrid [$P_{Ltot} = P$, as per (2.1)].

According to the CPT [**68**], a balanced system must consist in only *equivalent balanced conductance* (G^b), which means only dotted line circles. Then, to compensate the unbalance and attaining a balanced system ($G_m = G^b$), it is needed to minimize the dark grey areas of Fig. 6.4(a). Thus, one can note that the dark grey areas are different among the phases, resulting in an imbalance contribution of the EGs

(a)   **(b)**
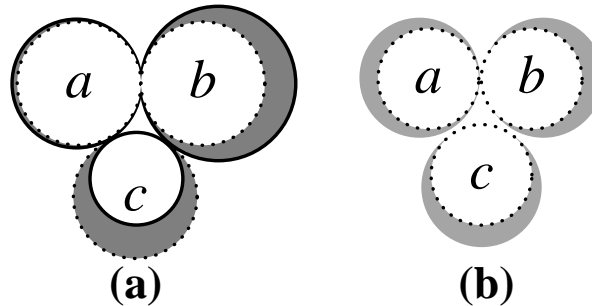
Fig. 6.4: Representation of unbalance compensation: equivalent phase parameter (solid line circles); equivalent balanced parameter (dotted line circles); difference between phase and balanced parameters (dark grey areas) and uniform power generation (light grey areas).

among the phases. Furthermore, the balance is always ensured if the EGs capability allows a uniform power generation profile to the whole microgrid, as represented by the light grey areas in Fig. 6.4(b). Of course, under limited power capacity only a partial balancing of the m-th phase system can be achieved by the EGs, leaving the remained part to the UI.

The same concept is adopted to unbalanced reactive currents compensation handling the *equivalent phase reactivity* (B_m) and *equivalent balanced reactivity* (B^b). Note that the unbalanced active currents compensation is enhanced by EGs equipped with energy storage devices, which gives them the flexibility of delivering or storing active power. However, it is worth remarking the effectiveness of the unbalanced reactive currents compensation that does not rely on the storage device, since it handles only reactive power. Moreover, the unbalance compensation is only related to conservative power terms, i.e., *active power* and *reactive energy*, and it can be applied to any voltage condition, even under distorted and asymmetrical voltages.

6.3.   Application example

As an application example of the proposed control strategy, the circuit of Fig. 6.2 is considered, representing a real three-phase four-wire metropolitan power distribution system with aerial wiring currently installed in Brazil. The system was developed in PSIM environment, in order to evaluate the proposed control approach in various operating conditions. The DERs were represented as ideal current sources driven by the power commands, thus neglecting the (irrelevant) influence of the fast current control loops in the analysis of the proposed control technique.

6.3.1.   Comparison between phase-dependent and phase-independent control strategies

In this section two different control strategies to calculate EGs power contributions are considered and compared. Using the first, called *phase-independent strategy*, EGs contribute to provide the total power required from the microgrid in proportion to their local power availability—measured according to the power-based control principles, detailed in chapter 4—and, notably, in an *independent* way with respect to the particular phase at which EGs are connected. Using the second strategy, called *phase-dependent strategy*, the EGs connected to a particular phase contribute to the power needs of the same phase in proportion to their power availability (i.e., EG contributions are proportional to their power availability only if considered *per phase*). In this latter case, the power needs of each phase is calculated as described in Section 6.2, in order to attain a balanced system to be seen at PCC. This corresponds to perform an independent power sharing in each phase.

In order to highlight the effects of the both compensation strategies, the sequence of operating conditions represented in Fig. 6.5 is considered. In particular, interval #1 and #2 pertain to the operation of the system with EGs disabled, while intervals #3 and #4 pertain to the operation of the system with the EGs driven by the power-based control according to, respectively, the phase-independent and the phase-dependent strategies.

Considering Fig. 6.5, before 0.7 s, 100 % (interval #1) and 80 % (interval #2) of the nominal microgrid load is connected, with the EGs inactive and the loads fed by the UI during *islanded operation*. Observe that, in spite of the distorted and unbalanced loads, the UI acts as grid-forming device, and keeps nearly sinusoidal and symmetrical voltages at PCC, with nearly 2 % of THD. The load characteristics are quantitatively reported in Table 6.4 by means of CPT's power terms, as described in Section 2.1, while the voltage characteristics are reported in Table 6.5.

After 0.7 s, the results obtained with the *phase-independent* (#3) and the *phase-dependent* (#4) strategies in islanded operation are shown. From Fig. 6.5, Table 6.2 and Table 6.4, we notice that the *phase-independent strategy* drives all EGs to a proportional power contribution with respect to the complete microgrid. However, it fails to compensate the unbalance power (N_{PCC} = 7.8 kVA), which, instead, gets even worse due to the non-uniform active power generation by the EGs in the various phases. This imbalance can also be observed in Table 6.5, by means of the *voltage discrepancy factor* (i.e., ratio between highest and lowest voltage values – ΔV). In addition, from Table 6.4, we notice that the system loss decreases ($\approx$ 48 % of decrease) because the power generation becomes closer to the load [55]. On the other hand, the *phase-dependent strategy* closely compensates the unbalance power (N_{PCC} = 0.5 kVA) by adjusting individual load power sharing among the phases, while maintaining a proportional power contribution among EGs within the same phase. Besides, the amount of delivered active power from EGs is slightly higher (P_{Gtot} = 13.4 kW) than the previous case (P_{Gtot} = 13.1 kW), because the overall microgrid voltage profile increases (see Table 6.5) at the loads terminals, since they are modeled as *constant impedances*.
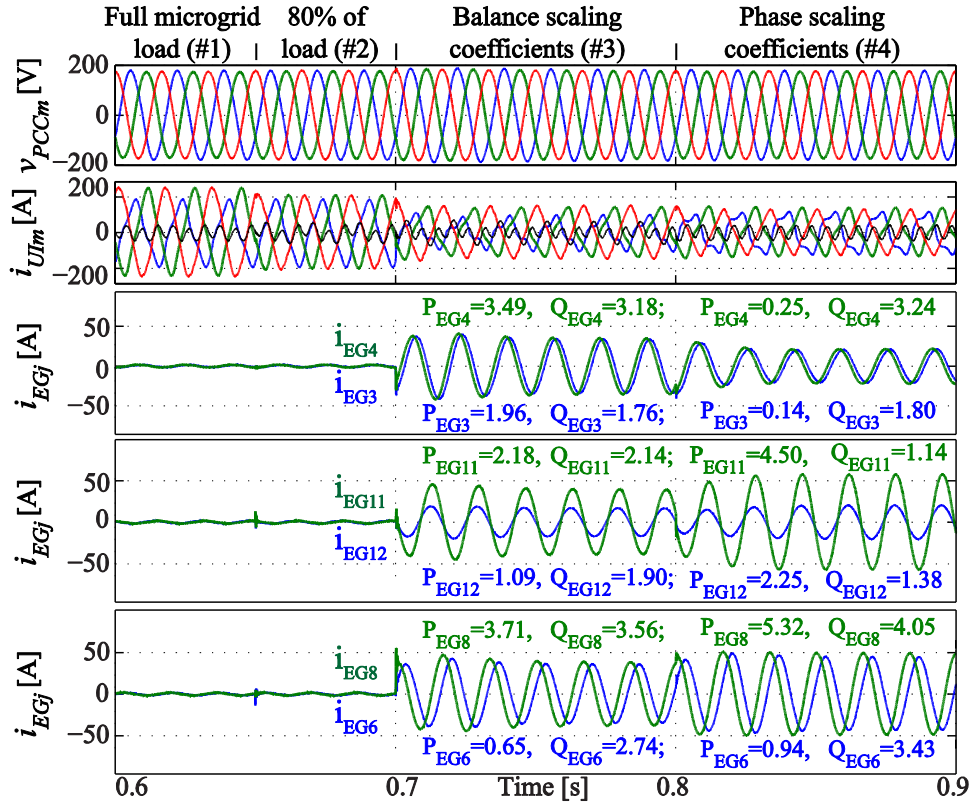
Fig. 6.5: From top to bottom: PCC voltages, UI currents, and EGs currents (per phase).

From Table 6.4, we note that the distribution loss is the same in both strategies. It corresponds to a quasi-optimum system operation, since reactive and unbalance currents nearly vanish, and the active power properly shares among EGs. The UI supplies only the necessary active power, $P_{UIa} = P_{UIb} = P_{UIc} = 10.5$ kW, and harmonic currents ($D_{PCC} = 6.3$ kVA), which usually involves relatively low power.

Analyzing Table 6.5, we notice that the power-based control enhances the power quality at the PCC of the microgrid more than the power quality within the microgrid, accordingly, the control has improved the PCC discrepancy factor, ΔV_{N1} [%], more than the discrepancy factor over the microgrid, ΔV_{MG}. Still, it does not impair the overall microgrid power quality.

Table 6.4: CPT's power terms of PCC and scaling coefficients for Fig. 6.5.

Parameters	(#1)	(#2)	(#3)	(#4)
A_{PCC} [kVA]	56.5	46.9	33.1	32.2
P_{PCC} [kW]	50.6	43.1	31.5	31.5
Q_{PCC} [kVar]	20.9	16.5	1.1	1.2
N_{PCC} [kVA]	12.2	5.7	7.8	0.5
D_{PCC} [kVA]	6.5	6.2	6.2	6.3
α_{Pa}	---	---	1.438	1.031
α_{Pb}	---	---	1.438	1.902
α_{Pc}	---	---	1.438	1.627
α_{Qa}	---	---	0.396	0.362
α_{Qb}	---	---	0.396	0.298
α_{Qc}	---	---	0.396	0.498
P_{EGtot} [kW]	---	---	13.1	13.4
Loss [kW]	2.49	1.76	0.92	0.92

Table 6.5: RMS value of the PCC and microgrid voltages for Fig. 6.5.

Voltages [V]	(#1)	(#2)	(#3)	(#4)
V_{aN1}	124.5	124.9	126.8	125.3
V_{bN1}	121.9	125.3	124.5	125.6
V_{cN1}	122.6	125.3	125.5	125.5
ΔV_{N1} [%]	2.1	0.3	1.8	0.2
V_{EGN3}	118.9	119.5	125.0	121.7
V_{EGN4}	119.9	120.5	125.0	122.2
V_{EGN6}	115.5	119.8	122.7	123.5
V_{EGN8}	118.1	122.2	123.9	124.3
V_{EGN11}	116.2	120.4	121.9	123.1
V_{EGN10}	114.9	119.7	121.8	123.6
ΔV_{MG} [%]	4.2	2.2	2.6	2.1

6.3.2. Power flow control among different phases

In order to evaluate the coordinated control strategy of power sharing and power flow exchange among the phases, the microgrid is then connected to the mains with zero current exchange at the PCC (P^*_{Gm}, $Q^*_{Gm} = 0$), similar to the islanded mode of case (#4) in Fig. 6.5. The result is shown in Fig. 6.6.

Supposing the condition that phase a drains active power (e.g., to charge its energy storage devices) the MC can adjust the power sharing among the phases and control the power flow from phases b or c to phase a. To this end, the references P^*_{PCCm} of (6.5) are set to $P_{PCCa} = P_{PCCb} = 11$ kW and $P_{PCCc} = 9.5$ kW, corresponding to the phase power supplied by the UI. The phase scaling coefficients assume the following values in steady state $(\alpha_{Pa}, \alpha_{Pb}, \alpha_{Pc}) = (0.841, 1.901, 1.865)$ and $(\alpha_{Qa}, \alpha_{Qb}, \alpha_{Qc}) = (0.293, 0.444, 0.538)$, which corresponds to $(P_{Gatot}, P_{Gbtot}, P_{Gctot}) = (-2.00, 6.75, 8.65)$ kW and $P_{Gtot} = 13.4$ kW. It shows that the EGs connected to phase c increase their power generation, while the EGs of phase a store energy. In addition, despite of the fact that the UI provides phase unbalance power, the grid currents remain balanced, notably, the power flow through PCC is practically null, see i_{Gm} on top of Fig. 6.6. We remark that the UI provides the same amount of power, as previously discussed.
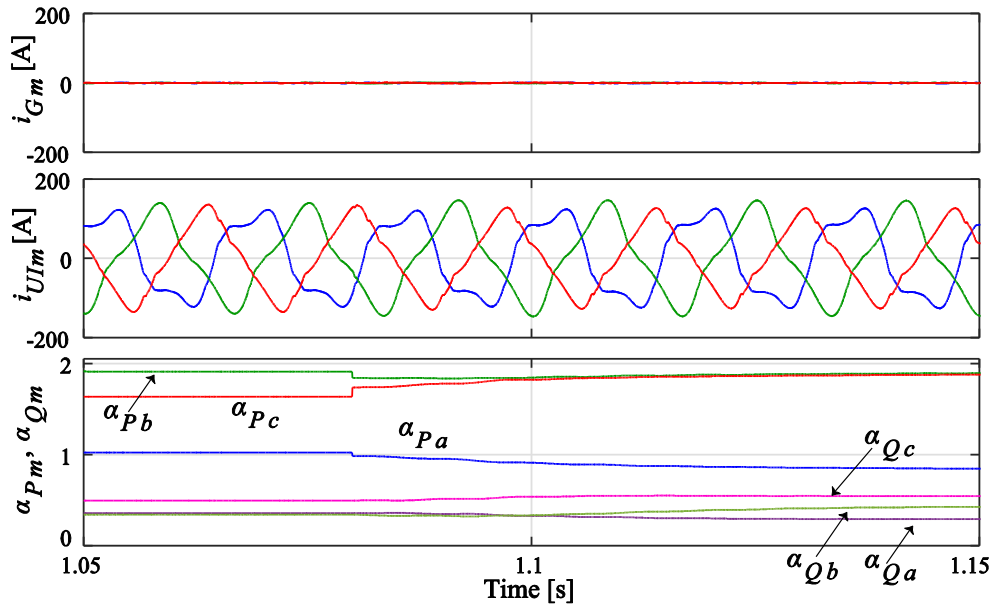
Fig. 6.6: From top to bottom: grid currents, UI currents, and phase scaling coefficients (per phase).

6.3.3. Different microgrid operating modes under sinusoidal and symmetrical voltages

For the sake of showing the effectiveness of controlling and compensating the reactive and unbalance current terms, and highlighting the role of the UI, under deteriorated grid voltages (see Table 6.1), a simulation comprising different operating modes and disturbances was performed. The results are reported in Fig. 6.7 and Fig. 6.8.

Instant $t0$ corresponds to the last instant of the previously described Fig. 6.5. At $t1$ the mains are restored. Between $t1$ and $t2$, the UI synchronizes with the mains [94] and prepares the transition of the microgrid to the grid-connected operation, which is established in $t2$. After the connection instant, the total grid current reference is gradually changed from zero to its final set point ($P^*_{PCC} = 8$ kW). The

connection procedure occurs without any critical transient, and completes at instant *t3*. Then, the microgrid keeps the steady state until *t4*. In this situation, the UI currents (i_{UIm}) contain only active and harmonic terms, since all reactive and unbalance current terms are compensated by the EGs. At *t4*, the nominal microgrid load is switched on, and the steady state is restored within three cycles. In this condition, some coefficients (α_{Pb} and α_{Pc}) reach their maximum value, because the microgrid demand exceeds the per-phase power capacity, which is highlighted in Fig. 6.8. As discussed in Section 6.2, the full unbalance power compensation, clearly, cannot be accomplished by the sole contribution of the EGs

Fig. 6.7: Obtained results in case of sinusoidal and symmetrical voltages. From top to bottom: grid and PCC voltages, UI and grid currents.
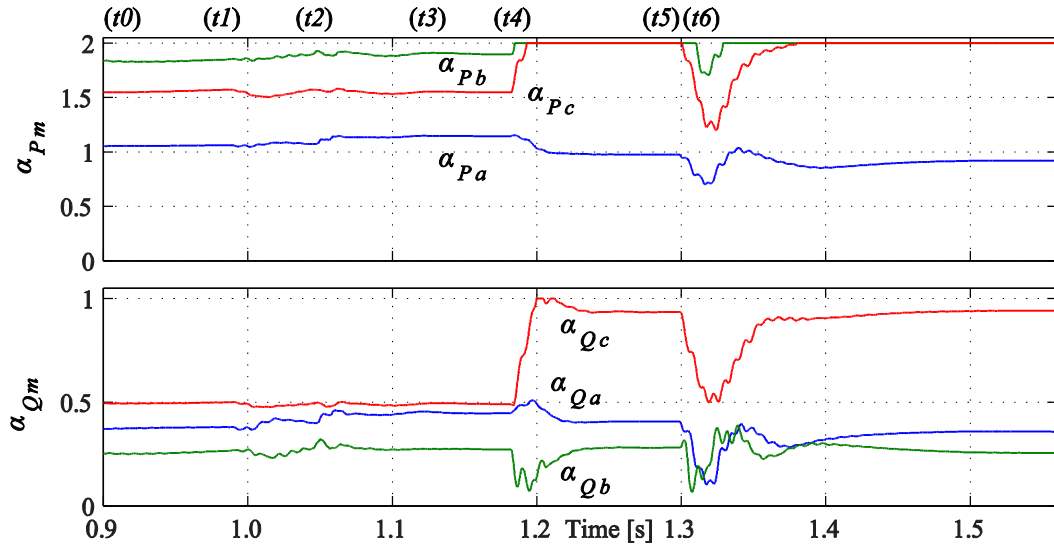
Fig. 6.8: Phase scaling coefficients related to Fig. 6.7.

if their actual power is not sufficient to fulfill the needs of the loads; in this case the UI, behaving as an active filter, provides for the remaining unbalance currents (see i_{UIm} in Fig. 6.7). Thus, even so, the grid currents (i_{Gm}) are balanced and nearly distortion-free with $THD_{iG} \approx 1.5\%$. Of course, after some time, some loads, generators, and/or P^*_{PCC} might be readjusted.

Finally, at instant *t5*, the mains is suddenly disconnected, causing a non-intentional transition to the islanded operation. The MC processes and eventually detects the islanded condition during the interval between instants *t5* and *t6*, successively; UI becomes the grid-forming voltage source for the islanded microgrid. Across the transition to the non-intentional island we notice a small transient consisting in a voltage sag occurring during the islanding detection interval, that is promptly cleared as soon as the islanded operation is detected (see v_{PCCm}, in Fig. 6.7). Despite of that, the system reaction is prompt and smooth. After *t6*, the system operates again in stand-alone, with power-based control enabled. This means that UI provides only a portion of the load currents, while the remaining part is requested to distributed EGs. We highlight that even under islanded operation at full load, the reactive (i^b_r) and unbalanced reactive (i^u_r) current terms are fully compensated by the EGs, since the α_{Qm} coefficients are not saturated, as it can be noticed by inspecting the last instants of the simulation in Fig. 6.8.

6.3.4. Different microgrid operating modes under distorted and asymmetrical voltages

In order to evaluate the strategies with respect to different voltage conditions, Fig. 6.9 considers the same scenario of Fig. 6.7 under distorted and asymmetrical grid voltage (as in Table 6.1). Similar
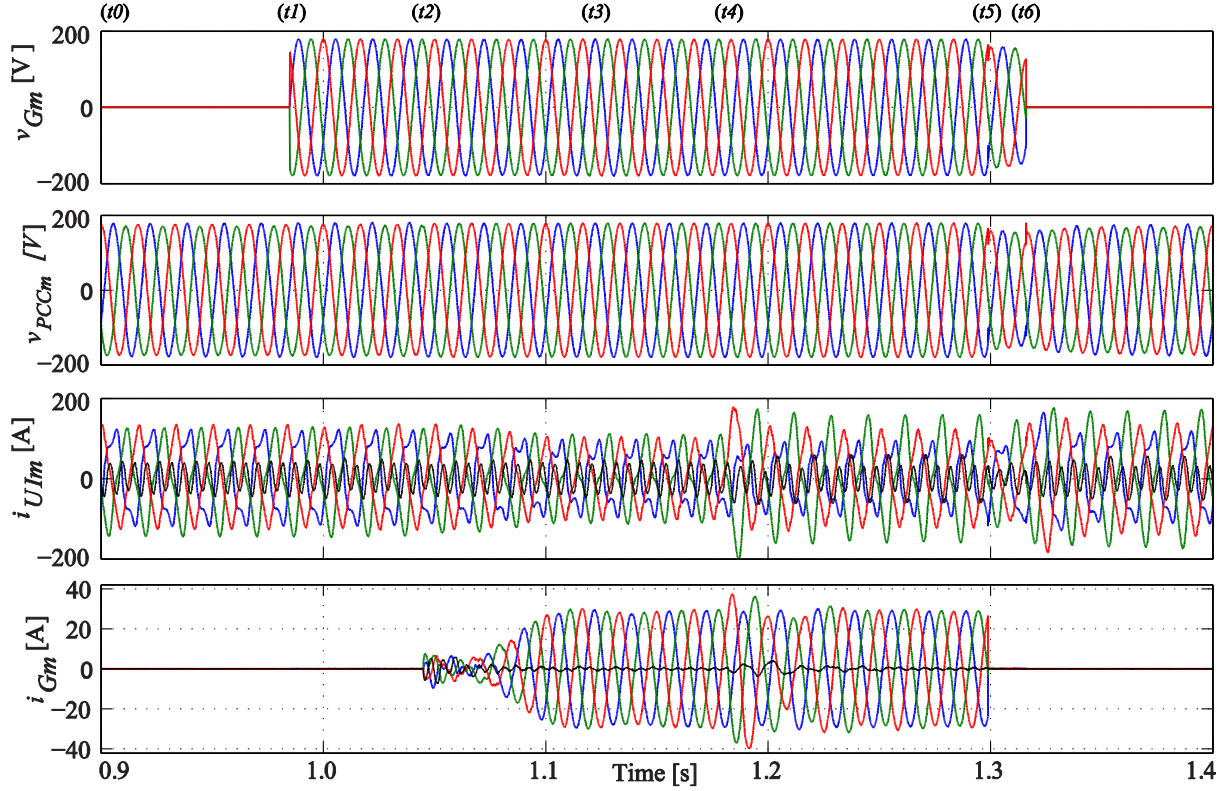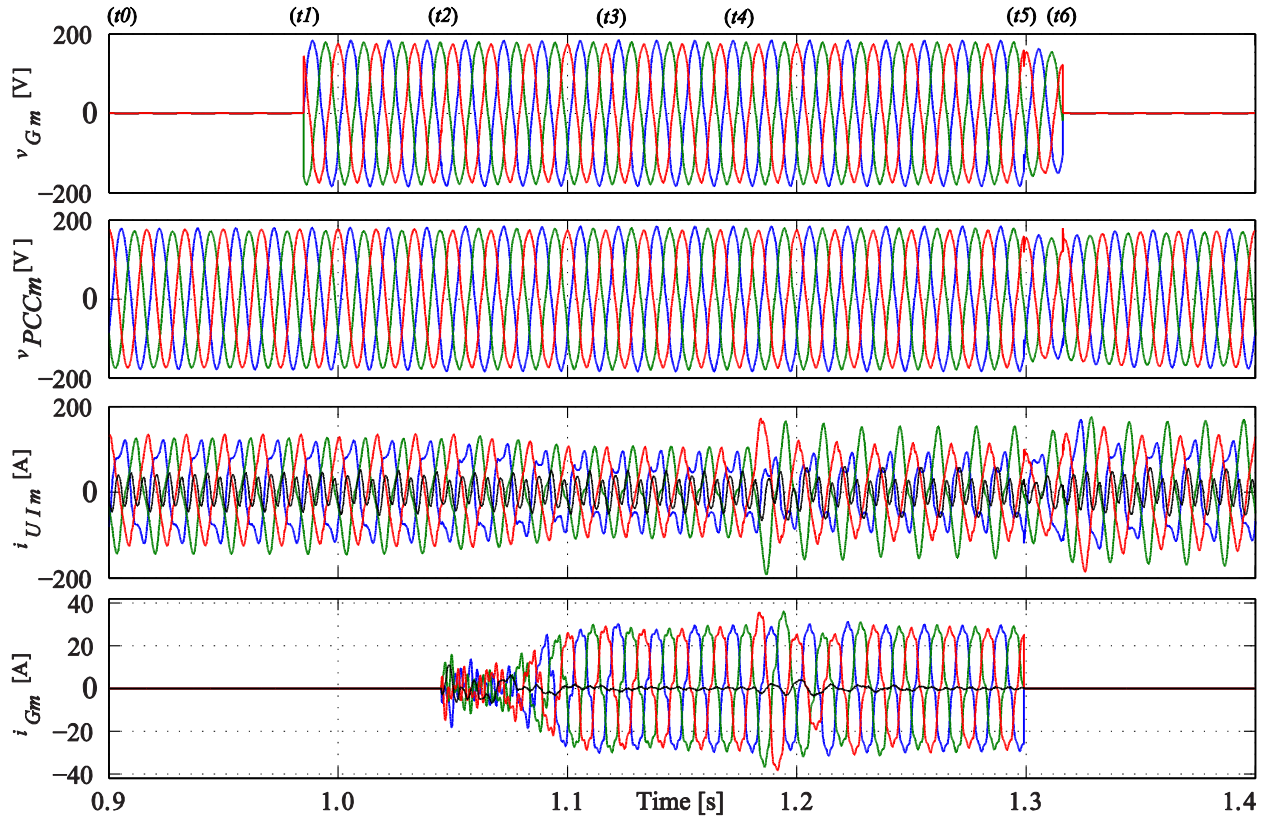

Fig. 6.9: Obtained results in case of distorted and asymmetrical voltages. From top to bottom: grid and PCC voltages, UI and grid currents.

considerations made for Fig. 6.7 can be done here. During islanded operation the PCC voltages are maintained practically sinusoidal by the UI. Also the connecting procedure occurs smoothly and without resonances – potentially triggered by the distorted grid voltages – thus indicating an adequate control of the UI, as in Section 3.3.2. In grid-connected mode, grid current waveforms (i_{Gm}) become proportional to phase voltages (v_{Gm}), resulting in a unitary power factor at PCC, which complying with the definition of balanced system with $G_m = G^b$ and $B_m = B^b$ to all frequencies. Finally, we remark how the behavior observed in this last case (Section 6.4) related to the non-intentional islanding with distorted and asymmetrical voltages is similar to what observed during the transition with sinusoidal and symmetrical voltages (Section 6.3.3).

6.4. Conclusions

The cooperative operation in this approach is meant as a coordinated operation of various individual units engaged in achieving a common goal. So, in this context, this chapter proposed a novel control strategy to coordinate the power flow among the phases of a three-phase LV microgrid with arbitrarily connected single-phase inverters.

The strategy works properly even under weak-grid conditions (distorted and asymmetrical voltages), and ensures optimum power sharing among phases so as to compensate reactive and unbalance current terms. It enhances the microgrid flexibility and reliability, and achieves unity power factor at PCC. Moreover, it keeps small the voltage deviations at grid nodes and minimizes the distribution loss.

The proposed control is applicable to any kind of microgrid, irrespective of topology, inverter connection codes, and line impedances. Moreover, even the harmonic and homopolar currents can be eliminated by a proper control of line-to-neutral connected inverters and, in grid-connected operation, of the UI.

As the coordinated control makes use of conservative power terms, it keeps good performance and stability even under deteriorated grid voltages. In terms of implementation, the proposed control requires a reliable, but non-time-critical, communication link between the master controller and the distributed slave units.

Chapter 7

7. General Conclusions

The thesis described a fully-dispatchable microgrid structure, based on a master-slave control architecture, where the distributed generation units are coordinated by means of the recently developed power-based control. The main advantages of the proposed architecture are the scalability and capability of distributed operation of slave units without synchronization among the microgrid nodes or knowledge of line impedances. Moreover, the microgrid manages promptly the interaction with the mains by means of an UI, which is a three-phase grid-interactive inverter equipped with ES. This allows a number of advantages, including compensation of load unbalance, reduction of harmonic injection, fast reaction to load and line transients, and smooth transition between operating modes. On the other hand, in order to provide demand response, reactive power control, and full utilization of distributed energy resources, the microgrid employs a communication link among distributed units, characterized by a non-time critical link, so that the proper operation of the microgrid is not jeopardized under communication failures or delays.

In Chapter 2, the local controller of the slave unit (i.e., EG) was described for arbitrary connection of inverters. It addressed the main *basic control functions*, *specific functions* and *ancillary services*, such as active and reactive current references generation, overvoltage control stability and current compensation. It also proposed a formulation, based on a linear problem, to optimize the compensation of reactive power, harmonic distortion and load unbalance by means of DERs with multifunctional capabilities. This latter proposal improves local power quality exploiting the surplus

power capacity of DERs.

In Chapter 3, firstly, three different current control solutions for an UI are compared. The three controllers, namely a PI, a predictive and a fully digital hysteresis controller exploit oversampling and a FPGA implementation to maximize their reference tracking performance. The different small-signal characteristics are analyzed and experimentally evaluated. Based on this assessment, the fully digital hysteresis controller is chosen to sustain the UI voltage control loop. Altogether, the controller guarantees excellent rejection of load perturbations and smooth transitions between grid-connected and islanded operation modes. Secondly, the modeling, control and design of the UI were described, as well as the proposed passive islanding detection. Finally, they were evaluated by experimental results.

Chapter 4 presented the newly developed power-based algorithm, used to perform the proportional power sharing. The algorithm was fully described, while its robustness was evaluated by Fig. 4.1 and Fig. 4.2. The simulation application example has showed the advantages of this algorithm, its effect on the system loss and enhancement on the voltage profile. The UI converter and the power-based control were deeply analyzed in Chapter 5, by means of extensive experimental results. Besides, the developed laboratory-scale microgrid prototype was described.

Chapter 6 adapted the proposed power-based control to be applied to a three-phase system, performing individually power sharing per each phase. It also contributes to mitigate unbalance current circulation. The per phase power-based control was evaluated under a real metropolitan microgrid scenario, and simulation results have indicated excellent performances in terms of power quality in the steady state, prompt response to load and line transients, and smooth transitions from grid-connected to islanded operating modes, and vice versa. The control strategy shows good performance applied to both sinusoidal/symmetrical and distorted/asymmetrical voltage conditions, since only conservative power terms are exchanged between MC and distributed units.

Chapter 6 still proposed a simple and effective distributed control strategy applied to arbitrarily connected inverters (i.e., line-to-neutral and line-to-line) for the sake of regulate the power flow among different phases of the microgrid. These last issues have not been investigated in the literature.

Finally, the proposed master-slave architecture presents some further advantages. Integrated into traditional low voltage grids, it may potentially support, along the paradigm of provisional microgrids [137], the transition to future smart microgrids, with a limited impact on the existing infrastructure, while enabling most of the functionalities that are expected [5], [44]. Similarly, the proposed structure, and the power-based control, may facilitate the transition towards the advanced scenarios contemplating the use of solid state transformers to couple low voltage grids to the medium-voltage system [138], since the required power electronics infrastructure would already be available and the control implementation would not need additional investments. For both reasons, it can represent an intermediate step towards the ultimate realization of real smart microgrids.

7.1. Thesis contribution

This section presents the main contributions of this thesis. Note that the preface also highlight the author's contributions and avoid the readers have mislead the contributions among the institutions and research groups related to this project.

- Implement and experimentally validate the microgrid structure based on a master-slave architecture based on the PB control and the UI converter (Chapter 5);

- Formulate a linear problem using standard algorithm to optimize the compensation of reactive power, harmonic and load unbalance by means of DERs during limited capability (Section 2.4);

- Study the inverters connected arbitrarily. We underline that it has not been investigate in the literature (Chapter 6);

- Propose the unbalance current compensation, by means of distributed single phase inverters. We highlight that it has been hardly ever investigate in the literature (Chapter 6);

- Propose the power flow control among different phases of a three-phase microgrid. We highlight that it has been rarely investigate in the literature (Chapter 6).

7.2. Future works

As typical in master-slave grid architectures, the proposed microgrid may pose some challenges in systems requiring high reliability during islanded operation. Hence, the MC, as a data processing unit, does not bring significant reliability issues. In any case, it can be easily endowed with redundancy, deploying it on more than one computing platform. The UI, instead, being the only voltage-forming converter for the microgrid during islanded operation, should integrate suitable hardware redundancy to ensure continuity of operation in case of fault. Besides, some microgrids may have more than one PCC and, accordingly, more than one UI installed. Then, the suitable coordination and hierarchical control of multi PCC and UI microgrid may lead to a more reliable scenario, where a failure of one UI should be replaced by a second one already installed. However, UI redundancy is out of the scope of this work and it is put out as future work.

7.2.1. Topics for future works

- Implementation of a laboratory-scale three-phase microgrid. So, the three-phase UI and the unbalance current compensation could be validated;

- Development of an adaptive controller for the grid current control loop of the UI for enhance the system robustness against parameter variations;

- Study the power-based control and UI applied to a ring electrical network;

- An accurate design for the passive and semiconductor elements of the UI, as well as for its DC side. This latter was briefly discussed in Section 3.4.

- Development of distributed strategy to cooperatively compensate the harmonic currents by means of DERs spread over the microgrid;
- Study and development of better communication networks applied to microgrid applications;
- Discussion about recommendations and standards applied to utility-grid interactive converters.

7.3. Related publications

1. F. P. Marafão, D. I. Brandão, A. Costabeber, and H. K. M. Paredes, "Multi-task control strategy for grid-tied inverters based on conservative power theory," *IET Renewable Power Generation*, vol. 9, no. 2, pp. 154-165, 2015.

2. D. I. Brandão, F. P. Marafão, M. G. Simões, and J. A. Pomilio, "Considerations on the modeling and control scheme of grid connected inverter with voltage support capability," *in Brazilian Power Electronics Conference (COBEP)*, Gramado, 2013.

3. T. Caldognetto, S. Buso, P. Tenti, and D. I. Brandao, "Power-based control of low-voltage microgrids," *IEEE Journal of Emerging and Selected Topics in Power Electronics*, vol. PP, no. 99, p. 1, 2015.

4. S. Buso, T. Caldognetto, and D. I. Brandao, "Oversampled deadbeat current controller for voltage source converters," *in Applied Power Electronics Conference and Exposition (APEC)*, 2015, pp. 1493-1500.

5. D. I. Brandao, H. Guillardi Júnior, J. A. Pomilio, and H. K. M. Paredes, "Optimized compensation based on linear programming applied to distributed electronic power processors," *in IEEE International Symposium on Industrial Electronics (ISIE)*, Búzios, Brazil, 2015.

6. T. Caldognetto, S. Buso, P. Tenti, and D. I. Brandao, "Experimental verification of an active microgrid with distributed power-based control," *in International Conference and Exposition on Electrical and Power Engineering (EPE)*, 2015, pp. 1-1.

7. D. Brandao, H. K. P. Paredes, A. Costabeber, and F. P. Marafao, "Flexible active compensation based on load conformity factors applied to non-sinusoidal and asymmetrical voltage conditions," *IET Power Electronics*, vol. PP, no. PP, pp. 1-1, 2015.

8. T. Caldognetto, S. Buso, P. Tenti, and D. I. Brandao, "A dynamic overvoltage limiting technique for low-voltage microgrids," *in IEEE Energy Conversion Congress and Exposition (ECCE)*, Montreal, Canada, 2015, pp. 1-1.

9. S. Buso, T. Caldognetto, and D. I. Brandao, "Comparison of oversampled current controllers for micro-grid utility interface converters," in *IEEE Energy Conversion Congress and Exposition (ECCE)*, Montreal, Canada, 2015, pp. 1-1.

10. T. Caldognetto, P. Tenti, P. Mattavelli, S. Buso, D. I. Brandao, "Cooperative compensation of unwanted current terms in low-voltage micrigrids by distributed power-based control," *in Brazilian Power Electronics Conference (COBEP)*, Fortaleza, 2015.

11. S. Buso, T. Caldognetto, and D. I. Brandao, "Dead-beat current controller for voltage source converter with improved large-signal response," *IEEE Transaction on Industry Applications*, vol. PP, no. 99, p. 1, 2015.

References

[1] U.S. Energy Information Administration, "International Energy Outlook 2013," DOE/EIA-0484, 2013.

[2] Empresa de Pesquisa Energética (EPE), "Projeção da demanda de energia elétrica para os próximos 10 anos (2015-2024) ," 03/15, 2015.

[3] Agência Nacional de Energia Elétrica (ANEEL), "Estabelece as condições gerais para o acesso de microgeração e minigeração distribuída aos sistemas de distribuição de energia elétrica, o sistema de compensação de energia elétrica e da outras providências," Resolução normativa Nº 482, 2012.

[4] B. M. Eid, N. A. Rahim, J. Selvaraj, and A. H. El Khateb, "Control methods and objectives for electronically coupled distributed energy resources in microgrids: a review," *IEEE Systems Journal*, pp. 1-13, 2014.

[5] N. D. Hatziargyriou and et al., "Trends in microgrid control," *IEEE Transaction on Smart Grid*, vol. 5, no. 4, pp. 1905-1919, 2014.

[6] G. Strbac et al., "Microgrids," *IEEE Power and Energy Magazine*, vol. 13, no. 3, pp. 35-43, 2015.

[7] Energy Information Administration, "Annual Energy Outlook 2014 - with projections to 2040," Energy Information Administration (EIA), Relatório técnico, DOE/EIA-0383(2014), 2014.

[8] M. Shahidehpour, S. Pullins, and others, "The maturation of microgrids," *Electrification Magazine*, vol. 2, 2014.

[9] F. Blaabjerg, Ke Ma, and Y. Yang, "Power electronics for renewable energy system – status and trends," in *International Conference on Integrated Power Systems*, 2014, pp. 1-11.

[10] Dan T. Ton and W-T Paul Wang, "A more resilient grid," *IEEE Power and Energy Magazine*, vol. 13, no. 3, pp. 26-34, 2015.

[11] S. Kouro, J. I. Leon, D. Vinnikov, and L. G. Franquelo, "Grid-connected photovoltaic system: An overview of recent research and emerging PV converter technology," *IEEE Industrial Electronics Magazine*, vol. 9, no. 1, pp. 47-61, 2015.

[12] D. Li and Z. Q. Zhu, "A novel integrated power quality controller for microgrid," *IEEE Transactions on Industrial Electronics*, vol. 62, no. 5, pp. 2848-2858, 2015.

[13] F. Pinhabel Marafão, D. Iglesias Brandão, A. Costabeber, and H. K. Morales Paredes, "Multi-task control strategy for grid-tied inverters based on conservative power theory," *IET Renewable Power Generation*, vol. 9, no. 2, pp. 154-165, 2015.

[14] D. I. Brandão, "Multifunctional photovoltaic generation system," Universidade Estadual Paulista, Bauru, Master dissertation 2013.

[15] J. P. Bonaldo and J. A. Pomilio, "Multi-functional use of single-phase power converters," in *IEEE Conference on Innovative Smart Grid Technologies*, 2013.

[16] Y. Wang, P. Zhang, Wenyuan Li, Weidong Xian, and A. Abdollahi, "Online overvoltage prevention control of photovoltaic generators in microgrids," *IEEE Transactions on Smart Grid*, vol. 3, no. 4, pp. 2071-2078, 2012.

[17] J. M. Guerrero, M. Chandorkar, T. Lee, and P. C. Loh, "Advanced control architectures for intelligent microgrids—part I: decentralized and hierarchical control," *IEEE Transactions on Industrial Electronics*, vol. 60, no. 4, pp. 1254-1262, 2013.

[18] Jinwei He and Yun Wei Li, "An enhanced microgrid load demand sharing strategy," *IEEE Transaction on Power Electronics*, vol. 27, no. 9, pp. 3984-3995, 2012.

[19] J. H. R. Enslin and P. J. M. Heskes, "Harmonic interaction between a large number of distributed power inverters and the distribution network," in *IEEE Power Electronics Specialist Conference*,

2003, pp. 1742-1747.

[20] T. Caldognetto and P. Tenti, "Microgrids operation based on master–slave cooperative control," *IEEE Journal of Emerging and Selected Topics in Power Electronics*, vol. 2, no. 4, pp. 1081-1088, 2014.

[21] A. Chuang, M. McGranaghan, and M. Grady, "Master controller requirements specification for perfect power systems," Galvin Electricity Initiative, 2007.

[22] J. A. Peas Lopes, C. L. Moreira, and A. G. Madureira, "Defining control strategies for microgrids islanded operation," *IEEE Transactions on Power Systems*, vol. 21, no. 2, pp. 916-924, 2006.

[23] A. Bidram and A. Davoudi, "Hierarchical structure of microgrids control system," *IEEE Transaction on Smart Grid*, vol. 3, no. 4, pp. 1963-1976, 2012.

[24] J. M. Guerrero, P. C. Loh, T. Lee, and M. Chandorkar, "Advanced control architectures for intelligent microgrids—part II: power quality, energy storage, and AC/DC microgrids," *IEEE Transactions on Industrial Electronics*, vol. 60, no. 4, pp. 1263-1270, 2013.

[25] A. Costabeber, P. Tenti, T. Erseghe, S. Tomasin, and P. Mattavelli, "Distributed control of smart microgrids by dynamic grid mapping," in *IEEE Industrial Electronics Society (IECON)* , 2011, pp. 1323-1328.

[26] E. Tedeschi, P. Tenti, P. Mattavelli, and D. Trombetti, "Cooperative control of electronic power processors in micro-grids," in *Brazilian Power Electronics Conference*, vol. 14, 2009, pp. 1-8.

[27] P. Tenti, A. Costabeber, P. Mattavelli, and D. Trombetti, "Distribution loss minimization by token ring control of power electronic interfaces in residential microgrids," *IEEE Transactions on Industrial Electronics* , vol. 59, no. 10, pp. 3817-3826 , 2012.

[28] P. Tenti, A. Costabeber, D. Trombetti, and P. Mattavelli, "Plug & play operation of distributed energy resources in micro-grids," in *International Telecommunications Energy Conference (INTELEC)*, 2010, pp. 1-6.

[29] A. Costabeber, P. Tenti, and P. Mattavelli, "Surround control of distributed energy resources in micro-grids," in *IEEE International Conference on Sustainable Energy Technologies (ICSET)*, 2010, pp. 1-6.

[30] J. Lagorse, M. Simões, and A. Miraoui, "A multiagent fuzzy-logic-based energy management of hybrid systems," *IEEE Transaction on Industry Applications*, vol. 45, no. 6, pp. 2123-2129, 2009.

[31] J. M. Guerrero, J. C. Vasquez, J. Matas, L. G. de Vicuña, and M. Castilla, "Hierarchical control of droop-controlled AC and DC microgrids - a general approach toward standardization," *IEEE Transactions on Industrial Electronics*, vol. 58, no. 1, pp. 158-172, 2011.

[32] F. Luo, Y. M. Lai, K. H. Loo, C. K. Tse, and X. Ruan, "A generalized droop-control scheme for decentralized control of inverter-interfaced microgrids," in *IEEE International Symposium on Circuits and Systems*, 2013, pp. 1320-1323.

[33] I.U. Nutkani, Poh Chiang Loh, Peng Wang, and F. Blaabjerg, "Cost-prioritized droop schemes for autonomous AC microgrids," *IEEE Transactions on Power Electronics*, vol. 30, no. 2, pp. 1109-1119, 2015.

[34] R. Olfati-Sabe, J. A. Fax, and R. M. Murray, "Consensus and cooperation in networked multi-agent systems," *Proceedings of the IEEE*, vol. 95, no. 1, pp. 215-233, 2007.

[35] T. Caldognetto, S. Buso, P. Tenti, and D. I. Brandao, "Power-based control of low-voltage microgrids," *IEEE Journal of Emerging and Selected Topics in Power Electronics*, vol. PP, no. 99, p. 1, 2015.

[36] P. Tenti, T. Caldognetto, S. Buso, and A. Costabeber, "Control of utility interfaces in low voltage microgrids," in *IEEE International Symposium on Power Electronics for Distributed Generation Systems*, 2014, pp. 1-8.

[37] Y. Sunjae, O. Hyeongmin, and C. Sewan, "Controller design and implementation of indirect current control based utility-interactive inverter system," *IEEE Transactions on Power Electronics*, vol. 28, no. 1, pp. 26-30, 2013.

[38] "IEEE standard for interconnecting distributed resources with electric power systems," IEEE Std

1547, 2003.

[39] C. Gavriluta, I. Candela, J. Rocabert, I. Etxeberria-Otadui, and P. Rodriguez, "Storage system requirements for grid supporting PV-power plants," in *IEEE Energy Conversion Congress and Exposition*, 2014, pp. 5323-5330.

[40] "IEEE Approved Draft Guide for the Interoperability of Energy Storage Systems Integrated with the Electric Power Infrastructure," IEEE P2030.2/D9.0, December 2014, pp. 1-136, 2015.

[41] T. L. Vandoorn, J. D. M. De Kooning, B. Meersman, and L. Vandevelde, "Review of primary control strategies for islanded microgrids with power-electronic interfaces," *Renewable and Sustainable Energy Reviews*, vol. 19, pp. 613-628, 2013.

[42] T. B. Lazzarin, G. A. T. Bauer, and I. Barbi, "A control strategy for parallel operation of single-phase voltage source inverters: analysis, design and experimental results," *IEEE Transactions on Industrial Electronics*, vol. 60, no. 6, pp. 2194-2204, 2013.

[43] T. Caldognetto, S. Buso, P. Tenti, and D. I. Brandao, "A dynamic overvoltage limiting technique for low-voltage microgrids," in *IEEE Energy Conversion Congress and Exposition*, Montreal, Canada, 2015, pp. 1-1.

[44] T. Strasser et al., "A review of architectures and concepts for intelligence in future electric energy systems," *IEEE Transactions on Industrial Electronics*, vol. 62, no. 4, pp. 2424-2438, 2015.

[45] R. Carnieletto, D. I. Brandao, S. Suryanarayanan, M. G. Simões, and F. A. Farret, "Smart grid initiative: a multifunctional single-phase voltage source inverter," *IEEE Transactions on Industry Applications Magazine*, vol. 17, no. 5, pp. 27-35, 2011.

[46] J. M. Guerrero, J. Matas, L. G. de Vicuña, M. Castilla, and J. Miret, "Wireless-control strategy for parallel operation of distributed-generation inverters," *IEEE Transactions on Industrial Electronics*, vol. 53, no. 5, pp. 1461-1470, 2006.

[47] M. C. Chandorkar, D. M. Divan, and R. Adapa, "Control of parallel connected inverters in standalone AC supply systems," *IEEE Transactions on Industry Applications*, vol. 29, no. 1, pp. 136-143, 1993.

[48] J. M. Guerrero, Lijun Hang, and J. Uceda, "Control of distributed uninterruptible power supply systems," *IEEE Transactions on Industrial Electronics*, vol. 55, no. 8, pp. 2845-2859, 2008.

[49] Hua Han, Yao Liu, Yao Sun, Mei Su, and J. M. Guerrero, "An improved droop control strategy for reactive power sharing in islanded microgrid," *IEEE Transactions on Power Electronics*, vol. 30, no. 6, pp. 3133-3141, 2015.

[50] A. Tuladhar, Hua Jin, T. Unger, and K. Mauch, "Control of parallel inverters in distributed AC power systems with consideration of line impedance effect," *IEEE Transactions on Industry Applications*, vol. 36, no. 1, pp. 131-138, 2000.

[51] J. M. Guerrero, J. Matas, Luis Garcia de Vicuna, M. Castilla, and J. Miret, "Decentralized control for parallel operation of distributed generation inverters using resistive output impedance," *IEEE Transactions on Industrial Electronics*, vol. 54, no. 2, pp. 994-1004, 2007.

[52] B. B. Johnson, S. V. Dhople, A. O. Hamadeh, and P. T. Krein, "Synchronization of parallel single-phase inverters with virtual oscillator control," *IEEE Transactions on Power Electronics*, vol. 29, no. 11, pp. 6124-6138, 2014.

[53] V. Nasirian, Q. Shafiee, J. Guerrero, F. Lewis, and A. Davoudi, "Droop-free distributed control for AC microgrids," *IEEE Transactions on Power Electronics*, vol. PP, no. 99, p. 1, 2015.

[54] V. C. Gungor et al., "Smart grid technologies: communication technologies and standards," *IEEE Transactions on Industrial Informatics*, vol. 7, no. 4, pp. 529-539, 2011.

[55] T. Caldognetto, P. Tenti, A. Costabeber, and P. Mattavelli, "Improving microgrid performance by cooperative control of distributed energy sources," *IEEE Transactions on Industry Applications*, vol. 50, no. 6, pp. 3921-3930, 2014.

[56] J. Rocabert, A. Luna, F. Blaabjerg, and P. Rodriguez, "Control of power converters in AC microgrids," *IEEE Transactions on Power Electronics*, vol. 27, no. 11, pp. 4734-, 2012.

[57] Wei Du, Q. Jiang, M. J. Erickson, and R. H. Lasseter, "Voltage-source control of PV inverter in a

CERTS microgrid," *IEEE Transaction on Power Delivery*, vol. 29, no. 4, pp. 1726-1734, 2014.

[58] A. Timbus, M. Liserre, R. Teodorescu, P. Rodriguez, and F. Blaabjerg, "Evaluation of current controllers for distributed power generation systems," *IEEE Transactions on Power Electronics*, vol. 24, no. 3, pp. 654-664, 2009.

[59] Jinwei He, Yun Wei Li, and F. Blaabjerg, "Flexible microgrid power quality enhancement using adaptive hybrid voltage and current controller," *IEEE Transactions on Industrial Electronics*, vol. 61, no. 6, pp. 2784-2794, 2014.

[60] "Electromagnetic compatibility (EMC) - Part 3-2: Limits - Limits for harmonic current emissions (equipment input current ≤ 16 A per phase)," IEC 61000-3-2:2014, 2014.

[61] "IEEE recommended practice and requirements for harmonic control in electric power systems," IEEE Std 519-2014, (Revision of IEEE Std 519-1992), 2014.

[62] "Reference technical rules for the connection of active and passive users to the LV electrical utilities," CEI 0-21, 2014.

[63] "IEEE recommended practice for utility interface of photovoltaic (PV) systems," IEEE Std. 929-2000, 2000.

[64] A. Bidram, A. Davoudi, F. L. Lewis, and J. M. Guerrero, "Distributed cooperative secondary control of microgrids using feedback linearization," *IEEE Transactions on Power Systems*, vol. 28, no. 3, pp. 3462-3470, 2013.

[65] F. P. Marafao, D. I. Brandao, A. Costabeber, and H. K. P. Paredes, "Multi-task control strategy for grid-tied inverters based on conservative power theory," *IET Renewable Power Generation*, vol. 9, no. 2, pp. 154-165, 2015.

[66] A. F. Q. Goncalves, R. F. Bastos, C. R. Aguiar, and R. Q. Machado, "Three-phase VSI supplied by renewable energy sources and controlled in voltage and power modes for grid-tie operation," in *IEEE International Symposium on Power Electronics for Distributed Generation Systems (PEDG)*, 2014, pp. 1-6.

[67] R. Destro, L. Matakas, W. Komatsu, and N. R. Nasri Ama, "Implementation aspects of adaptive window moving average filter applied to PLLs — comparative study," in *Brazilian Power Electronics Conference (COBEP)*, 2013.

[68] P. Tenti, H. K. M. Paredes, and P. Mattavelli, "Conservative Power Theory, a framework to approach control and accountability issues in smart microgrids," *IEEE Transactions on Power Electronics*, vol. 26, no. 3, pp. 664-673, 2011.

[69] H. K. M. Paredes, "Teoria de Potência Conservativa: uma nova abordagem para o controle cooperativo de condicionadores de energia e considerações sobre atribuição de responsabilidade," University of Campinas, Thesis 2011.

[70] S. Fryze, "Active, reactive and appatent power in circuits with nonsinusoidal voltage and current," *Przeglad Elektrotechniczny*, no. 7, pp. 193-203, 1931.

[71] F. P. Marafão, W. A. Souza, E. V. Liberado, L. C. P. da Silva, and H. K. M. Paredes, "Load analyser using Conservative Power Theory," *Przeglad Elektrotechniczny*, vol. 12, pp. 1-6, 2013.

[72] H. K. M. Paredes, F.P. Marafao, and L. C. P. da Silva, "A comparative analysis of FBD, PQ and CPT current decompositions — Part II: Three-phase four-wire systems," in *IEEE Bucharest PowerTech*, 2009, pp. 1-6.

[73] M. A. G. de Brito, L. Galotto, L. P. Sampaio, G. de Azevedo e Melo, and C. A. Canesin, "Evaluation of the main MPPT techniques for photovoltaic applications," *IEEE Transactions on Industrial Electronics*, vol. 60, no. 3, pp. 1156-1167, 2013.

[74] F. P. Marafão, D. I. Brandão, F. A. S. Gonçalves, and H. K. M. Paredes, "Decoupled reference generator for shunt active filters using the conservative power theory," *Journal of Control, Automation and Electrical Systems*, vol. 24, no. 4, pp. 522-534, 2013.

[75] T. E. N. Zuniga and J. A. Pomilio, "Shunt active power filter synthesizing resistive load," *IEEE Transaction on Power Electronics*, vol. 16, no. 2, pp. 273-278, 2002.

[76] D. I. Brandao, H. Guillardi Júnior, J. A. Pomilio, and H. K. M. Paredes, "Optimized compensation

based on linear programming applied to distributed electronic power processors," in *IEEE International Symposium on Industrial Electronics*, Búzios, Brazil, 2015.

[77] D. G. Luenberger and Ylnyu Ye, *Linear and nonlinear programming*, 3rd ed.: Springer, 2008.

[78] J. C. Alfonso-Gil, E. Pérez, C. Ariño, and H. Beltran, "Optimization algorithm for selective compensation in a shunt active power filter," *IEEE Transaction on Industrial Electronics*, vol. 62, no. 6, pp. 3351-3361, 2015.

[79] B. Singh and V. Verma, "Selective compensation of power-quality problems through active power filter by current decomposition," *IEEE Transaction on Power Delivery*, vol. 23, no. 2, pp. 792-799, 2008.

[80] D. I. Brandao, H. K. P. Paredes, A. Costabeber, and F. P. Marafao, "Flexible active compensation based on load conformity factors applied to non-sinusoidal and asymmetrical voltage conditions," *IET Power Electronics*, vol. PP, no. 00, pp. 1-9, 2015.

[81] Yongheng Yang, P. Enjeti, F. Blaabjerg, and Huai Wang, "Suggested grid code modifications to ensure wide-scale adoption of photovoltaic energy in distributed power generation systems," in *IEEE Industry Applications Society Annual Meeting*, 2013, pp. 1-8.

[82] Q.-C. Zhong and T. Hornik, "Cascaded current–voltage control to improve the power quality for a grid-connected inverter with a local load," *IEEE Transactions on Industrial Electronics*, vol. 60, no. 4, pp. 1344-1355, 2013.

[83] S. Weckx, C. Gonzalez, and J. Driesen, "Combined central andlocal active and reactive power control of PV inverters," *IEEE Transactions on Sustainable Energy*, vol. 5, no. 3, pp. 776-784, 2014.

[84] M. Vandenbergh et al., "Prioritisation of technical solutions available for the integration of PV into the distribution grid," DER Lab, 2013.

[85] T. Stetz, F. Marten, and M. Braun, "Improved low voltage grid-integration of photovoltaic systems in Germany," *IEEE Transactions on Sustainable Energy*, vol. 4, no. 2, pp. 534-542, 2013.

[86] C. L. Masters, "Voltage rise: the big issue when connecting embedded generation to long 11 kV overhead lines," *Power Engineering Journal*, vol. 16, no. 1, pp. 5-12, 2002.

[87] G. Mokhtari, G. Nourbakhsh, and A. Ghosh, "Smart coordination of energy storage units (ESUs) for voltage and loading management in distribution networks," *IEEE Transactions on Power Systems*, vol. 28, no. 4, pp. 4812-4820, 2013.

[88] R. Tonkoski, L. A. C. Lopes, and T. H. M. El-Fouly, "Coordinated active power curtailment of grid connected PV inverters for overvoltage prevention," *IEEE Transactions on Sustainable Energy*, vol. 2, no. 2, pp. 139-147, 2011.

[89] Yuzuru Ueda, K. Kurokawa, T. Tanabe, K. Kitamura, and H. Sugihara, "Analysis results of output power loss due to the grid voltage rise in grid-connected photovoltaic power generation systems," *IEEE Transactions on Industrial Electronics*, vol. 55, no. 7, pp. 2744-2751, 2008.

[90] P. M. S. Carvalho, Pedro F. Correia, and L. A. F. Ferreira, "Distributed reactive power generation control for voltage rise mitigation in distribution networks," *IEEE Transactions on Power Systems*, vol. 23, no. 2, pp. 766-772, 2008.

[91] Y. Yang, F. Blaabjerg, and H. Wang, "Constant power generation of photovoltaic systems considering the distributed grid capacity," in *Annual IEEE Applied Power Electronics Conference and Exposition*, 2014, pp. 379–385.

[92] D. I. Brandão, F. P. Marafão, M. G. Simões, and J. A. Pomilio, "Considerations on the modeling and control scheme of grid connected inverter with voltage support capability," in *Brazilian Power Electronics Conference*, Gramado, 2013.

[93] A. Ahmed, L. Ran, S. Moon, and J. H. Park, "A fast PV power tracking control algorithm with reduced power mode," *IEEE Transactions on Energy Conversion*, vol. 28, pp. 565-575, 2013.

[94] S. M. Deckmann, F. P. Marafão, and M. S. Pádua, "Frequency-adjustable positive sequence detector for power conditioning applications," in *IEEE Power Electronics Specialists Conference*, 2005, pp. 1928-1934.

[95] Jinwei He and Yun Wei Li, "Hybrid voltage and current control approach for DG-Grid interfacing converters with LCL filters," *IEEE Transactions on Industrial Electronics*, vol. 60, no. 5, pp. 1797-1809, 2013.

[96] M. A. Abusara, J. M. Guerrero, and M. Sharkh, "Line-interactive UPS for microgrids," *IEEE Transactions on Industrial Electronics*, vol. 61, pp. 1292-1300, 2014.

[97] Z. Liu and J. Liu, "Indirect current control based seamless transfer of three-phase inverter in distributed generation," *IEEE Transactions on Power Electronics*, vol. 29, no. 7, pp. 3368-3383, 2014.

[98] S. Buso, T. Caldognetto, and D. I. Brandao, "Oversampled deadbeat current controller for voltage source converters," in *Applied Power Electronics Conference and Exposition (APEC)*, 2015, pp. 1493-1500.

[99] S. Buso and T. Caldognetto, "A non-linear wide bandwidth digital current controller for DC-DC and DC-AC converters," in *Annual Conference of the IEEE Industrial Electronics Society (IECON)* , 2014, pp. 1090-1096.

[100] S. Buso, T. Caldognetto, and D. I. Brandao, "Comparison of oversampled current controllers for micro-grid utility interface converters," in *IEEE Energy Conversion Congress and Exposition*, Montreal, Canada, 2015, pp. 1-1.

[101] A. V. Peterchev and S. R. Sanders, "Quantization resolution and limit cycling in digitally controlled PWM converters," *IEEE Transactions on Power Electronics*, vol. 18, no. 1, pp. 301-308, 2003.

[102] M. Bradley, E. Alarcon, and O. Feely, "Design-oriented analysis of quantization-induced limit cycles in a multiple-sampled digitally controlled buck converter," *IEEE Transactions on Circuits and Systems I, Regular Paper*, vol. 61, no. 4, pp. 1192-105, 2014.

[103] L. Corradini and P. Mattavelli, "Modeling of multisampled pulse width modulators for digitally controlled DC–DC converters," *IEEE Transactions on Power Electronics*, vol. 23, no. 4, pp. 1839-1847, 2008.

[104] J. Xu, T. Tang, and S. Xie, "Evaluations of current control in weak grid case for grid-connected LCL-filtered inverter," *IET Power Electronics*, vol. 6, no. 2, pp. 227-234, 2013.

[105] D. Dong, T. Thacker, R. Burgos, F. Wang, and D. Boroyevich, "On zero steady-state error voltage control of single-phase PWM inverters with differentload types," *IEEE Transactions on Power Electronics*, vol. 26, no. 11, pp. 3285-3297, 2011.

[106] M. Monfared, S. Golestan, and J. M. Guerrero, "Analysis, design, and experimental verification of a synchronous reference frame voltage control for single-phase inverters," *IEEE Transactions on Industrial Electronics*, vol. 61, no. 1, pp. 258-269, 2014.

[107] G. Weiss, Q.-C. Zhong, T. C. Green, and L. Jun, "H∞ repetitive control of DC-AC converters in microgrids," *IEEE Transactions on Power Electronics*, vol. 19, no. 1, pp. 219-230, 2004.

[108] Q.-C. Zhong, P.-L. Nguyen, Zhenyu Ma, and W. Sheng , "Self-synchronized synchronverters: inverters without a dedicated synchronization unit," *IEEE Transactions on Power Electronics*, vol. 29, no. 2, pp. 617-630, 2014.

[109] S. Buso, S. Fasolo, L. Malesani, and P. Mattavelli, "A dead-beat adaptive hysteresis current control," *IEEE Transactions on Industry Applications*, vol. 36, no. 4, pp. 1174-1180, 2000.

[110] L. Herman, I. Papic, and B. Blazic, "A Proportional-Resonant Current Controller for Selective Harmonic Compensation in a Hybrid Active Power Filter," *IEEE Transactions on Power Delivery*, no. 10.1109/TPWRD.2014.2344770 , 2014.

[111] A. G. Yepes, F. D. Freijedo, O. Lopez, and J Doval-Gandoy, "Analysis and design of resonant current controllers for voltage-source converters by means of Nyquist diagrams and sensitivity function," *IEEE Transactions on Industrial Electronics*, vol. 58, no. 11, pp. 5231-5250, 2011.

[112] A. G. Yepes et al., "Effects of discretization methods on the performance of resonant controllers," *IEEE Transactions on Power Electronics*, vol. 25, no. 7, pp. 1692-1712, 2010.

[113] E. J. Estebanez, V. M. Moreno, A. Pigazo, and M. Liserre, "An overview of anti-islanding detection algorithms in photovoltaic systems in case of multiple current-controlled inverters," in *Annual*

Conference of IEEE Industrial Electronics (IECON), 2009.

[114] Independent Statistics & Analysis. (2013, Dezember) U.S. Energy Information Administration. [Online]. www.eia.gov/electricity, accessed in 10/27/2015.

[115] S. Bacha, D. Picault, B. Burger, Ion Etxeberria-Otadui, and J. Martins, "Photovoltaics in microgrids: an overview of grid integration and energy management aspects," *IEEE Industrial Electronics Magazine*, vol. 9, no. 1, pp. 33-46, 2015.

[116] T. Erseghe, "Distributed optimal power flow using ADMM," *IEEE Transactions on Power Systems*, vol. 29, no. 5, pp. 2370-2380, 2014.

[117] S. Bolognani, R. Carli, G. Cavraro, and S. Zampieri, "Distributed reactive power feedback control for voltage regulation and loss minimization," *IEEE Transactions on Automatic Control*, vol. 60, no. 4, pp. 966-981, 2015.

[118] W. Saad, Zhu Han, and H. V. Poor, "Coalitional game theory for cooperative micro-grid distribution networks," in *IEEE International Conference on Communications Workshops*, 2011, pp. 1-5.

[119] N. C. Ekneligoda and W. W. Weaver, "Game-theoretic communication structures in microgrids," *IEEE Transactions on Power Delivery*, vol. 27, no. 4, pp. 2334-2341, 2012.

[120] N. C. Ekneligoda and W.W. Weaver, "Optimal transient control of microgrids using a game theoretic approach," in *IEEE Energy Conversion Congress and Exposition*, 2011, pp. 935-942.

[121] E. Planas, A. Gil-de-Muro, J. Andreu, I. Kortabarria, and I. Martínez de Alegría, "General aspects, hierarchical controls and droop methods in microgrids: a review," *Renewable and Sustainable Energy Reviews*, vol. 17, pp. 147-159, 2013.

[122] S. Bolognani and S. Zampieri, "A distributed control strategy for reactive power compensation in smart microgrids," *IEEE Transactions on Automatic Control*, vol. 58, no. 11, pp. 2818-2833, 2013.

[123] P. Tenti, A. Costabeber, T. Caldognetto, and P. Mattavelli, "Cooperative control of smart micro-grids based on conservative power commands," *Conference-Seminar International School on Nonsinusoidal Currents and Compensation*, vol. 89, no. 6, pp. 32-40, 2013.

[124] A. Hooshmand, H. A. Malki, and J. Mohammadpour, "Power flow management of microgrid networks using model predictive control," *Computers & Mathematics with Applications*, vol. 64, no. 5, pp. 869-876, 2012.

[125] Jong-Yul Kim, Seul-Ki Kim, and Jin-Hong Jeon, "Coordinated state-of-charge control strategy for microgrid during islanded operation," in *IEEE International Symposium on Power Electronics for Distributed Generation Systems*, 2012, pp. 133-139.

[126] Jong-Yul Kim et al., "Cooperative control strategy of energy storage system and microsources for stabilizing the microgrid during islanded operation," *IEEE Transactions on Power Electronics*, vol. 25, no. 12, pp. 3037-3048, 2010.

[127] M. J. Erickson, T. M. Jahns, and R. H. Lasseter, "Comparison of PV inverter controller configurations for CERTS microgrid applications," *IEEE Energy Conversion Congress and Exposition*, pp. 659-666, 2011.

[128] P. Tenti, A. Costabeber, F. Sichirollo, and P. Mattavelli, "Minimum loss control of low-voltage residential microgrids," in *Annual Conference on IEEE Industrial Electronics Society*, 2012, pp. 5650-5656.

[129] Xiaonan Lu et al., "Hierarchical control of parallel AC-DC converter interfaces for hybrid microgrids," *IEEE Transactions on Smart Grid*, vol. 5, no. 2, pp. 683-692, 2014.

[130] S. Buso and T. Caldognetto, "Rapid prototyping of digital controllers for microgrid inverters," *IEEE Journal of Emerging and Selected Topics in Power Electronics*, vol. 3, no. 2, pp. 440-450, 2015.

[131] S. Bala, *Integration of single-phase microgrids*, 1st ed.: ProQuest, 2008.

[132] AC Power Source Summary. [Online]. www.hyvac.com/tech_support/electrical_sources_worldwide.pdf, accessed in 10/27/2015.

[133] M. Hojo, Y. Iwase, T. Funabashi, and Y. Ueda, "A method of three-phase balancing in microgrid

by photovoltaic generation systems," in *Power Electronics and Motion Control Conference*, 2008, pp. 2487-2491.

[134] A. Ghosh and A. Joshi, "A new approach to load balancing and power factor correction in power distribution system," *IEEE Transactions on Power Delivery*, vol. 15, no. 1, pp. 417-422, 2000.

[135] Zhihua Qu and Ali Maknouninejad, "Realizing unified microgrid voltage profile and loss minimization: a cooperative distributed optimization and control approach," *IEEE Transactions on Smart Grid*, vol. 5, no. 4, pp. 1621-1630, 2014.

[136] S. Munir and Yun Wei Li, "Residential distribution system harmonic compensation using PV interfacing inverter," *IEEE Transaction on Smart Grid*, vol. 4, no. 2, pp. 816-827, 2013.

[137] A. Khodaei, "Provisional microgrids," *IEEE Transactions on Smart Grid*, vol. 6, no. 3, pp. 1107-1115, 2015.

[138] Xu She, A. Q. Huang, and R. Burgos, "Review of solid-state transformer technologies and their application in power distribution systems," *IEEE Journal of Emerging and Selected Topics in Power Electronics*, vol. 1, no. 3, pp. 186-198, 2013.

A. Appendix A

Experimental results of selective and partial compensation of unwanted current terms

To analyze the proposed compensation scheme and validate the selective and partial generator of load current compensation references, the electrical circuit of Fig. A.1 and Table A.1 was experimentally developed in laboratory. The set-up includes a three-phase four-leg VSI with IGBTs (SKM 100GB128D, driven by a SKPC 22/2 –from Semikron). The current control scheme and CPT's current and power decompositions were implemented using a fixed-point DSP - digital signal processor (TMS320F2812). The three-phase converter is controlled as a shunt APF, driven by PWM technique with duty cycle equal to 50% on 4th leg. Details of its parameters and current controller can be found in [**80**]. A picture of the laboratory-scale prototype is shown in Fig. A.2.
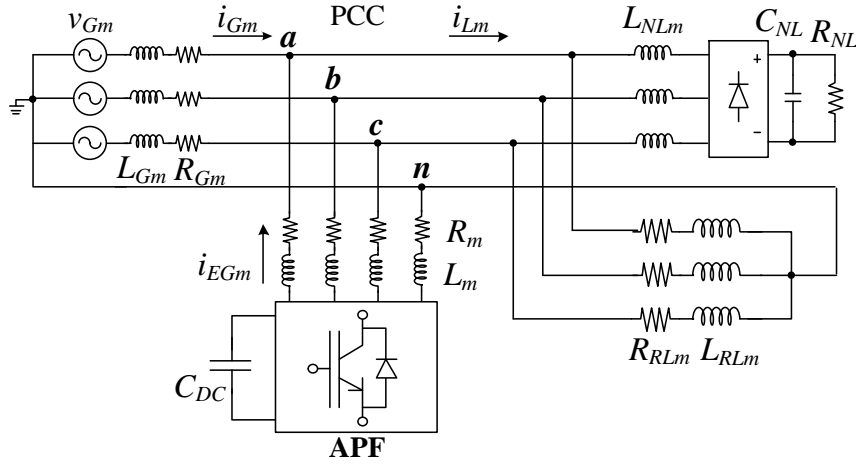
Fig. A.1: Nonlinear and unbalance three-phase four-wire circuit, © IET 2015 [**80**].

Table A.1: Parameters of the system, © IET 2015 [80].

Load parameters
R_{RLa}=4.4Ω; L_{RLa}=15mH;
R_{RLb}=4.1Ω; L_{RLb}=18mH;
R_{RLc}=3.7Ω; L_{RLc}=30mH.
L_{NLa}=1mH; L_{NLb}=1mH; L_{NLc}=1mH;
R_{NL}=42Ω; C_{NL}=2.35mF.
Sinusoidal three-phase source (60Hz)
V_{Ga}=127∠0°V; V_{Gb}=127∠-120°V; V_{Gc}=127∠120°V;
L_{Gm}=0.5mH; R_{Gm}=0.05Ω.
Distorted and asymmetrical three-phase source (60Hz)
V_{Ga}=122∠0° + 3.7∠3·0° + 3.7∠5·0° + 1.8∠7·0°V;
V_{Gb}=127∠-120° + 3.8∠3·(-120°) + 3.8∠5·(-120°) + 1.9∠7·(-120°)V;
V_{Gc}=115∠120° + 3.4∠3·(120°) + 3.4∠5·(120°) + 1.7∠7·(120°)V.

(**a**) three-phase APF prototype.

(**b**) Three-phase inverter from Semikron.

(**c**) DSP TMS320F2812 from Texas Instruments.

Fig. A.2: The experimental laboratory-scale prototype implemented at Universidade Estadual Paulista – UNESP-Sorocaba, Brazil.

1.   Operation under sinusoidal and symmetrical voltage grid

Fig. A.3(a). shows the instantaneous three-phase PCC voltages and load currents, including neutral wire current, without compensation ($k_Q=k_N=k_D=0$). Note that the PCC voltages are slightly distorted and asymmetrical due to the effect of the nonlinear and unbalance currents flowing through the line impedances. The RMS and THD values of the load phase currents are: 20.9 A, 10.98 % (phase *a*); 17.4 A, 13.33 % (phase *b*) and 16.1 A, 14.73 % (phase *c*), respectively. See Table A.2 for more details concerning to the RMS and THD voltage and current values. Besides, the load unbalance effect can be observed by the presence of neutral current.

In Fig. A.3(b), the scaling coefficients are set to one ($k_Q=k_N=k_D=1$), which means full power factor compensation. This strategy leads to ideal grid currents: waveforms are practically sinusoidal (see THD in Table A.2), in phase with PCC voltages and free of unbalance components, even the neutral wire current is close to zero. However, this full compensation needs a significant amount of power/current ratio of EPP, increasing its cost. See Table A.2 for a quantitative analysis of RMS current values in each compensation strategy. Fig. A.3(c) and Fig. A.3(d) show the reactivity ($k_Q=1$ and $k_N=k_D=0$) and unbalance ($k_N=1$ and $k_Q=k_D=0$) conformity factor compensation strategies, respectively. In the first, only the reactive power is compensated, whereas in the latter only the unbalance power is minimized. Observe that both strategies require less amount of power/current ratio of EPP.

(a) load ($k_Q=k_N=k_D=0$)

(c) i^b_r ($k_Q=1$ and $k_N=k_D=0$)

(b) i_{na} ($k_Q=k_N=k_D=1$)

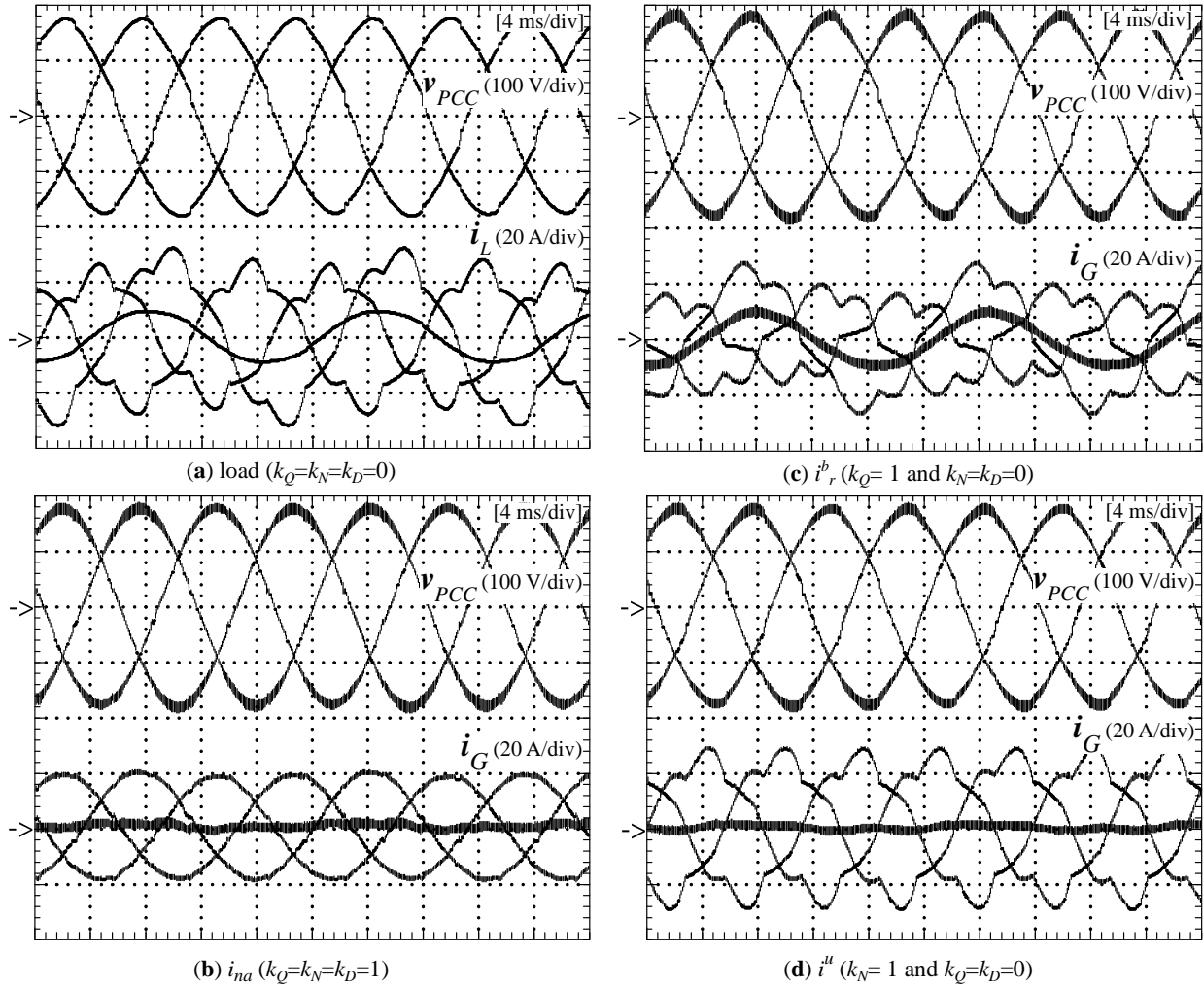(d) i^u ($k_N=1$ and $k_Q=k_D=0$)

Fig. A.3: Selective load current compensation under sinusoidal voltage grid operation, © IET 2015 [80].

Table A.2: PCC voltages, currents and power and filter currents of selective compensation under sinusoidal grid voltage, © IET 2015 [80].

Parameters.	Load	i_{na}	i^b_r	i^u	i_v
A[kVA]	6.71	5.02	5.21	6.67	6.71
P[kW]	4.46	5.01	4.96	4.69	4.69
Q[kVAr]	4.80	**0.03**	**0.01**	4.65	4.64
N[kVA]	1.16	**0.10**	1.25	**0.08**	1.16
D[kVA]	0.92	**0.36**	0.95	0.90	**0.38**
V_a [V] (THD[%])	122.3 (2.29)	124.8 (0.92)	124.6 (2.14)	**122.5** (2.24)	122.3 (**0.81**)
V_b [V] (THD[%])	121.9 (2.27)	124.5 (0.87)	124.3 (2.20)	**122.3** (2.18)	121.8 (**0.84**)
V_c [V] (THD[%])	123.4 (2.26)	125.4 (0.90)	126.0 (2.25)	**123.3** (2.22)	123.7 (**0.80**)
I_{Ga} [A] (THD[%])	20.88 (10.98)	**13.74 (3.13)**	17.81 (13.60)	18.39 (12.41)	20.98 (2.08)
I_{Gb} [A] (THD[%])	17.43 (13.33)	**13.21 (2.20)**	12.77 (19.27)	17.97 (12.87)	17.34 (1.80)
I_{Gc} [A] (THD[%])	16.12 (14.73)	**13.24 (1.82)**	10.01 (25.06)	18.00 (12.79)	15.97 (1.76)
I_{fa} [A]	---	**13.3**	13.1	**3.2**	**2.2**
I_{fb} [A]	---	**13.7**	13.2	**1.2**	**3.3**
I_{fc} [A]	---	**14.3**	13.0	**4.1**	**2.7**

Besides, in order to evaluate the flexible selective compensation capability and its practical feasibility, we have decided to set two scaling coefficients and then vary the third one. Table A.3, Table A.4 and Table A.5 show the following configurations: (λ_Q^* and $k_N=k_D=0$); (λ_N^* and $k_Q=k_D=0$) and (λ_D^* and $k_Q=k_N=0$). Finally, in Table A.6 is shown the result where all the load conformity factors have been selectively driven by the set of references (λ_Q^*, λ_N^*, λ_D^*). From these results, we can see that the decomposed CPT's current terms are, indeed, orthogonal to each other and, the compensation is accurately, thanks to the adopted current controller (PI-type iterative learning control), as described in [**80**].

Table A.3: Flexible reactivity conformity factor compensation ($\boldsymbol{\lambda_Q^*}$ and $k_N=k_D=0$), © IET 2015 [80].

λ_Q^*	**0.000**	**0.300**	**0.440**	**0.520**
λ	0.960	0.918	0.867	0.826
λ_Q	**0.000**	**0.301**	**0.439**	**0.523**
λ_N	0.215	0.205	0.196	0.186
λ_D	0.185	0.182	0.176	0.167

Table A.4: Flexible unbalance conformity factor compensation ($\boldsymbol{\lambda_N^*}$ and $k_Q=k_D=0$), © IET 2015 [80].

λ_N^*	**0.000**	**0.050**	**0.100**	**0.120**
λ	0.701	0.709	0.689	0.698
λ_Q	0.706	0.697	0.715	0.705
λ_N	**0.013**	**0.053**	**0.096**	**0.111**
λ_D	0.141	0.139	0.138	0.141

Table A.5: Flexible distortion conformity factor compensation ($\boldsymbol{\lambda_D^*}$ and $k_Q=k_N=0$), © IET 2015 [80].

λ_D^*	**0.000**	**0.080**	**0.100**	**0.120**
λ	0.693	0.686	0.694	0.682
λ_Q	0.712	0.717	0.708	0.718
λ_N	0.152	0.154	0.154	0.154
λ_D	**0.061**	**0.088**	**0.106**	**0.126**

Table A.6: Flexible current reference generator ($\boldsymbol{\lambda_Q^*}$, $\boldsymbol{\lambda_N^*}$, $\boldsymbol{\lambda_D^*}$), © IET 2015 [80].

λ_Q^*=0.200	λ_N^*=0.100	λ_D^*=0.080	λ^*=0.972
0.200	0.115	0.084	0.970

2. *Operation under distorted and asymmetrical voltage grid*

To evaluate the selective compensation under non-ideal voltage conditions, the load was supplied by distorted and asymmetrical voltages, as shown in Table A.1. Fig. A.4 and Table A.7 report the corresponding results.

Fig. A.4(a) shows the instantaneous three-phase PCC voltages and load currents, including neutral wire current, without compensation ($k_Q=k_N=k_D=0$). In this case, a portion of neutral wire current is caused by the unbalanced load and other portion is caused by the distorted and asymmetrical voltages.

Fig. A.4(b) shows the full power factor compensation ($k_Q=k_N=k_D=1$) under non-ideal voltage grid operation. As expected, the grid current waveforms assume the same waveforms of the PCC voltages (*resistive load synthesis*), and the neutral wire current is reduced to the contribution from the grid voltages non-ideality. Fig. A.4(c) shows the unbalance ($k_N=1$ and $k_Q=k_D=0$) conformity factor compensation under distorted and asymmetrical voltages. Note that the unbalance power is minimized; however, the neutral current is not eliminated so as the asymmetry existing in the voltages. Fig. A.4(d) shows the distortion ($k_D=1$ and $k_Q=k_N=0$) factor compensation under these polluted voltages. In this case, one can notice that even reducing the distortion power (void currents), the resulting currents are still distorted due to the influence of the distorted grid voltages. See Table A.7 for a quantitative analysis.

(a) Load ($k_Q=k_N=k_D=0$)

(b) i_{na} ($k_Q=k_N=k_D=1$)

(c) i^u ($k_N=1$ and $k_Q=k_D=0$)

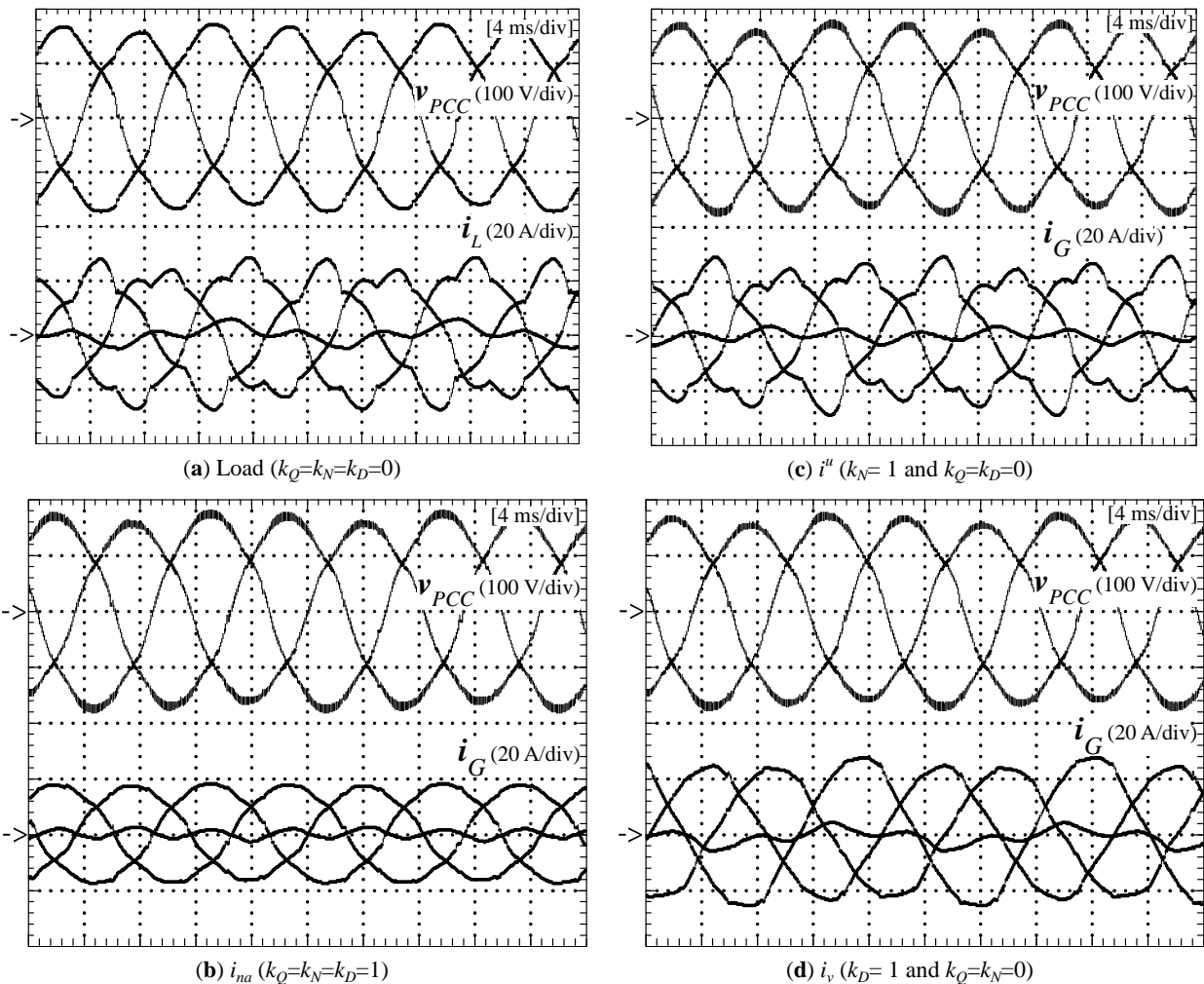**(d)** i_v ($k_D=1$ and $k_Q=k_N=0$)

Fig. A.4: Selective load current compensation under distorted and asymmetrical voltage grid operation, © IET 2015 [80].

Finally, to validate the selective compensation and its feasibility during non-ideal conditions, we have applied the power factor compensation (λ^*) and the unbalance conformity factor compensation (λ_N^* and $k_Q=k_D=0$) strategies. These results are reported in Table A.8 and Table A.9, where the effectiveness of these strategies has been confirmed even under operation with deteriorated grid voltages.

Table A.7: PCC voltages, currents and power and filter currents for selective compensation under distorted and asymmetrical grid voltage, © IET 2015 [80].

Parameters	Load	i_{na}	i_r^b	i^u	i_v
V [V]	202.5	206.6	206.4	202.7	202.5
I [A]	29.5	21.7	22.0	29.6	29.7
A[kVA]	6.03	4.48	4.64	6.03	6.06
P[kW]	3.95	4.48	4.46	4.16	4.23
Q[kVAr]	4.40	**0.01**	**0.01**	4.27	4.24
N[kVA]	0.86	**0.07**	0.92	**0.07**	0.89
D[kVA]	0.87	**0.21**	0.92	0.90	**0.26**
V_a **[V] (THD[%])**	110.9 (5.76)	112.7 (4.52)	112.9 (5.77)	110.9 (5.91)	111.0 (4.85)
V_b **[V] (THD[%])**	122.3 (6.13)	124.3 (4.92)	124.9 (6.21)	122.2 (6.37)	122.2 (5.11)
V_c **[V] (THD[%])**	117.5 (6.76)	120.4 (4.71)	119.9 (6.60)	118.0 (6.34)	117.4 (5.42)
I_{Ga} **[A] (THD[%])**	16.3 (13.07)	12.1 (5.54)	14.6 (16.36)	16.5 (13.77)	16.4 (5.05)
I_{Gb} **[A] (THD[%])**	18.7 (10.08)	12.9 (5.95)	13.6 (15.77)	17.6 (10.54)	18.8 (4.14)
I_{Gc} **[A] (THD[%])**	16.5 (15.63)	12.6 (6.04)	10.4 (27.69)	17.4 (16.25)	16.3 (4.41)

Table A.8: Flexible power factor compensation, © IET 2015 [80].

λ^*	**0.980**	**0.950**	**0.920**	**0.900**
λ	**0.981**	**0.958**	**0.929**	**0.916**
λ_Q	0.179	0.270	0.353	0.383
λ_N	0.048	0.069	0.083	0.09
λ_D	0.059	0.074	0.087	0.094

Table A.9: Flexible unbalance conformity factor compensation (λ_N^* and $k_Q=k_D=0$), © IET 2015 [80].

λ_N^*	**0.050**	**0.080**	**0.100**	**0.120**
λ	0.68	0.684	0.668	0.689
λ_Q	0.725	0.720	0.735	0.713
λ_N	**0.056**	**0.085**	**0.104**	**0.122**
λ_D	0.146	0.144	0.14	0.144

B. Appendix B

Simulation results of optimized compensation of unwanted current terms by DER

To analyze and evaluate the proposed optimized compensation strategy applied to an individual DER and the system dynamic behavior, we have implemented the power circuit of Fig. B.1 using PSIM environment and the formulated linear programming into a MatLab code (see annex A). The linear programming was updated once per fundamental cycle of grid voltage.
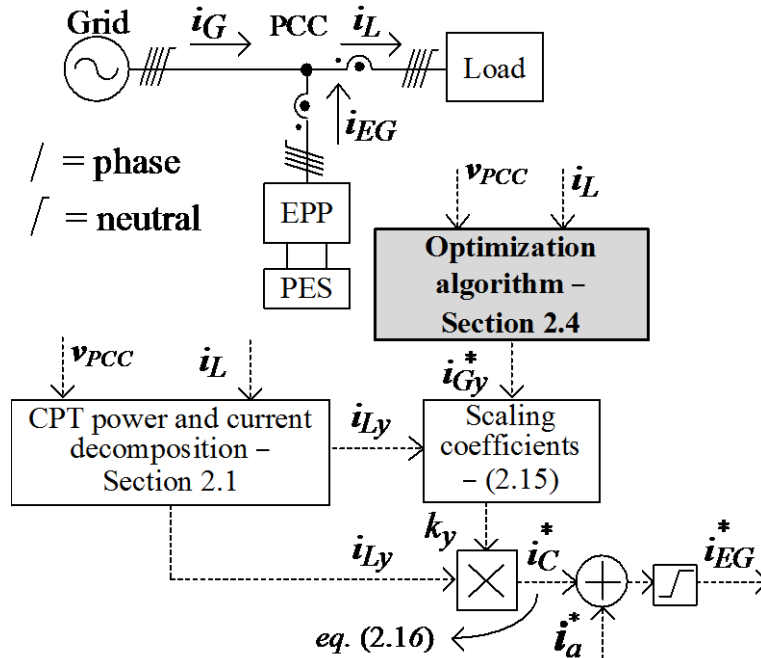

Fig. B.1: Three-phase four-wire circuit with the block diagram of the optimized compensation strategy, © IEEE 2015 [76].

1)   PES power variation during ideal voltage operation

Considering the EPP nominal collective current equal to 40 A, the PES power generation has been varied setting three different cases. #1) $\Delta I_{EG} \geq I_{Lna}$; #2) $I_{Lna} > \Delta I_{EG} \geq I_C^{min}$); #3) $\Delta I_{EG} < I_C^{min}$. The results are shown in Fig. B.2 and Fig. B.3.

At the beginning of the simulation (case #1), the EG has enough available power capacity to compensate all the unwanted load currents. Thus, all scaling coefficients are unity, as well as λ, while the grid currents have about 2 % of THD_{iG} and, practically, zero neutral current. After 0.15 s (case #2), the PES increases its power generation forcing EG to reduce its compensation rate, because the active power injection has top priority in the optimization algorithm by means of (2.23). However, the optimized compensation operates, in steady state, at the optimal point, maximizing the currents compensation

$(k_Q = 0.96, k_D = 0.85$ and $k_N = 0.89)$. At the end (case #3), the power generation increases close to PES nominal value. As a result, EG cannot comply anymore with the preset constraints and must run using (2.28) to compensate as much unwanted currents as possible.
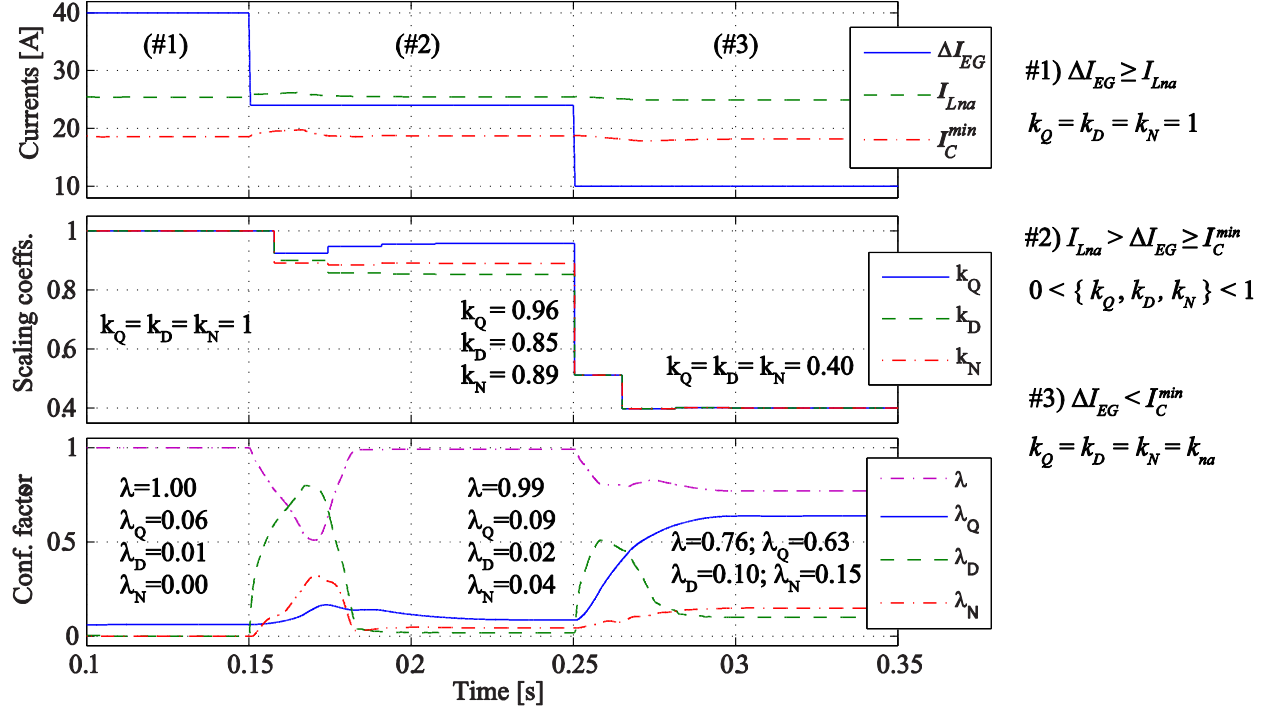

Fig. B.2: Optimized compensation under PES power variation and ideal voltages. From top to bottom: currents, scaling coefficients and PCC conformity factors, © IEEE 2015 [**76**].
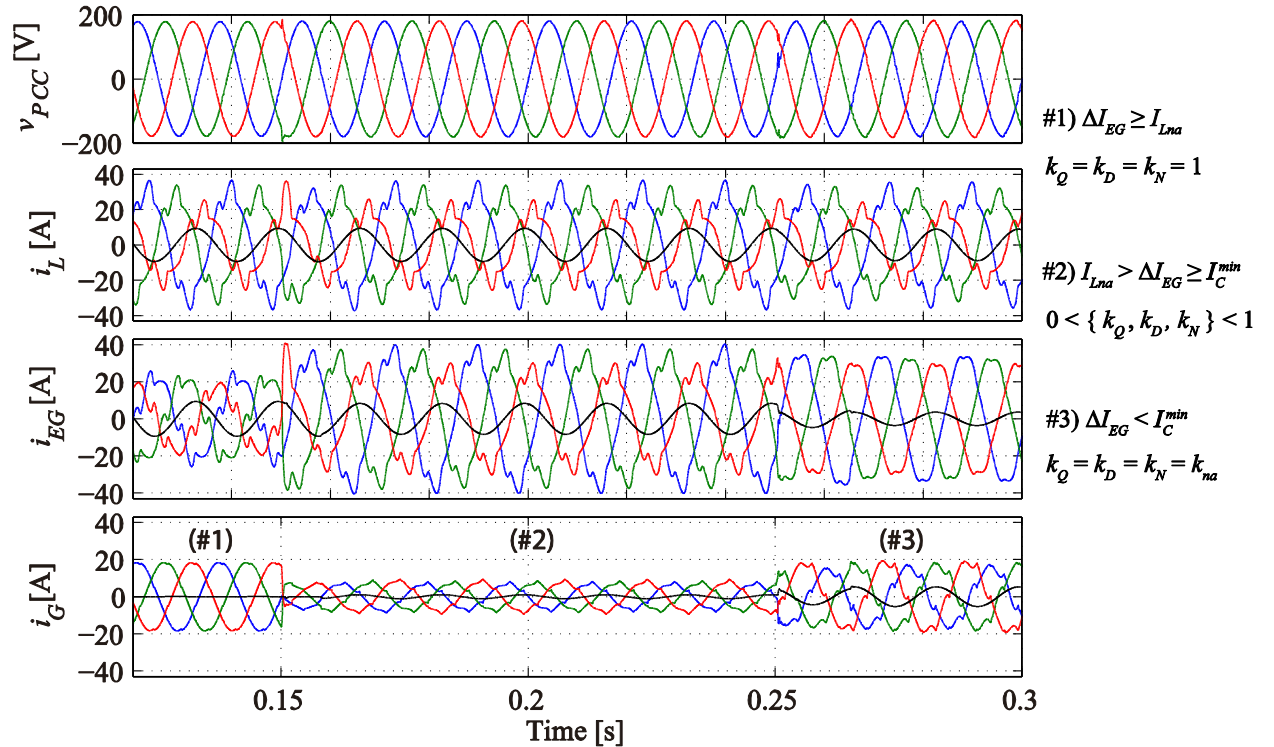

Fig. B.3: Optimized compensation under PES power variation and ideal voltages. From top to bottom: PCC voltages, load, EG and grid currents, © IEEE 2015 [**76**].

The *dynamic response* of the scaling coefficients is mostly dominated by the RMS algorithm used in (2.15) and (2.28), which was implemented using MAFs with one fundamental cycle of time response. The scaling coefficients are updated once per fundamental cycle and the steady state is achieved in two to three cycles. The conformity factors have slower dynamic response due to their more complex calculation. However, these factors are used only to PCC analysis and not into the optimized compensation strategy, which is then an *online open loop strategy*. This can be verified in Fig. B.3, where the EG and grid current waveforms show fast response.

Note that λ_Q increasing after 0.25 s is a consequence of limited compensation capability of EG in addition to the lower *active power* flowing through the PCC port, since the CPT's factors are relative indexes (2.12). The amount of reactive power has not changed.

2)   Local load variation

The local load variation occurred in two steps up of 25 % of the final power load value. The results are shown in Fig. B.4 and Fig. B.5. At the begging of the simulation, the PES provides about 37.8 A and the load has 50 % of demand. In this condition, the EG has capability to supply all the active power plus compensate all the unwanted load current terms. Then, the optimal point is located at the origin of Fig. 2.6 (all scalar coefficients are unity) and grid current waveforms are practically sinusoidal, with 1.5 % of THD_{iG} and almost no neutral current. With 75 % of load demand, the optimal compensation acts within the feasible region and the steady state of the scaling coefficients correspond to the optimal solution, attending all the preset constraints. At the end, with full load, the EG injects all the active power and compensates as much as possible on the basis of (2.28), because $\Delta I_{EG} < I_C^{min}$.

Notice from the top of Fig. B.4 that while the load demand (I_L) increases, the grid current (I_G) decreases, because of the load drains the active power from PES. This active power flow variation impacts the PCC voltage due to the line impedances. However, it is taken into account by the optimal compensation algorithm. It shall be highlighted that EPP capability is fully exploited (see I_{EG} from Fig. B.4), increasing its efficiency and its overall cost-benefit.
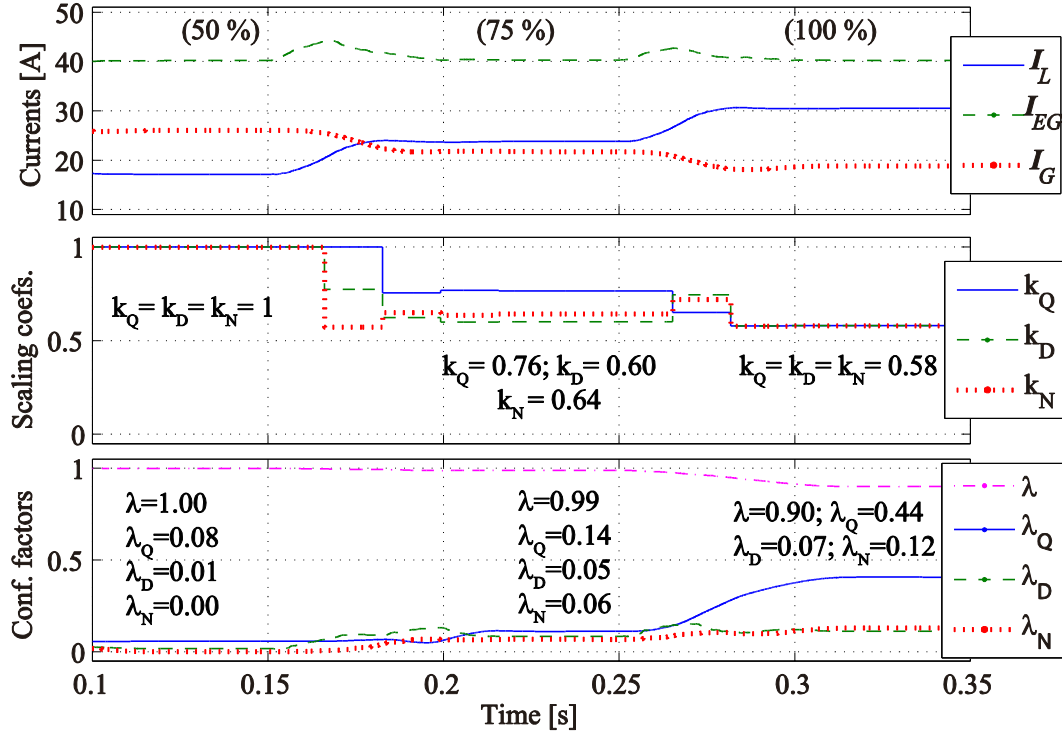
Fig. B.4: Optimized compensation under load step and ideal voltages. From top to bottom: currents, scaling coefficients and PCC conformity factors, © IEEE 2015 [**76**].
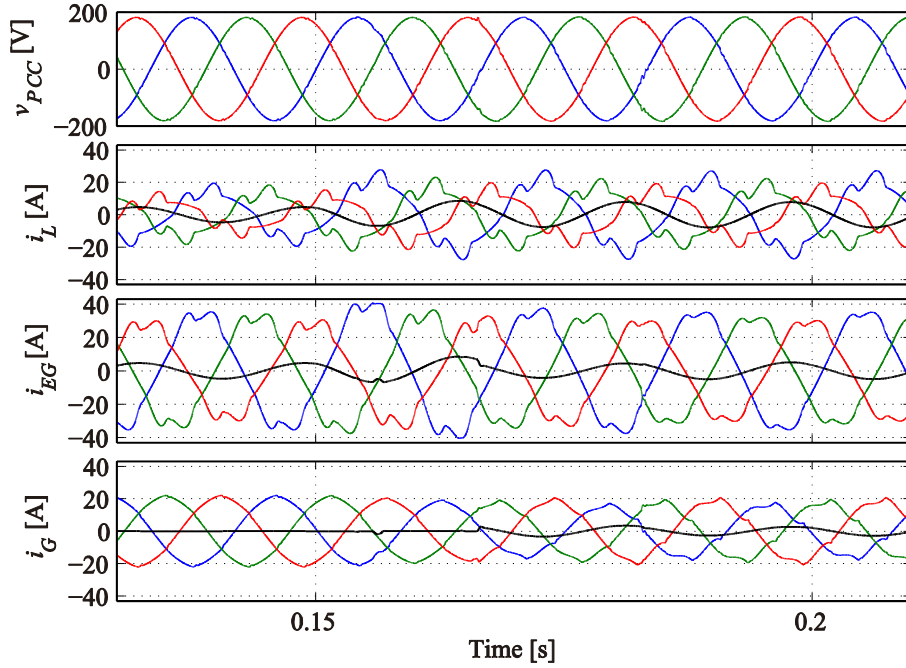

Fig. B.5: Optimized compensation under load step and ideal voltages. From top to bottom: PCC voltages, load, EG and grid current waveforms, © IEEE 2015 [**76**].

3)   PES power variation under non-ideal voltage operation

Here, the PCC voltages have been set to have 3 % of 3rd, 5th and 7th harmonic, totalizing THD of 5.2 % and, -3 % (phase *a*) and 3 % (phase *c*) of asymmetry.

Considering again the EG nominal collective current equals to 40 A, the PES power generation has been varied setting three different cases. #1) $\Delta I_{EG} \geq I_{Lna}$; #2) $I_{Lna} > \Delta I_{EG} \geq I_C^{min}$); #3) $\Delta I_{EG} < I_C^{min}$. The results are shown in Fig. B.6 and Fig. B.7.

At the beginning (case #1), the EG has enough available current capacity to compensate all the unwanted load currents. Thus, all scaling coefficients are unity, as well as λ. The performed compensation strategy is *resistive load synthesis* and not *sinusoidal source current synthesis*, as discussed in Section 2.3. Consequently, the grid current waveforms are proportional to PCC voltage waveforms and have about 5.2 % of THD$_{iG}$ and, practically, zero neutral current. The residual neutral current is related to the PCC voltage non-idealities, as in Fig. A.4(b). As discussed in Section 2.1.2, CPT's factors are concentrated on the *load behavior* and not just on the current waveforms.
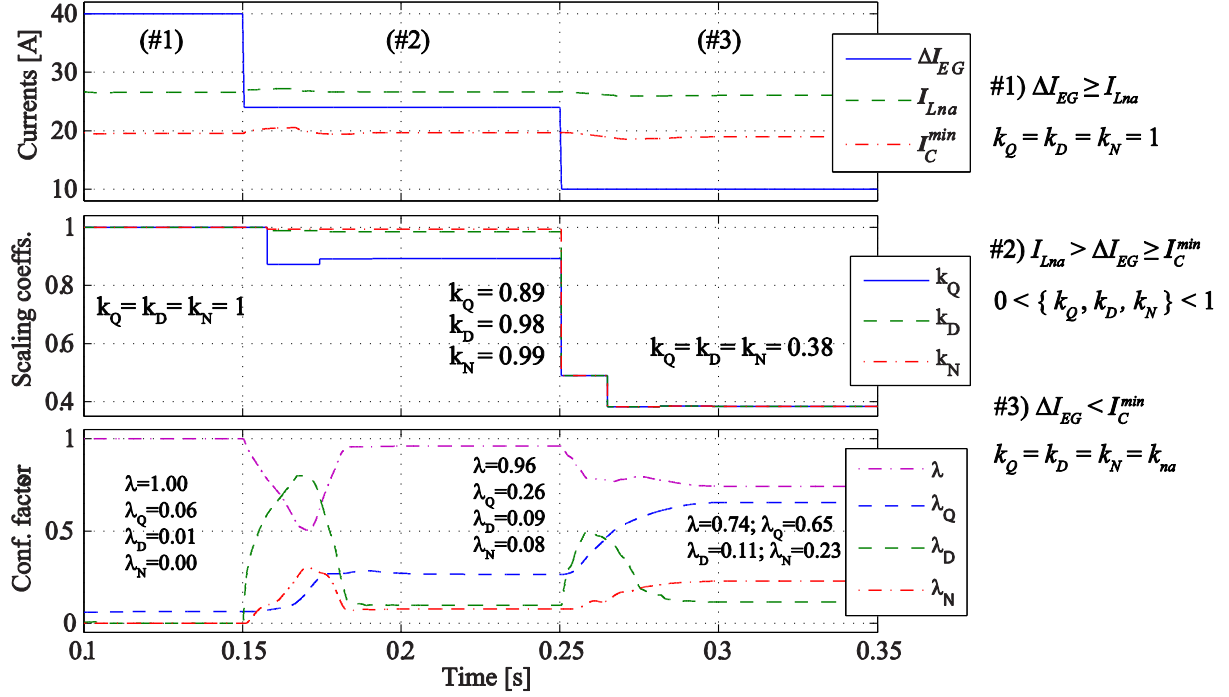

Fig. B.6: Optimized compensation under PES power variation and non-ideal voltages operation. From top to bottom: currents, scaling coefficients and PCC conformity factors.
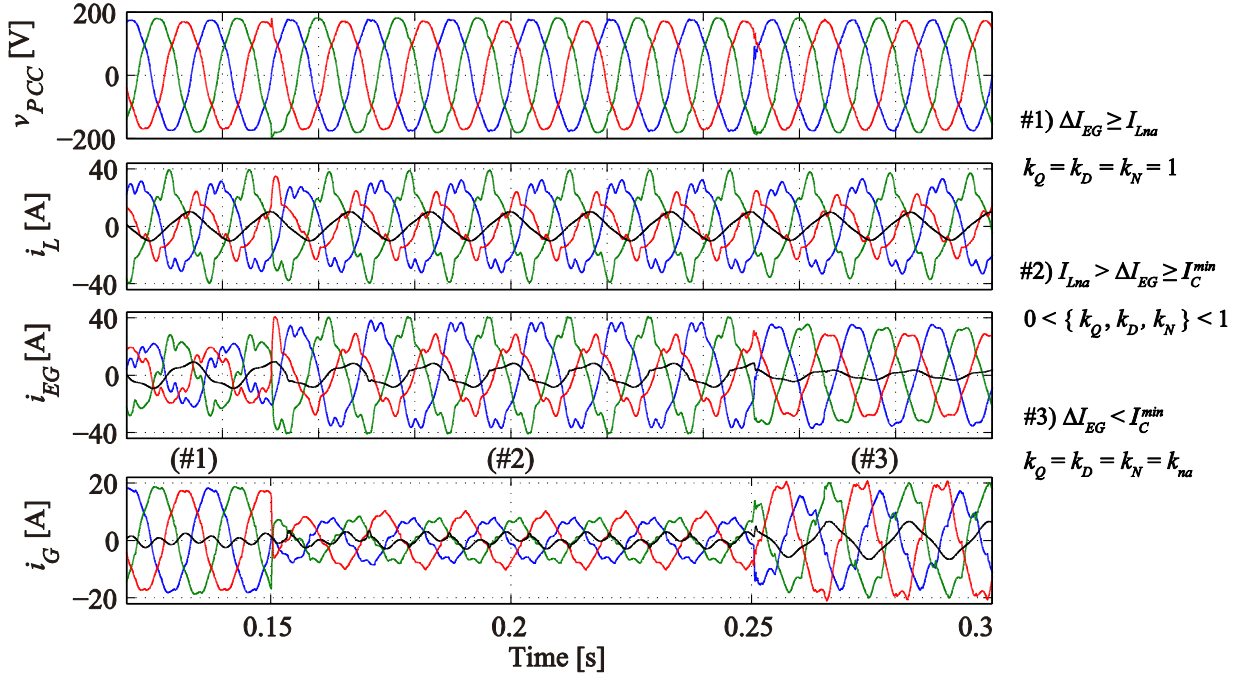

Fig. B.7: Optimized compensation under PES power variation and non-ideal voltages operation. From top to bottom: PCC voltages, load, EG and grid current waveforms.

After 0.15 s (case #2), the PES increases its power generation forcing EG to reduce its compensation rate, operating in optimized compensation in steady state. After 0.25 s (case #3), the power generation increases close to PES nominal value. Thus, EG cannot comply with the preset constraints and must run using (2.28) to compensate as much unwanted currents as possible. We can see the similarities between Fig. B.2 and Fig. B.6; however, they are not identical because the collective value of the load non-active currents has changed from 24.4 A to 26.6 A, respectively. Despite the ΔI_{EG} be equal to both situations, the I_{Lna} variation alters the plane formed by (2.25), consequently, changing the optimal point.

4)   Non-ideal voltage grid variation

To analyze the system performance under distorted PCC voltage and its dynamic response under voltage variation, the previous distorted grid voltages were set to have a 7 % step down PCC voltage reduction at 0.15 s and restored to its nominal value at 0.25 s. Fig. B.8 and Fig. B.9 show the results.

At the begging, the system runs with partial compensation, due to its power capacity. During the voltage reduction, the load demand decreases and the EG moves to a better compensation point, where the optimal solution is $\lambda = 0.99$, $\lambda_Q = 0.08$, $\lambda_D = 0.08$, $\lambda_N = 0.07$. When the grid is restored, the scaling coefficients return to the initial optimal point.

Partial conclusion

The problem formulated as a linear problem used to optimize the compensation of EPPs, usually applied to multi-task DERs under limited capability. Using the proposed method, the DERs are able to compensate reactive power, harmonic distortion and load unbalances, optimizing the results in terms of the most important disturbing phenomena to be minimized, while injecting available active power in case of DERs supplied by intermittent power sources.

The proposed approach takes advantage of the formulated linear problem, based on power quality requirements, to define a set of source performance indices and constraints. It goes beyond other approaches that consider only current constraints. In addition, it enables full exploitation of DERs capability.

The operation dynamics and steady state behavior have been also discussed. The former is dominated by the RMS algorithm used in (2.15) and (2.28), and the latter depends on the implemented control strategy and current controller. However, it is faster than typically DC link voltage regulators applied in DER applications. Finally, it is worth mention that the proposed methodology was applied here to a three-phase system, nevertheless it can be easily adapted to single-phase systems.
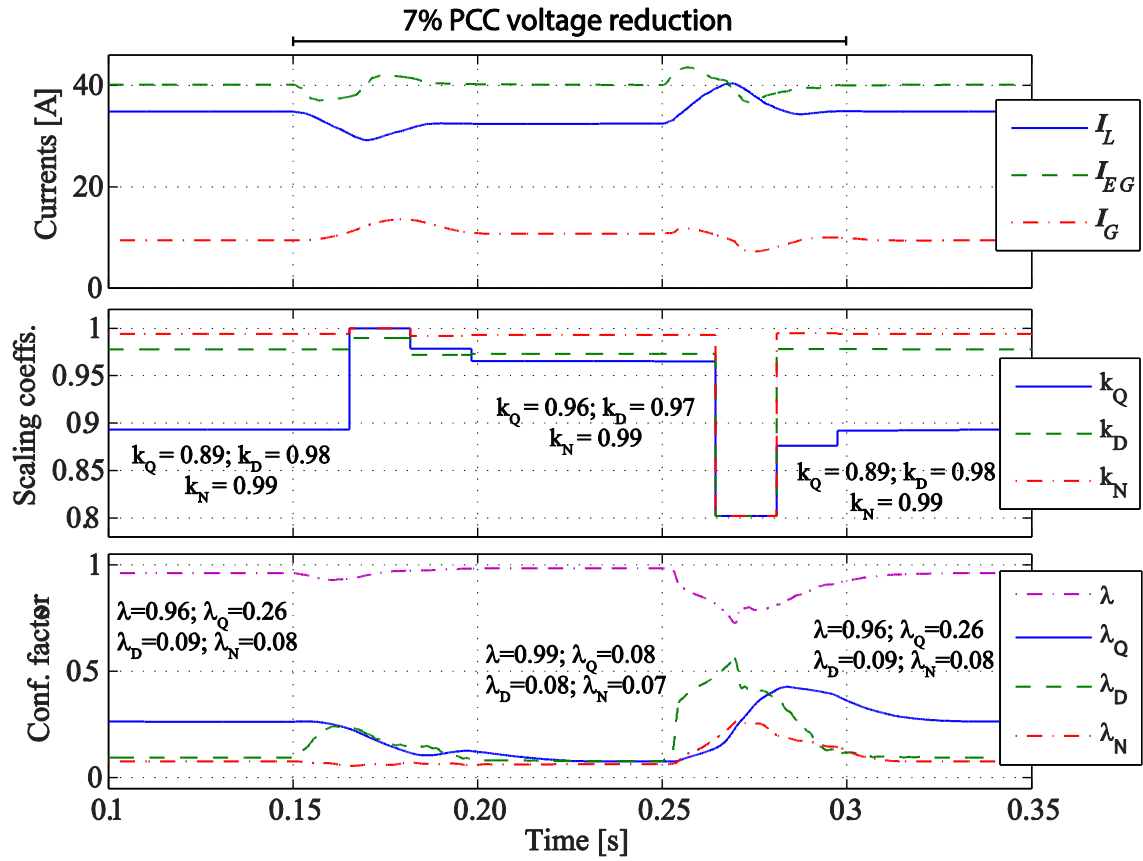
Fig. B.8: Optimized compensation under non-ideal voltage variation. From top to bottom: currents, scaling coefficients and PCC conformity factors.
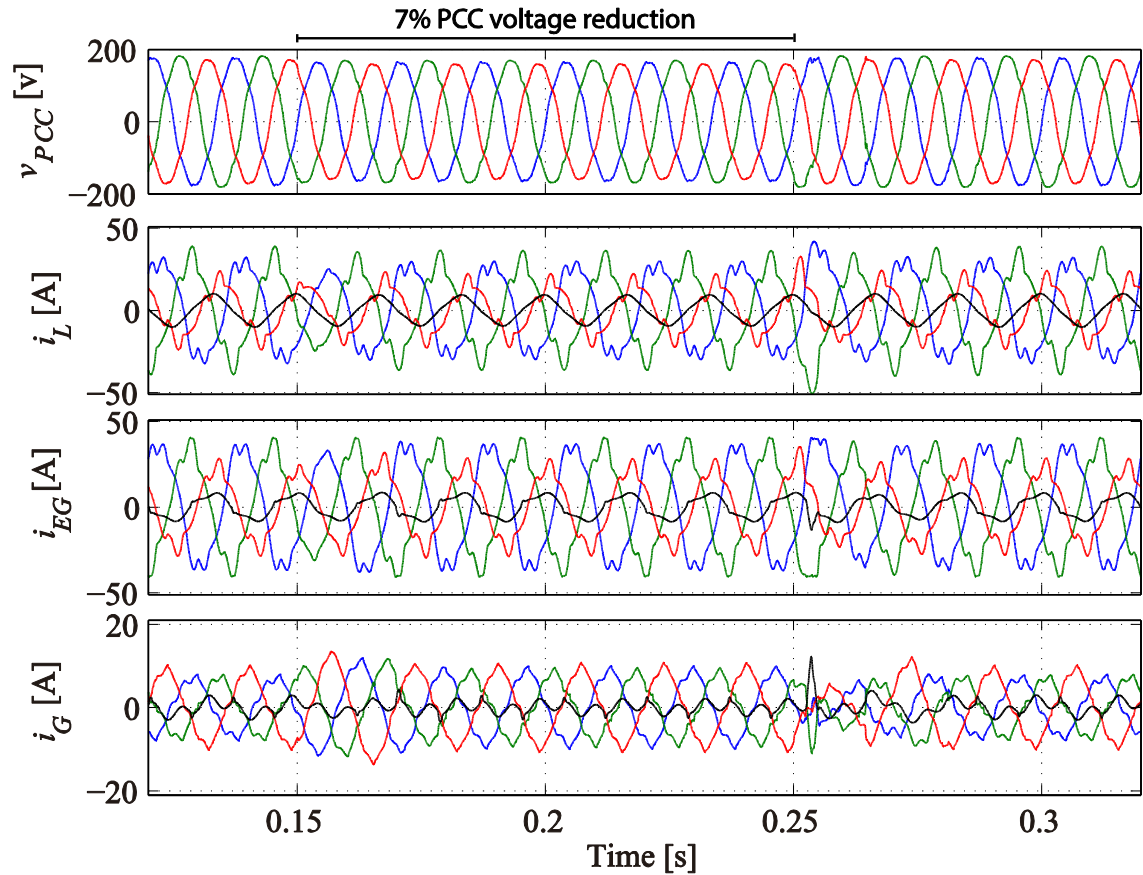

Fig. B.9: Optimized compensation under non-ideal voltage variation. From top to bottom: PCC voltages, load, EG and grid current waveforms.

A. Annex A

% Optimized compensation

A = [1 1 1;1 0 0;-1 (1-λ^*_D^2)/λ^*_D^2 -1;-1 0 (1-λ^*_N^2)/λ^*_N^2;-1 -1 -1;-1 0 0;0 -1 0;0 0 -1];

b = [I^b_a^2.((1-λ^2)/λ^2);I^b_a^2.(λ^*_Q^2/(1-λ^*_Q^2));I^b_a^2; I^b_a^2;-(I_{na}-ΔI_{EG})^2;0;0;0];

x0 = [0;0;0];

x = fmincon(@myfun_optimized_comp, x0, A, b)

function f = myfun_optimized_comp(x)

f = x(1).(I^b_{Lr}^2) + x(2).(I_{Lv}^2) + x(3).(I^u_L^2)

end

% Minimum compensation

x = fmincon(@myfun_minimum_comp, x0, A, b)

function f = myfun_minimum_comp(x)

f = x(1).(-1/I^b_{Lr}^2) + x(2).(-1/I_{Lv}^2) + x(3).(-1/I^u_L^2)

end